TU Delft

Delft University of Technology

Document Version
Final published version

Citation (APA)
Undseth, B. W. (2026). *Engineering silicon spin qubits*. [Dissertation (TU Delft), Delft University of Technology]. https://doi.org/10.4233/uuid:b5bd5ffc-929d-4f40-953a-e4d159708cd7

Important note
To cite this publication, please use the final published version (if applicable).
Please check the document version above.

Copyright
In case the licence states “Dutch Copyright Act (Article 25fa)”, this publication was made available Green Open Access via the TU Delft Institutional Repository pursuant to Dutch Copyright Act (Article 25fa, the Taverne amendment). This provision does not affect copyright ownership.
Unless copyright is transferred by contract or statute, it remains with the copyright holder.

Sharing and reuse
Other than for strictly personal use, it is not permitted to download, forward or distribute the text or part of it, without the consent of the author(s) and/or copyright holder(s), unless the work is under an open content license such as Creative Commons.

Takedown policy
Please contact us and provide details if you believe this document breaches copyrights.
We will remove access to the work immediately and investigate your claim.

This work is downloaded from Delft University of Technology.

Engineering Silicon Spin Qubits

Brennan Undseth



Propositions

accompanying the dissertation

Engineering silicon spin qubits

by

Brennan Wade UNDSETH

1. Operating semiconductor spin qubit devices at 100 mK temperature scales is the easiest means of mitigating pulse-induced resonance shifts and transient changes in rf-reflectometry circuits.
   (*This proposition pertains to this dissertation*)
2. On-chip magnets are a versatile means of engineering semiconductor spin Hamiltonians and should be pursued further.
   (*This proposition pertains to this dissertation*)
3. The reliable implementation of high-fidelity two-qubit gates in multi-qubit devices is the most urgent bottleneck in advancing spin-based quantum processors.
   (*This proposition pertains to this dissertation*)
4. Sparse spin qubit arrays leveraging shuttling are more scalable than dense arrays.
5. The future of controlling spin qubits should be viewed through the lens of “bringing qubits to gates” rather than “bringing gates to qubits”.
6. Basic economic principles are underused in decision-making by research groups, to the detriment of scientific and technological progress.
7. Populist and far-left or far-right parties should be welcomed into, not shut out of, coalition governments to both moderate them and avoid ostracizing their voter base.
8. The European zeitgeist is rightfully critical of many aspects of American culture but is too dismissive of the features that make it uniquely successful.
9. The phrase “paves the way” and similar trite idioms should be banished from scientific writing.

These propositions are regarded as opposable and defendable, and have been approved as such by the promotor Prof. dr. ir. L.M.K. Vandersypen and the copromotor Dr. E. Greplová.

Engineering silicon spin qubits

Engineering silicon spin qubits

Dissertation

for the purpose of obtaining the degree of doctor
at Delft University of Technology
by the authority of the Rector Magnificus, Prof. dr. ir. H. Bijl,
Chair of the Board for Doctorates
to be defended publicly on
Friday, 10 July 2026, at 12:30

by

Brennan Wade UNDSETH

This dissertation has been approved by the promotors.

Composition of the doctoral committee:

Rector Magnificus,	Chairperson
Prof. dr. ir. L.M.K. Vandersypen,	Delft University of Technology, promotor
Dr. E. Greplová,	Delft University of Technology, promotor

Independent members:

Prof. dr. L. DiCarlo,	Delft University of Technology
Prof. dr. ir. M. Veldhorst,	Delft University of Technology
Prof. dr. S.C. Benjamin,	University of Oxford, UK
Dr. T.D. Ladd,	HRL Laboratories, USA
Dr. G. Scappucci,	Delft University of Technology, *reserve member*











Printed by: Gildeprint

Copyright © 2026 by B.W. Undseth

ISBN 978-94-6384-987-6

An electronic copy of this dissertation is available at
https://repository.tudelft.nl/.

Let me not think of my work as a stepping stone to something else.
And if it is, let me become fascinated with the shape of the stone.

-Ze Frank

CONTENTS

Summary xi

Samenvatting xiii

1 Introduction 1
- 1.1 Motivation . . . 2
- 1.2 From quantum mechanics to quantum computation . . . 3
- 1.3 Building a quantum computer from semiconductor-based spins 4
- 1.4 This thesis . . . 5

2 The silicon spin qubit engineer's handbook 15
- 2.1 Overview . . . 16
- 2.2 Prototype spin qubits . . . 16
- 2.3 Single-spin qubit control . . . 18
  - 2.3.1 Resonant Control . . . 19
  - 2.3.2 Diabatic control . . . 22
  - 2.3.3 Fidelity and Decoherence . . . 22
- 2.4 Spin qubits in an inhomogeneous magnetic field . . . 26
  - 2.4.1 Inhomogeneity within a dot: synthetic spin-orbit interaction and electric-dipole spin resonance . . . 26
  - 2.4.2 Inhomogeneity between dots: tunneling and hopping control . . . 31
  - 2.4.3 Conveyor shuttling . . . 33
  - 2.4.4 Controlling many individual spins . . . 35
  - 2.4.5 Two-qubit control . . . 36
  - 2.4.6 Pauli Spin Blockade . . . 40
  - 2.4.7 Simulation strategies . . . 42
- 2.5 Electron spin qubits in silicon . . . 44
  - 2.5.1 Bulk silicon . . . 44
  - 2.5.2 Moving to a strained silicon quantum well . . . 45
  - 2.5.3 Intrinsic spin-orbit interaction . . . 45
  - 2.5.4 Valley physics . . . 48

3 Hotter is easier: unexpected temperature dependence of spin qubit frequencies 65
- 3.1 Introduction . . . 66
- 3.2 Device control and thermalization . . . 67

3.3 Temperature dependence of qubit frequencies 70
3.4 The heating effect 71
3.4.1 Microwave-induced heating 71
3.4.2 Baseband-induced heating 74
3.4.3 Cooling effect 76
3.5 Crosstalk and mitigation 77
3.5.1 Phenomenological picture 77
3.5.2 Benefit of warmer operation 79
3.6 Origin of the temperature dependence 82
3.7 Conclusion 85
3.8 Supplementary material 86
3.8.1 Temperature dependence of rf-reflectometry measurements 86
3.8.2 Probing charge defects and temperature-dependent Stark shifts 88
3.8.3 Electron temperature measurements 92
3.8.4 Spin coherence at 200 mK 93
3.8.5 Exchange interaction and temperature 94

4 Baseband control of single-electron silicon spin qubits in two-dimensions 103
4.1 Introduction 104
4.2 A 2x2 silicon quantum processor based on EDSR 105
4.3 Baseband operation 109
4.4 Architecture proposal 115
4.5 Conclusion 118
4.6 Methods 119
4.6.1 Device design and fabrication 119
4.6.2 Initialization, control, and readout 120
4.6.3 Randomized benchmarking 121
4.6.4 Tip angle fitting 124
4.7 Supplementary material 125
4.7.1 Micromagnet simulations 125
4.7.2 Nanomagnet simulations 128
4.7.3 Sign extraction from crosstalk experiments 128
4.7.4 Estimating the infidelity of resonant qubit control 131
4.7.5 Hopping control and the diabaticity condition 132
4.7.6 Estimating leakage with blind randomized benchmarking 134
4.7.7 Supplementary figures 136

5 Weight-four parity checks in a spin-shuttling architecture 153
5.1 Introduction 154
5.2 Device concept 155
5.3 Remote tuning 157

5.4 QPU characterization . . . 159
5.5 Parity checks . . . 161
5.6 Conclusion . . . 164
5.7 Supplementary material . . . 165
5.7.1 Device fabrication . . . 165
5.7.2 Experimental setup . . . 165
5.7.3 Initial device testing . . . 166
5.7.4 Ancilla readout . . . 167
5.7.5 Conveyor-mode shuttling . . . 170
5.7.6 Single-spin remote tuning . . . 171
5.7.7 Spin reloading . . . 175
5.7.8 QND measurement . . . 176
5.7.9 Universal spin control . . . 179
5.7.10 Gate calibration protocols . . . 181
5.7.11 Single-qubit characterization . . . 186
5.7.12 Two-qubit characterization . . . 188
5.7.13 Error-budget for logical state preparation . . . 189
5.7.14 Quantum state tomography . . . 192
5.7.15 Parity check analysis . . . 196
5.7.16 Electrostatic design . . . 197
5.7.17 Magnetostatic design . . . 200

6 Conclusions and outlook **213**
6.1 The heating effect: redux . . . 214
6.2 Logical spin qubits and more . . . 216
6.3 Low-field and baseband operation . . . 222
6.4 Additional perspectives . . . 227
6.4.1 Readout . . . 227
6.4.2 Two-qubit gate fidelities . . . 227
6.4.3 On-chip magnetic sources . . . 229
6.5 Why single-spins in silicon? . . . 230

Acknowledgements **237**

Curriculum Vitæ **243**

List of Publications **245**

SUMMARY

The dominance of silicon in digital computation inspired the idea that this solid-state environment could also be a “suitable arena” for quantum computation, in the words of Loss and DiVincenzo. Over the past three decades, researchers have established proofs-of-principle that such qubits are adequate for universal quantum computation, and greater attention is now being placed on scaling these demonstrations towards fault-tolerance. Far from being a pejorative “engineering problem”, the versatility with which qubits in the solid-state can now be designed and controlled creates a large canvas upon which to build quantum processors, and the process of marrying idealized architectural visions with real-world constraints demands its own type of creativity.

In this thesis, I present a body of work that advances the degree to which the silicon-based spin qubits proposed by Loss and DiVincenzo can be engineered for performing quantum information processing. In contrast to the state-of-play at the outset of my doctoral work, spin qubits and their interactions can now be controlled with both low- and high-frequency pulses in a variety of geometries, and they can be readily transported on-chip. Chapter 2 summarizes how all of these strategies can be understood through the same practical lens for the purposes of designing larger spin-based processors.

Chapters 3-5 comprise the bulk of my doctoral work. First, the heating effect of control signals on spin qubits is investigated, and it is found that spin qubits can be more easily calibrated and controlled by operating them at slightly warmer temperatures than was previously routine in the field. Next, the operation of spin qubits in two-dimensions is explored. By taking advantage of on-chip magnets, we demonstrate that Loss-DiVincenzo silicon spin qubits can be operated at low magnetic fields with low-frequency baseband pulses, and we show that this opens new architectural paradigms. Finally, a new sparse spin qubit array leveraging coherent spin shuttling is commissioned. With this capstone work, the flexible qubit connectivity is used to demonstrate weight-four parity checks, a key ingredient for implementing quantum error-correction, for the first time with spin qubits.

In the outlook of Chapter 6, I discuss how the advancements in this thesis bring the field to the threshold of implementing logical Loss-DiVincenzo spin qubits. Furthermore, the engineering toolkit has progressed suffi-

ciently far to begin realizing more ambitious fault-tolerant architectures in the silicon arena.

SAMENVATTING

De dominantie van silicium in de klassieke informatietechnologie inspireerde Loss en DiVincenzo tot het idee dat deze vaste-stofomgeving ook een geschikt platform zou kunnen zijn voor kwantumcomputatie. In de afgelopen drie decennia hebben onderzoekers bewijzen geleverd dat dergelijke qubits geschikt zijn voor universele kwantumcomputatie, en er wordt nu meer aandacht besteed aan het opschalen van deze demonstraties tot fouttolerante systemen. Verre van een pejoratief “technisch probleem”, biedt de veelzijdigheid waarmee qubits in vastestofsystemen nu ontworpen en gecontroleerd kunnen worden net een groot speelveld voor de ontwikkeling van kwantumprocessoren. Het combineren van geïdealiseerde architectonische visies met realistische beperkingen vereist een eigen vorm van creativiteit.

In dit proefschrift presenteer ik een reeks onderzoeken die de ontwerpmogelijkheden voor kwantuminformatieverwerking de door Loss en DiVincenzo voorgestelde siliciumgebaseerde spin-qubits uitbreiden. In tegenstelling tot de stand van zaken aan het begin van mijn promotieonderzoek, kunnen spin-qubits en hun interacties nu worden aangestuurd met zowel laag- als hoogfrequente pulsen in verschillende geometrieën, en kunnen ze gemakkelijk over de chip worden getransporteerd. Hoofdstuk 2 vat samen hoe al deze strategieën kunnen worden begrepen vanuit hetzelfde praktische perspectief voor het ontwerpen van grotere spin-gebaseerde processoren.

Hoofdstukken 3-5 vormen het grootste deel van mijn promotieonderzoek. Eerst wordt het opwarmingseffect van stuursignalen op spin-qubits onderzocht, en wordt geconstateerd dat spin-qubits gemakkelijker kunnen worden gekalibreerd en aangestuurd door ze te laten werken bij iets hogere temperaturen dan voorheen gebruikelijk was. Vervolgens wordt de werking van spin-qubits in tweedimensionale geometrieën onderzocht. Door gebruik te maken van geïntegreerde magneten tonen we aan dat Loss-DiVincenzo silicium spin-qubits kunnen worden bediend bij lage magnetische velden met laagfrequente basisbandpulsen, en we laten zien dat dit nieuwe architecturale paradigma’s opent. Ten slotte wordt een nieuwe schaarse spin-qubit-array, waarin coherente spin-shuttling wordt toegepast. In dit afsluitende werk wordt een flexibele qubit-connectiviteit gebruikt om pariteitscontroles met gewicht vier te demonstreren, een essentieel onderdeel voor de implementatie van kwantumfoutcorrectie, dat

voor het eerst met spin-qubits gerealiseerd.

Tot slot bespreek ik in hoofdstuk 6 hoe de vooruitgang in dit proefschrift het vakgebied dichter brengt bij de implementatie van logische Loss-DiVincenzo spin-qubits. De technische toolkit is inmiddels voldoende ontwikkeld om deze volgende stap binnen bereik te brengen.

1

INTRODUCTION

1

1.1. MOTIVATION

Some observers of quantum technology joke that quantum computing risks becoming like fusion energy: a world-changing technology that is always decades away. The basic premise that quantum mechanical principles could be used to solve useful problems dates back to the 1980s. Since then, the Internet was invented, widely-accessible classical computation and communication has overhauled swathes of the economy, and, more recently, artificial intelligence (AI) is disrupting how humans interact with technology. Those uninitiated with the concepts of superposition and entanglement are justified in wondering why they should care about quantum computing.

A first argument is that a quantum computer is something that you would not like your adversary to have if you did not also have one. This argument particularly holds weight for entities like governments and militaries, and it is made tangible by the example of Shor's algorithm, which can efficiently break common encryption algorithms [1].

A second, more enlightened, argument is that quantum computers are scientifically interesting even in the pursuit of their realization and potential applications. This is reinforced by the volume of conferences, publications and grants that allude to "quantum information" and the growing number of people that devote a substantial amount of time pursuing it. Contemporary surveys of quantum algorithms make for sober reading if one stakes their purpose on outcomes and not the process [2, 3]. However, big research teams like Google and IBM continue gnawing away at preliminary applications that hold governments' and investors' interest to the benefit of both fundamental and applied science [4]. Similar to AI, it may be very difficult to prove, in a mathematically rigorous sense, that a quantum computer provides an unquestionable speed-up in useful-problem solving over other methods. But that is a distinct conclusion from a quantum computer being the easiest or most straightforward instrument with which to solve a problem.

A third argument is that building a quantum computer appears to be very difficult. Similar to the race to put humans on the moon, it is a massive, multidisciplinary task that will require lots of public resources but has a fuzzy economic payoff. However, in facing this challenge, new insights can be discovered about the fundamental limits of the universe. As Robin Bluhm-Kohout said during his colloquium at QuTech in 2023, "it must be good for something!"[1]

This dissertation covers a few aspects of stepping towards this goal with single-electron spin qubits confined in silicon quantum dots.

[1] Stated with an exasperated emphasis on "something."

1.2. FROM QUANTUM MECHANICS TO QUANTUM COMPUTATION

The many possible ways to build a quantum computer follow from the widely-applicable theory of quantum mechanics that underpins the microscopic workings of our world. I subscribe to the view, proselytized by Scott Aaronson, that quantum mechanics is, at its essence, a theory of probability where the numbers are permitted to be negative. Because, as far as science knows, the universe behaves in this fundamentally probabilistic way, the *state* of a physical system must be identified like a probability distribution and not by a single number. This abstract statement about probability distributions has profound consequences for the amount of information that is required to keep track of "what's happening". If one tosses a handful of N coins on the ground, it only requires N pieces of information to describe the heads/tails configuration of the result. But expressing the probability distribution for the handful of coins to land in all the possible configurations requires $2^N - 1$ pieces of information. For a handful containing a few hundred coins, this amount of information exceeds the number of atoms in the universe. It is far easier for us mortals to condense this information by assuming each coin has an independent 50% probability of landing on heads or tails.

But Nature, remarkably, keeps track of the coins far more precisely: what was their orientation when they were thrown? And how do they bump into each other as they scatter through the air? If we could control how these degrees of freedom interact with each other precisely enough, we could engineer coin tosses where the coins land all-heads or all-tails. More interestingly, we could engineer the coin tosses to solve answers to very difficult problems, letting Nature's universe-spanning workspace crunch the numbers for us. In fact, this sort of *analog computer* can be used to solve very hard (i.e. NP-complete) problems given the ability to perform operations on real numbers in single time steps [5, 6]. The fundamental problem with such a scheme is the reliance on arbitrarily high precision and the inability to escape the chaos that originates from uncertain initial conditions.

Digital classical computing and quantum computing are distinguished from theoretically-powerful-yet-impractical analog classical computing by the property of being robust against sufficiently small errors [7]. Quantum computing's allure is to provide a compromise of both worlds: access to a large workspace of massive probability distributions and the possibility to be *fault-tolerant* to realistic errors. This does not provide any prescription of how to make a quantum computer useful, but it does provide a framework for how to build one: we need a quantum system with a large probability distribution that is initializable, controllable, measurable, and whose errors are extractable and correctable. In similar words, the

system must satisfy the DiVincenzo criteria [8].

1.3. BUILDING A QUANTUM COMPUTER FROM SEMICONDUCTOR-BASED SPINS

The size of the probability distribution can be quantified in terms of qubits - the quantum analogues to classical coin flips. The operations that can act on the probability distribution can be abstracted as logical gates that act on a subset of the constituent qubits [9]. Generally, the more qubits at one's disposal and the more logical gates that can be performed on them before their probability distribution is lost, the more powerful the resulting quantum computer may be [10]. Given ongoing research on topics such as quantum error correction and algorithm implementations, it is challenging to say what is "good enough". Previous resource estimates for running Shor's factoring algorithm to break a relevant RSA encryption hovered around millions of qubits using billions of quantum gates over the course of days [11], and the specifics will depend heavily on the architecture and physical platform that is used [12]. Very recent work on atomic qubits claims elliptic curve cryptography may be tractable with tens of thousands of qubits [13]. While qubits based on superconducting circuits [14], trapped ions [15], and neutral atoms [16] have achieved impressive demonstrations with hundreds of qubits in recent years, the general consensus is that this count must increase by some orders of magnitude to be able to run the gold-standard quantum algorithms, such as Shor's. Even with enough qubits, the operations must also be fast enough, e.g. MHz instead of kHz, such that an "efficient" quantum computer requires hours, not years, to solve one problem.

One field of technology where such numbers and speeds are not so daunting is the semiconductor industry, where immense scientific progress and industrial investment has resulted in small chips containing billions of nearly-identical transistors (classical bits) that are able to operate quickly and accurately for a long time. Early proposals to make use of the semiconductor platform for quantum computing by Loss & DiVincenzo [17] and Kane [18] acknowledged this potential for scalability, and the field of semiconductor-based qubits has grown enormously in the subsequent years [19–21].

This thesis relates to the specific platform of single-electron spin qubits confined in gate-defined silicon quantum dots[2]. Scaling spin qubits is somewhat of an inverse problem to other platforms. It is not unthinkable to pattern millions of gate electrodes on a single chip, cool it down to

[2] In this thesis, I will often condense this mouthful to simply "spin qubit" and refer to other flavours of donor spins, hole spins, different encodings and material platforms, etc. explicitly when intended

millikelvin temperatures, apply a constant voltage to them to accumulate a million isolated charges, turn on a magnetic field, and "have" a million qubits on a little chip. In fact, projects to statistically characterize semiconductor qubits *en masse* take this approach [22].

The problems arise when we must control, interact, and measure them as is necessary for quantum computation. Around the beginning of my PhD, these problems had largely been addressed at the few-qubit level. The field of semiconductor-based spin qubits did not start with silicon: progress could leverage the extensive body of knowledge and experience built in the GaAs platform, which, although atomically clean, is filled with non-zero nuclear spins which make for a noisy environment for electron spins [23]. With relatively minor technical adaptations, demonstrations of universal qubit control in silicon have scaled from 1 [24, 25] to 2 [26–28], to 3 [29], to 6 [30] over the previous decade, and the first demonstrations of industrially-fabricated spin qubits were made [31, 32]. The quality of the operations had also steadily improved to exceed 99.9% for single-qubit logical gates [33, 34] and 99% fidelity for two-qubit logical gates [35–37]. Fast and reasonably high-fidelity measurement had been established at the few-qubit scale [38, 39].

Ideas for how to integrate these essential few-qubit ingredients in the large-scale existed in similar proof-of-principle ways. The notion of coupling qubits at a larger distance to make space for co-integrated control electronics had existed for some time [40, 41], with the two most prominent ideas being a resonator-mediated coupling [42, 43] and direct spin-carrier shuttling [44]. That these qubits could be operated at "hot" temperatures on the order of 1 K [45, 46] and offer some degree of co-integration with classical electronics [47] was promising.

The lack of any firm roadblock is a good start. However, the field was far from reaching a consensus on a particular blueprint that could be sent to an industrial semiconductor fabrication facility with the expectation of receiving a functioning fault-tolerant quantum computer [48–52]. It is the collective task of the field to answer the big question of how we move from few-qubit demonstrations to the millions of usefully-connected qubits we'd like to see. This dissertation tries to keep the ball rolling on a good path.

1.4. THIS THESIS

My PhD began with the good fortune of inheriting the state-of-the-art six-qubit device reported in [30] and trying to answer the question: "what comes next?" The answer is provided in three central pieces of original work. The unifying theme is that they all add elements to the toolkit available for engineering subsequent generations of silicon spin qubit devices. As such, Chapter 2 will introduce the key theoretical building

blocks that have been essential in this pursuit.

Chapter 3 addresses one of the must urgent limitations of silicon spin qubits: the so-called “heating effect”. This effect is believed to originate from the dissipation of necessary control signals and decreases the quality with which qubits can be controlled. It is challenging to compensate for, and the problems only compound as more qubits are added. We present a simple solution that has, for the most part, withstood the test of time and spurred continued research into the physical mechanism of the heating effect.

Chapter 4 tackles a dimensionality problem that was common to all silicon spin qubit demonstrations up to 2021. All such processors have been linear arrays, and scaling in a line is of limited use for qubits that can only interact with their nearest neighbours. Here, a 2x2 array of silicon spin qubits is demonstrated as a minimal two-dimensional example. Moreover, this experiment provided a playground for what can be done with on-chip magnets for engineering spin qubit Hamiltonians in the second dimension, and we use this freedom to explore baseband-controlled hopping spins in silicon for the first time.

Chapter 5 is the *pièce de résistance* of this dissertation. It provides a ground-up example of engineering silicon spin qubits and gives a tangible solution to the question “what comes next?” in two parts. First, we implement a surface code plaquette capable of weight-four parity checks. This provides an essential step towards implementing quantum error correction with silicon spin qubits. Second, the new device leverages qubit shuttling in a sparse array. This confers unique advantages over previous dense arrays, but it also requires a new approach to tuning and operation. The methods we develop are, compared to existing protocols, straightforward to extend from N to $N+1$, and they allow for modular optimization.

The work of this thesis did not occur in a vacuum, and many contemporary developments have greatly influenced the core topic of this dissertation. The advent of high-fidelity coherent spin shuttling over greater distances than was possible in 2021 is one such example [53]. That shuttling coincides with theoretical advances in error correction (e.g. “good” qLDPC codes [54]) and experimental advances in reconfigurable qubit arrays (e.g. neutral atoms [55]) has made such progress all the more relevant. Within the semiconductor spin qubit world, large strides have also been made with spin qubits of different flavours, most notably work on exchange only qubits by Intel and HRL Laboratories, hole spins in germanium by QuTech [56], and phosphorus donors by Silicon Quantum Computing and Shenzhen [57, 58]. In Chapter 6, I will outline how the work presented here stands in 2026, and I will begin to probe the question: “what comes after this?”

REFERENCES

[1] P. Shor. “Algorithms for quantum computation: discrete logarithms and factoring”. In: *Proceedings 35th Annual Symposium on Foundations of Computer Science*. 1994, pp. 124–134. doi: 10.1109/SFCS.1994.365700.

[2] K. Bharti *et al.* “Noisy intermediate-scale quantum algorithms”. In: *Rev. Mod. Phys.* 94 (1 Feb. 2022), p. 015004. doi: 10.1103/RevModPhys.94.015004. url: https://link.aps.org/doi/10.1103/RevModPhys.94.015004.

[3] A. M. Dalzell *et al. Quantum algorithms: A survey of applications and end-to-end complexities*. 2023. arXiv: 2310.03011 [quant-ph]. url: https://arxiv.org/abs/2310.03011.

[4] G. Q. AI and Collaborators. “Observation of constructive interference at the edge of quantum ergodicity”. en. In: *Nature* 646.8086 (Oct. 2025), pp. 825–830. issn: 1476-4687. doi: 10.1038/s41586-025-09526-6.

[5] A. Schönhage. “On the power of random access machines”. In: *Automata, Languages and Programming*. Ed. by H. A. Maurer. Berlin, Heidelberg: Springer Berlin Heidelberg, 1979, pp. 520–529. isbn: 978-3-540-35168-9.

[6] S. Aaronson. *NP-complete Problems and Physical Reality*. 2005. arXiv: quant-ph/0502072 [quant-ph]. url: https://arxiv.org/abs/quant-ph/0502072.

[7] S. Aaronson. *Quantum Computing since Democritus*. Cambridge University Press, 2013.

[8] D. P. DiVincenzo. *Topics in Quantum Computers*. 1996. arXiv: cond-mat/9612126 [cond-mat.mes-hall]. url: https://arxiv.org/abs/cond-mat/9612126.

[9] M. A. Nielsen and I. L. Chuang. *Quantum Computation and Quantum Information: 10th Anniversary Edition*. Cambridge University Press, 2010.

[10] A. W. Cross *et al.* “Validating quantum computers using randomized model circuits”. In: *Phys. Rev. A* 100 (3 Sept. 2019), p. 032328. doi: 10.1103/PhysRevA.100.032328. url: https://link.aps.org/doi/10.1103/PhysRevA.100.032328.

[11] C. Gidney and M. Ekerå. “How to factor 2048 bit RSA integers in 8 hours using 20 million noisy qubits”. In: *Quantum* 5 (Apr. 2021), p. 433. issn: 2521-327X. doi: 10.22331/q-2021-04-15-433. url: http://dx.doi.org/10.22331/q-2021-04-15-433.

[12] R. V. Meter, K. M. Itoh, and T. D. Ladd. *Architecture-Dependent Execution Time of Shor’s Algorithm*. 2006. arXiv: quant-ph/0507023 [quant-ph]. url: https://arxiv.org/abs/quant-ph/0507023.

[13] M. Cain *et al. Shor’s algorithm is possible with as few as 10,000 reconfigurable atomic qubits*. 2026. arXiv: 2603.28627 [quant-ph]. url: https://arxiv.org/abs/2603.28627.

[14] G. Q. AI. “Suppressing quantum errors by scaling a surface code logical qubit”. en. In: *Nature* 614.7949 (Feb. 2023), pp. 676–681. issn: 1476-4687. doi: 10.1038/s41586-022-05434-1.

[15] S. A. Moses *et al.* “A Race-Track Trapped-Ion Quantum Processor”. In: *Phys. Rev. X* 13 (4 Dec. 2023), p. 041052. doi: 10.1103/PhysRevX.13.041052. url: https://link.aps.org/doi/10.1103/PhysRevX.13.041052.

[16] D. Bluvstein *et al.* “Logical quantum processor based on reconfigurable atom arrays”. en. In: *Nature* 626.7997 (Feb. 2024), pp. 58–65. issn: 1476-4687. doi: 10.1038/s41586-023-06927-3.

[17] D. Loss and D. P. DiVincenzo. “Quantum computation with quantum dots”. In: *Phys. Rev. A* 57 (1 Jan. 1998), pp. 120–126. doi: 10.1103/PhysRevA.57.120. url: https://link.aps.org/doi/10.1103/PhysRevA.57.120.

[18] B. E. Kane. “A silicon-based nuclear spin quantum computer”. en. In: *Nature* 393.6681 (May 1998), pp. 133–137. issn: 1476-4687. doi: 10.1038/30156.

[19] R. Hanson *et al.* “Spins in few-electron quantum dots”. In: *Reviews of Modern Physics* 79.4 (Oct. 2007), pp. 1217–1265. issn: 1539-0756. doi: 10.1103/revmodphys.79.1217. url: http://dx.doi.org/10.1103/RevModPhys.79.1217.

[20] F. A. Zwanenburg *et al.* “Silicon quantum electronics”. In: *Rev. Mod. Phys.* 85 (3 July 2013), pp. 961–1019. doi: 10.1103/RevModPhys.85.961. url: https://link.aps.org/doi/10.1103/RevModPhys.85.961.

[21] G. Burkard *et al.* “Semiconductor spin qubits”. In: *Rev. Mod. Phys.* 95 (2 June 2023), p. 025003. doi: 10.1103/RevModPhys.95.025003. url: https://link.aps.org/doi/10.1103/RevModPhys.95.025003.

[22] A. Tosato *et al. QARPET: A Crossbar Chip for Benchmarking Semiconductor Spin Qubits*. 2025. arXiv: 2504.05460 [cond-mat.mes-hall]. url: https://arxiv.org/abs/2504.05460.

[23] R. Hanson *et al.* “Spins in few-electron quantum dots”. In: *Reviews of Modern Physics* 79.4 (Oct. 2007), pp. 1217–1265. issn: 1539-0756. url: http://dx.doi.org/10.1103/RevModPhys.79.1217.

[24] M. Veldhorst *et al.* “An addressable quantum dot qubit with fault-tolerant control-fidelity”. In: *Nature Nanotechnology* 9.12 (Oct. 2014), pp. 981–985. issn: 1748-3395. doi: 10.1038/nnano.2014.216. url: http://dx.doi.org/10.1038/nnano.2014.216.

[25] E. Kawakami *et al.* “Electrical control of a long-lived spin qubit in a Si/SiGe quantum dot”. In: *Nature Nanotechnology* 9.9 (Aug. 2014), pp. 666–670. issn: 1748-3395. doi: 10.1038/nnano.2014.153. url: http://dx.doi.org/10.1038/nnano.2014.153.

[26] M. Veldhorst *et al.* “A two-qubit logic gate in silicon”. In: *Nature* 526.7573 (Oct. 2015), pp. 410–414. issn: 1476-4687. doi: 10.1038/nature15263. url: http://dx.doi.org/10.1038/nature15263.

[27] T. F. Watson *et al.* “A programmable two-qubit quantum processor in silicon”. In: *Nature* 555.7698 (Feb. 2018), pp. 633–637. issn: 1476-4687. doi: 10.1038/nature25766. url: http://dx.doi.org/10.1038/nature25766.

[28] D. M. Zajac *et al.* “Resonantly driven CNOT gate for electron spins”. In: *Science* 359.6374 (Jan. 2018), pp. 439–442. issn: 1095-9203. doi: 10.1126/science.aao5965. url: http://dx.doi.org/10.1126/science.aao5965.

[29] K. Takeda *et al.* “Quantum tomography of an entangled three-qubit state in silicon”. In: *Nature Nanotechnology* 16.9 (June 2021), pp. 965–969. issn: 1748-3395. doi: 10.1038/s41565-021-00925-0. url: http://dx.doi.org/10.1038/s41565-021-00925-0.

[30] S. G. J. Philips *et al.* “Universal control of a six-qubit quantum processor in silicon”. In: *Nature* 609.7929 (Sept. 2022), pp. 919–924. issn: 1476-4687. doi: 10.1038/s41586-022-05117-x. url: http://dx.doi.org/10.1038/s41586-022-05117-x.

[31] R. Maurand *et al.* “A CMOS silicon spin qubit”. In: *Nature Communications* 7.1 (Nov. 2016). issn: 2041-1723. doi: 10.1038/ncomms13575. url: http://dx.doi.org/10.1038/ncomms13575.

[32] A. M. J. Zwerver *et al.* “Qubits made by advanced semiconductor manufacturing”. In: *Nature Electronics* 5.3 (Mar. 2022), pp. 184–190. issn: 2520-1131. doi: 10.1038/s41928-022-00727-9. url: http://dx.doi.org/10.1038/s41928-022-00727-9.

[33] J. Yoneda *et al.* “A quantum-dot spin qubit with coherence limited by charge noise and fidelity higher than 99.9%”. In: *Nature Nanotechnology* 13.2 (Dec. 2017), pp. 102–106. issn: 1748-3395. doi: 10.1038/s41565-017-0014-x. url: http://dx.doi.org/10.1038/s41565-017-0014-x.

[34] C. H. Yang *et al.* “Silicon qubit fidelities approaching incoherent noise limits via pulse engineering”. In: *Nature Electronics* 2.4 (Apr. 2019), pp. 151–158. issn: 2520-1131. doi: 10.1038/s41928-019-0234-1. url: http://dx.doi.org/10.1038/s41928-019-0234-1.

[35] X. Xue *et al.* “Quantum logic with spin qubits crossing the surface code threshold”. In: *Nature* 601.7893 (Jan. 2022), pp. 343–347. issn: 1476-4687. doi: 10.1038/s41586-021-04273-w. url: http://dx.doi.org/10.1038/s41586-021-04273-w.

[36] A. Noiri *et al.* “Fast universal quantum gate above the fault-tolerance threshold in silicon”. In: *Nature* 601.7893 (Jan. 2022), pp. 338–342. issn: 1476-4687. doi: 10.1038/s41586-021-04182-y. url: http://dx.doi.org/10.1038/s41586-021-04182-y.

[37] A. R. Mills *et al.* “Two-qubit silicon quantum processor with operation fidelity exceeding 99%”. In: *Science Advances* 8.14 (Apr. 2022). issn: 2375-2548. doi: 10.1126/sciadv.abn5130. url: http://dx.doi.org/10.1126/sciadv.abn5130.

[38] G. Zheng *et al.* “Rapid gate-based spin read-out in silicon using an on-chip resonator”. In: *Nature Nanotechnology* 14.8 (July 2019), pp. 742–746. issn: 1748-3395. doi: 10.1038/s41565-019-0488-9. url: http://dx.doi.org/10.1038/s41565-019-0488-9.

[39] Y.-Y. Liu *et al.* “Radio-Frequency Reflectometry in Silicon-Based Quantum Dots”. In: *Physical Review Applied* 16.1 (July 2021). issn: 2331-7019. doi: 10.1103/physrevapplied.16.014057. url: http://dx.doi.org/10.1103/PhysRevApplied.16.014057.

[40] J. M. Taylor *et al.* “Fault-tolerant architecture for quantum computation using electrically controlled semiconductor spins”. In: *Nature Physics* 1.3 (Dec. 2005). Citation Key: Taylor2005, pp. 177–183. issn: 17452481. doi: 10.1038/nphys174.

[41] L. M. K. Vandersypen *et al.* “Interfacing spin qubits in quantum dots and donors—hot, dense, and coherent”. In: *npj Quantum Information* 3.1 (Sept. 2017). issn: 2056-6387. doi: 10.1038/s41534-017-0038-y. url: http://dx.doi.org/10.1038/s41534-017-0038-y.

[42] F. Borjans *et al.* “Resonant microwave-mediated interactions between distant electron spins”. In: *Nature* 577.7789 (Dec. 2019), pp. 195–198. issn: 1476-4687. doi: 10.1038/s41586-019-1867-y. url: http://dx.doi.org/10.1038/s41586-019-1867-y.

[43] P. Harvey-Collard *et al.* “Coherent Spin-Spin Coupling Mediated by Virtual Microwave Photons”. In: *Physical Review X* 12.2 (May 2022). issn: 2160-3308. doi: 10.1103/physrevx.12.021026. url: http://dx.doi.org/10.1103/PhysRevX.12.021026.

[44] J. Yoneda *et al.* “Coherent spin qubit transport in silicon”. In: *Nature Communications* 12.1 (July 2021). issn: 2041-1723. doi: 10.1038/s41467-021-24371-7. url: http://dx.doi.org/10.1038/s41467-021-24371-7.

[45] L. Petit *et al.* “Universal quantum logic in hot silicon qubits”. In: *Nature* 580.7803 (Apr. 2020), pp. 355–359. issn: 1476-4687. doi: 10.1038/s41586-020-2170-7. url: http://dx.doi.org/10.1038/s41586-020-2170-7.

[46] C. H. Yang *et al.* “Operation of a silicon quantum processor unit cell above one kelvin”. In: *Nature* 580.7803 (Apr. 2020), pp. 350–354. issn: 1476-4687. doi: 10.1038/s41586-020-2171-6. url: http://dx.doi.org/10.1038/s41586-020-2171-6.

[47] X. Xue *et al.* “CMOS-based cryogenic control of silicon quantum circuits”. In: *Nature* 593.7858 (May 2021), pp. 205–210. issn: 1476-4687. doi: 10.1038/s41586-021-03469-4. url: http://dx.doi.org/10.1038/s41586-021-03469-4.

[48] M. Veldhorst *et al.* “Silicon CMOS architecture for a spin-based quantum computer”. In: *Nature Communications* 8.1 (Dec. 2017). issn: 2041-1723. doi: 10.1038/s41467-017-01905-6. url: http://dx.doi.org/10.1038/s41467-017-01905-6.

[49] R. Li *et al.* “A crossbar network for silicon quantum dot qubits”. In: *Science Advances* 4.7 (July 2018). issn: 2375-2548. doi: 10.1126/sciadv.aar3960. url: http://dx.doi.org/10.1126/sciadv.aar3960.

[50] B. Buonacorsi *et al.* “Network architecture for a topological quantum computer in silicon”. In: *Quantum Science and Technology* 4.2 (Jan. 2019), p. 025003. issn: 2058-9565. doi: 10.1088/2058-9565/aaf3c4. url: http://dx.doi.org/10.1088/2058-9565/aaf3c4.

[51] M. Tadokoro *et al.* “Designs for a two-dimensional Si quantum dot array with spin qubit addressability”. en. In: *Scientific Reports* 11.11 (Sept. 2021), p. 19406. issn: 2045-2322. doi: 10.1038/s41598-021-98212-4.

[52] J. M. Boter *et al.* “Spiderweb Array: A Sparse Spin-Qubit Array”. In: *Physical Review Applied* 18.2 (Aug. 2022). issn: 2331-7019. doi: 10.1103/physrevapplied.18.024053. url: http://dx.doi.org/10.1103/PhysRevApplied.18.024053.

[53] M. De Smet *et al.* “High-fidelity single-spin shuttling in silicon”. In: *Nature Nanotechnology* 20.7 (June 2025), pp. 866–872. issn: 1748-3395. url: http://dx.doi.org/10.1038/s41565-025-01920-5.

[54] T. J. Yoder *et al.* *Tour de gross: A modular quantum computer based on bivariate bicycle codes*. 2025. arXiv: 2506.03094 [quant-ph]. url: https://arxiv.org/abs/2506.03094.

[55] D. Bluvstein *et al.* “A fault-tolerant neutral-atom architecture for universal quantum computation”. en. In: *Nature* 649.8095 (Jan. 2026), pp. 39–46. issn: 1476-4687. doi: 10.1038/s41586-025-09848-5.

[56] J. J. Dijkema *et al.* *Simultaneous operation of an 18-qubit modular array in germanium*. 2026. arXiv: 2604.01063 [cond-mat.mes-hall]. url: https://arxiv.org/abs/2604.01063.

[57] H. Edlbauer *et al.* “An 11-qubit atom processor in silicon”. en. In: *Nature* 648.8094 (Dec. 2025), pp. 569–575. issn: 1476-4687. doi: 10.1038/s41586-025-09827-w.

[58] C. Zhang *et al.* “Universal logical operations in a silicon quantum processor”. en. In: *Nature Nanotechnology* (Mar. 2026), pp. 1–7. issn: 1748-3395. doi: 10.1038/s41565-026-02140-1.

2

THE SILICON SPIN QUBIT ENGINEER'S HANDBOOK

Most of the analysis in this chapter can be verified or built on from the Mathematica notebook saved on the group's network drive along with the source for this thesis.

2.1. OVERVIEW

Silicon spins are an appealing canvas upon which to engineer qubits because their properties are dominated by features we choose to add to devices rather than what they inherit from the devices intrinsically. I begin describing silicon spin qubits in the simplest textbook picture to which nearly everything can be conceptually reduced. Then, I introduce the ways we can engineer the spin Hamiltonian with inhomogeneous magnetic fields. This forms the picture through which the most advanced semiconductor spin qubit devices to date can be understood. Finally, I survey the physics intrinsic to silicon spin qubits that is generally beyond our ability control. Understanding what can and cannot be engineered ultimately determines the most robust design strategies for future silicon spin devices.

Silicon spin qubits are well-studied systems, and rigorous theoretical descriptions and experimental surveys can be readily found in recent reviews and the references therein [1, 2]. QTCAD, although itself proprietary software, provides freely-available documentation on how to rigorously model silicon spin qubits [3]. Erika Kawakami's thesis [4] also provides a very thorough introduction to the characterization of individual silicon spin qubits and remains valuable for experimentalists. In the spirit of avoiding unnecessary repetition, the tone of this chapter will be more applied and focus on rules-of-thumb and back-of-the-envelope calculations that are not so easy to identify in the scientific literature.

2.2. PROTOTYPE SPIN QUBITS

We first focus on a generic representation of an electron spin qubit confined in the conduction band of some solid-state material platform (ideally one compatible with industrial fabrication). An unconditional request we make of the material platform is that it confines the electron's wavefunction in at least one spatial direction; it is impossible to confine a charged particle with static fields alone. We consider confinement along the z-coordinate, so that we may separate the spatial wavefunction as $\psi(\mathbf{r}) = \psi(x, y)\psi(z)$. Ideally, $\psi(z)$ will be the ground eigenstate of a 1D quantum well that is sufficiently thin such that there are no relevant dynamics in this sector.

The Hamiltonian for the confined spin-1/2 electrons can be written using an effective mass approximation [2]:

$$H_{\text{EMA}} = \frac{\mathbf{p}^2}{2m^*} + V(x, y) + g\mu_B \mathbf{B} \cdot \mathbf{S} \tag{2.1}$$

where m^* is the effective mass of the electron confined in the x-y plane, p is the momentum operator, $V(x, y)$ is the electrostatic confinement

potential, g is the scalar effective g-factor of the spin-1/2 particle, μ_B is the Bohr magneton, $\mathbf{B}$ is the external magnetic field, and $\mathbf{S}$ is the spin-1/2 operator. As we are already assuming that both the effective mass and g-tensor are isotropic in this hypothetical platform, Eq. 2.1 is about as close to a textbook problem as we can get.

The electrostatic potential $V(x,y)$ is generated by patterned gate electrodes and can be simulated directly using a Poisson solver accompanying a faithful finite-element model of the device geometry. The stray electrostatic potential for a well-defined quantum dot must be locally harmonic, and therefore the single-electron solutions for localized potentials $V(x,y) = V(r,\phi) = \frac{m^*\omega_0}{2}r^2$ should form a good basis set for treating the multi-electron Hamiltonian[1]. The spatial wavefunctions satisfying this potential are the Fock-Darwin states [5, 6]:

$$\psi_{N,M}(r,\phi) = \frac{1}{a_0}\sqrt{\frac{N!}{\pi(N+|M|)!}}e^{-iM\phi}\left(\frac{r}{a_0}\right)^{|M|}e^{-r^2/2a_0^2}L_N^{|M|}\left(\frac{r^2}{a_0^2}\right), \tag{2.2}$$

written in cylindrical coordinates where $r^2 = x^2 + y^2$ and $\phi = \tan^{-1}(y/x)$. $N = 0, 1, 2, \ldots$ is the principal quantum number and $M = 0, \pm1, \pm2, \ldots$ is the azimuthal quantum number. $\mathcal{L}_N^{|M|}$ is the generalized Laguerre polynomial and $a_0 = \sqrt{\hbar/m^*\omega_0}$ provides a natural length scale. The energy levels are given by:

$$E_{N,M} = \hbar\omega_0(2N + |M| + 1). \tag{2.3}$$

For the ground state $N = M = 0$, Eq. 2.2 simplifies to a normalized 2D Gaussian distribution. For state-of-the-art silicon quantum dots where m^* is 19% of the free electron mass m_e, the orbital energy spacing $\hbar\omega_0 \approx 3$ meV and length scale $a_0 \approx 10$ nm (see Chapter 5 for an explicit example).

This basis of single-electron states of spin s localized at site i is useful for writing the Fermi-Hubbard Hamiltonian in terms of the respective electron creation and annihilation operators $c_{i,s}^\dagger$ and $c_{i,s}$:

$$H_{\mathrm{FH}} = \sum_{i,s}\mu_i c_{i,s}^\dagger c_{i,s} + \sum_{i,j,s}t_{c,ij}c_{i,s}^\dagger c_{j,s} + \sum_i U_i c_{i,\uparrow}^\dagger c_{i,\uparrow}c_{i,\downarrow}^\dagger c_{i,\downarrow} + g\mu_B \mathrm{B}\cdot\sum_i \mathrm{S_i} \tag{2.4}$$

Eq. 2.4 describes a system of weakly-coupled quantum dots and introduces the most important language for translating between theory

[1] In particular, we will be interested in relatively weak and predominantly in-plane magnetic fields such that the confinement harmonicity ω_0 is much larger than the cyclotron frequency. We also expect the dot-to-dot separation to be large with respect to the length scale $a_0 = \sqrt{\hbar/m^*\omega_0}$ of the confined wavefunctions.

and experiment. The first term describes the electrochemical potential μ_i of each individual quantum dot at location i relative to others, the second term describes the bare tunnel coupling $t_{c,ij}$ between quantum dots at locations i and j, and the third term describes the charging energy U_i required to place two electrons at location i. The fourth term is the Zeeman component operating on the spin state at each site[2]. In state-of-the-art silicon quantum dots, $U \approx 12$ meV, t_c may be controlled from effectively zero to the order of tens of μeV, and differences between the adjacent electrochemical potentials μ_i are tunable beyond the energy scale of U to permit transferring charges between dots.

Eq. 2.4 can be expanded into the Heisenberg spin Hamiltonian to make explicit the exchange interaction arising from the fermionic nature of the spin-1/2 electrons in singly-occupied quantum dots [7]:

$$H_{\mathrm{H}} = \sum_{i,j} J_{i,j} \mathbf{S}_i \cdot \mathbf{S}_j + g\mu_B \mathbf{B} \cdot \sum_i \mathbf{S}_i. \tag{2.5}$$

where $J_{i,j}$ is the exchange energy that separates the singlet and triplet spin states of two coupled and singly occupied quantum dots.[3] For a double dot system with $\mu_i = \mu_j$, $t_{c,ij} = t_c$ and $U_i = U_j = U$, $J_{i,j} \approx t_c^2/4U$ follows from perturbation theory (see Sec. 2.4.5).

2.3. SINGLE-SPIN QUBIT CONTROL

With Eq. 2.5 alone, one can encode exchange-only (EO) qubits, construct a universal gate set, and not have to worry about controlling individual spins [8]. However, there are many benefits to being able to control spins individually, and it permits using the Heisenberg exchange interaction to implement two-qubit logic between single-spin qubits.

The first order of business is to establish what the qubit is. This sounds (and is) trivial, but a substantial amount of time can be lost if one is inconsistent. This is particularly relevant for translating to and from the rotating frame, and the proliferation of spin shuttling means this is becoming more and more common. The conventional spin operator S_z acts on spin states as $S_z|\downarrow\rangle = -\frac{\hbar}{2}|\downarrow\rangle$, $S_z|\uparrow\rangle = \frac{\hbar}{2}|\uparrow\rangle$, and the states are labeled according to their orientation with respect to the orientation of the magnetic field $\mathbf{B}$ they are placed in [9]. Using the convention of a positive g-factor, $|\downarrow\rangle$ is the lower energy eigenstate. Since quantum information

[2] Note that electron-electron interactions between adjacent dots and excited orbital states will also contribute higher-order terms.

[3] Eq. 2.5 is truncated and in general higher-order multispin terms will arise that depend not only on the Fermi-Hubbard parameters but also on the magnetic flux passing through a closed loop of tunnel-coupled spins. The model will also cease to hold if the cyclotron frequency begins to compete with the harmonic confinement, but this is not the regime of interest here.

theorists typically talk about T_1 relaxation from the $|1\rangle$ qubit state to the $|0\rangle$ qubit state, it is logical to map $|\downarrow\rangle$ to $|0\rangle$. But quantum information theorists also have a habit of placing $|0\rangle$ at the top of the Bloch sphere such that it is the +1 eigenstate of the Pauli operator σ_z [10]. The most sensical thing to do is define our Loss-DiVincenzo qubit operators (i.e. the Pauli operators) in terms of the spin operators such that:

$$\sigma_z = -\frac{2}{\hbar} S_z, \tag{2.6}$$

and conventionally orient the total magnetic field vector along the positive z-axis, or "quantization axis". Theoretically, one is free to work in whatever basis they like as long as they are self-consistent. Experimentally, this choice of sign manifests in the hardware when one decides (consciously or not) how phases add up to perform virtual-Z rotations in the rotating frame.

We can now rewrite the Heisenberg Hamiltonian in terms of the qubit (Pauli) operators and assign $\hbar = 1$:

$$H_{\mathrm{H}} = \sum_{ij} 2\pi J_{ij} \left(\frac{\sigma_i \cdot \sigma_j}{4} - \frac{1}{4} \right) - \sum_i \frac{1}{2} g\mu_B \mathbf{B} \cdot \sigma_i, \tag{2.7}$$

and we may consider the limit of no exchange and a single spin as the Zeeman Hamiltonian:

$$H_Z = -\frac{1}{2} g\mu_B \mathbf{B} \cdot \sigma. \tag{2.8}$$

In a constant magnetic field, it is useful to identify the Larmor frequency $\omega_L = g\mu_B|\mathbf{B}|/\hbar$ and the Zeeman energy $E_Z = \hbar\omega_L$. For our prototypical spin qubit, the only control parameter is the magnetic field. In theory, we can use the magnetic field to produce whatever 2x2 Hamiltonian our heart desires. In practice, there are two cases which warrant a deeper dive: resonant and diabatic control.

2.3.1. RESONANT CONTROL

In the first case, we consider a time-dependent oscillatory magnetic field $\mathbf{B} = (\Omega \cos(\omega_{\mathrm{MW}} t + \phi), 0, \omega_L)^T / g\mu_B$ that induces electron spin resonance (ESR). The control signal can be generated by mixing a local oscillator

$$\begin{aligned} s_{\mathrm{LO}}(t) &= \exp(i\omega_{\mathrm{LO}} t) \\ &= \cos(\omega_{\mathrm{LO}} t) + i \sin(\omega_{\mathrm{LO}} t) \\ &= I_{\mathrm{LO}}(t) + i Q_{\mathrm{LO}}(t), \end{aligned}$$

with baseband signals

$$\begin{aligned} s_{\mathrm{AWG}}(t,\phi) &= A\exp(i(\omega_{\mathrm{MW}}-\omega_{\mathrm{LO}})t+\phi) \\ &= A\cos((\omega_{\mathrm{MW}}-\omega_{\mathrm{LO}})t+\phi)+iA\sin((\omega_{\mathrm{MW}}-\omega_{\mathrm{LO}})t+\phi) \\ &= AI_{\mathrm{AWG}}(t,\phi)+AQ_{\mathrm{AWG}}(t,\phi), \end{aligned}$$

such that

$$\begin{aligned} \Re(s_{\mathrm{LO}}(t)s_{\mathrm{AWG}}(t,\phi)) &= A\cos(\omega_{\mathrm{MW}}t+\phi) \\ &= AI_{\mathrm{LO}}(t)I_{\mathrm{AWG}}(t,\phi)-AQ_{\mathrm{LO}}(t)Q_{\mathrm{AWG}}(t,\phi). \end{aligned}$$

The spin dynamics when $\Omega \ll \omega_L$ are most easily understood in the rotating frame where $|\tilde{\psi}(t)\rangle = R_z(\omega_{\mathrm{MW}}t)\,|\psi(t)\rangle$. The unitary operator $R_n(\alpha)=\exp(-i\alpha\hat{n}\cdot\sigma/2)$ represents a positive rotation in the Bloch sphere about the unit vector $\hat{n}=(n_x,n_y,n_z)$ by an angle α. The rotating frame Hamiltonian, neglecting fast oscillating terms with the rotating wave approximation (RWA), is given by:

$$\tilde{H}_Z = R_z(\omega_{\mathrm{MW}}t)H_Z R_z^\dagger(\omega_{\mathrm{MW}}t) + i\hbar\frac{dR_z(\omega_{\mathrm{MW}}t)}{dt}R_z^\dagger(\omega_{\mathrm{MW}}t) \tag{2.9}$$

$$= \frac{\Delta}{2}\sigma_z + \frac{\Omega}{2}(\cos\phi\sigma_x - \sin\phi\sigma_y), \tag{2.10}$$

where $\Delta=\omega_{\mathrm{MW}}-\omega_L$. During free evolution (i.e. $\Omega=0$) in the lab frame for a time t, $H_{Z,\mathrm{free}}=-\frac{\omega_L}{2}\sigma_z$, and the state evolves with $U_{\mathrm{free}}(t)=R_z(-\omega_{\mathrm{L}}t)$. During free evolution in the rotating frame, $\tilde{H}_{\mathrm{free}}=\frac{\Delta}{2}\sigma_z$, and the state evolves with $\tilde{U}_{\mathrm{free}}(t)=R_z(\Delta t)$. The general unitary evolution generated by Eq. 2.10 is a rotation $R_n(\alpha)$ about an axis $\hat{n}=(\Omega\cos\phi,-\Omega\sin\phi,\Delta)^T/\sqrt{\Omega^2+\Delta^2}$ by an angle $\alpha=\sqrt{\Omega^2+\Delta^2}t$, and the probability of a $|0\rangle\rightarrow|1\rangle$ transition is given by Rabi's formula:

$$P_{0\rightarrow1} = |\langle 1|R_{\tilde{n}}(\tilde{\alpha})|0\rangle|^2 = \frac{\Omega^2}{\Omega_{\mathrm{R}}^2}\sin^2\left(\frac{\Omega_{\mathrm{R}}t}{2}\right), \tag{2.11}$$

where $\Omega_{\mathrm{R}}=\sqrt{\Omega^2+\Delta^2}$ is the Rabi frequency.

In the resonant case where $\Delta=0$, a universal single-qubit gate set is achieved by choosing $\phi=0$ for positive rotations about the x-axis and $\phi=-\pi/2$ for rotations about the y-axis. Rotations about the z-axis can be implemented virtually by using the identity:

$$\begin{aligned} R_{n'}(\alpha)R_z(\phi) &= R_z(\phi)R_z^\dagger(\phi)R_{n'}(\alpha)R_z(\phi) \\ &= R_z(\phi)R_{n''}(\alpha), \end{aligned}$$

where n' is a unit vector in the xy-plane and $n'' = R_z(-\phi)n'$. This means that any $R_z(\phi)$ operation can be performed by *adding* ϕ to the phase of the next resonant burst.[4]

The time-dependent magnitude and duration of a resonant drive $\Omega_R(t)$ determines the angle of rotation. It is practical to construct useful gate sets like the Clifford gates from 90-degree rotations of duration t_{90}, which means:

$$\int_0^{t_{90}} \Omega_R(t)dt = \frac{\pi}{2}. \tag{2.12}$$

In the case that the spin is driven off-resonantly such that $\Omega^2 \ll \Delta^2$, the ac Stark shift arises. In this limit, the spin precesses at $\Omega_R = \omega_{MW} - (\omega_L + \delta_{acS})$ in the off-resonant rotating frame such that:

$$\delta_{acS} = \Delta - \Omega_R \approx -\frac{\Omega^2}{2\Delta}. \tag{2.13}$$

The above treatment is helpful to keep handy in one's mind for intuitive qubit control, but there is relevant physics that is washed away in the RWA. One efficient toolkit to investigate more closely is the time-dependent Schrieffer-Wolff framework introduced in [11]. This approach, valid when $\Omega \ll \omega_L$, allows one to consider misaligned driving fields, the Bloch-Siegert shift, and subharmonic transitions.[5]

First, if the driving field is misaligned[6] by an angle ϑ such that $g\mu_B \mathbf{B} = (\Omega\cos\vartheta\cos(\omega_{MW}t + \phi), 0, \omega_L + \Omega\sin\vartheta\cos(\omega_{MW}t + \phi))^T$, we can rest assured that perfect spin flips are still possible and the Rabi frequency on-resonance is $\Omega\cos\vartheta$. The longitudinal drive given by nonzero $\sin\vartheta$ enables sub-harmonic transitions.

The Bloch-Siegert shift of the resonance condition is given by:

$$\delta_{BS} = \frac{\Omega_R^2 \cos\vartheta^2}{4\omega_L}. \tag{2.14}$$

Typically δ_{BS} is very small, but conceptually it may be relevant if δ_{BS} is substantial compared to the linewidth of the driven transition and a

[4] This is where consistency with the qubit definition meets hardware. Had we chosen $|0\rangle = |\uparrow\rangle$ instead, our rotating frame would rotate the other way (i.e. $\Delta = \omega_L - \omega_{MW}$), and we would have to *subtract* the phase of virtual-Z rotations from subsequent microwave bursts. The pulse-lib package used by the spin qubit groups in Delft uses the convention in the main text at the time of writing.

[5] This physics can be derived more directly in the case of ESR, but this particular approach can be readily extended to electric-dipole spin resonance and more esoteric cases like bichromatic driving [12, 13].

[6] This means driving both transverse and longitudinal magnetic components with respect to the static magnetic field.

pulse-shape is given to the driving amplitude Ω_R such that the resonance condition moves during an operation [14].

2.3.2. DIABATIC CONTROL

At the opposite end of the conceptual spectrum, a spin state may be manipulated by suddenly changing its Hamiltonian such that the original state is conserved, then allowing the state to evolve under the new Hamiltonian such that a new state is reached. I will refer to this leveraging of the sudden approximation as diabatic control. For the Zeeman Hamiltonian of Eq. 2.8 where the eigenstates are separated by E_Z, this would entail changing the magnetic field $\mathbf{B}(t)$ on a timescale T such that [15]:

$$T \ll \frac{2\pi\hbar}{E_Z}. \tag{2.15}$$

As the Zeeman energy increases, the Hamiltonian must change faster in order to remain diabatic.

If the system is originally in the magnetic field $\mathbf{B} = (0, 0, B_0)^T$, an $R_x(\pi/2)$ unitary operation may be performed by changing the field to $\mathbf{B}' = (B_0, 0, 0)^T$ considerably faster than $h/g\mu_B B_0$, allowing the system to precess for approximately $h/4g\mu_B B_0$ (plus any integer multiple of $h/g\mu_B B_0$), then changing the field back to $\mathbf{B} = (0, 0, B_0)^T$. For changes in the magnetic field orientation by less than 90 degrees, multiple transitions are required to achieve $R_x(\pi/2)$.

2.3.3. FIDELITY AND DECOHERENCE

The quality of quantum operations will be limited by the accuracy of the control signals sent and the coherence properties of the target qubit. For our prototype spin qubit, incoherent noise enters the Hamiltonian via fluctuations in the effective magnetic field such that $\mathbf{B} = (\mathrm{d}\omega_{\perp,x}, \mathrm{d}\omega_{\perp,y}, \omega_L + \mathrm{d}\omega_\parallel)^T/g\mu_B$. T_1 relaxation will arise from fluctuations of frequency ω_L that are orthogonal to $\mathbf{B}$ (i.e. $\omega_\perp = \sqrt{\omega_{\perp,x}^2 + \omega_{\perp,y}^2}$) and therefore able to induce spin flips. Generally this timescale is substantially longer (e.g. hundreds of ms or more) than any T_2 dephasing timescale (e.g. on the order of ms with dynamical decoupling) such that we don't need to consider it.[7]

T_2 dephasing will be dominated by fluctuations of any frequency that are parallel to the qubit's quantization axis, since $\mathrm{d}\omega_L \approx \mathrm{d}\omega_\parallel + \mathrm{d}\omega_\perp^2/2\omega_L$

[7] Working at particularly high temperatures is one such instance where we may have to consider T_1 relaxation, which drops rapidly with temperature, although realistic T_2 timescales will also decrease and typically still be limiting.

for small magnetic fluctuations $\omega_\perp \ll \omega_L$ and $\omega_\parallel \ll \omega_L$. The filter function formalism can be used to analyze the relationship between bands of the noise spectrum and the resulting dephasing timescales [16].

Regardless of the physical origin of noise, it is useful to be able to roughly quantify the performance of operations. One of the most common metrics is the average gate fidelity which, when comparing unitary operations, can be written as [17]:

$$F = \frac{d + \left|\mathrm{Tr}\left[U_{\mathrm{ideal}}^{\dagger} U_{\mathrm{actual}}\right]\right|^2}{d(d+1)}, \tag{2.16}$$

where d is the dimension of the relevant Hilbert space, U_{ideal} is the gate one would like to perform, and U_{actual} is the unitary one actually performs.[8] Taking resonant control as an example, the infidelity $1-F$ of an intended $X_{90} = R_x(\pi/2)$ operation will vary as $\Delta^2/3\Omega^2$, $\phi^2/3$, and $\mathrm{d}\alpha^2/6$ around the optimal parameters $\Delta = 0$, $\phi = 0$, and $\mathrm{d}\alpha = \int_0^{t_{90}} \Omega_R \mathrm{d}t - \pi/2 = 0$ assuming the others are perfect.

The dephasing due to Gaussian quasi-static noise can be directly related to the standard deviation of the noise distribution as $T_2^* = \sqrt{2}/\sigma_\omega$. By extrapolating $\Delta \approx \sigma_\omega$, an estimate of the X_{90} error rate due to quasi-static noise causing a miscalibration of the Larmor frequency can be made based on Eq. 2.16[9]:

$$\varepsilon_{X90}^* \approx \frac{2}{3(\Omega_R T_2^*)^2}, \tag{2.17}$$

where the infidelity is being used as a heuristic for the error rate. Isolating this source, a 99.9% fidelity X_{90} driven at $\Omega_R/2\pi = 1$ MHz requires a T_2^* of about 4 µs when not employing decoupling pulses[10].

While resonantly driving, the spin's coherence will decay on a timescale T_2^R. In the limit of a perfect driving field, this decay will, like T_1, be most sensitive to transverse noise of frequency ω_L since $\mathrm{d}\Omega_R \approx \mathrm{d}\omega_\perp + \mathrm{d}\omega_\parallel^2/2\Omega$ for $\Delta \ll \Omega$. Imperfections in the driving field's amplitude and phase stability as well as Larmor frequency fluctuations will also contribute to T_2^R.

A lower bound for the error rate of an operation with duration t_{op} can be roughly related to the decay timescale τ as:

[8] Sometimes the closely related entanglement/process fidelity $F_e = |\mathrm{Tr}[U_{\mathrm{ideal}}^{\dagger} U_{\mathrm{actual}}]|^2/d^2$ is used.

[9] By assuming the quasi-static noise is Gaussian, we can take advantage of the convenient relation that $\int_{-\infty}^{\infty} \frac{1}{\sqrt{2\pi}\sigma} e^{-x^2/2\sigma^2} x^2 dx = \sigma^2$.

[10] The T_2^* of relevance is the one integrated over the amount of time one expects to be performing the gate between calibration cycles.

$$\varepsilon \approx 1 - e^{-(t_{\mathrm{op}}/\tau)^{\alpha}} \approx \left(\frac{t_{\mathrm{op}}}{\tau}\right)^{\alpha} = \left(\frac{1}{Q}\right)^{\alpha}, \tag{2.18}$$

where α is the exponent of decay (typically ranging from 1 for white noise to 2 for quasi-static noise) and in the last line we have defined the quality factor Q as the ratio of the number of times an operation can repeat within its associated decay timescale. In the case of the resonant $R_x(\pi/2)$:

$$\varepsilon^{\mathrm{R}}_{X90} \approx \left(\frac{\pi}{2\Omega_{\mathrm{R}} T_2^{\mathrm{R}}}\right)^{\alpha}, \tag{2.19}$$

and a 99.9% fidelity X_{90} through this lens requires a T_2^{R} of about 250 µs assuming $\Omega_{\mathrm{R}}/2\pi = 1$ MHz and taking $\alpha = 1$. Note that the estimated error is quite sensitive to the decay exponent.

As a sanity check, we can predict T_2^{R} when subjected only to Gaussian quasistatic fluctuations of the Larmor frequency $\mathrm{d}\omega_{\parallel}$ with variance σ_ω^2 (i.e. how does T_2^* limit T_2^{R}). In this case, the driven spin picks up a phase $\exp(-it\mathrm{d}\omega_{\parallel}^2/2\Omega)$, and, solving the weighted integral over $\mathrm{d}\omega_{\parallel}$, the coherence of this phase will decay as $1/\sqrt[4]{1+(\sigma_\omega^2 t/\Omega)^2}$ [18]. Using $T_2^* = \sqrt{2}/\sigma_\omega$, the $1/e$ decay time is $(T_2^*)^2\Omega\frac{\sqrt{e^4-1}}{2}$. Assuming $\Omega/2\pi = 1$ MHz, a 4 µs T_2^* corresponds to a decay time of 368 µs. The estimate based on Eq. 2.16 is therefore more stringent. However, if the measured T_2^{R} is substantially shorter than what is expected from quasistatic Larmor frequency fluctuations alone, it probably means the resonant gate fidelity is limited by something else, like higher-frequency noise, imperfections in the drive, and heating.

In the case of diabatic gates, an error limit will also be set by the T_2^* decay, as gates are performed by precessing freely. The $R_x(\pi/2)$ gate time is bounded by $\pi/2\omega_{\mathrm{L}}$ such that:

$$\varepsilon^{*}_{X90,\mathrm{dia}} \approx \left(\frac{\pi}{2\omega_{\mathrm{L}} T_2^*}\right)^{\alpha}. \tag{2.20}$$

A 99.99% fidelity X_{90} where $\omega_{\mathrm{L}}/2\pi = 100$ MHz and $\alpha = 2$ requires a T_2^* of about 250 ns. In practice, diabaticity errors and jitter $\mathrm{d}t_{\mathrm{jitter}}$ in switching the Hamiltonian will place more stringent limits. The latter causes a distribution of under- and over-rotation errors which result in:

$$\varepsilon^{\mathrm{jitter}}_{X90,\mathrm{dia}} \approx \frac{\left(\omega_{\mathrm{L}}\mathrm{d}t_{\mathrm{jitter}}\right)^2}{6}, \tag{2.21}$$

and the 99.99% X_{90} fidelity for $\omega_L/2\pi = 100$ MHz limits dt_{jitter} to about 40 ps. In the case that multiple diabatic transitions are required to implement the gate, this limit becomes even tighter.

Using Eq. 2.18, one could estimate the infidelity of idling for a certain time t_{idle} given the relevant T_2 dephasing timescale and decay exponent. The error will therefore depend on whether dynamical decoupling or, in the case of shuttling, motional narrowing is applicable.

The quality of two-spin interactions via exchange can be quantified analogously. Considering only the exchange term of Eq. 2.7, a SWAP unitary is achieved by activating J for a duration $1/2J$[11]. The infidelity due to quasi-static fluctuations σ_J in the magnitude of exchange is:

$$\varepsilon^*_{SWAP} \approx \frac{3\pi^2\sigma_J^2}{20J^2}, \tag{2.22}$$

which suggests that operating at higher values of exchange is more forgiving (though the magnitude of fluctuations may also increase with J). For $J = 5$ MHz, a 99% fidelity SWAP gate by this estimate requires $\sigma_J < 0.4$ MHz. This corresponds to a singlet-triplet T_2^* of about 0.6 µs. However, when the exchange interaction is stronger, the spins are generally more exposed to higher-frequency noise, and the T_2 coherence of the individual spins will decrease as J increases. Dynamical decoupling may also be used, as it commutes with exchange[12]. It is therefore also useful to estimate the error based on the quality factor:

$$\varepsilon_{SWAP} \approx \left(\frac{1}{2JT_2}\right)^{\alpha}. \tag{2.23}$$

Assuming $\alpha = 1.8$ (implying whiter-than-pink noise, which is consistent with many measurements in this thesis) and $J = 5$ MHz, a 99% fidelity SWAP requires a T_2 of about 1.3 µs. Again, the estimated error is sensitive to the decay exponent. The quality factor typically varies with the magnitude of J, and it is typically optimal for intermediate range that is neither too small nor too large.

For more rigorous benchmarking, one must turn to protocols like randomized benchmarking (RB) [19] or gate-set tomography [20]. However, these "black-box" protocols often suffer from the fact that the results they yield depend on how well the device under test obeys the requisite assumptions, such as having Markovian noise and constant state preparation and measurement (SPAM) errors. Their implementation

[11] Although it is the $\sqrt{SWAP}$ that is maximally entangling, two $\sqrt{SWAP}$ gates, each with duration $1/4J$, are required to compile a CNOT or CZ.

[12] It is useful to note that when using dynamical decoupling on a qubit exposed to a noise bath with power spectral density $1/\omega^\alpha$, the exponent of the decay envelope will go as $\exp(-(t/T_2)^{1+\alpha})$ [16].

is not always trivial, especially when logical operations are embedded in composite sequences including shuttling and refocusing pulses as is the case in Chapter 5. While these rules-of-thumb cannot replace rigorous benchmarking, they can inform an experimentalist what quantity they should expect from a benchmarking protocol from very easy-to-access metrics.

2.4. SPIN QUBITS IN AN INHOMOGENEOUS MAGNETIC FIELD

Although the exchange interaction in a homogeneous magnetic field may be used to produce the entangling $\sqrt{SWAP}$ gate between single-spin qubits, the absence of addressable spin control renders the Loss-DiVincenzo qubit encoding useless. In order to make this encoding practical, there must be some inhomogeneity: either among the spins, in the spatial extent of the control signals, or both. I will focus largely on the first and consider the case where the inhomogeneity is engineered in the context of an otherwise-perfect platform, which is the most relevant paradigm for the work in this thesis.

The best-explored means of engineering magnetic inhomogeneity in spin qubit devices is through patterning on-chip ferromagnets [21–34]. Fig. 2.1a provides a sketch of a common micromagnet pattern. On-chip DC currents, for example carried through on-chip superconducting wires patterned in the device gate stack [35] may also produce inhomogeneous magnetic fields. The Meisner effect of on-chip superconductors has also been considered [36].

Regardless of the implementation, Maxwell's equations provide constraints. For instance, having a magnetic field $\mathbf{B}(\mathbf{r}) = (0, 0, B_z(\mathbf{r}))^T$ is not possible in general as $\nabla \cdot \mathbf{B} = 0$ always and $\nabla \times \mathbf{B}$ is constrained by the (absence of) currents and time-varying electric fields. The situation is therefore more complicated than simply giving each spin a unique Larmor frequency, and the orientation of the magnetic field will also vary site-to-site. This, however, also provides opportunities.

Here, I will survey the consequences of introducing a stray magnetic vector field $\mathbf{B}(\mathbf{r})$, whatever its origin. Chapters 4 and 5 provide concrete examples of this engineering in practice.

2.4.1. INHOMOGENEITY WITHIN A DOT: SYNTHETIC SPIN-ORBIT INTERACTION AND ELECTRIC-DIPOLE SPIN RESONANCE

It has been over two decades since it was first proposed that introducing an inhomogeneous transverse field via an on-chip micromagnet allows electrical, as opposed to magnetic, spin control via electric-dipole spin resonance (EDSR) [37]. Furthermore, variation in the static magnetic field permits spectral addressability. However, the so-called synthetic

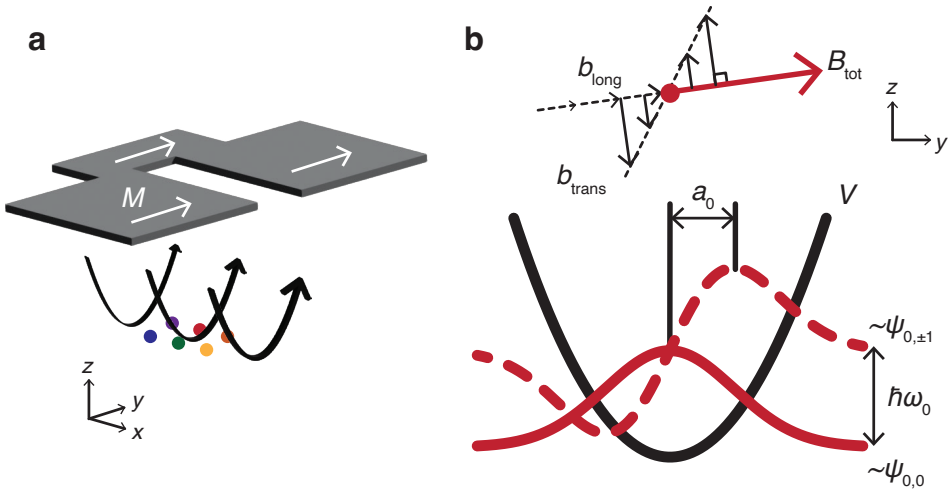


Figure 2.1: **a** Sketch of a typical micromagnet design and the stray field lines it creates. The magnitude of the magnetization vector $|\mathbf{M}| = M$ is assumed to be homogeneous throughout the bulk ferromagnetic material. Dot locations (not to scale) are represented as coloured dots below the magnetic layer. The black arrows represent streamlines of the stray magnetic field. The thicker streamlines indicate increasing total magnetic field and therefore spectral addressability along the long axis of the gap. **b** Sketch of the relevant parameters for EDSR control and charge-noise-induced dephasing in a single quantum dot projected to one spatial dimension. The two relevant Fock-Darwin wavefunctions $|\psi_{0,0}\rangle$ and $|\psi_{0,\pm1}\rangle$ are spatially represented by the analogous eigenstates of a 1D quantum harmonic oscillator $V(y) = \frac{1}{2}\hbar\omega_0\left(\frac{y}{a_0}\right)^2$. The characteristic length scale a_0 and orbital energy scale $\hbar\omega_0$ do not depend on the dimensionality. The spin experiences a total magnetic field $|\mathrm{B}| = B_{\mathrm{tot}}$, transverse gradient $\left|\frac{\partial B_\perp}{\partial y}\right| = b_{\mathrm{trans}}$ and longitudinal gradient $\left|\frac{\partial B_{\mathrm{tot}}}{\partial y}\right| = b_{\mathrm{long}}$.

spin-orbit interaction (sSOI) also permits electrical noise to couple to the spin and cause dephasing. The EDSR Hamiltonian allows us to introduce all of these aspects and reduce the physical intuition to the case of ESR as described in Sec. 2.3.1. Similar derivations may be found in [38] and [39], though here we will be more direct. The Hamiltonian has the form:

$$H_{\mathrm{EDSR}} = -\frac{\omega_{\mathrm{L}}}{2}\sigma_z - \frac{\omega_o}{2}\tau_z - \frac{\Lambda}{2}\tau_x\sigma_x - \frac{\lambda}{2}\tau_z\sigma_z + E(t)\tau_x, \tag{2.24}$$

and follows from writing Eq. 2.1 in a four-level spin-orbit basis where σ and τ denote Pauli matrices that act on the 2-level spin state or (truncated) 2-level orbital state respectively. The orbital sector can be treated as such by assuming we have harmonic confinement, because the position operator $\hat{x}$ expressed in the Fock-Darwin basis only couples the ground state $\psi_{0,0}$ to excited states $\psi_{0,\pm1}$. Since $\langle\psi_{0,\pm1}|\hat{x}|\psi_{0,0}\rangle = a_0/2$, the total dipole is $a_0/\sqrt{2}$ as in the case of a 1D harmonic oscillator. This

1D picture is sketched in Fig. 2.1b.

$E(t) = E^{\text{drive}}(t) + E^{\text{noise}}(t)$ represents a time-dependent electric field that may consist of an intentional drive as well as environmental charge noise. The electric driving field is given by $E^{\text{drive}}(t) = a_0 e E_{\text{ac}}^{\text{drive}} \cos(\omega_{\text{MW}} t + \phi)/\sqrt{2}\hbar$ and is oriented along the in-plane unit vector $\hat{\mathbf{r}} = r_x \hat{\mathbf{x}} + r_y \hat{\mathbf{y}}$. We assume any out-of-plane component does not participate in the EDSR mechanism as the z-axis confinement is sufficiently strong such that there is no relevant dipole to couple to. e is the elementary charge of the electron and $E_{\text{ac}}^{\text{drive}}$ is the amplitude of the electric field in units V/m. Similarly, any incoherent electric fluctuations may be expressed as $E^{\text{noise}}(t) = a_0 e E_{\text{ac}}^{\text{noise}}(t)/\sqrt{2}\hbar$.

$\Lambda = \frac{g\mu_B a_0}{\sqrt{2}\hbar} \left| \frac{\partial B_\perp}{\partial \mathbf{r}} \right|$ gives the energy scale for the sSOI where $\left| \frac{\partial B_\perp}{\partial \mathbf{r}} \right| \mathbf{r}$ is the transverse field along the axis of the time-dependent electric fluctuations at the location of the quantum dot. The orientation of $B_\perp$ is ambiguous, because there are two orthogonal axes to the quantization axis. This would give rise to $\tau_x \sigma_x$ and $\tau_x \sigma_y$ couplings in the Hamiltonian. By rotating the spin basis about the quantization axis, these contributions can be combined into a single energy scale. $\lambda = \frac{g\mu_B a_0}{\sqrt{2}\hbar} \frac{\partial |\mathbf{B}|}{\partial \mathbf{r}}$ describes the effect of the decoherence gradient, whereby the qubit energy may fluctuate due to electrical noise, such as charge noise from the dielectrics. While we can engineer the orientation of an applied electric drive, charge noise may push the confined electron in any direction, so $\frac{\partial |\mathbf{B}|}{\partial \mathbf{r}}$ is best thought of as the worst-case bound.

Considering the Larmor frequency ω_{L}, spin-orbit couplings Λ and λ and time-dependent fluctuation $E(t)$ energy scales as small with respect to the orbital splitting $\hbar\omega_0$, Schrieffer-Wolff perturbation theory may be used to derive the effective driving field $\Omega'(t)$ as well as the effective Larmor frequency fluctuation $\delta\omega_{\text{L}}$ induced by the electric fields to leading order:

$$\Omega' \cos(\omega_{\text{MW}} t + \phi) = \frac{2E(t)\Lambda}{\omega_0} = \frac{g\mu_B \left| \frac{\partial B_\perp}{\partial \mathbf{r}} \right| e E_{\text{ac}}^{\text{drive}} \cos(\omega_{\text{MW}} t + \phi)}{\hbar m^* \omega_o^2}, \tag{2.25}$$

$$\mathrm{d}\omega_{\text{L}}(t) = \frac{2E(t)\lambda}{\omega_0} = \frac{g\mu_B \left| \frac{\partial |\mathbf{B}|}{\partial \mathbf{r}} \right| e E_{\text{ac}}^{\text{noise}}(t)}{\hbar m^* \omega_o^2}. \tag{2.26}$$

The sSOI also introduces a small, constant renormalization δ_{EDSR} to the bare Larmor frequency:

$$\omega_{\text{L}}' = \omega_{\text{L}} - \frac{\Lambda^2 \omega_{\text{L}}}{2\left(\omega_0^2 - \omega_{\text{L}}^2\right)} \tag{2.27}$$

but this correction is unimportant in the context of qubit operation as it is the hybridized spin Larmor frequency which is measured directly. Together, the renormalized Larmor frequency ω_L' and effective transverse magnetic field $2\hbar\Omega'/g\mu_B$ can be interpreted in the framework of ESR for most practical purposes. Similarly, a driving field misaligned by an angle ϑ will observe on-resonance Rabi frequencies reduced to $\Omega' \cos\vartheta$. That is, any driving along the longitudinal gradient will not inhibit perfect spin flips but enables sub-harmonic transitions [11].

Meaningful differences between ESR and EDSR arise when studying sub-harmonic transitions, bichromatic driving, and the Bloch-Siegert shift. For example, the EDSR Bloch-Siegert shift is [11, 40]:

$$\delta_{\mathrm{BS,EDSR}} = -\frac{\Omega'^2 \cos^2\theta}{4\omega_L}, \tag{2.28}$$

which differs in sign from the case for ESR. Importantly, no bits of theory arise from this picture that explain the anomalous phase shifts that are the subject of Chapter 3.

For experiments with silicon quantum dots, a_0 typically ranges from 10 to 20 nm corresponding to $\hbar\omega_0$ of 1 to 3 meV, $\omega_L/2\pi$ is on the order of GHz, $E_{\mathrm{ac}}^{\mathrm{drive}}$ is on the order of 1000 V/m, and $E_{\mathrm{ac}}^{\mathrm{noise}}$ is on the order of 10 V/m. These parameter ranges correspond to a magnitude of inhomogeneity required to obtain good qubit control speed and lifetimes. Explicitly, one can state that good EDSR control ($\Omega'/2\pi > 5$ MHz) may be achieved when $|\partial B_\perp/\partial \mathbf{r}| > 1$ mT/nm and good charge-noise-limited coherence properties ($T_2^* \approx 1/\mathrm{d}\omega_L > 10\,\mu$s) should restrict $|\partial|\mathbf{B}|/\partial\mathbf{r}| < 0.1$ mT/nm. This latter condition ought to apply even if the qubit is not intended to be controlled via EDSR, as dephasing will still be induced by electrical fluctuations provided there is sSOI.

The gradients $|\partial B_\perp/\partial\mathbf{r}|$ and $|\partial|\mathbf{B}|/\partial\mathbf{r}|$ can be engineered, and to do this it is important to relate these quantities to the overall magnetic vector field $\mathbf{B}(\mathbf{r})$ present on the chip. Regardless of how the magnetic vector field is generated, the relevant quantities for understanding spin control can be computed in the same way. We represent the sum of the global external field and local stray field as a total vector field:

$$\mathbf{B}(\mathbf{r}) = \begin{pmatrix} B_x(\mathbf{r}) \\ B_y(\mathbf{r}) \\ B_z(\mathbf{r}) \end{pmatrix}. \tag{2.29}$$

We assume that the qubit locations are point-like as the field varies slowly over the length scale of the electron wavefunction.[13] The total magnetic field $B_{\mathrm{tot}}(\mathbf{r}) = |\mathbf{B}(\mathbf{r})|$ setting the Zeeman energy is:

[13] For more intricate magnetic designs, for example ones using nanomagnets, the field could be more accurately calculated as an integral weighted by $|\psi_{0,0}(\mathbf{r})|^2$.

$$B_{\text{tot}}(\mathbf{r}) = \sqrt{B_x(\mathbf{r})^2 + B_y(\mathbf{r})^2 + B_z(\mathbf{r})^2}. \tag{2.30}$$

We currently assume the g-factor of the confined electron spin is isotropic, so the quantization axis is set by the direction of the total magnetic field:

$$\hat{\mathbf{u}}_{\text{tot}} = \frac{B_x}{B_{\text{tot}}}\hat{\mathbf{x}} + \frac{B_y}{B_{\text{tot}}}\hat{\mathbf{y}} + \frac{B_z}{B_{\text{tot}}}\hat{\mathbf{z}}. \tag{2.31}$$

We can find the perpendicular axes using the Gram-Schmidt process, taking $\{\hat{\mathbf{u}}_{\text{tot}}, \hat{\mathbf{x}}, \hat{\mathbf{z}}\}$ as the starting set of normal vectors:

$$\hat{\mathbf{u}}_{\perp,1} = \hat{\mathbf{x}} - (\hat{\mathbf{u}}_{\text{tot}} \cdot \hat{\mathbf{x}})\hat{\mathbf{u}}_{\text{tot}}, \hat{\mathbf{u}}_{\perp,2} = \hat{\mathbf{z}} - (\hat{\mathbf{u}}_{\text{tot}} \cdot \hat{\mathbf{z}})\hat{\mathbf{u}}_{\text{tot}} - (\hat{\mathbf{u}}_{\perp,1} \cdot \hat{\mathbf{z}})\hat{\mathbf{u}}_{\perp,1}, \tag{2.32}$$

The transverse fields are therefore $B_{\perp,1/2} = \mathbf{B} \cdot \hat{\mathbf{u}}_{\perp,1/2}$ and equal 0 at the qubit locations. The total transverse gradient is found by taking the total directional derivative of each gradient along the driving axis:

$$\left|\frac{\partial B_\perp}{\partial \mathbf{r}}\right| = \sqrt{(\hat{\mathbf{r}} \cdot \nabla B_{\perp,1})^2 + (\hat{\mathbf{r}} \cdot \nabla B_{\perp,2})^2} \tag{2.33}$$

$$= \sqrt{\left(\frac{\partial B_{\perp,1}}{\partial x} r_x + \frac{\partial B_{\perp,1}}{\partial y} r_y\right)^2 + \left(\frac{\partial B_{\perp,2}}{\partial x} r_x + \frac{\partial B_{\perp,2}}{\partial y} r_y\right)^2}. \tag{2.34}$$

Eq. 2.34 may be called the transverse or driving gradient.

For a particular fluctuation axis $\hat{\mathbf{r}'} = r'_x\hat{\mathbf{x}} + r'_y\hat{\mathbf{y}}$, the decoherence gradient is given by the directional derivative:

$$\left|\frac{\partial B_{\text{tot}}}{\partial \mathbf{r}'}\right| = \left|\hat{\mathbf{r}'} \cdot \nabla B_{\text{tot}}\right|. \tag{2.35}$$

Since we don't know along which axis charge noise will predominantly push the dot, we can estimate a bound by taking the norm of the in-plane gradient:

$$\left|\frac{\partial B_{\text{tot}}}{\partial \mathbf{r}'}\right|_{\max} \approx \sqrt{(\hat{\mathbf{x}} \cdot \nabla B_{\text{tot}})^2 + (\hat{\mathbf{y}} \cdot \nabla B_{\text{tot}})^2}. \tag{2.36}$$

Eq. 2.36 is the decoherence or addressability gradient. A decoherence gradient of 0.1 mT/nm corresponds to a neighbouring dot-to-dot Larmor frequency difference of about 250 MHz when $g = 2$.

Eq. 2.34 and Eq. 2.36 hold for general 2D arrays of quantum dots, though simplifications can be made for arrays with higher symmetry. Often, the driving axis is designed to align with the same cartesian axis as the external field (e.g. $\hat{\mathbf{y}}$) and the transverse field is dominated by

another cartesian component (e.g. $\hat{\mathbf{z}}$) such that the driving gradient can be approximated as $|\partial B_z/\partial y|$. Similarly, the decoherence gradient can be approximated as $|\partial B_y/\partial x|$.

2.4.2. INHOMOGENEITY BETWEEN DOTS: TUNNELING AND HOPPING CONTROL

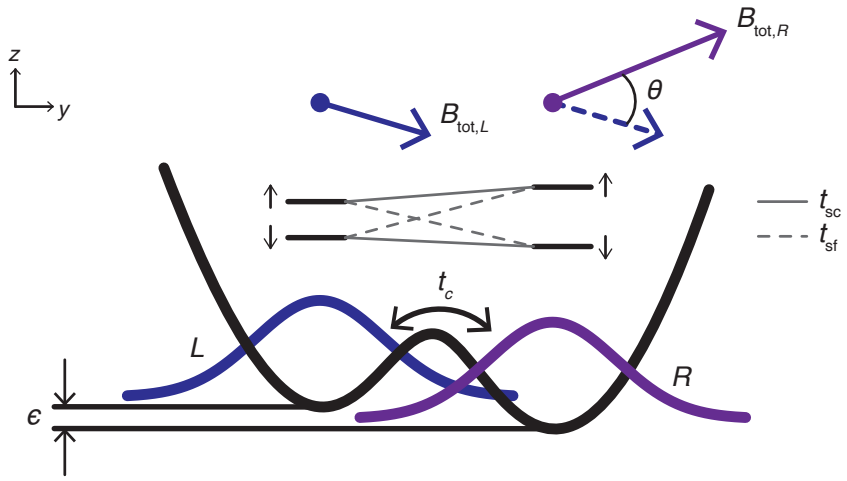


Figure 2.2: Sketch of the relevant parameters for single-electron tunneling and hopping in a double-dot potential with ground orbital states $|L\rangle$ and $|R\rangle$. The electrochemical potential detuning $\epsilon = \mu_L - \mu_R$ and bare tunnel coupling t_c from the Fermi-Hubbard model are shown. The different magnetic field vectors at the two spin locations and the angle θ between them are shown. The four resulting spin-orbit eigenstates $|L,\downarrow\rangle$, $|L,\uparrow\rangle$, $|R,\downarrow\rangle$, and $|R,\uparrow\rangle$ are coupled by spin-conserving and spin-flipping tunnel couplings $t_{\text{sc}} = t_c \cos(\theta/2)$ and $t_{\text{sf}} = t_c \sin(\theta/2)$ as indicated.

Magnetic inhomogeneity is important when considering how electron spins tunnel between adjacent dots. We can now consider the Fermi-Hubbard Hamiltonian of Eq. 2.4 for a singly-occupied double-dot potential with the addition of a site-dependent magnetic field. The bare tunnel coupling t_c of the Fermi-Hubbard Hamiltonian is spin-conserving. The principal effect of a transverse magnetic field difference between quantum dots is to allow for both spin-conserving and spin-flipping elements.

For any double dot system, it is always possible to use a basis where the relative change in magnetic field between sites consists of a parallel and perpendicular component with the third component of the magnetic field vector constantly zero. The Fermi-Hubbard Hamiltonian for a single-electron can therefore be written as [41, 42]:

$$H_{\mathrm{DQD,1e}} = \frac{\epsilon}{2}\tau_z + t_c\tau_x - |L\rangle\langle L| \otimes \frac{\omega_{\mathrm{L},L}}{2}\sigma_z - |R\rangle\langle R| \otimes \left(\frac{\omega_{\mathrm{L},R}\cos\theta}{2}\sigma_z + \frac{\omega_{\mathrm{L},R}\sin\theta}{2}\sigma_x\right), \quad (2.37)$$

where τ are Pauli matrices that act on the localized Gaussian orbital states $|L\rangle$ and $|R\rangle$ ($\tau_z|L\rangle = +|L\rangle$ and $\tau_z|R\rangle = -|R\rangle$), σ are Pauli matrices that act on the spin, $|L\rangle$ and $|R\rangle$ differ in electrochemical potential by the detuning $\epsilon = \mu_L - \mu_R$, $|\mathbf{B}_L| = \hbar\omega_{\mathrm{L},L}/g\mu_\mathrm{B} = B_{\mathrm{tot},L}$ is the total magnetic field at dot L, $|\mathbf{B}_R| = \hbar\omega_{\mathrm{L},R}/g\mu_\mathrm{B} = B_{\mathrm{tot},R}$ is the total magnetic field at dot R, and θ is the quantization axis tip between the two sites. This setup is sketched in Fig. 2.2. This tip angle can be easily computed from the respective magnetic field vectors:

$$\theta = \cos^{-1}\left(\frac{\mathbf{B}_L \cdot \mathbf{B}_R}{|\mathbf{B}_L||\mathbf{B}_R|}\right). \quad (2.38)$$

Eq. 2.37 can be unitarily transformed into the mutually diagonal basis with $U = |L\rangle\langle L| \otimes I + |R\rangle\langle R| \otimes R_y(-\theta)$:

$$UH_{\mathrm{DQD,1e}}U^\dagger = \frac{\epsilon}{2}\tau_z - |L\rangle\langle L| \otimes \frac{\omega_{\mathrm{L},L}}{2}\sigma_z - |R\rangle\langle R| \otimes \frac{\omega_{\mathrm{L},R}}{2}\sigma_z + t_{\mathrm{sc}}\tau_x \otimes I + t_{\mathrm{sf}}\tau_y \otimes \sigma_y, \quad (2.39)$$

where a spin-conserving tunnel coupling $t_{\mathrm{sc}} = t_c\cos(\theta/2)$ and a spin-flipping tunnel coupling $t_{\mathrm{sf}} = t_c\sin(\theta/2)$ can be identified.

In the interest of transporting an electron from one dot to another, we are generally interested in the regime $t_c \geq \omega_{\mathrm{L},L}, \omega_{\mathrm{L},R}$ such that the avoided crossing between $|L\rangle$ and $|R\rangle$ orbital states is quite large. The Landau-Zener formula provides a basis for estimating the probability of a diabatic transition when the detuning is ramped linearly with rate v:

$$P_{\mathrm{LZ}} = \exp\left(\frac{-2\pi t^2}{\hbar v}\right), \quad (2.40)$$

where t is the relevant spin-conserving or spin-flipping tunnel coupling element.

The tip angle θ plays a role in the spin physics during the transition. In the absence of a diabatic orbital transition, the spin physics is clarified by transforming to the instantaneous ground state of the orbital sector with $U_a = \exp\left(-i\tan^{-1}\left(\frac{-2t_c}{\epsilon}\right)\tau_y \otimes I/2\right)$ and isolating the effective Zeeman Hamiltonian:

$$U_a H_{\mathrm{DQD,1e}} U_a^\dagger = -\left[\frac{\omega_{\mathrm{L},L}}{4}\left(1-\frac{\epsilon}{\sqrt{4t_c^2+\epsilon^2}}\right)+\frac{\omega_{\mathrm{L},R}}{4}\cos\theta\left(1+\frac{\epsilon}{\sqrt{4t_c^2+\epsilon^2}}\right)\right]\sigma_z - \frac{\omega_{\mathrm{L},R}}{4}\sin\theta\left(1+\frac{\epsilon}{\sqrt{4t_c^2+\epsilon^2}}\right)\sigma_x, \quad (2.41)$$

where the orbital energy $-\sqrt{4t_c^2+\epsilon^2}/2$ has been subtracted out. Eq. 2.41 can be understood in the framework of Sec. 2.3.2 where the effective magnetic field is controlled via $\epsilon(t)$ and t_c. If the tunneling event happens quickly enough, the spin state is preserved under the sudden approximation and logical operations can be performed. In this instance, the sigmoid-shaped $\epsilon/\sqrt{4t_c^2+\epsilon^2}$ relationship aids diabaticity, since the change in the effective Hamiltonian happens over a small range within $|\epsilon/t_c| \approx 2$. These so-called hopping operations were first explored in hole spins hosted in Germanium where quantization axis tips arise due to g-tensor anisotropy [43]. We explore them with electron spins for the first time in Chapter 4. If the tunneling event is adiabatic, the spin only acquires a phase from the evolving effective magnetic field, and the spin's polarization is preserved.

2.4.3. CONVEYOR SHUTTLING

The idea of conveyor-mode shuttling has existed in some form for decades, both theoretically [44] and experimentally with surface acoustic waves in GaAs [45], but the high-fidelity transfer of single-spins has only been recently demonstrated in silicon [46, 47]. This has caused a resurgence of interest in theoretically modeling spin shuttling using modern approaches [48–50] as well as a growing number of spin-qubit architecture proposals that are heavily based on shuttling operations [51–55]. Details about tuning up, operating, and benchmarking a conveyor can be found in Chapter 5, so here I aim only to provide a basic conceptual description in order to connect it to the other ideas in this chapter.

The ideal operation of a conveyor is to move a charge, and therefore the spin associated with it, and induce minimal dynamics in the charge sector by simply translating the harmonic confinement potential $V(\mathbf{r}-\mathbf{r}_c(t))$ in the xy-plane without distorting the shape. If the trajectory of the potential minimum is $\mathbf{r}_c(t)$, the unitary displacement $U = \exp(-i\mathbf{p}\cdot\mathbf{r}_c(t)/\hbar)$ transforms the effective-mass Hamiltonian into the moving-dot frame as [56]:

$$\tilde{H}_{\text{EMA}} = UH_{\text{EMA}}(t)U^\dagger + i\hbar\frac{\mathrm{d}U}{\mathrm{d}t}U^\dagger \tag{2.42}$$

$$= \frac{\mathbf{p}^2}{2m^*} + V(U(\mathbf{r}-\mathbf{r}_c(t))U^\dagger) - \frac{1}{2}g\mu_{\text{B}}\mathbf{B}(U\mathbf{r}U^\dagger)\cdot\sigma + \frac{\mathrm{d}\mathbf{r}_c(t)}{\mathrm{d}t}\cdot\mathbf{p} \tag{2.43}$$

$$\rightarrow \frac{\mathbf{p}'^2}{2m^*} + V(\mathbf{r}') - \frac{1}{2}g\mu_{\text{B}}\mathbf{B}(\mathbf{r}'+\mathbf{r}_c(t))\cdot\sigma - \frac{1}{2}m^*\left(\frac{\mathrm{d}\mathbf{r}_c(t)}{\mathrm{d}t}\right)^2. \tag{2.44}$$

where $\mathbf{r}' = \mathbf{r} - \mathbf{r}_c(t)$ and $\mathbf{p}' = \mathbf{p} + m^*\frac{\mathrm{d}\mathbf{r}_c(t)}{\mathrm{d}t}$. The result is an effective-mass Hamiltonian in the moving-dot frame $(\mathbf{r}',\mathbf{p}')$ where the magnetic field now evolves as a function of time and the electron has gained momentum $m^*\frac{\mathrm{d}\mathbf{r}_c(t)}{\mathrm{d}t}$ with respect to the lab frame $(\mathbf{r},\mathbf{p})$. In the absence of any momentum-dependence in the Hamiltonian, a perfectly-conveyored spin with the orbital wavefunction always localized in the ground Gaussian state will be unaffected by this change. Therefore, the effective Hamiltonian can once again be interpreted as a Zeeman Hamiltonian with a time-dependent magnetic field $\mathbf{B}(t)$, and both ESR-like and diabatic spin control are possible by engineering the conveyor motion and spatial magnetic field appropriately.

Meaningful differences can arise between conventional ESR and conveyor-mode EDSR. As the electron may move over a distance much larger than a_0, nonlinearities in $\mathbf{B}(\mathbf{r}(t))$ may generate effective harmonics of the driving frequency. For example, if the shuttling path $\mathbf{r}_c(t)\cdot\hat{\mathbf{x}} \propto \cos(\omega t)$ passes through a field with a term $\mathbf{B}(\mathbf{r})\cdot\hat{\mathbf{u}}_\perp \propto x^2$, $\mathbf{B}(\mathbf{r}(t))\cdot\hat{\mathbf{u}}_\perp \propto \cos(2\omega t)$. This allows for sub-harmonic driving in a way that is distinct from misaligned ESR.

The conveyor path $\mathbf{r}(t)$ need not be oscillatory. Diabatic control may be permitted provided the effective magnetic field $\mathbf{B}(\mathbf{r}(t))$ changes sufficiently fast as outlined in Sec. 2.3.2. One setup to achieve this is to have a one-way conveyor with $\mathbf{r}(t) = vt$. Similar to the hopping control of Sec. 2.4.2, where the electron moves very quickly during tunneling, a fast change in the effective Hamiltonian needs to be present over a short length scale. It may also be desired to transport a spin adiabatically such that the net unitary action of the shuttling process is a phase pickup. In this case, the shuttling needs to be sufficiently slow with respect to the changing Hamiltonian.

Both adiabatic and diabatic driving via conveyor-mode shuttling have been experimentally demonstrated by De Smet, et al. and a manuscript is currently in preparation.

2.4.4. CONTROLLING MANY INDIVIDUAL SPINS

Unlike in Sec. 2.2, an inhomogeneous magnetic field permits the addressable control of many individual spins, either through spectral or spatial addressability. Spectral addressability has traditionally been important due to the difficulty of localizing high-frequency signals to the length-scale of individual quantum dots. The current trend of lower-frequency operation, hopping gates, and conveyor-mode shuttling provides many opportunities for spatial control, and I will discuss them further in Sec. 6.

Assuming reasonable qubit control can be engineered using any of the aforementioned strategies, the next challenge is to maximize the idling fidelity of the unaddressed qubits that also experience (some of) the control signal. If spins are spatially addressed via hopping or shuttling, this commonly means accounting for the phase pickup that accrues due to any stray electric field that pushes spectating qubits in the decoherence gradient. While calibrating explicit phase corrections is feasible on paper, this can result in a large overhead. A more efficient alternative is using refocusing pulses and interacting qubits symmetrically, as is the case in Chapter 5, though this restricts how quantum circuits must be compiled.

For resonant control, spectator qubits that are spectrally far from the target frequency will pick up phase via the ac Stark shift given by Eq. 2.13 that may be accounted for via phase updates (i.e. virtual-Z gates). Any residual rotation around a non-z axis in the Bloch sphere cannot be accounted for in this way and must be tackled explicitly.

Any constant-frequency control pulse of duration t_{pulse} will have a main lobe width of about $1/t_{\text{pulse}}$, and a window function $W(t)$ may be applied to suppress the amplitude and shape of the side lobes of the remaining spectrum. This is helpful for reducing by about 20 dB the magnitude of side lobes that may cause coherent rotations on spectator qubits. However, the central lobe will always be present to cause off-resonant driving itself. If a spectator qubit's frequency is relatively close to a driven qubit's resonance, the best remaining option is to synchronize the operations such that the time of a desired operation induces a net identity gate and $\Omega_R t = 2\pi n$ [57]. If two spins are separated by frequency $\Delta/2\pi$, then this synchronization condition for a $R_x(\pi/2)$ operation is:

$$\Omega = \frac{|\Delta|}{\sqrt{16n^2 - 1}}, \tag{2.45}$$

where n is an integer (typically 1 or 2). This assumes that the magnitude of the drive is equal for both qubits and that a rectangular window function is used. In general, the synchronization condition will be overconstrained for multiple spins, and therefore one must either ensure a sufficiently large Δ between all qubits, drive more slowly to minimize the spectral

width of the drive, or else engineer a degree of spatial addressability as well.

EXCEPTIONS TO THE RULE

The above crosstalk mechanisms are unavoidable even in the limit of theoretical perfection. However, many of the recent challenges in engineering multi-spin quantum processors are anomalous within this framework. For example, the ac Stark shift should only take place while a driving tone is present, yet it has frequently been observed that transient frequency shifts persist after off-resonant drives are removed, and the community has termed such behaviour as heating effect. Heating effects are a pernicious form of crosstalk that makes operations contextual upon what preceded them. Not only does this make calibration much more difficult for experimentalists, but it also ruins the assumptions of independent noise relied upon by many protocols, including randomized benchmarking and quantum error correction. A rigorous study of heating effects as well as an easy mitigation strategy is the topic of Chapter 3.

2.4.5. TWO-QUBIT CONTROL

With inhomogeneity in the local Zeeman splitting, the exchange interaction gives rise to a richer set of two-qubit gates than only $\sqrt{SWAP}$. We can return to the Fermi-Hubbard Hamiltonian for a double-dot potential and consider the more general case where a difference in local magnetic fields between the two dots gives rise to both a spin-conserving tunneling $t_{\mathrm{sc}} = t_c \cos(\theta/2)$ and a spin-flip tunneling $t_{\mathrm{sf}} = t_c \sin(\theta/2)$, as introduced in Sec. 2.4.2.

Taking the four (1,1) spin product states ($c^\dagger_{L,\downarrow}c^\dagger_{R,\downarrow}|0\rangle$, $c^\dagger_{L,\downarrow}c^\dagger_{R,\uparrow}|0\rangle$, $c^\dagger_{L,\uparrow}c^\dagger_{R,\downarrow}|0\rangle$, and $c^\dagger_{L,\uparrow}c^\dagger_{R,\uparrow}|0\rangle$) and singlet (2,0) and (0,2) states ($c^\dagger_{\mathrm{L},\downarrow}c^\dagger_{\mathrm{L},\uparrow}|0\rangle$ and $c^\dagger_{\mathrm{R},\downarrow}c^\dagger_{\mathrm{R},\uparrow}|0\rangle$) as the relevant basis, the two-spin Fermi-Hubbard Hamiltonian can be expressed as[14]:

[14] Here I've only considered $\tau_x \otimes I$ and $\tau_y \otimes \sigma_y$ spin-conserving and spin-flipping terms respectively that appear in the single-particle Hamiltonian of Eq. 2.37, which give rise to the coupling terms $t_{\mathrm{sc}}(c^\dagger_{L,\downarrow}c_{R,\downarrow} + c^\dagger_{L,\uparrow}c_{R,\uparrow}) + t_{\mathrm{sf}}(c^\dagger_{L,\uparrow}c_{R,\downarrow} - c^\dagger_{L,\downarrow}c_{R,\uparrow}) + \mathrm{h.c.}$ in the two-particle Hamiltonian. This is a simplification of a more complicated general picture that permits more possible terms owing to spin-orbit interaction and the anisotropic spin g-tensor [58–60], but these terms capture the necessary physics.

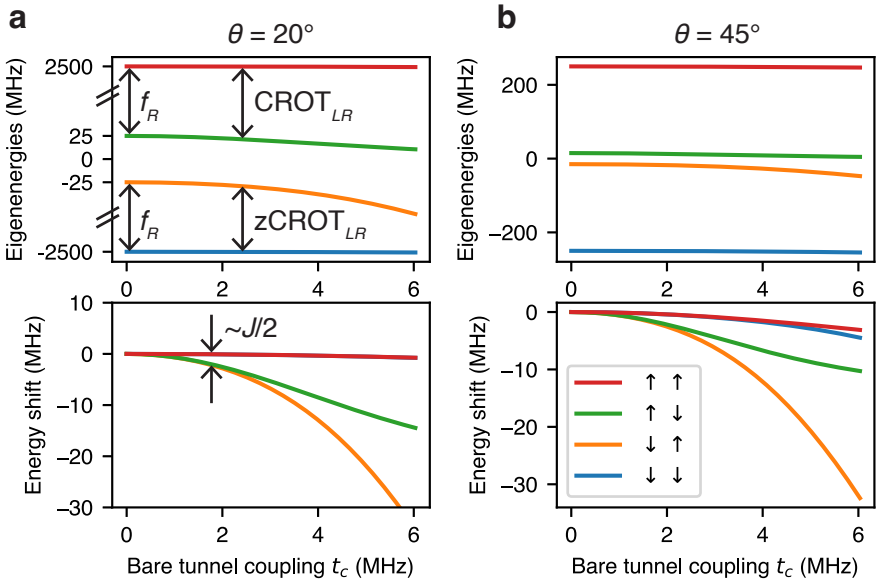


Figure 2.3: Eigenenergies of the (1,1) spin states of Eq. 2.46 as a function of t_c when $\epsilon = 0$ and $U = 12$ meV. The absolute energies (top) and relative shift (bottom) are plotted for clarity. The legend indicates the spin product state corresponding to each instantaneous eigenstate when $t_c = 0$. **a** Parameters similar to a bus stop interaction in Chapter 5 where $\bar{\omega}_L/2\pi = 2.5$ GHz, $d\omega_L/2\pi = 50$ MHz and $\theta = 20°$. The top panel illustrates the unconditional Larmor frequency of the spin in $|R\rangle$ when $t_c = 0$ and the two conditional rotations that arise as the tunnel coupling is increased. The bottom panel illustrates the approximate frequency shifts in terms of J when $2\pi J \ll d\omega_L$. **b** Parameters similar to the low-field regime in Chapter 4 where $\bar{\omega}_L/2\pi = 250$ MHz, $d\omega_L/2\pi = 30$ MHz and $\theta = 45°$.

$$H_{\mathrm{DQD,2e}} = \begin{pmatrix} -\bar{\omega}_L & 0 & 0 & 0 & t_{sf} & t_{sf} \\ 0 & \frac{-d\omega_L}{2} & 0 & 0 & t_{sc} & t_{sc} \\ 0 & 0 & \frac{d\omega_L}{2} & 0 & -t_{sc} & -t_{sc} \\ 0 & 0 & 0 & \bar{\omega}_L & t_{sf} & t_{sf} \\ t_{sf} & t_{sc} & -t_{sc} & t_{sf} & \epsilon + U & 0 \\ t_{sf} & t_{sc} & -t_{sc} & t_{sf} & 0 & -\epsilon + U \end{pmatrix}, \tag{2.46}$$

where $\bar{\omega}_L$ is the average Larmor frequency of the spins located in the two sites, and $d\omega_L$ is the difference in Larmor frequency between the two sites. $d\omega_L$, θ, and U are essentially fixed by the device design, and only ϵ and t_c may be controlled to induce two-qubit interaction.

It is informative to perform a Schrieffer-Wolf transformation to isolate the (1,1) sector in the regime when all energy scales are perturbative with respect to U such that:

$$H_{\mathrm{DQD,2e}} \approx \begin{pmatrix} -\bar{\omega}_{\mathrm{L}} - \frac{2t_{\mathrm{sf}}^2 U}{U^2-\epsilon^2} & -\frac{2t_{\mathrm{sc}}t_{\mathrm{sf}}U}{U^2-\epsilon^2} & \frac{2t_{\mathrm{sc}}t_{\mathrm{sf}}U}{U^2-\epsilon^2} & -\frac{2t_{\mathrm{sf}}^2 U}{U^2-\epsilon^2} \\ -\frac{2t_{\mathrm{sc}}t_{\mathrm{sf}}U}{U^2-\epsilon^2} & \frac{-d\omega_{\mathrm{L}}}{2} - \frac{2t_{\mathrm{sc}}^2 U}{U^2-\epsilon^2} & \frac{2t_{\mathrm{sc}}^2 U}{U^2-\epsilon^2} & -\frac{2t_{\mathrm{sc}}t_{\mathrm{sf}}U}{U^2-\epsilon^2} \\ \frac{2t_{\mathrm{sc}}t_{\mathrm{sf}}U}{U^2-\epsilon^2} & \frac{2t_{\mathrm{sc}}^2 U}{U^2-\epsilon^2} & \frac{d\omega_{\mathrm{L}}}{2} - \frac{2t_{\mathrm{sc}}^2 U}{U^2-\epsilon^2} & \frac{2t_{\mathrm{sc}}t_{\mathrm{sf}}U}{U^2-\epsilon^2} \\ -\frac{2t_{\mathrm{sf}}^2 U}{U^2-\epsilon^2} & -\frac{2t_{\mathrm{sc}}t_{\mathrm{sf}}U}{U^2-\epsilon^2} & \frac{2t_{\mathrm{sc}}t_{\mathrm{sf}}U}{U^2-\epsilon^2} & \bar{\omega}_{\mathrm{L}} - \frac{2t_{\mathrm{sf}}^2 U}{U^2-\epsilon^2} \end{pmatrix}. \tag{2.47}$$

There are a few important observations about this Hamiltonian. One is that the traditional Heisenberg Hamiltonian of Eq. 2.7 is recovered when $t_{\mathrm{sf}} \to 0$ such that $2\pi J = \frac{4t_{\mathrm{sc}}^2}{U(1-\epsilon^2/U^2)}$. Another is that all of the terms have zero derivative with respect to the detuning when $\epsilon = 0$, motivating all two-qubit interactions to take place at this symmetry point in order to be as robust to noise as possible [61, 62]. Last, the dynamics generated by the Hamiltonian are complicated in the presence of spin-flip tunnel coupling as all matrix elements become non-zero, and "clean" two-qubit gates emerge in limiting cases [63].

The most simplifying limit is when $d\omega_{\mathrm{L}} \gg 4t_{\mathrm{sc}}^2/U$ such that:

$$H_{\mathrm{DQD,2e}} \approx \begin{pmatrix} -\bar{\omega}_{\mathrm{L}} & 0 & 0 & 0 \\ 0 & \frac{-d\omega_{\mathrm{L}}}{2} - \frac{2\pi J}{2} & 0 & 0 \\ 0 & 0 & \frac{d\omega_{L}}{2} - \frac{2\pi J}{2} & 0 \\ 0 & 0 & 0 & \bar{\omega}_{\mathrm{L}} \end{pmatrix}. \tag{2.48}$$

In this limit, one can construct a resonantly-driven CNOT or a baseband CZ gate.

The former is achieved by noticing that the two bare spin resonances split into two branches as illustrated in Fig. 2.3a, explicitly given by $f_{L/R,\downarrow/\uparrow} = \bar{\omega}_{\mathrm{L}} \pm \frac{d\omega_{\mathrm{L}}}{2} \pm \frac{2\pi J}{2}$. Each of these resonances may be driven by ESR or EDSR and understood in the framework of Eq. 2.3.1. A CNOT is achieved by selecting the desired resonance and applying a conditional rotation (CROT). The ideal CROT unitary is given by $|0\rangle\langle 0| \otimes I + |1\rangle\langle 1| \otimes R_x(\pi)$ and a CNOT is compiled with the addition of a $R_z(\pi/2)$ on the control qubit.

To maximize the fidelity of the CROT, the undesired conditional resonance (labeled zCROT in Fig. 2.3a) should be synchronized away. The best strategy is to activate exchange adiabatically and apply the resonant drive with a rectangular window. As the undesired branch is detuned by approximately J, the synchronization condition reads:

$$\Omega = \frac{J}{\sqrt{4n^2-1}}. \tag{2.49}$$

The ease of synchronizing with a rectangular window comes with the notable disadvantage of having a broader spectrum that may

off-resonantly drive other nearby transitions.

Generally, the baseband CZ primitive is preferred over the CROT for coherent control as phase tracking is simpler and there is no microwave crosstalk. However, the simplicity of calibrating the CROT makes it appealing for quantum non-demolition readout (QND), where only conditional spin flips are required and phase tracking does not matter (see Chapter 5).

In the $d\omega_L \gg J$ limit, a baseband CZ is implemented by activating $H_{DQD,2e}$ for a duration $1/2J$ and applying $R_z(-\pi/2)$ to both qubits. The fidelity is maximized by ensuring adiabaticity to avoid any unwanted SWAP-like dynamics, which is tantamount to minimizing the Fourier component of the modulated Hamiltonian term which is resonant with the undesired diabatic transition (i.e. $d\omega_L$) [43, 64, 65]. The required gate duration is approximately given by $8\pi/d\omega_L$ when optimal pulse shapes are used, so having a Larmor frequency difference of tens of MHz between participating spins is desirable for implementing fast adiabatic CZ gates [66]. We can use the limiting case of large $d\omega_L$ to estimate the fidelity of a CZ gate subject to noise in exchange using Eq. 2.16. Assuming perfect single-qubit phase corrections, we can estimate the infidelity due to quasi-static fluctuations in the magnitude of exchange, σ_J as:

$$\varepsilon^*_{CZ} \approx \frac{\pi^2 \sigma_J^2}{20J^2}. \tag{2.50}$$

For $J = 5$ MHz, a 99% fidelity CZ gate by this estimate requires $\sigma_J < 0.7$ MHz. The quality factor estimate is identical to that of the SWAP presented in Sec. 2.3.3.

The CNOT and CZ primitives still work in the presence of finite spin-flip tunnel coupling, but more care must be taken in the case where $d\omega_L$ is more modest. An example is illustrated in Fig. 2.3b, where all four energy levels move as the tunnel coupling is modulated. In general, the best approach is to activate t_c adiabatically such that the total unitary is $U_{2Q} = \mathrm{diag}\left(1, e^{-i\phi_{01}}, e^{-i\phi_{10}}, e^{-i\phi_{11}}\right)$. A CZ gate can always be implemented by applying single-qubit phase gates such that $R_z(\phi_{10}) \otimes R_z(\phi_{01}) U_{2Q} = \mathrm{diag}\left(1, 1, 1, e^{i(\phi_{01}+\phi_{10}-\phi_{11})}\right)$ and $\phi_{01}+\phi_{10}-\phi_{11} = \pi$. The requisite phase pickups can be calibrated explicitly, or a decoupled CZ (DCZ) can be used to refocus them [67]. As a rule of thumb, the gate time for a 99.9% fidelity adiabatic CZ gate goes as $8\pi/d\omega_L$, so $d\omega_L/2\pi$ should be designed to be at least on the order of tens of MHz at the location of the two-qubit interaction to ensure gate times on the order of 100 ns [66].

Two-qubit interactions can also be a source of entangling crosstalk if there is a finite residual exchange coupling that is relevant over the timescale of an experiment. Furthermore, exchange can be sensitive to

capacitive crosstalk, as barrier gates are generally difficult to virtualize with respect to one another in silicon. As exchange is controlled locally, the easiest mitigation strategy on both fronts is to spatially separate the qubits more such that residual exchange is minimized [68, 69] (see also Chapter 5).

2.4.6. PAULI SPIN BLOCKADE

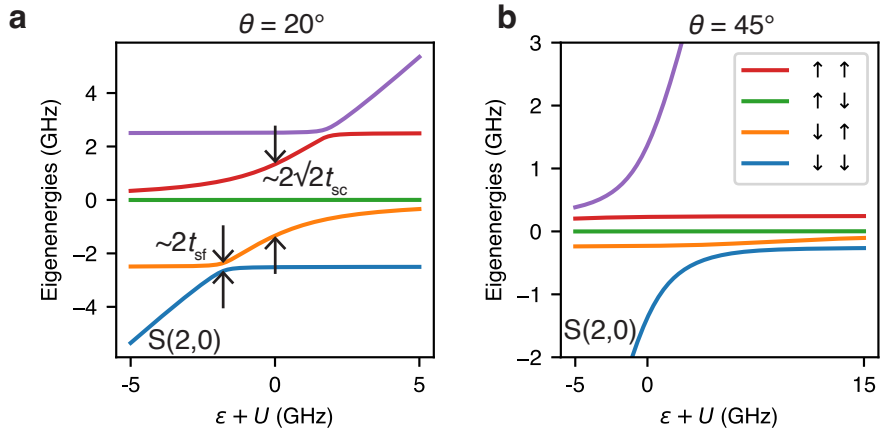


Figure 2.4: Eigenenergies of the (1,1) and S(2,0) spin states of Eq. 2.46 as a function of ϵ near the S(1,1)-S(2,0) avoided crossing when $t_c = 4$ μeV and $U = 12$ meV. The legend indicates the spin product state corresponding to each instantaneous (1,1) eigenstate when $\epsilon = 0$ (and $t_c \to 0$). **a** Parameters similar to a bus stop interaction in Chapter 5 where $\bar{\omega}_L/2\pi = 2.5$ GHz, $d\omega_L/2\pi = 50$ MHz and $\theta = 20°$. The $\Delta_{ST_}$ and S(1,1)-S(2,0) avoided crossings are indicated. **b** Parameters similar to the low field regime in Chapter 4 where $\bar{\omega}_L/2\pi = 250$ MHz, $d\omega_L/2\pi = 30$ MHz and $\theta = 45°$.

Pauli spin blockade (PSB) constitutes the most relevant strategy for spin-to-charge conversion used by spin qubits currently. As the relevant energy scale is the singlet-triplet of a dot (i.e. approximately the orbital splitting on the order of a few meV), it is thermally robust and insensitive to the average Larmor frequency of the participating spins. The mechanism can be understood by plotting the eigenvalues of Eq. 2.46 as shown in Fig. 2.4.

The difference in charge configuration (1,1) or (2,0) can be detected by an rf-SET, for example, as it is throughout all work presented in this thesis [70]. If a detected (2,0) charge configuration is ramped to the (1,1) charge configuration, one of three outcomes is possible.

If the ramp is slow enough to be adiabatic with respect to the avoided crossing formed between the $S(2,0)$-like and T_--like eigenstates, the latter spin state will be initialized. The question of adiabaticity can

be treated as a Landau-Zener problem, where the relevant energy gap $\Delta_{ST_-} \approx 2|t_{sf}|$ can be inferred from the model of Eq. 2.46.

If the ramp is fast enough to be diabatic with respect to the Δ_{ST_-} gap, but adiabatic with respect to the $S(2,0)$-$S(1,1)$-like avoided crossing separated by $2\sqrt{2}t_{sc}$, either a $|\downarrow\uparrow\rangle$ or $S(1,1)$ will be initialized. The adiabaticity can be evaluated through the lens of the sudden approximation given by Eq. 2.15 by comparing the energy scale of the Hamiltonian change and the duration of the change. The former is given by $\sqrt{J_{start}^2 + d\omega_L^2} - \sqrt{J_{end}^2 + d\omega_L^2}$, where J_{start} is the exchange just after the $S(2,0)$-$S(1,1)$ has been traversed, and J_{end} is the level of exchange once the charge symmetry point is reached. The change in J may be a function of both t_{sc} and ϵ. The adiabatic initialization to $|\downarrow\uparrow\rangle$ is consistent with a large t_{sc} which also maximizes the adiabaticity of the $S(2,0)$-$S(1,1)$ evolution. This is therefore the preferred initialization trajectory for silicon.

Of course, if the ramp is diabatic with respect to the $S(2,0)$-T_--like and $S(2,0)$-$S(1,1)$-like avoided crossings, one also shoots through the $S(2,0)$-T_+ gap, and whatever state is initialized will depend on the eventual relaxation of the preserved $S(2,0)$ state.

Readout generally works inversely, where any spin state that couples to the $S(2,0)$ when ramping the detuning at the appropriate speed will be unblockaded and therefore detectable as a (2,0) charge state, while any state that doesn't couple is blockaded in the (1,1) charge state. However, such a (1,1) state is only metastable and will ultimately relax to the (2,0) state subject to noise. This relaxation ultimately determines the readout mechanism [71]. In short, if $d\omega_L \ll J$, PSB will distinguish the $S(1,1)$ spin state from the spin triplet states for so-called single-triplet readout. Singlet-triplet readout, corresponding to the operator $\vec{\sigma}\cdot\vec{\sigma}$, is inherently a QND projective measurement because the triplet states are preserved while the $S(1,1)$ can be reinitialized from the $S(2,0)$ state to which it evolves, but it is unable to distinguish between the triplet states in the absence of multi-qubit control and multiple readout rounds.

Otherwise, $d\omega_L$ couples $S(1,1)$ to T_0 such that the latter also relaxes to the ground state $S(2,0)$. This gives rise to so-called parity-mode PSB readout [71], with the operator $Z \otimes Z$, where odd-parity spin states are unblockaded and vice versa. It is not a QND measurement because information about which odd-parity spin state evolved to the (2,0) configuration is lost. However, the addition of two-qubit logic enables computational basis readout [72]. If one of the spins is treated as a fixed measurement ancilla, QND readout of one of the spins with parity-mode PSB is possible, and this is leveraged in Chapter 5.

With an engineered inhomogeneous magnetic field, where $d\omega_L$ may be on the order of tens of MHz while t_{sf} can be small, the intermediate

initialization to the $|\downarrow,\uparrow\rangle$ state is most reliable, and parity-mode PSB is available for readout. Usually, a post-selection or heralding scheme with feedback is the most efficient way to achieve a low initialization error [72–74].

2.4.7. SIMULATION STRATEGIES

Silicon spin qubit control, in the idealized case, boils down to having good control of the positions of quantum dots, the bare tunnel coupling t_c between them and the spatial stray magnetic field $\mathbf{B}(\mathbf{r})$. Fortunately, these values can be predicted relatively easily with simple simulations. Chapter 5 contains a worked-out example of both electrostatic and magnetostatic simulations, but the workflow is summarized here. More rigorous descriptions of electrostatic simulation [3, 75] and magnetostatic simulation [24, 34] can be referred to as necessary.

SIMULATING ELECTROSTATICS

Using a nominal device design and the corresponding material properties, a finite-element Poisson solver can be used to determine the resulting potential energy landscape $V(x, y)$. The resulting single-particle Schrödinger equation can be solved using this potential to find the orbital energy spectrum. The finite-element model needs to only be large enough so that the natural boundary conditions do not affect the convergence of the result, and the focus on few confined charges means that the marginal returns of full Schrödinger-Poisson self-consistency are not worth the hassle of implementation.

By varying the electrostatic boundary conditions, the centers-of-mass of the resulting orbital ground states serve as good estimates of dot position/trajectory for feeding into magnetostatic simulations, and the orbital energy separation $\hbar\omega_0$ and length scale a_0 can also be extracted. The charging energy U generally must be extracted from a two-body integral to account for the electron-electron interaction, but this is numerically tractable for a double-dot system[15].

In the case of a balanced double-dot potential, the ground and excited orbital states will be bonding and antibonding with an energy separation of $\sqrt{\epsilon^2 + (2t_c)^2}$. Packages like QTCAD have built-in methods for numerically minimizing this separation and therefore estimating the bare tunnel coupling t_c between dots. One can verify through simulations

[15] One can also note that the charging energy is approximated as $U = e^2/C$ in the limit where the orbital energy scale is small, where $C = 8\epsilon a_0$ is the capacitance for a disk of radius a_0 and permittivity ϵ (silicon has a relative permittivity of 11.7). A typical U of 12 meV corresponds to a_0 of 16 nm. Since a_0 may also be estimated from the orbital energy spacing of a single-particle solution, estimating the charging energy in this way bypasses the many-body integral.

that barrier gates will modulate t_c exponentially over a wide range (with deviation possible at very low and high values of exchange). Since $J \propto t_c^2$ at the symmetry point, this leads to the empirical model:

$$J \approx J_{\text{res}} e^{\alpha BB}, \tag{2.51}$$

where α describes how strongly the barrier voltage BB modulates exchange and J_{res} is the residual exchange between two coupled spins when $BB = 0$. This empirical relation will typically be valid in the two-qubit-logic regime where pulse shaping is relevant. In state-of-the-art device geometries one will find $\alpha \approx 0.1\,\text{mV}^{-1}$ or smaller, though the optimal lever arm for maximizing two-qubit fidelity in the presence of noise is still the subject of debate.

SIMULATING MAGNETIC FIELDS

With dot positions estimated from electrostatic simulations, all other relevant device parameters can be estimated from $\mathbf{B}(\mathbf{r})$ according to Sec. 2.4.1 and Sec. 2.4.2. The remaining task is to faithfully design and simulate $\mathbf{B}(\mathbf{r})$. The best choice will depend on the source of the magnetic field.

For micromagnet simulations where the ferromagnetic material can be approximated as bulk (or if current sources are used), we can leverage the efficient magnetic field calculations of the Python package magpylib. Such simulations treat the micromagnet as having a homogeneous polarization with no microscopic crystal structure such that the analytic form of the stray field for constituent magnet shapes can be used to calculate the total magnetic vector field. This is very efficient for quickly designing qualitative properties of the magnetic field, but there are several sources of uncertainty. At a fundamental level, no time-dynamics or domain wall formation is accounted for in the simulations, nor is uniaxial magnetic anisotropy, which originates in the crystal structure of the magnetic material, considered. Consequently, it is generally not the case that the on-chip magnets are "fully magnetized". Nevertheless, we can estimate an effective homogeneous magnetization from experiment by measuring qubit Larmor frequencies as a function of the applied external field and fitting the approximate simulations accordingly.

For the (bulk) cobalt micromagnets used in all devices covered in this thesis, it is generally safe to approximate that a saturated polarization[16] of 1.5 T is achieved in external fields of 200 mT or greater after the magnet has been polarized in a field of about 1 T or greater. Below 200 mT, the micromagnet will demagnetize but will remain completely stable at low temperatures even if the external field is set to oppose the remanence of

[16] Polarization $\mathbf{J}$ is given in units T and relates to magnetization $\mathbf{M}$ in units A/m as $\mathbf{J} = \mu\mathbf{M}$, where μ is the permeability.

the micromagnet. For example, the experiments in Chapters 4 and 5 were taken over the course of several months with no systematic drift in qubit frequencies observed. The magnets will depolarize slightly (by about 1%) when heated to 4 K and reset if thermal-cycled to room temperature, though the precise temperature threshold at which this occurs has not been characterized.

Moving to smaller nanomagnets will confer additional advantages in future devices. They enable more precise magnetic domain engineering by exploiting shape anisotropy, for example, and retain their polarization at room temperature without any external field applied [32]. To fully capture their behaviour, more powerful simulation packages such as OOMMF or mumax3 are necessary (see Chapter 4).

2.5. ELECTRON SPIN QUBITS IN SILICON

The previous sections have restricted attention to what can be engineered to some degree of tolerance, namely the device electrostatics and magnetic environment. However, unless atomic precision can be guaranteed, disorder in the solid-state environment will always give rise to a statistical spread in quantum dot and spin qubit properties. Furthermore, no solid-state material platform is a perfectly boring host. We must therefore account for the personality silicon spin qubits inherit from their environment.

2.5.1. BULK SILICON

Silicon and its robust native oxide form the backbone of the modern semiconductor industry, and silicon's ability to host spins with long T_1 times was established decades before the Loss-DiVincenzo proposal [1]. For quantum information processing, the motivation to also use electron spins in silicon is largely derived from the ability to isotopically purify the substrate to consist almost entirely of the ^{28}Si isotope which has zero nuclear spin. Furthermore, the intrinsic spin-orbit interaction (iSOI) strength is low due to the high-degree of symmetry in the system. Together, these features mean that silicon creates a very quiet environment for a spin, as magnetic noise originating from nuclear spins can be reduced through isotopic purification and electrical charge noise, ubiquitous to any solid state environment, does not easily couple to the spin via iSOI.

However, bulk silicon is not ideal for isolating the two-level spin of a conduction band electron. Bulk silicon's conduction band has 6 degenerate valleys located at $k_0 \approx 0.85\frac{2\pi}{a_{\mathrm{Si}}}$ towards the Brillouin zone boundary along the $\langle 100 \rangle$ family of crystallographic directions, where $a_{\mathrm{Si}} \approx 0.543\,\mathrm{nm}$ is the lattice parameter of silicon's diamond cubic crystal

structure [1]. The dispersion relation at each valley is characterized by the longitudinal effective mass $0.92m_e$ parallel to the crystallographic direction and the transverse effective mass $0.19m_e$. In the absence of any iSOI, the g-factor of a conduction band electron is effectively 2, but in the presence of the weak iSOI gives rise to a g-tensor that is technically anisotropic [76].

2.5.2. MOVING TO A STRAINED SILICON QUANTUM WELL

The material must provide a degree of confinement, and this necessarily reduces the symmetry in the system. I will focus on the case of quantum wells in SiGe heterostructures, though the physical implications are mostly analogous for Si-MOS and other similar platforms.

By straining a thin silicon quantum well between two layers of $Si_{0.3}Ge_{0.7}$ alloy, the conduction band minimum is lowered by about 160 meV with respect to the SiGe, allowing for the accumulation of electrons. The two valleys corresponding to the growth direction of the silicon quantum well, typically taken as [001], will be lower in energy than the other four owing to the tensile strain and lower longitudinal effective mass [1]. These valleys are therefore denoted as $|+z\rangle$ and $|-z\rangle$. The remaining degeneracy between these valleys is broken by the nature of their coupling at the Si/SiGe interface. This interface also adds a degree of structural inversion asymmetry and contributes to the iSOI present in the system. This has consequences for the spin g-tensor and for how strongly electric fields couple to the spin.

As SiGe is an alloy with a statistical mixture of atoms, the interface it forms with the quantum well inherits this variability, and the variability permeates to the Hamiltonian of the spin qubits through a combination of iSOI and valley physics. The following sections summarize how these contributions affect our understanding of how accurately spin qubits can be engineered.

2.5.3. INTRINSIC SPIN-ORBIT INTERACTION

For conduction band electrons in silicon, iSOI can be summarized as Rashba and Dresselhaus contributions that give rise to the following terms in the effective-mass Hamiltonian given in Eq. 2.1:

$$H_{\mathrm{iSOI,R}} = \alpha(p_{x'}\sigma_{y'} - p_{y'}\sigma_{x'}), \tag{2.52}$$

and

$$H_{\mathrm{iSOI,D}} = \beta(p_{x'}\sigma_{x'} - p_{y'}\sigma_{y'}) \tag{2.53}$$

where the prime coordinates are with respect to the crystallographic axes in the lab frame. The magnitude of the components therefore depends

on the orientation of the spin's motion. Estimates for the magnitude of α and β are typically on the order of 100 m/s, and are sometimes reported as $\hbar/m^*\lambda_{SO}$ in terms of a spin-orbit length λ_{SO} that is on the order of 1 µm [77, 78].

Due to its dependence on momentum, iSOI will influence the behaviour of spins in motion. For conveyor-mode spin shuttling, given by Eq. 2.44, this gives rise to an effective magnetic field of $\frac{2\sqrt{\alpha^2+\beta^2}\langle \mathbf{p} \rangle}{g\mu_B}$ as the electron moves. For shuttling speeds on the order of 10 m/s, this effective magnetic field can have a magnitude on the order of 0.1 mT. If the direction of motion is reversed, so will the orientation of the effective magnetic field. If the electron is shaken at its Larmor frequency, this will give rise to EDSR[17]. When an external magnetic field is also applied, the spin evolves according to the total effective Zeeman Hamiltonian. If the external magnetic field dominates, one can expect electron motion to manifest as a phase pickup due to adiabatic state evolution. If the effective magnetic field dominates, a more general unitary operation may occur depending on the speed of shuttling. Regardless, the presence of iSOI generally means one cannot assume that electron spin shuttling is equivalent to an identity operation on the spin, even in a perfectly uniform magnetic field.

The iSOI will also affect the nature of tunnel coupling between two dots. Whereas in Sec. 2.4.2, coupling terms of $\tau_x \otimes I$ and $\tau_y \otimes \sigma_y$ gave rise to spin-conserving and spin-flipping tunnel coupling terms, iSOI allows for an even more general expression of coupling terms summarized as [41]:

$$H_{SO} = t_c \tau_x \otimes I + \tau_y \otimes \mathbf{t}_{\mathrm{iSOI}} \cdot \sigma, \tag{2.54}$$

where $\mathbf{t}_{\mathrm{iSOI}}$ is a vector of real numbers. Their magnitude will depend on the strength of iSOI, given by α and β as well as the matrix elements of the momentum operator. For a typical double-dot system in silicon, $|\mathbf{t}_{\mathrm{iSOI}}|$ is on the order of 1 µeV. Combined with the effects of an inhomogeneous magnetic field, this results in more complicated expressions for t_{sc} and t_{sf}, but the physics can still be interpreted in the simplified case of Sec. 2.4.2.

Generally, t_c will be an order of magnitude larger than $|\mathbf{t}_{\mathrm{iSOI}}|$, therefore the relative values of t_{sc} and t_{sf} will be dominated by the quantization axis tip θ. However, the contribution from iSOI also means that one cannot assume t_{sf} is zero even in a uniform magnetic field. Generally, all elements of the two-qubit exchange Hamiltonian will be nonzero, and

[17] This EDSR is can be interpreted in the context of Sec. 2.3.1, but it is fundamentally different from the EDSR mediated by a magnetic stray field of Sec. 2.4.1 due to the time-reversal symmetry present in the former case [79]. One consequence of this is that the Rabi frequency of EDSR mediated by iSOI is proportional to the external field strength, whereas this is not the case for sSOI.

an avoided crossing between the $S(2,0)$ and $T_{-/+}$ states will be exist in the context of Eq. 2.46. Provided the gap is small enough for diabatic passage, good initialization via PSB remains possible, and an adiabatic CZ gate will be disinterested in the small non-zero matrix elements of the Fermi-Hubbard Hamiltonian.

A more consequential effect is the way iSOI renormalizes the g-factor of confined electron spins. In the g-tensor formalism that applies in the solid-state, the Zeeman term reads:

$$H = \frac{\mu_B}{2} \mathbf{B} \cdot \mathbf{g} \cdot \sigma. \tag{2.55}$$

In this form the g-tensor is expected to have the form [80]:

$$\mathbf{g} = \begin{pmatrix} g_\perp - \frac{2}{\mu_B}\alpha^* & \frac{2}{\mu_B}\beta^* & 0 \\ \frac{2}{\mu_B}\beta^* & g_\perp - \frac{2}{\mu_B}\alpha^* & 0 \\ 0 & 0 & g_\parallel \end{pmatrix}, \tag{2.56}$$

where $g_\perp \approx 2$ and $g_\parallel \approx 2$ are the g-factors for bulk silicon with the magnetic field oriented perpendicular and parallel to the [001] growth axis respectively. Here, $\alpha^* = e\langle z' - z'_i \rangle \alpha/\hbar$ and $\beta^* = e\langle z' - z'_i \rangle \beta/\hbar$ are given in units MHz/T and depend on the spread of the wavefunction in the z'-direction relative to the interface located at z'_i. Given that the iSOI will vary depending on local electric fields and interface disorder, microscopic dot-to-dot differences give rise to differences in spin-orbit coupling perturbations $\Delta\alpha^*$ and $\Delta\beta^*$ across a device. The g-factor difference between two quantum dots follows as [80, 81]:

$$\Delta g = \frac{1}{\mu_B} \left| \Delta\alpha^* - \Delta\beta^* \sin(2\phi_B) \right| \sin^2 \theta_B, \tag{2.57}$$

where here ϕ_B is the azimuthal angle of the total magnetic field with respect to the [100] crystallographic axis and θ_B is the polar angle of the total magnetic field with respect to the [001] growth axis. Δg is expected to be on the order of 10^{-3} [82], with recent data across eight dots in a SiMOS device corroborating this variance [83].

The impact of this variance can be contextualized in the framework of Sec. 2.3.3. If all qubits in a device were driven at a Rabi frequency of 1 MHz with a global field, to maintain 99.9% fidelity X_{90} operations would require all qubits to fall within about 50 kHz of the driving frequency $\omega_{\mathrm{MW}}/2\pi$[18]. This limit is exceeded above an average Larmor frequency of about 50 MHz, and therefore even in the very homogeneous silicon environment there is too much disorder to pursue global driving without further tricks, such as locally Stark-shifting the spins using iSOI [84] or homogenizing qubit frequencies by shuttling [85].

[18] This is very approximate, because the error would be coherent.

Alternatively, one could view g-factor variations from iSOI as a means of spectral addressability by increasing the average Larmor frequency to the order of 10 GHz such that the 0.1% g-factor variance separates qubits by about 10 MHz. However, such addressability is probabilistic and cannot circumvent unwanted off-resonant driving. The introduction of on-chip magnets provides a much better degree of spectral addressability at the expense of adding a further source of on-chip variability. Therefore when on-chip magnets are used, g-factor variability due to iSOI can be effectively neglected, but the problem of addressing multiple spins is still an open problem at scale. In Sec. 6, I discuss an example where a combination of spectral and spatial addressability is used to circumvent this issue.

2.5.4. VALLEY PHYSICS

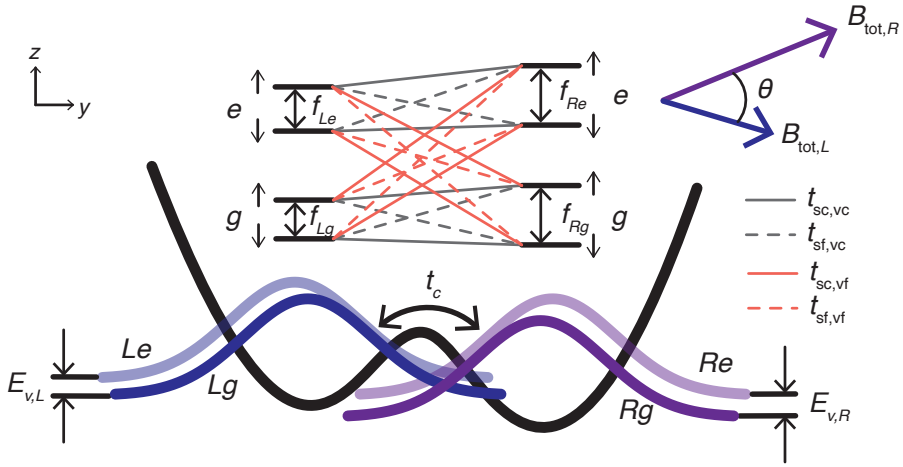


Figure 2.5: A graphical representation of the modified picture of a single electron in a double-dot potential when valley effects are included. Each dot contains an s-like ground $|L/R, g\rangle$ and excited $|L/R, e\rangle$ valley-orbit state separated by $E_{v,L}$ and $E_{v,R}$ respectively. Due to interface disorder, the envelope functions of each valley-orbit state may be shifted, giving rise to a finite valley dipole. As a consequence of iSOI and an inhomogeneous magnetic field, the spin experiences a different environment in each valley state, giving rise to spin-valley-orbit coupling. The spin Larmor frequency $f_{L/R,g/e}$ may be different depending on its valley-orbital state. The valley phase difference $d\phi_v$, magnetic field tip angle θ, and iSOI give rise to four distinct tunneling processes that may flip or conserve the spin or valley. The valley phase difference dominates the valley aspect, while magnetic field misalignment dominates the spin aspect. However, spin-valley-orbit coupling means that these aspects are interdependent to a small extent.

The effective-mass Hamiltonian of Eq. 2.1 uses $m^* = 0.19m_e$, the transverse effective mass of the conduction band valleys, to understand

the $\psi(x, y)$ envelope of the three-dimensional electron wavefunction $\psi(\mathbf{r})$. Valley physics manifests in the z aspect that was previously neglected. Along this spatial direction, corresponding to the [001] crystallographic growth direction, the basis states for the electron's wavefunction can be expressed as a product of the total envelope function $\psi(\mathbf{r})$ and the oscillatory components associated with the $|\pm z\rangle$ valleys [86]:

$$\psi_{\pm}(\mathbf{r}) \approx e^{\pm ik_0 z}\psi(\mathbf{r}). \tag{2.58}$$

A perturbative potential $\phi_V(\mathbf{r})$ is introduced which couples the valley components without altering the envelope function:

$$\Delta = |\Delta| e^{i\phi_V} = \langle \phi_+ | \phi_V(\mathbf{r}) | \phi_- \rangle = \int d\mathbf{r} e^{-i2k_0 z} \phi_V(\mathbf{r}) |\psi(\mathbf{r})|^2 . \tag{2.59}$$

The valley eigenstates solve the Schrödinger equation with the Hamiltonian (expressed in the $\{|\psi_{\pm}\rangle\}$ basis):

$$H_V = \begin{pmatrix} 0 & \Delta \\ \Delta^* & 0 \end{pmatrix}, \tag{2.60}$$

The ground (g) and excited (e) eigenstates are [87]:

$$\psi_{g/e}(\mathbf{r}) = \frac{1}{\sqrt{2}} \left(e^{ik_0 z} u_{+k_0}(\mathbf{r}) \pm e^{i\phi_V} e^{-ik_0 z} u_{-k_0}(\mathbf{r}) \right) \psi(\mathbf{r}), \tag{2.61}$$

where $u_{\pm k_0}$ is the periodic component of the Bloch functions. ψ_g and ψ_e are energetically separated by the valley splitting $E_V = 2|\Delta|$. To isolate a two-level spin system in the ψ_g state, it is generally desirable to have ψ_e separated by a sufficiently large E_V such that its occupation is negligible.

The form of Eq. 2.59 makes clear that any effort to augment the valley splitting must maximize the Fourier component of $\phi_V(\mathbf{r})$ with frequency $2k_0$. Approaches range from engineering a sharp interface to depositing Ge in the quantum well during material growth with the correct periodicity. Both approaches are limited by imperfect microscopic control and an inherent degree of alloy disorder. Therefore, the valley splitting must be understood as something that can be engineered on average, but not from dot to dot. The valley phase is relatively less discussed but has very real consequences. Unlike the valley splitting, it will vary almost randomly from dot to dot [88].

The valley degree of freedom percolates into the spin qubit engineering we'd like to be doing in many ways. First, consider the case of a single dot. The states ψ_g and ψ_e should be understood as hybridized valley-orbit states. Generally in Si/SiGe, where valley splittings up to hundreds of μeV are typical, E_V is smaller than the orbital splitting $\hbar\omega_0 \approx 3$ meV. The valley-orbit states can therefore be interpreted as filling the same

Fock-Darwin shells, given by Eq. 2.3, but with an effective spin-valley degeneracy of 4 [89].

In the first silicon experiments, when energy-selective tunneling from a reservoir was used for initialization, having too low valley splitting meant that the Fermi-level of the electron reservoir could probabilistically populate the two lowest valley-orbit eigenstates. This is an enormous problem, because the spin physics will be slightly different between the two valleys. As the two valley-orbit states interact differently with the Si/SiGe interface, they generally sample a slightly different iSOI and, if applicable, inhomogeneous magnetic field, and therefore have different Larmor frequencies [90, 91]. This spin-valley coupling affects the quality of single-qubit control.

At present, a lower-than-normal valley splitting is not catastrophic by default, because initialization by PSB should be tunable to avoid populating the excited valley eigenstate. Here, the primary threat to good spin qubit performance is if the Zeeman energy is nearly degenerate with the valley splitting such that a fast relaxation channel appears [92]. Since average valley splittings in modern materials typically exceed tens of μeV [93], using spin Larmor frequencies below 5 GHz, for example, makes such a degeneracy unlikely (though not impossible). While a finite dipole moment can be present between the lowest valley-orbit states (i.e. $e\langle\psi_e|\mathbf{r}|\psi_g\rangle \neq 0$ and therefore support EDSR, this should be dwarfed by the dipole moment with the next p-like Fock-Darwin orbital. EDSR will only be greatly affected if, again, the Zeeman splitting approaches the valley splitting [94]. The problem of g-factor variation due to varying iSOI is neither improved nor worsened by the presence of valley.

During conveyor-mode shuttling, traversing a region of low valley splitting increases the likelihood of leakage out of the ground valley-orbital state. Similar to the case of energy-selective initialization, the probabilistic occupation of a different valley-orbital state at the final destination of the conveyor is deleterious for subsequent spin operations. Maximizing the valley splitting landscape and shuttling at modest magnetic fields generally optimizes performance [48].

The valley phase ϕ_v is relatively less discussed but very relevant when coupling dots together. Tunneling, as defined in the Fermi-Hubbard Hamiltonian, will be modified according to the valley phase difference $d\phi_v = \phi_{v,L} - \phi_{v,R}$ between dots [95]:

$$\begin{aligned} t_{\mathrm{vc}} &= \frac{1}{2} t_c \left(1 + e^{-id\phi_v}\right) \\ t_{\mathrm{vf}} &= \frac{1}{2} t_c \left(1 - e^{-id\phi_v}\right), \end{aligned} \tag{2.62}$$

where t_{vc} is the valley-conserving (intravalley) tunnel coupling and t_{vf} is the valley-flipping (intervalley) tunnel coupling. These couplings are

illustrated in Fig. 2.5. Unlike for the spin-conserving and spin-flipping analogues t_{sc} and t_{sf}, one has no practical control over the relative magnitudes of t_{vc} and t_{vf}. The resulting energy level diagram for single-electron tunneling between dots as described in Eq. 2.41 becomes quite complicated [41, 96, 97]. For the purposes of coherent spin operation, one wants to minimize the possibility of intermediate Landau-Zener transitions, which is generally achieved when the valley splittings are large with respect to the bare tunnel coupling and Zeeman energies.

A valley phase difference also affects how two spins couple. Generally, the spins will occupy the ground valley state in their respective dots. Therefore $J \propto |t_{vc}|^2 = \frac{t_c^2}{2}(1+\cos(d\phi_v))$ [88]. We can therefore state the relation:

$$J = \frac{J_0}{2}(1+\cos(d\phi_v)), \tag{2.63}$$

where J_0 is the bare exchange one would expect from a Fermi-Hubbard Hamiltonian with no valley degree of freedom and spin-conserving tunnel coupling. Both J and J_0 should scale with the relevant barrier gate voltage in the same way, but the amount of exchange observed at a fixed voltage will differ based on the valley phase difference. If multiple valley states are being probabilistically occupied in an exchange spectroscopy experiment, one may observe two exchange splittings that turn on at different barrier pulse amplitudes [62]. Such an effect is obviously bad for two-qubit control.

Finally, the valley degree of freedom may complicate the Pauli spin blockade for spin-to-charge conversion, as the valley splitting E_V sets the energy scale at which blockade is lifted. The most common technique to bypass this is to perform readout at the (3,1)-(4,0) interdot charge transition. The ground valley "shell" of the triply-occupied dot is filled such that it is the orbital energy scale $\hbar\omega_0$ which sets the energy scale for lifting blockade [72]. One avoids initializing the double-dot system into an excited valley state by ensuring adiabaticity at the S(4,0)-S(3,1) avoided crossing. A comprehensive summary of the effects of valley on PSB in silicon is given in [98].

In summary, the presence of valley is not a deal-breaker in present experiments, both due to improvements in the materials but also due to the evolution in methods by which silicon spins are controlled. However, the presence of the valley does cause difficulties because of its microscopic origin and associated variance across devices. Measuring both the valley splitting and valley phase is possible, but less straightforward and more time-consuming than many other device parameters [95, 99]. Working at modest Zeeman energies such that the spin splitting is almost always below the valley splitting avoids many potential complications, as does

avoiding operations like bucket-brigade spin shuttling through empty quantum dots that may probabilistically populate an excited valley state even if the origin and target dots have large valley splittings.

REFERENCES

[1] F. A. Zwanenburg *et al.* “Silicon quantum electronics”. In: *Rev. Mod. Phys.* 85 (3 July 2013), pp. 961–1019. doi: 10.1103/RevModPhys.85.961. url: https://link.aps.org/doi/10.1103/RevModPhys.85.961.

[2] G. Burkard *et al.* “Semiconductor spin qubits”. In: *Rev. Mod. Phys.* 95 (2 June 2023), p. 025003. doi: 10.1103/RevModPhys.95.025003. url: https://link.aps.org/doi/10.1103/RevModPhys.95.025003.

[3] F. Beaudoin *et al.* “Robust technology computer-aided design of gated quantum dots at cryogenic temperature”. In: *Applied Physics Letters* 120.26 (June 2022), p. 264001. issn: 0003-6951. doi: 10.1063/5.0097202.

[4] E. Kawakami. “Characterization of an electron spin qubit in a Si/SiGe quantum dot”. English. Dissertation (TU Delft). Delft University of Technology, 2016. isbn: 978-90-8593-266-6. doi: 10.4233/uuid:dd0886f0-2f3a-421d-ac92-bdc4da5985b5.

[5] V. Fock. “Bemerkung zur Quantelung des harmonischen Oszillators im Magnetfeld”. de. In: *Zeitschrift für Physik* 47.5 (May 1928), pp. 446–448. issn: 0044-3328. doi: 10.1007/BF01390750.

[6] M. Rontani *et al.* “Coulomb correlation effects in semiconductor quantum dots: The role of dimensionality”. In: *Phys. Rev. B* 59 (15 Apr. 1999), pp. 10165–10175. doi: 10.1103/PhysRevB.59.10165. url: https://link.aps.org/doi/10.1103/PhysRevB.59.10165.

[7] V. W. Scarola and S. Das Sarma. “Exchange gate in solid-state spin-quantum computation: The applicability of the Heisenberg model”. In: *Physical Review A* 71.3 (Mar. 2005), p. 032340. doi: 10.1103/PhysRevA.71.032340.

[8] A. J. Weinstein *et al.* “Universal logic with encoded spin qubits in silicon”. In: *Nature* 615.7954 (Feb. 2023), pp. 817–822. issn: 1476-4687. doi: 10.1038/s41586-023-05777-3. url: http://dx.doi.org/10.1038/s41586-023-05777-3.

[9] R. Hanson *et al.* “Spins in few-electron quantum dots”. In: *Reviews of Modern Physics* 79.4 (Oct. 2007), pp. 1217–1265. issn: 1539-0756. url: http://dx.doi.org/10.1103/RevModPhys.79.1217.

[10] M. A. Nielsen and I. L. Chuang. *Quantum Computation and Quantum Information: 10th Anniversary Edition*. Cambridge University Press, 2010.

[11] J. Romhányi, G. Burkard, and A. Pályi. “Subharmonic transitions and Bloch-Siegert shift in electrically driven spin resonance”. In: *Physical Review B - Condensed Matter and Materials Physics* 92.5 (2015), pp. 1–16. issn: 1550235X. doi: 10.1103/PhysRevB.92.054422.

[12] Z. György, A. Pályi, and G. Széchenyi. “Electrically driven spin resonance with bichromatic driving”. In: *Physical Review B* 106.15 (Oct. 2022). issn: 2469-9969. doi: 10.1103/physrevb.106.155412. url: http://dx.doi.org/10.1103/PhysRevB.106.155412.

[13] V. John *et al.* “Bichromatic Rabi Control of Semiconductor Qubits”. In: *Physical Review Letters* 132.6 (Feb. 2024). issn: 1079-7114. doi: 10.1103/physrevlett.132.067001. url: http://dx.doi.org/10.1103/PhysRevLett.132.067001.

[14] M. Steffen, L. M. Vandersypen, and I. L. Chuang. “Simultaneous Soft Pulses Applied at Nearby Frequencies”. In: *Journal of Magnetic Resonance* 146.2 (2000), pp. 369–374. issn: 1090-7807. doi: https://doi.org/10.1006/jmre.2000.2178. url: https://www.sciencedirect.com/science/article/pii/S1090780700921785.

[15] J. J. Sakurai and J. Napolitano. *Modern Quantum Mechanics*. 3rd ed. Cambridge University Press, 2020.

[16] Ł. Cywiński *et al.* “How to enhance dephasing time in superconducting qubits”. In: *Phys. Rev. B* 77 (17 May 2008), p. 174509. doi: 10.1103/PhysRevB.77.174509. url: https://link.aps.org/doi/10.1103/PhysRevB.77.174509.

[17] M. A. Nielsen. “A simple formula for the average gate fidelity of a quantum dynamical operation”. In: *Physics Letters A* 303.4 (Oct. 2002), pp. 249–252. issn: 0375-9601. doi: 10.1016/s0375-9601(02)01272-0. url: http://dx.doi.org/10.1016/S0375-9601(02)01272-0.

[18] T. Nakajima *et al.* “Coherence of a Driven Electron Spin Qubit Actively Decoupled from Quasistatic Noise”. In: *Phys. Rev. X* 10 (1 Mar. 2020), p. 011060. doi: 10.1103/PhysRevX.10.011060. url: https://link.aps.org/doi/10.1103/PhysRevX.10.011060.

[19] A. Silva and E. Greplova. “Hands-on introduction to randomized benchmarking”. In: *SciPost Physics Lecture Notes* (July 2025). issn: 2590-1990. doi: 10.21468/scipostphyslectnotes.97. url: http://dx.doi.org/10.21468/SciPostPhysLectNotes.97.

[20] D. Greenbaum. *Introduction to Quantum Gate Set Tomography*. 2015. arXiv: 1509.02921 [quant-ph]. url: https://arxiv.org/abs/1509.02921.

[21] Y. Tokura *et al.* “Coherent single electron spin control in a slanting zeeman field”. In: *Physical Review Letters* 96.4 (2006). issn: 10797114. doi: 10.1103/PhysRevLett.96.047202.

[22] M. Pioro-Ladrière *et al.* “Micromagnets for coherent control of spin-charge qubit in lateral quantum dots”. In: *Applied Physics Letters* 90.2 (Jan. 2007), p. 024105. issn: 0003-6951. doi: 10.1063/1.2430906.

[23] F. Forster *et al.* “Electric-dipole-induced spin resonance in a lateral double quantum dot incorporating two single-domain nanomagnets”. In: *Physical Review B* 91.19 (May 2015), p. 195417. doi: 10.1103/PhysRevB.91.195417.

[24] R. Neumann and L. R. Schreiber. “Simulation of micro-magnet stray-field dynamics for spin qubit manipulation”. In: *Journal of Applied Physics* 117.19 (May 2015). issn: 10897550. doi: 10.1063/1.4921291.

[25] J. Yoneda *et al.* “Robust micromagnet design for fast electrical manipulations of single spins in quantum dots”. In: *Applied Physics Express* 8.8 (Aug. 2015). issn: 18820786. doi: 10.7567/APEX.8.084401.

[26] N. I. D. Stuyck *et al.* “Low dephasing and robust micromagnet designs for silicon spin qubits”. en. In: *Applied Physics Letters* 119.9 (Aug. 2021), p. 094001. issn: 0003-6951, 1077-3118. doi: 10.1063/5.0059939.

[27] M. Tadokoro *et al.* “Designs for a two-dimensional Si quantum dot array with spin qubit addressability”. en. In: *Scientific Reports* 11.11 (Sept. 2021), p. 19406. issn: 2045-2322. doi: 10.1038/s41598-021-98212-4.

[28] M. Niknam *et al.* “Quantum control of spin qubits using nanomagnets”. en. In: *Communications Physics* 5.1 (Nov. 2022), pp. 1–10. issn: 2399-3650. doi: 10.1038/s42005-022-01041-8.

[29] S. Nakamura, H. Kiyama, and A. Oiwa. “Micromagnet design for addressable fast spin manipulations in a 2×2 quantum dot array”. In: *Journal of Applied Physics* 132.22 (Dec. 2022), p. 224301. issn: 0021-8979. doi: 10.1063/5.0088840.

[30] W. Legrand *et al.* “Optimal design of nanomagnets for on-chip field gradients”. In: *Physical Review Applied* 20.4 (Oct. 2023), p. 044062. doi: 10.1103/PhysRevApplied.20.044062.

[31] C.-H. Chang *et al.* “A Hyperbolic Micromagnet for Multiple Spin Qubits With Fast Rabi Oscillations and High Addressability”. In: *IEEE Electron Device Letters* 45.4 (2024), pp. 526–529. doi: 10.1109/LED.2024.3368408.

[32] M. Aldeghi, R. Allenspach, and G. Salis. “Modular nanomagnet design for spin qubits confined in a linear chain”. In: *Applied Physics Letters* 122.13 (Mar. 2023). issn: 1077-3118. doi: 10.1063/5.0139670. url: http://dx.doi.org/10.1063/5.0139670.

[33] F. Bersano *et al.* “Integration of Cobalt Ferromagnetic Control Gates for Electrical and Magnetic Manipulation of Semiconductor Quantum Dots”. In: *Advanced Functional Materials* 35.14 (Jan. 2025). issn: 1616-3028. doi: 10.1002/adfm.202419940. url: http://dx.doi.org/10.1002/adfm.202419940.

[34] M. Aldeghi *et al.* “Simulation and Measurement of Stray Fields for the Manipulation of Spin Qubits in One- and Two-Dimensional Arrays”. In: *Nano Letters* 25.5 (Feb. 2025), pp. 1838–1844. issn: 1530-6984. doi: 10.1021/acs.nanolett.4c05037.

[35] R. Li *et al.* “A crossbar network for silicon quantum dot qubits”. In: *Science Advances* 4.7 (July 2018). issn: 2375-2548. doi: 10.1126/sciadv.aar3960. url: http://dx.doi.org/10.1126/sciadv.aar3960.

[36] S. Philips. “Scaling a spin qubit quantum processor from two to six qubits”. English. Dissertation (TU Delft). Delft University of Technology, 2023. doi: 0.4233/uuid:62dcc7a6-df92-43e1-b40c-9879f97eabb6.

[37] R. Allenspach and G. R. Salis. “Magnetic random access memory”. Patent US7336515B2. Feb. 2008. url: https://patents.google.com/patent/US20050276149A1/en.

[38] M. Pioro-Ladrière *et al.* “Electrically driven single-electron spin resonance in a slanting Zeeman field”. In: *Nature Physics* 4.10 (2008), pp. 776–779. issn: 17452481. doi: 10.1038/nphys1053.

[39] J. Yoneda *et al.* “A quantum-dot spin qubit with coherence limited by charge noise and fidelity higher than 99.9%”. In: *Nature Nanotechnology* 13.2 (Feb. 2018), pp. 102–106. issn: 17483395. doi: 10.1038/s41565-017-0014-x.

[40] B. Undseth *et al.* “Nonlinear Response and Crosstalk of Electrically Driven Silicon Spin Qubits”. In: *Physical Review Applied* 19.4 (Apr. 2023). issn: 2331-7019. doi: 10.1103/physrevapplied.19.044078. url: http://dx.doi.org/10.1103/PhysRevApplied.19.044078.

[41] F. Ginzel *et al.* “Spin shuttling in a silicon double quantum dot”. In: *Physical Review B* 102.19 (Nov. 2020). issn: 24699969. doi: 10.1103/PhysRevB.102.195418.

[42] F. van Riggelen-Doelman *et al.* “Coherent spin qubit shuttling through germanium quantum dots”. In: *Nature Communications* 15.1 (July 2024). issn: 2041-1723. doi: 10.1038/s41467-024-49358-y. url: http://dx.doi.org/10.1038/s41467-024-49358-y.

[43] C.-A. Wang *et al.* “Operating semiconductor quantum processors with hopping spins”. In: *Science* 385.6707 (July 2024), pp. 447–452. issn: 1095-9203. doi: 10.1126/science.ado5915. url: http://dx.doi.org/10.1126/science.ado5915.

[44] J. M. Taylor *et al.* “Fault-tolerant architecture for quantum computation using electrically controlled semiconductor spins”. In: *Nature Physics* 1.3 (Dec. 2005), pp. 177–183. issn: 17452481. doi: 10.1038/nphys174.

[45] J. M. Shilton *et al.* “High-frequency single-electron transport in a quasi-one-dimensional GaAs channel induced by surface acoustic waves”. In: *Journal of Physics: Condensed Matter* 8.38 (Sept. 1996), p. L531. doi: 10.1088/0953-8984/8/38/001. url: https://doi.org/10.1088/0953-8984/8/38/001.

[46] T. Struck *et al.* “Spin-EPR-pair separation by conveyor-mode single electron shuttling in Si/SiGe”. In: *Nature Communications* 15.1 (Feb. 2024). issn: 2041-1723. url: http://dx.doi.org/10.1038/s41467-024-45583-7.

[47] M. De Smet *et al.* “High-fidelity single-spin shuttling in silicon”. In: *Nature Nanotechnology* 20.7 (June 2025), pp. 866–872. issn: 1748-3395. url: http://dx.doi.org/10.1038/s41565-025-01920-5.

[48] V. Langrock *et al.* “Blueprint of a Scalable Spin Qubit Shuttle Device for Coherent Mid-Range Qubit Transfer in Disordered Si/SiGe/SiO_2”. In: *PRX Quantum* 4 (2 Apr. 2023), p. 020305. url: https://link.aps.org/doi/10.1103/PRXQuantum.4.020305.

[49] Y.-N. Zhang, A. S. Mokeev, and V. V. Dobrovitski. “Decoherence and fidelity enhancement during shuttling of entangled spin qubits”. In: *Phys. Rev. B* 112 (20 Nov. 2025), p. 205301. doi: 10.1103/78sg-ttth. url: https://link.aps.org/doi/10.1103/78sg-ttth.

[50] J. A. Krzywda *et al. Coherence Protection for Mobile Spin Qubits in Silicon*. 2026. arXiv: 2602.09179 [cond-mat.mes-hall]. url: https://arxiv.org/abs/2602.09179.

[51] B. Buonacorsi *et al.* “Network architecture for a topological quantum computer in silicon”. In: *Quantum Science and Technology* 4.2 (Jan. 2019), p. 025003. issn: 2058-9565. doi: 10.1088/2058-9565/aaf3c4. url: http://dx.doi.org/10.1088/2058-9565/aaf3c4.

[52] J. M. Boter *et al.* “Spiderweb Array: A Sparse Spin-Qubit Array”. In: *Physical Review Applied* 18.2 (Aug. 2022). issn: 2331-7019. doi: 10.1103/physrevapplied.18.024053. url: http://dx.doi.org/10.1103/PhysRevApplied.18.024053.

[53] Z. Cai, A. Siegel, and S. Benjamin. “Looped Pipelines Enabling Effective 3D Qubit Lattices in a Strictly 2D Device”. In: *PRX Quantum* 4.2 (June 2023). issn: 2691-3399. url: http://dx.doi.org/10.1103/PRXQuantum.4.020345.

[54] M. Künne *et al.* “The SpinBus architecture for scaling spin qubits with electron shuttling”. In: *Nature Communications* 15.1 (June 2024). issn: 2041-1723. url: http://dx.doi.org/10.1038/s41467-024-49182-4.

[55] A. Siegel *et al. Snakes on a Plane: mobile, low dimensional logical qubits on a 2D surface*. 2025. arXiv: 2501.02120 [quant-ph].

[56] E. I. Rashba. “Theory of electric dipole spin resonance in quantum dots: Mean field theory with Gaussian fluctuations and beyond”. In: *Physical Review B* 78.19 (Nov. 2008). issn: 1550-235X. doi: 10.1103/physrevb.78.195302. url: http://dx.doi.org/10.1103/PhysRevB.78.195302.

[57] M. Russ *et al.* “High-fidelity quantum gates in Si/SiGe double quantum dots”. In: *Physical Review B* 97.8 (Feb. 2018). issn: 2469-9969. doi: 10.1103/physrevb.97.085421. url: http://dx.doi.org/10.1103/PhysRevB.97.085421.

[58] J. Danon and Y. V. Nazarov. “Pauli spin blockade in the presence of strong spin-orbit coupling”. In: *Phys. Rev. B* 80 (4 July 2009), p. 041301. doi: 10.1103/PhysRevB.80.041301. url: https://link.aps.org/doi/10.1103/PhysRevB.80.041301.

[59] P. M. Mutter and G. Burkard. “All-electrical control of hole singlet-triplet spin qubits at low-leakage points”. In: *Phys. Rev. B* 104 (19 Nov. 2021), p. 195421. doi: 10.1103/PhysRevB.104.195421. url: https://link.aps.org/doi/10.1103/PhysRevB.104.195421.

[60] S. Geyer *et al.* “Anisotropic exchange interaction of two hole-spin qubits”. In: *Nature Physics* 20.7 (May 2024), pp. 1152–1157. issn: 1745-2481. doi: 10.1038/s41567-024-02481-5. url: http://dx.doi.org/10.1038/s41567-024-02481-5.

[61] F. Martins *et al.* “Noise Suppression Using Symmetric Exchange Gates in Spin Qubits”. In: *Phys. Rev. Lett.* 116 (11 Mar. 2016), p. 116801. doi: 10.1103/PhysRevLett.116.116801. url: https://link.aps.org/doi/10.1103/PhysRevLett.116.116801.

[62] M. Reed *et al.* “Reduced Sensitivity to Charge Noise in Semiconductor Spin Qubits via Symmetric Operation”. In: *Physical Review Letters* 116.11 (Mar. 2016). issn: 1079-7114. doi: 10.1103/physrevlett.116.110402. url: http://dx.doi.org/10.1103/PhysRevLett.116.110402.

[63] T. Meunier, V. E. Calado, and L. M. Vandersypen. “Efficient controlled-phase gate for single-spin qubits in quantum dots”. In: *Physical Review B - Condensed Matter and Materials Physics* 83.12 (Mar. 2011). issn: 10980121. doi: 10.1103/PhysRevB.83.121403.

[64] J. M. Martinis and M. R. Geller. “Fast adiabatic qubit gates using only σ_z control”. In: *Phys. Rev. A* 90 (2 Aug. 2014), p. 022307. doi: 10.1103/PhysRevA.90.022307. url: https://link.aps.org/doi/10.1103/PhysRevA.90.022307.

[65] X. Xue *et al.* “Quantum logic with spin qubits crossing the surface code threshold”. In: *Nature* 601.7893 (Jan. 2022), pp. 343–347. issn: 1476-4687. doi: 10.1038/s41586-021-04273-w. url: http://dx.doi.org/10.1038/s41586-021-04273-w.

[66] M. Rimbach-Russ *et al.* “Simple framework for systematic high-fidelity gate operations”. In: *Quantum Science and Technology* 8.4 (Sept. 2023), p. 045025. url: https://doi.org/10.1088/2058-9565/acf786.

[67] T. F. Watson *et al.* “A programmable two-qubit quantum processor in silicon”. In: *Nature* 555.7698 (Feb. 2018), pp. 633–637. issn: 1476-4687. doi: 10.1038/nature25766. url: http://dx.doi.org/10.1038/nature25766.

[68] A. Noiri *et al.* “A shuttling-based two-qubit logic gate for linking distant silicon quantum processors”. In: *Nature Communications* 13.1 (Sept. 2022). issn: 2041-1723. url: http://dx.doi.org/10.1038/s41467-022-33453-z.

[69] Y. Matsumoto *et al. Two-qubit logic and teleportation with mobile spin qubits in silicon*. 2025. arXiv: 2503.15434 [quant-ph].

[70] Y.-Y. Liu *et al.* “Radio-Frequency Reflectometry in Silicon-Based Quantum Dots”. In: *Physical Review Applied* 16.1 (July 2021). issn: 2331-7019. doi: 10.1103/physrevapplied.16.014057. url: http://dx.doi.org/10.1103/PhysRevApplied.16.014057.

[71] A. E. Seedhouse *et al.* “Pauli Blockade in Silicon Quantum Dots with Spin-Orbit Control”. In: *PRX Quantum* 2.1 (Jan. 2021). issn: 2691-3399. url: http://dx.doi.org/10.1103/PRXQuantum.2.010303.

[72] S. G. J. Philips *et al.* “Universal control of a six-qubit quantum processor in silicon”. In: *Nature* 609.7929 (Sept. 2022), pp. 919–924. issn: 1476-4687. doi: 10.1038/s41586-022-05117-x. url: http://dx.doi.org/10.1038/s41586-022-05117-x.

[73] I. Fernández de Fuentes *et al.* “Running a Six-Qubit Quantum Circuit on a Silicon Spin-Qubit Array”. In: *PRX Quantum* 7 (1 Jan. 2026), p. 010308. doi: 10.1103/f285-l2v5. url: https://link.aps.org/doi/10.1103/f285-l2v5.

[74] J. Y. Huang *et al.* “High-fidelity spin qubit operation and algorithmic initialization above 1 K”. In: *Nature* 627.8005 (Mar. 2024), pp. 772–777. issn: 1476-4687. doi: 10.1038/s41586-024-07160-2. url: http://dx.doi.org/10.1038/s41586-024-07160-2.

[75] X. Gao *et al.* “Quantum computer aided design simulation and optimization of semiconductor quantum dots”. In: *Journal of Applied Physics* 114.16 (Oct. 2013). issn: 1089-7550. doi: 10.1063/1.4825209. url: http://dx.doi.org/10.1063/1.4825209.

[76] L. M. Roth. “g Factor and Donor Spin-Lattice Relaxation for Electrons in Germanium and Silicon”. In: *Phys. Rev.* 118 (6 June 1960), pp. 1534–1540. doi: 10.1103/PhysRev.118.1534. url: https://link.aps.org/doi/10.1103/PhysRev.118.1534.

[77] T. Tanttu *et al.* “Controlling Spin-Orbit Interactions in Silicon Quantum Dots Using Magnetic Field Direction”. In: *Phys. Rev. X* 9 (2 May 2019), p. 021028. doi: 10.1103/PhysRevX.9.021028. url: https://link.aps.org/doi/10.1103/PhysRevX.9.021028.

[78] P. Harvey-Collard *et al.* “Spin-orbit Interactions for Singlet-Triplet Qubits in Silicon”. In: *Phys. Rev. Lett.* 122 (21 May 2019), p. 217702. doi: 10.1103/PhysRevLett.122.217702. url: https://link.aps.org/doi/10.1103/PhysRevLett.122.217702.

[79] P. Huang and X. Hu. “Spin manipulation and decoherence in a quantum dot mediated by a synthetic spin–orbit coupling of broken T-symmetry”. In: *New Journal of Physics* 24.1 (Dec. 2021), p. 013002. doi: 10.1088/1367-2630/ac430c. url: https://doi.org/10.1088/1367-2630/ac430c.

[80] R. M. Jock *et al.* “A silicon metal-oxide-semiconductor electron spin-orbit qubit”. In: *Nature Communications* 9.1 (Dec. 2018). issn: 20411723. doi: 10.1038/s41467-018-04200-0.

[81] R. Ruskov *et al.* “Electron *g*-factor of valley states in realistic silicon quantum dots”. In: *Phys. Rev. B* 98 (24 Dec. 2018), p. 245424. doi: 10.1103/PhysRevB.98.245424. url: https://link.aps.org/doi/10.1103/PhysRevB.98.245424.

[82] J. D. Cifuentes *et al.* “Bounds to electron spin qubit variability for scalable CMOS architectures”. In: *Nature Communications* 15.1 (May 2024). issn: 2041-1723. doi: 10.1038/s41467-024-48557-x. url: http://dx.doi.org/10.1038/s41467-024-48557-x.

[83] A. Nickl *et al. Eight-Qubit Operation of a 300 mm SiMOS Foundry-Fabricated Device*. 2025. arXiv: 2512.10174 [quant-ph]. url: https://arxiv.org/abs/2512.10174.

[84] I. Hansen *et al.* “Pulse engineering of a global field for robust and universal quantum computation”. In: *Physical Review A* 104.6 (Dec. 2021). issn: 2469-9934. doi: 10.1103/physreva.104.062415. url: http://dx.doi.org/10.1103/PhysRevA.104.062415.

[85] H. Jnane, A. Siegel, and M. F. Gonzalez-Zalba. *Harnessing electron motion for global spin qubit control*. 2025. arXiv: 2503.12767 [quant-ph]. url: https://arxiv.org/abs/2503.12767.

[86] M. P. Losert *et al.* “Practical strategies for enhancing the valley splitting in Si/SiGe quantum wells”. In: *Physical Review B* 108.12 (Sept. 2023), p. 125405. doi: 10.1103/PhysRevB.108.125405.

[87] J. K. Gamble *et al.* “Disorder-induced valley-orbit hybrid states in Si quantum dots”. In: *Physical Review B* 88.3 (July 2013). issn: 1550-235X. doi: 10.1103/physrevb.88.035310. url: http://dx.doi.org/10.1103/PhysRevB.88.035310.

[88] N. M. Zimmerman, P. Huang, and D. Culcer. “Valley Phase and Voltage Control of Coherent Manipulation in Si Quantum Dots”. In: *Nano Letters* 17.7 (June 2017), pp. 4461–4465. issn: 1530-6992. doi: 10.1021/acs.nanolett.7b01677. url: http://dx.doi.org/10.1021/acs.nanolett.7b01677.

[89] R. C. C. Leon *et al.* “Coherent spin control of s-, p-, d- and f-electrons in a silicon quantum dot”. In: *Nature Communications* 11.1 (Feb. 2020). issn: 2041-1723. doi: 10.1038/s41467-019-14053-w. url: http://dx.doi.org/10.1038/s41467-019-14053-w.

[90] E. Kawakami *et al.* “Electrical control of a long-lived spin qubit in a Si/SiGe quantum dot”. In: *Nature Nanotechnology* 9.9 (Aug. 2014), pp. 666–670. issn: 1748-3395. doi: 10.1038/nnano.2014.153. url: http://dx.doi.org/10.1038/nnano.2014.153.

[91] R. Ferdous *et al.* “Valley dependent anisotropic spin splitting in silicon quantum dots”. In: *npj Quantum Information* 4.1 (June 2018). issn: 2056-6387. doi: 10.1038/s41534-018-0075-1. url: http://dx.doi.org/10.1038/s41534-018-0075-1.

[92] C. H. Yang *et al.* “Spin-valley lifetimes in a silicon quantum dot with tunable valley splitting”. In: *Nature Communications* 4.1 (June 2013). issn: 2041-1723. doi: 10.1038/ncomms3069. url: http://dx.doi.org/10.1038/ncomms3069.

[93] D. Degli Esposti *et al.* “Low disorder and high valley splitting in silicon”. In: *npj Quantum Information* 10.1 (Mar. 2024). issn: 2056-6387. url: http://dx.doi.org/10.1038/s41534-024-00826-9.

[94] P. Huang and X. Hu. “Fast spin-valley-based quantum gates in Si with micromagnets”. en. In: *npj Quantum Information* 7.1 (Nov. 2021), p. 162. issn: 2056-6387. doi: 10.1038/s41534-021-00500-4.

[95] F. Borjans *et al.* “Probing the Variation of the Intervalley Tunnel Coupling in a Silicon Triple Quantum Dot”. In: *PRX Quantum* 2.2 (Apr. 2021). issn: 2691-3399. doi: 10.1103/prxquantum.2.020309. url: http://dx.doi.org/10.1103/PRXQuantum.2.020309.

[96] X. Zhao and X. Hu. *Coherent electron transport in silicon quantum dots*. 2019. arXiv: 1803.00749 [cond-mat.mes-hall]. url: https://arxiv.org/abs/1803.00749.

[97] B. Buonacorsi, B. Shaw, and J. Baugh. “Simulated coherent electron shuttling in silicon quantum dots”. In: *Physical Review B* 102.12 (Sept. 2020). issn: 2469-9969. doi: 10.1103/physrevb.102.125406. url: http://dx.doi.org/10.1103/PhysRevB.102.125406.

[98] M. L. V. Tagliaferri *et al.* “Impact of valley phase and splitting on readout of silicon spin qubits”. In: *Phys. Rev. B* 97 (24 June 2018), p. 245412. doi: 10.1103/PhysRevB.97.245412. url: https://link.aps.org/doi/10.1103/PhysRevB.97.245412.

[99] M. Volmer *et al.* “Mapping of valley splitting by conveyor-mode spin-coherent electron shuttling”. In: *npj Quantum Information* 10.1 (June 2024). issn: 2056-6387. doi: 10.1038/s41534-024-00852-7. url: http://dx.doi.org/10.1038/s41534-024-00852-7.

3

HOTTER IS EASIER: UNEXPECTED TEMPERATURE DEPENDENCE OF SPIN QUBIT FREQUENCIES

The heating effect is where the elegance and flexibility of resonant control of spins in the rotating frame confronts the messiness of the solid-state environment. The premise is simple: In order to control qubits, signals must be applied. However, in the cryogenic solid-state environment of the spins, even tiny bits of stray radiation can heat and alter their environment. For much of the past decade, experimentalists in the field have collectively blamed a number of mysterious but reproducible phenomena on "the heating effect". These behaviors include spin Larmor frequencies that drift transiently, readout fidelity that degrades after control sequences, and unaccounted phase pickups appearing on idling spins. At the time of this study, not only had the heating effect become a bottleneck for state-of-the-art devices, but no theoretical or experimental study had been conducted to investigate its origin. In this chapter, we deepen our understanding of this effect and propose a counterintuitive solution to avoid it: heat up the chip.

Parts of this chapter have been published in Phys. Rev. X **13**, 041015 (2023) [1].

3.1. INTRODUCTION

A major benefit of using semiconductor spins as the building blocks of a large-scale quantum computer is that they do not strictly require dilution refrigerator base temperatures (10-20 mK). Demonstrations of qubit operation above 1 K for electron spins confined in Si-MOS [2, 3], and recently at 4 K for a hole spin confined in a FinFET [4], are encouraging steps towards the realization of classical and quantum hardware coexisting at the same temperature.

However, several factors motivate the operation of spin qubits at lower temperatures of about 10 mK. These include the desires to limit charge noise as well as minimize electron temperature for widely used readout methods [5, 6]. The intuitive benefits of minimizing the environmental temperature of spin qubits contrasts with practicalities of their operation. Loss-DiVincenzo qubits, having shown the highest semiconductor-based qubit count and fidelities so far, require microwave control typically in the 5-40 GHz range [7–12]. Other encodings, such as singlet-triplet and exchange-only qubits, don't require such high frequencies but still require baseband pulses which contain spectral components on the order of 1-100 MHz [13, 14]. All of these signals dissipate electromagnetic radiation at the device which adds to the thermal load that must be cooled by the dilution refrigerator, depending on the quality of signal hygiene and device thermalization.

The consequences of this competition between thermal dissipation during qubit control and dilution refrigeration have arisen repeatedly in experiments over the past several years, particularly in experiments using high-frequency microwaves [15–21]. These effects, which we call "heating effects" for simplicity, are of increasing experimental significance due to their generally detrimental impact on qubit quality and adverse scaling with the number of control signals. The telltale evidence of the heating effect is a sizeable shift (typically of order 1 MHz) in a spin's Larmor frequency $\omega_0 = 2\pi f_0$, which is of particular importance when attempting to drive resonant Rabi oscillations. It is remarkable that such a widespread effect, affecting semiconductor qubit devices of different architectures and material platforms, is poorly understood. Glaringly, it had not, until now, been decisively shown that the "heating effect" had any concrete relation to device temperature or was some other artefact of microwave dissipation.

In a single-electron spin qubit, the heating effect was shown to be overcome by using tailored pulses, with the fitted scaling of the heating effect taken as an input parameter [17]. For relatively small frequency shifts, another pragmatic approach is calibrating an intermediate operating frequency that always permits qubit control at the expense of some systematic error [15]. In other experiments, an off-resonant microwave "prepulse" was used to bring the device to a steady state

before carrying out experiments [16]. In a recent demonstration of a universal six-qubit silicon processor, both prepulses and “wait times” on the order of several 100 µs were employed [20]. The former were required to achieve high single-qubit control fidelities, and the latter were found to be necessary to achieve satisfactory readout performance using Pauli-spin blockade (PSB) spin-to-charge conversion. None of these ad-hoc solutions are well-suited to scaling spin qubit platforms if they remain a requisite for achieving satisfactory fidelities. For example, they are incompatible with interleaved measurement and operation which will be necessary for implementing quantum error correction protocols. Furthermore, repeated observation of the heating effect implies there is missing, but important, physics in the standard Hamiltonians describing semiconductor spins. The heating effect is therefore of both fundamental and practical interest for the spin qubit community.

In this article, we present an in-depth study of the heating effect in a six-qubit silicon quantum processor. First, we outline how qubit control and measurement lead to on-chip temperature changes. Second, we make an explicit connection between device temperature and qubit frequency by directly controlling the mixing chamber temperature. This permits a phenomenological understanding of the heating effect that underpins the remaining results. Third, we illustrate how the heating effect manifests during base-temperature operation as a result of applying off-resonant microwave pulses. We show that lower-frequency baseband pulses result in frequency-shifts as well and that heat from these signals dissipates globally across the six-qubit linear array. Combining our understanding of the above effects, we are able to illustrate how the heating effect can cause non-Markovian crosstalk errors during data collection. Finally, we show how purposely increasing the mixing chamber temperature to 200 mK substantially mitigates the heating effect without compromising qubit coherence or controllability.

We cannot conclusively pinpoint a microscopic mechanism for the heat-induced frequency shift. However, taking into account our observations as well as those inferred from previous publications, we are able to eliminate several possible mechanisms, and furthermore argue that an interplay of two different mechanisms may be responsible.

3.2. DEVICE CONTROL AND THERMALIZATION

Extensive details on the design, control, and calibration of the six-qubit processor are already covered in [20]. However, it is pertinent to summarize the means through which heat makes its way from the room-temperature control electronics to the sample, as well as how heat dissipates from the device to the dilution refrigerator mixing chamber. This is summarized in Fig. 3.1.

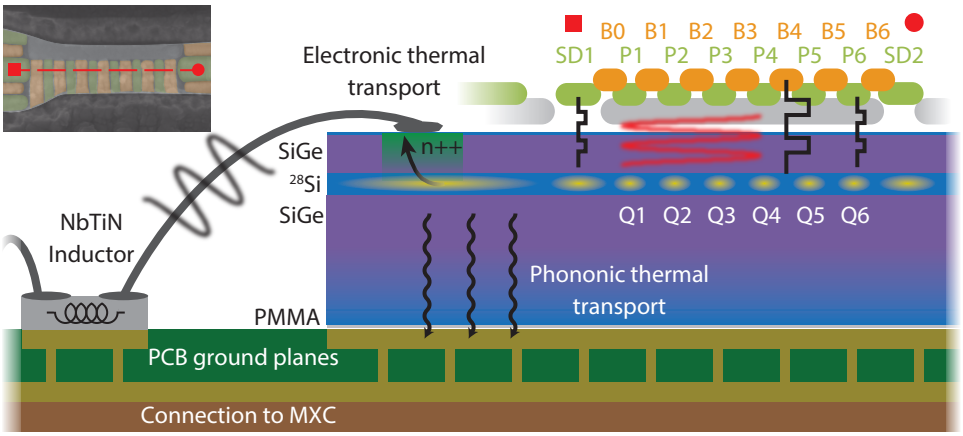


Figure 3.1: Cross-section of the bonded ^{28}Si/SiGe sample (not to scale) illustrating the relevant control signals and thermal dissipation contributing to thermalization of the qubit array. The dashed line on the scanning electron microscope (SEM) image indicates the gate region labelled in the schematic. The screening gate layer (grey) carries microwave-frequency signals for driving single-qubit gates via EDSR using the spin-orbit coupling generated by the micromagnet (dark grey in SEM) stray field. The plunger gate layer (light green) carries baseband pulses (10-60 mV) for the charge sensor and for manipulating charge states within the quantum dot array. The barrier layer (orange) carries baseband pulses (60-200 mV) for controlling the exchange interaction used to implement two-qubit gates. Barrier gate pulses are generally of a higher voltage due to the weaker lever arms in the higher gate layer combined with the need to control exchange with a sufficient dynamic range. Intermediate Al_2O_3 dielectric layers are not shown. Readout of the two SET sensing dots (SDs) via reflectometry makes use of an rf signal that travels through an off-chip superconducting NbTiN high kinetic-inductance inductor and through the accumulated 2DEG via the bonded n++ ohmic contact (the separate tank circuit used for measuring SD2 is not drawn). Phonons thermalize the crystal lattice to the dilution refrigerator through the PMMA glue between the sample and a PCB ground plane which is galvanically connected to the mixing chamber (MXC). Electrons may also carry some excess heat away from the quantum well by diffusing through the electron reservoirs, ohmic contacts, and bond wires. It is possible that the superconducting elements impede thermal transport via conduction electrons. In this case, the two ohmic contacts that are not bonded in series with an inductor may provide a better thermal anchor.

The sample is mounted to the gold-plated copper ground plane of a printed circuit board (PCB) with poly(methyl methacrylate) (PMMA). This is approximately a 0.5 mm distance below the quantum well and Ti:Pd gates. Gates holding only a static DC voltage can be stripped of high frequency components using a combination of RC, Pi, and metal powder filters [22]. However, ac signal paths must still allow high frequencies for baseband (1-100 MHz) and microwave frequency (10-20 GHz) control. In the absence of any signal, thermal fluctuations along the attenuated path will give rise to photons carrying heat toward the device. When ac signals are applied, radiation incident on the device is expected to

cause additional Joule heating through a combination of conductive and dielectric losses.

In quantum dot devices operated in a dilution refrigerator, it is a general rule that the minimum equilibrium electron temperature T_e of the accumulated electron reservoirs (2DEG) will be higher than the minimum mixing chamber temperature T_{MXC} [23]. In our setup, T_{MXC} can reach a base temperature of 12 mK. The electron temperature floor, in contrast, is measured to be about $T_e \approx 180$ mK (see Appendix 3.8.3). We believe that the local environment of the quantum dots (for instance the lattice and the bath of nearby fluctuators) reaches thermal equilibrium below the electron temperature floor due to measurable changes in the spin properties as the mixing chamber temperature is reduced below 180 mK (e.g. see Fig. 3.2).

When the lattice temperature is below T_e, cooling of the quantum dot region to the mixing chamber is only mediated by phonons which must pass through the substrate, the PMMA "glue" (which is an insulating material), the PCB, the cold finger to which it is mounted, and ultimately the mixing chamber itself. The rate at which phonons are able to carry heat from the quantum dot region to the mixing chamber will depend on their temperature difference and the thermal conductance along the path connecting them. When the local environment reaches a temperature above T_e, electronic heat transport also plays a role in the cooling of the device [24]. As illustrated in Fig. 3.1, the four doped ohmic contacts (two of which are in series with the rf reflectometry readout circuit) provide a conductive route for heat to dissipate through the wire bonds electrically connecting the sample to the PCB and the thermal anchoring of the wires at the mixing chamber.

In order to implement universal control across the six-qubit array, a variety of baseband pulses and high-frequency signals are required. Initialization and measurement of spins are performed with a combination of Pauli spin blockade (PSB) readout for spin-to-charge conversion as well as rf reflectometry to detect the change in resistance of a nearby single-electron transistor (SET). Two sets of signals are required. First, a combination of baseband pulses on plunger and barrier gates are used to tune the electrostatic landscape from the symmetric operation point to the interdot transition where PSB readout occurs [25]. Since the SET is typically tuned to Coulomb blockade during qubit operation to avoid unnecessary dissipation, baseband pulses are also used to tune the SET to a sensitive Coulomb peak flank while the measurement takes place. The baseband pulses consist of rise times in the range of 10-100 ns and magnitudes on the order of 10 mV at the quantum dot gate electrodes. Second, rf signals are applied through the electron reservoirs to measure changes in the sensing dot resistance. These tones are at 88 MHz and 94 MHz for the two charge sensors and have nominal powers of −30 dBm

and −33 dBm respectively for the duration of the measurement, which is on the order of 10 µs.

Single-qubit rotations are performed with electric-dipole spin resonance (EDSR) and require microwave frequencies in the range of 10-20 GHz, depending on the magnitude of the qubits' Zeeman energy. Our system can perform 90-180 degree rotations in the Bloch sphere with typical gate times of 100-200 ns. The nominal applied power of roughly −30 dBm is expected to produce an ac electric field amplitude of order 100-1000 V/m at the quantum dot array for EDSR of this frequency. Two-qubit operations require baseband pulses predominantly on the barrier gates between quantum dots. A typical CZ gate can be performed using a 100 ns baseband pulse. Due to the relatively smaller lever arm of the barrier gates, a larger pulse magnitude of 100-200 mV is required.

The heating caused by the combination of these operations is in competition with the rate of thermal dissipation away from the quantum well to the mixing chamber heat sink. Due to the high frequency, single-qubit control with microwaves, whether by EDSR or electron spin resonanace (ESR), has been the dominant origin of the heating effect in recent experiments. However, we will show that it is not the only relevant mechanism, as repeated baseband pulses will also lead to measurable frequency shifts.

3.3. TEMPERATURE DEPENDENCE OF QUBIT FREQUENCIES

To confirm that the heating effect can be related to the temperature of the device, we make use of a PID controller to manipulate the temperature of the dilution refrigerator mixing chamber from base temperature to 600 mK, as measured by a thermometer mounted to the mixing chamber, and let the device thermalize at each set point for several minutes to achieve a steady-state condition. Fig. 3.2 summarizes the results of performing a Ramsey measurement at each temperature, using the frequency difference between the fitted free-induction decay and a known "virtual" detuning to infer a shift in the qubit's Larmor frequency with an accuracy on the order of 10 kHz. The range of temperatures explored is limited by temperature dependence of the rf reflectometry readout, which is discussed in depth in Appendix 3.8.1.

Three features of the observed temperature dependence are particularly noteworthy. First, all six Larmor frequencies shift to higher frequencies. We may note that previously published results, making use of microwave pulses to probe the heating effect as opposed to directly varying the mixing chamber temperature, report both positive frequency shifts [15, 16, 21, 26] and negative frequency shifts [17, 19] (the latter reports both). Second, all six frequencies shift by a similar magnitude of roughly 1 MHz. This, again, is similar to previously reported pulse-induced shifts

which range from tens of kHz to a few MHz. Third, all shifts exhibit a striking non-monotonic trend. These observations suggest physics that acts globally across the qubit array with some degree of variation between quantum dots.

We are unaware of any theoretical precedent for describing how the qubit frequencies shift with temperature. As all qubit frequencies are in the 16 GHz band, a shift of 1 MHz constitutes less than a 0.01% change. Since the g-factor of the confined electron spins and the total magnetic field at the quantum dot are not known to this precision, there are many open possibilities regarding the microscopic origin of this effect. We save an in-depth discussion for Section 3.6.

It is worth noting that the "cold" qubit frequency, which we use as the origin for measuring any relative frequency shifts, is somewhat difficult to probe. As illustrated in Section 3.4.3, the device thermalizes very slowly at base temperature, and therefore the brief microwaves required to perform the Ramsey experiment cause a systematic self-heating. While long wait times of typically 0.5-1 ms are inserted between each measurement to mitigate this effect, we find it is still insufficient to keep the device at equilibrium with the 12 mK mixing chamber. Rather, the sparse sequence of X_{90} pulses may be enough to raise the average device temperature closer to 50 mK as suggested by the adjacent data point. As will be illustrated in Section 3.5, this systematic error becomes negligible as $T_{\mathrm{MXC}} \gtrapprox 150$ mK and the heat capacity of the heterostructure increases.

3.4. THE HEATING EFFECT

3.4.1. MICROWAVE-INDUCED HEATING

We now document the manifestation of the heating effect in all six qubits due to off-resonant microwave pulses while the mixing chamber is set to 20 mK. Fig. 3.3 illustrates two complementary microwave pulse experiments carried out at 20 mK. After initialization of the qubit under test, an off-resonant microwave burst at a constant frequency of 16 GHz is applied. This frequency is selected since it is approximately 100 MHz below the lowest qubit Larmor frequency and does not give rise to any significant coherent driving. The off-resonant frequency is held constant for all qubit experiments since different frequencies may transmit and dissipate in the device differently. To measure the pulse-induced frequency shift, we subsequently scan the frequency of a second microwave pulse, calibrated in length to result in a 180 degree rotation. The resonance peak may then be fit to Rabi's formula to estimate the Larmor frequency.

Since our measurement "probe", the resonant microwave pulse in

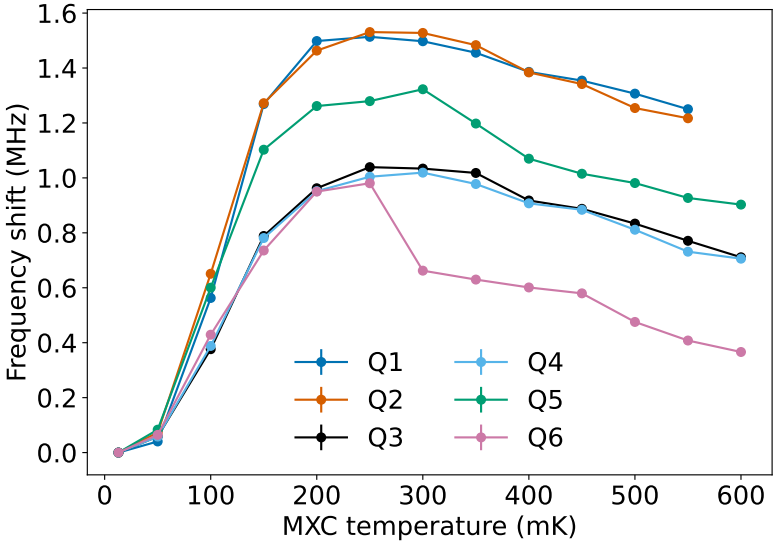


Figure 3.2: Larmor frequency shifts of all six qubits as a function of mixing chamber temperature measured via a Ramsey-type pulse sequence. The frequency shift is recorded relative to a measurement taken at 13 mK. The device was allowed to thermalize for several minutes before each data point was collected such that no time derivative in the separate mixing chamber thermometer was observed. DC voltages were unchanged throughout the experiment, which took course over the period of about 12 hours. Repeated experiments suggest the temperature dependence is smooth at this resolution. Occasionally, an environmental fluctuation caused a discrete shift in frequency as observed for qubit 6. Such features are not generally reproduced by changing the temperature.

combination with an rf reflectometry pulse, is also expected to deposit heat in the system, it is necessary to scrutinize to what extent our results are affected by "self-heating" of the measurement procedure itself. This will be discussed in further detail in Section 3.4.3. For now, we emphasize that the measurement pulse is shorter than most of the off-resonant pulses used during the scan, and therefore the self-heating should only account for a small fraction of the total effect. Furthermore, it is a constant for all experiments, so any difference in results can be attributed to the varied off-resonant pulse. To ensure the independence of all measurement shots, a long wait time between sequences of 500 µs is used to allow most accrued heat to dissipate before the next experiment begins.

Fig 3.3 shows the Larmor frequency shifts as a result of sweeping the off-resonant pulse amplitude and duration, respectively. When the amplitude and duration scales are converted to equivalent gate-operation

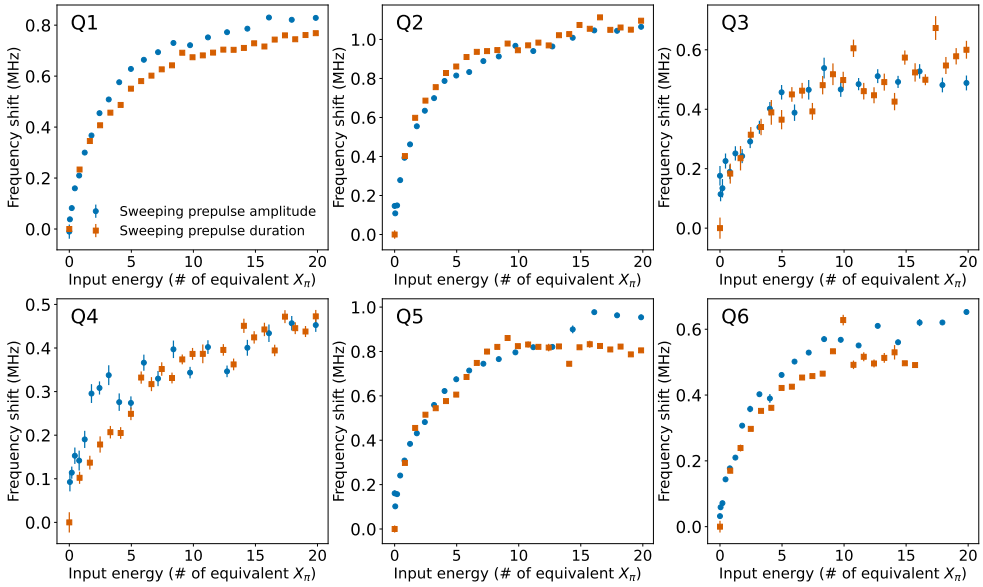


Figure 3.3: Frequency shifts at 20 mK mixing chamber temperature measured after applying an off-resonant pulse of various duration and amplitude. For a swept prepulse amplitude, a fixed duration of 2 µs was used. For a swept prepulse duration, a fixed amplitude corresponding to $f_{\mathrm{Rabi}} \approx 1.3$ MHz was used. Prepulse energy is scaled to "equivalent-gate" energy by averaging the relative pulse amplitudes and durations required to drive EDSR on all six qubits in the array with $f_{\mathrm{Rabi}} = 2$ MHz. The precise electric field amplitude of the prepulse at the quantum well is unknown, but expected to be on the order of 1000 V/m according to the estimated dot sizes, micromagnet gradient, and observed Rabi frequencies. A 0.5 ms wait time was implemented between all shots. Frequency shifts were measured by fitting a chevron-pattern line-cut after the off-resonant pulse was turned off. Q3 and Q4 data have a systematically larger uncertainty as these qubits are measured indirectly by mapping their state onto Q2 and Q5 respectively which decreases the visibility of the signal.

energies, the severity of the heating effect becomes evident [1]. After only approximately 10 X_π gates worth of energy, each qubit's Larmor frequency has shifted by 0.3-1 MHz. A microwave drive originally calibrated to a qubit's "cold" frequency is no longer able to drive complete spin rotations.

To plot the measured frequency shifts on a common energetic axis, a Joule heating model is assumed [27]:

$$E_{\mathrm{Joule}} = \int_t \mathrm{d}t \int_V \mathrm{d}\mathbf{r} \frac{\sigma(\mathbf{r}) + \omega\epsilon''(\mathbf{r})}{2} |E_{\mathrm{ac}}|^2. \tag{3.1}$$

In this model, the electromagnetic radiation propagating from the on-chip EDSR antenna will dissipate in the device due to a combination of

[1] For this conversion we use an amplitude equal to the average of the amplitudes used to drive each qubit independently with $f_{\mathrm{Rabi}} = 2$ MHz

conductive losses (σ), dielectric losses (ϵ'' is the complex component of the dielectric function $\epsilon = \epsilon' - j\epsilon''$) throughout the volume V penetrated by the fields. Magnetic loss due to complex permeability is neglected for simplicity. Due to the many different materials on the device, and the uncertain volume in which dissipation occurs, the exact integration is not possible to perform. However, by making the simplifying assumption that the electric field amplitude profile $f(\mathbf{r})$, where $E_{\mathrm{ac}}(\mathbf{r}, t) = |E_{\mathrm{ac}}| \cos(\omega t) f(\mathbf{r})$, is the same for all prepulses and that all material parameters are time-independent, the volume integration can be treated as a constant in all cases, and the deposited energy is estimated to scale quadratically with the drive amplitude and linearly with the drive duration. With this model, we find that the frequency shift is set by the energy deposited in the device. This, in addition to the observation that all qubit frequencies once again shift upwards, suggests that the dissipation of the applied microwave signal is consistent with the observed temperature dependence of the Larmor frequency. Although the presence of microwaves may enable other possible frequency-shift mechanisms, such as directly via the ac Stark effect or indirectly via coupling to environmental degrees of freedom, the temperature dependence is dominant.

3.4.2. BASEBAND-INDUCED HEATING

Although high frequency microwaves will dissipate more energy into the device than lower-frequency baseband pulses, it is prudent to check the effect of these necessary signals. We employ qubit 1 as an on-chip "thermometer" and send baseband pulses to plunger and barrier gates on the opposite side of the device as illustrated in Fig. 3.4(a). All of the participating gates have effectively zero dc lever-arm with respect to the quantum dot containing qubit 1.

In Fig. 3.4(b), we apply a variety of pulse amplitudes mimicking standard device operations. These operations are applied one at a time and cycle through the relevant gates from B3 to P6. Small plunger pulses (10 mV) mimic what is required to detune dots between the operation point and the Pauli spin blockade readout point. These contribute little heat to the device even after thousands of operations. Large plunger pulses (several tens of mV) replicate the amplitude with which one may scan gates while doing charge state tuning. The larger voltage ramps do cause heating after hundreds of pulses, and are consistent with our observation that the mixing chamber temperature increases by tens of mK when doing "video mode" charge state tuning with continuous rf reflectometry, despite the fact that there is no nominal attenuation in the high-frequency line at this temperature stage.

Barrier pulses cause the largest baseband heating effect as their relevant working mode - turning on and off the exchange interaction -

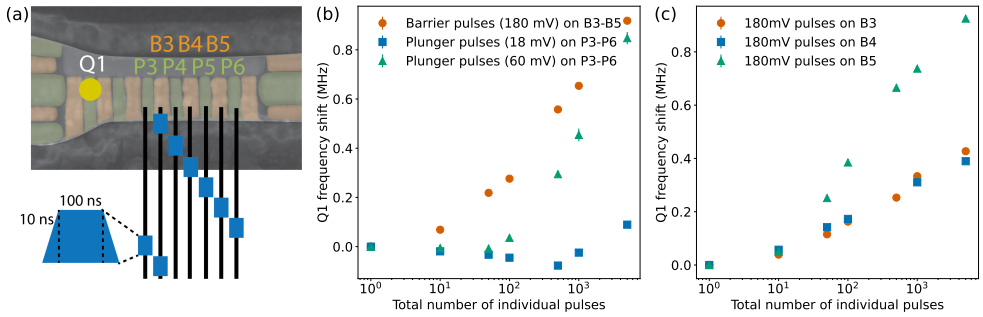


Figure 3.4: (a) Illustration of the serially applied pulses used to induce baseband signal heating. The frequency shift of qubit 1 can be correlated with the degree of nonlocal heating. (b) Frequency shift of qubit 1, measured via a Ramsey experiment, as a result of various combinations of applied pulses. All pulses are 100 ns in duration with 10 ns ramps. Pulses are applied back-to-back with no intermediate wait between ramp-down and ramp-up. As there is effectively zero lever arm between the gates used and the quantum dot hosting qubit 1, any shift is expected to arise due to heating and not due to a net shift in the micromagnet gradient. Data is normalized to the measurement with zero baseband pulses. The negative shift for 18 mV plunger pulses likely arises from some low-frequency drift in qubit frequency which can be as much as tens of kHz during hour-long measurements such as this one. In almost all cases, the associated uncertainty in the measured frequency shift is smaller than the markers. (c) Frequency shift of qubit 1 as a result in repeated pulses on individual barrier gates. Pulses sent to B5 appear to dissipate the most heat, causing a greater frequency shift in qubit 1 than for the same nominal pulses applied to B3 and B4.

requires the largest voltage pulses with fast rise times. Tens of barrier pulses have a substantial impact on qubit frequency due to the heating effect. This may also impact qubit encodings other than Loss-DiVincenzo qubits; exchange-only qubits already require 10-100 such pulses for small algorithms (although, in the absence of micromagnets, the effects may be less severe when operating at very low magnetic fields).

A sublinear relation between the number of pulses and the total frequency shift is observed, similar to what is observed when heating is induced by microwave prepulses and a saturation effect is seen as more energy is deposited into the device. We expect that, due to the tens-to-hundreds of microseconds of baseband pulses required to induce the frequency shifts, there will also be an interplay of device cooling and heating contributing to the net frequency shift measured.

By separating the gates receiving the baseband pulses, we can estimate the locality of the heating effect. In Fig. 3.4(c), we measure the frequency shift of qubit 1 after a series of pulses on individual barrier gates. Although pulses on all three tested gates have an effect, it is curious that the gate farthest from qubit 1, B5, imparts the largest shift. This suggests that the heating effect acts globally across the six qubit array. Larger qubit arrays

or bespoke test structures would be required to experimentally determine the length scale of dissipation.

3.4.3. COOLING EFFECT

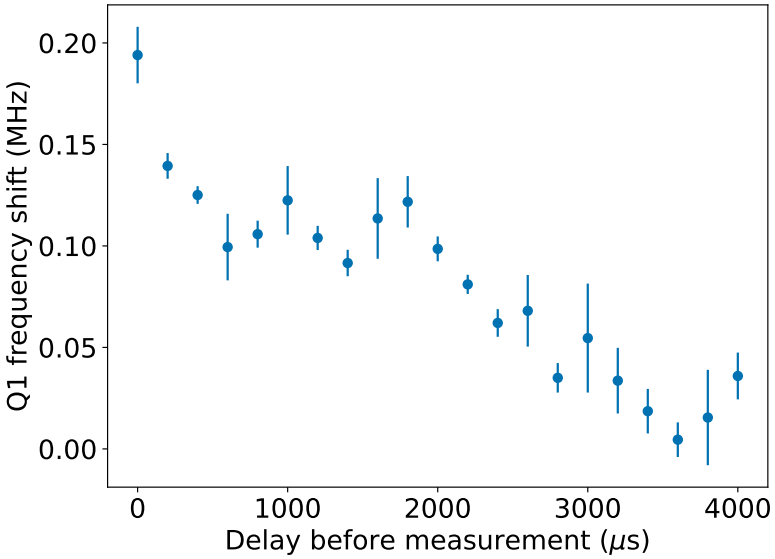


Figure 3.5: The cooling effect after applying a prepulse with approximately 3 X_π gates of energy at a mixing chamber temperature of 50 mK. The horizontal axis measures the time between the off-resonant prepulse and the qubit frequency measurement. A wait time of 5 ms is used between measurements to allow complete inter-shot cooling. The frequency shift is compared to the "true" 50 mK qubit frequency measured with a Ramsey experiment using the same long wait time

In analogy to the qubits showing a heating effect, they also exhibit a cooling effect. This is the frequency shift that occurs after a qubit has been warmed up by a microwave pulse as it equilibrates with its environment. Around base temperature operation, the cooling time is very slow with respect to the total time of a typical measurement cycle. The former has been measured to be milliseconds, and the latter is on the order of tens or hundreds of microseconds. Fig. 3.5 illustrates one instance of qubit 2 cooling down after an off-resonant microwave burst caused a 200 kHz heat-induced frequency shift. The cooling time-scale is not substantially influenced by the flow rate of the ^{3}He/^{4}He mixture through the dilution refrigerator, suggesting that the cooling is limited by thermal dissipation to the mixing chamber.

We may also comment that the cooling effect, unlike the heating effect, showed some variation over the total duration of the experiments

presented here. The cooling time scale varied by an order-unity factor that seemed to depend somewhat on the tuning history of the device. For example, a cooling experiment prior to the experiments of Fig. 3.3 suggested that 500 µs was sufficient for qubit frequencies to return to their origin after a prepulse-induced shift, whereas Fig. 3.5, conducted after several weeks during which a room-temperature thermal cycle of the device took place, suggests a longer wait time would be required. We remark that other experiments probing the effect of wait-time and readout shown in Fig. 3.8(b) also varied quantitatively over several weeks, such that the wait time necessary to recover visibility also varied by an order-unity factor. We were unable to study this systematically, but these observations suggest that on-chip thermal dissipation may be sensitive to tuning history. It is also challenging to measure cooling timescales at higher device temperatures, as the heating effect becomes negligible. We discuss this further in the next section.

3.5. CROSSTALK AND MITIGATION

3.5.1. PHENOMENOLOGICAL PICTURE

With the observed dependence of the qubits' Larmor frequencies on the device temperature, we can introduce a phenomenological picture of the heating effect, illustrated in Fig. 3.6(a), from which the following results can be qualitatively understood. The Larmor frequency of a particular qubit is well defined when the device is at thermal equilibrium with the mixing chamber. When high-frequency signals are applied, the dissipated heat will shift the Larmor frequency upwards. The maximum shift occurs within the approximate 100 ns of coherent microwave driving used to measure the absolute frequency shift, giving an upper bound for the time scale of the heating effect. In contrast, the cooling time scale is on the order of milliseconds for base temperature operation but much faster at higher temperatures as more efficient thermal pathways are made available. Due to competition between heat dissipation and cooling power, the resonance condition moves on a timescale similar to individual measurements. This makes it difficult to calibrate a microwave prepulse to deterministically shift the Larmor frequency during a series of measurements. The resulting frequency shifts, although systematic in nature, are not easily predictable and behave as an additional noise source. A qubit frequency that varies between experiments will negatively impact the T_2 coherence properties. An overall decrease in T_2^* when employing prepulsing at base-temperature operation was previously documented for all qubits in this device [20].

A systematic detuning error also limits the fidelities with which spins can be resonantly manipulated. As a concrete example, the infidelity of

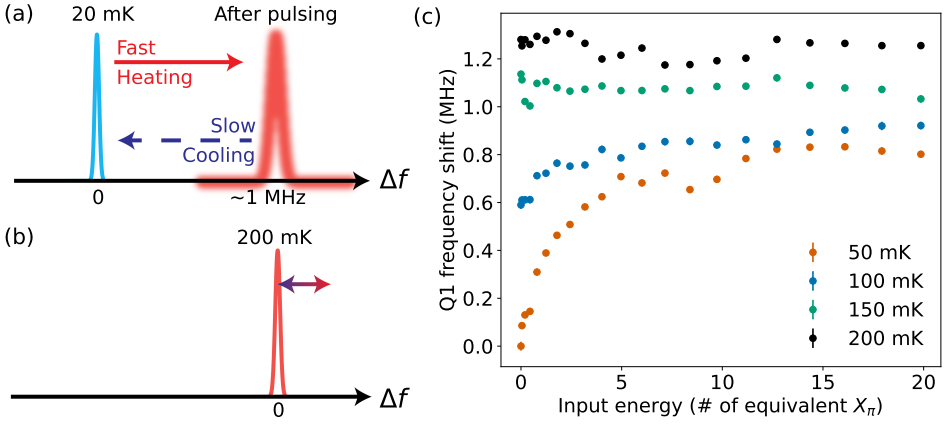


Figure 3.6: (a) Phenomenological illustration of a qubit resonance shifting in response to signal dissipation at 20 mK. The Larmor frequency will quickly shift upwards to an approximate steady state when the device temperature increases. Slow thermalization causes the resonance to drift back to its initial state. Because of this interplay, deterministically pulsing to a "warm" steady-state from base-temperature operation is difficult. (b) When the mixing chamber is regulated at 200 mK, the local temperature of the quantum dot array is more robust to the energy dissipated by control signals. Furthermore, a sweet-spot effect enhances the robustness of qubits to thermal fluctuations that do take place. (c) Frequency shifts of qubit 1 observed at various mixing chamber temperatures as a result of applying an off-resonant prepulse of varying energy and measuring the shift in the resulting chevron pattern. The energy scale is the same as that used in Fig. 3.3. The absolute increase in frequency with increasing temperature is directly comparable with the temperature dependence presented in Fig. 3.2. Other qubits in the array exhibit the same phenomenon.

a 180 degree resonant spin flip (in the single-qubit Hilbert space) scales as $1-F \approx \frac{2}{3}\left(\frac{\Delta^2}{\Omega^2+\Delta^2}\right)$ where $\Delta = \omega_{\mathrm{MW}} - \omega_0$ is the detuning between the microwave drive frequency (ω_{MW}) and the target qubit Larmor frequency (ω_0) and Ω is the effective drive amplitude regardless of whether ESR or EDSR is employed. When $\Delta = 0$, $\Omega/2\pi$ can be identified one-to-one with the Rabi frequency f_{Rabi}. For few-MHz Rabi frequencies often used in silicon spin qubit systems, a maximum detuning of about 100 kHz is required to achieve at least 99.9% fidelities. This range can be compared to the typical heating effect Larmor frequency shift of 1 MHz. Without bespoke calibration techniques [17, 20], high-fidelity operation is compromised.

It is also worth noting that a variable detuning is also deleterious for idling qubits. Since the microwave frequency also defines the "rotating frame" for each qubit wherein Pauli-Z operations can take place through phase updates, unaccounted dynamics in the Larmor frequency will result in unknown phase accumulation. Therefore, even

though a particular qubit may be spectrally well-separated from its resonantly-driven neighbour, the heating effect opens up a large channel for crosstalk errors that must also be systematically calibrated.

The spin qubit literature almost exclusively treats the Larmor frequency ω_0 as a constant, with some added random noise distribution giving rise to T_2-type decoherence as a result of charge noise and contact hyperfine interaction with nearby nuclear spins. This modeling breaks down in the presence of the heating effect, as ω_0 undergoes systematic and contextual shifts that are not accurately captured by a Markovian environment. These shifts can far exceed the intrinsic line width of the qubit resonances, which is estimated to be on the order of 10 kHz for the best published devices. Due to the fundamental role of ω_0 in spin-based quantum computing, the heating effect has impact beyond single-qubit control and also interferes in optimizing two-qubit gate fidelities, for example.

3.5.2. BENEFIT OF WARMER OPERATION

Next, we investigate whether the harmful frequency shifts from microwave excitation may be reduced by directly raising the device temperature via the dilution refrigerator mixing temperature as opposed to using microwave prepulsing. A PID controller connected to an off-chip resistance thermometer is used to regulate the sample temperature. The Pauli spin blockade readout mechanism, unlike energy-selective readout to an electron reservoir, is not compromised by operating at higher temperatures, and it is already established that universal quantum logic is achievable with spin qubits at these temperatures [3, 28].

Fig. 3.6(c) illustrates the effect of an off-resonant burst on qubit 1 at different mixing chamber temperatures. Curiously, the heating effect becomes smaller at a working temperature of 100 mK and seems to vanish completely at temperatures above 150 mK. Given the non-monotonic temperature dependence of the qubit frequency, it is natural to ask whether this is only a consequence of operation close to the temperature "sweet spot". The answer does not seem to be this simple. The 100 mK operating point sits at a steep slope of the Larmor frequency shift trend (see Fig. 3.2), yet the off-resonant pulses induce a smaller frequency shift here. Furthermore, the absence of a frequency shift at 150 mK would be peculiar since the derivative is nonzero here as well. These observations suggest that the sample temperature is less affected by microwave heating at higher temperatures, and that this also contributes to the smaller frequency shifts observed at higher temperatures.

Two possibilities are consistent with this picture. The first is that excess heat is able to dissipate more quickly as the device temperature is increased. In addition to the dilution refrigerator providing more

cooling power at higher temperatures, electronic thermal transport may be able to carry excess heat away from the qubit array more efficiently than phononic thermal transport when the device temperature is above the electron temperature floor. The second possibility is that the specific heat of the materials in the quantum dot region increases. It follows from the Debye model that the specific heat of the crystalline heterostructure should increase as T^3. Therefore, the heat deposited from signal dissipation will cause a much less significant temperature rise at $T \gtrapprox 150\,\mathrm{mK}$ versus $T \approx 15\,\mathrm{mK}$. In either case, the phenomenological picture is simply illustrated in Fig. 3.6(b), where, in contrast to microwave prepulsing, directly raising the temperature of the device via the mixing chamber leads to much less Larmor frequency shifting and, counter-intuitively, spins which are easier to control.

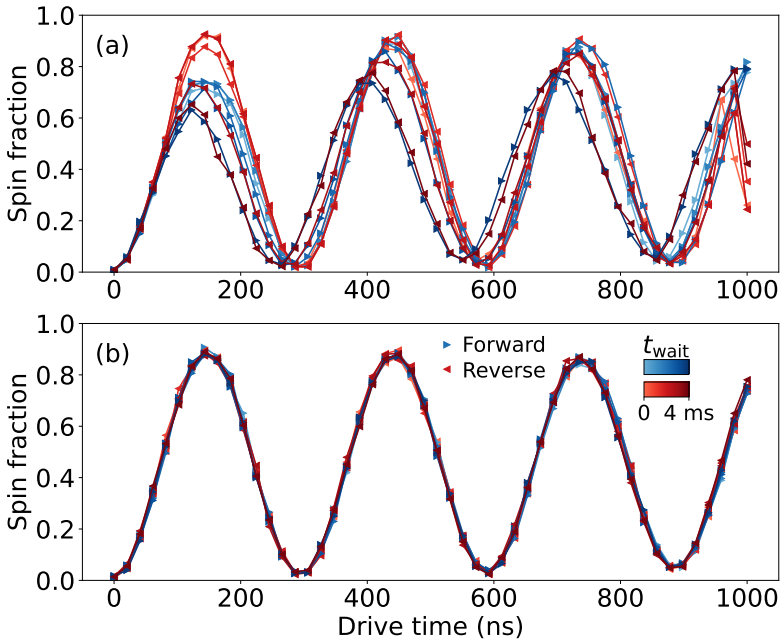


Figure 3.7: Rabi oscillations of qubit 1 collected at a mixing chamber temperature of (a) 12 mK and (b) 200 mK. For each set of measurements, the qubit frequency is calibrated using a "warm" chevron pattern. The wait time t_{wait} is added between measurement and initialization sequences, while "Forward" and "Reverse" scans collect data from 0 to 1000 ns and 1000 to 0 ns respectively. 2000 shots are averaged for each datapoint.

To illustrate the benefit of qubit operation at warm temperatures, we focus on a particular qubit and compare Rabi oscillations at 12 mK and 200 mK mixing chamber temperatures. The latter temperature is not uniquely special; it is high enough to mostly escape the heating effect

while low enough such that readout visibility is not compromised. Fig. 3.7 compares the two cases. At each temperature, the rotating frame is calibrated to the qubit's approximate "warm" Larmor frequency. Each data point consists of 2000 consecutive shots and experiments are run twice: from 0-1 µs and in reverse. Furthermore we vary the wait times used between experimental shots from zero (which still includes readout integration times and necessary delays for the electronics totalling tens of µs) to 4 ms.

Common intuition built off of a simple qubit Hamiltonian would suggest that all collected statistics would be identical. In fact this is what we see at the 200 mK operating point. At base temperature, however, the Rabi oscillations show a great degree of variation due to the interaction between the heating effect, the cooling effect, and the order and speed with which data is collected. The cumulative effect is a striking illustration of non-Markovian behaviour, where resonant spin control becomes highly contextual on the history of the device operation. Higher temperature operation no longer appears only convenient, but essential, for high-quality quantum computing with microwave-controlled qubits in the presence of the heating effect.

To further illustrate the utility of 200 mK operation, we perform single-qubit randomized benchmarking on all qubits and find all average single-qubit gate fidelities are in the range of 99.8%-99.9%. These values are directly comparable to previous values obtained at base temperature [20], but require no off-resonant prepulses, pulse-shaping, or other ad-hoc calibrations to achieve; fitting the chevron pattern to calibrate the Larmor frequency along with a fit of Rabi oscillations to set the gate time is sufficient to reach this level of performance. We expect these values could be further improved with an optimized f_{Rabi} and sophisticated pulse shaping. Furthermore, the phase picked up by idling qubits during the off-resonant drive scales linearly with the duration of the pulse making crosstalk calibration more straightforward. In future work, more sophisticated techniques such as gate set tomography and wildcard error modeling could be employed to quantitatively characterize the remaining sources of single-qubit gate error and the extent to which these errors are captured by a Markovian model [29]. Lastly, we comment that qubit coherence times are negligibly affected by working at the warmer temperature, as measurements of T_2^* shown in Appendix 3.8.4 illustrate[2].

[2] Unfortunately, an additional manuscript summarzing the extensive data collected on qubit coherence and noise as a function of temperature was never completed.

3.6. ORIGIN OF THE TEMPERATURE DEPENDENCE

The physics underpinning the heating effect is the explicit temperature dependence of the qubits' Larmor frequencies on device temperature. It is difficult to identify the precise microscopic origin of this effect, but we may comment on the plausibility of a number of potential mechanisms in light of the experimental data presented here. Each qubit frequency can be expressed as $\omega_i = g_i \mu_B B_{\mathrm{tot,i}}/\hbar$, where g_i is the electron spin g-factor, $B_{\mathrm{tot,i}}$ is the total magnetic field at the quantum dot location, μ_B is the Bohr magneton, and $\hbar$ is the reduced Planck constant. In general, both g_i and $B_{\mathrm{tot,i}}$ may exhibit temperature dependence directly or indirectly.

In principle, it is possible to experimentally isolate g_i from $B_{\mathrm{tot,i}}$ in our setup by measuring the qubit frequency as a function of the total magnetic field. However, we are interested in a shift with a relative magnitude of 0.01%. Measuring the g-factor with this degree of accuracy requires knowing the total magnetic field at the quantum dot location with high precision. While we operate in a regime where the micromagnet magnetization is effectively saturated (i.e. the qubit frequency scales linearly with the external field), we cannot guarantee this to within 0.01% accuracy and thus directly measuring the g-factor change is impractical.

In Appendix 3.8.2, we include temperature-dependent Larmor frequency measurements taken at three different external magnetic field settings. We do observe larger frequency shifts at higher external field values, which is consistent with observations of the heating effect in devices without a micromagnet that suggest the frequency shift originates with the g-factor [15, 19, 21]. The magnitude of the shift does not appear to scale linearly, however, which implies the magnetic environment of the qubits may also be changing. A sub-Kelvin temperature change should have no effect on the field provided from the external magnet as the superconducting solenoid is far from the mixing chamber and carries a persistent superconducting current. One could conceive of mechanisms that change the magnetic environment of the sample as a result of heating the entire cold finger, which is thermalized to the mixing chamber, due to thermal strain or nuclear spin polarization, for example. However, it is doubtful that any such macroscopic effect would result from a single microwave pulse at qubit-logic amplitude.

Pulse-induced frequency shifts reported in the literature illustrate that both positive and negative shifts of different orders of magnitude can arise and provide evidence that an on-chip micromagnet is not a prerequisite to observe such effects. The origin, however universal, appears to show sufficient device-to-device variation to allow for various manifestations of the heating effect in practice. In the following paragraphs, we summarize a variety of mechanisms that can lead to a temperature dependence in the (effective) local magnetic field experienced by the spins or in their (effective) g-factor. We also comment on their plausibility given the

available data.

Residual ^{29}Si in the purified quantum well and ^{73}Ge nuclear spins in the SiGe buffer contribute to an effective Overhauser field that may exhibit temperature dependence through Boltzmann statistics. Both isotopes have negative gyromagnetic ratios of $-8.46\,\mathrm{MHz/T}$ and $-1.49\,\mathrm{MHz/T}$. The energy splitting of these nuclear spin states is on the order of $0.01\,\mu\mathrm{eV}$, meaning that at base temperature where $k_B T \approx 1\,\mu\mathrm{eV}$ there is a very slight nuclear polarization opposing the external field. As the temperature is increased, the magnitude of the Overhauser field will monotonically decrease. Therefore, the contribution from the nuclear spins should cause a monotonic increase in the effective magnetic field, and therefore a monotonic increase in the spin's Larmor frequency [3]. Modeling of quantum dots occupying a ^{28}Si quantum well isotopically purified of nuclear spins to 800 ppm suggests that perhaps tens of ^{29}Si nuclei may have a sizeable hyperfine coupling, for example such that $A_j/2\pi > 10\,\mathrm{kHz}$, to each electron spin [31]. We may expect only a few of these to flip due to the change in the thermal equilibrium from 20 mK to 200 mK, and the resulting shift is an order-of-magnitude too small to account for the observed temperature dependence. Moreover, such nuclear spin flips would appear as discrete jumps in frequency. In contrast, we repeatedly observed the trend to be smooth.

Similar arguments hold for unpaired electron spins in the environment which may couple to the qubit spin through magnetic dipolar interactions. The gyromagnetic ratio of these spins would also be negative but with a magnitude that is three orders of magnitude larger. While essentially none of these environmental spins occupy the excited state at base temperature, a few percent of an ensemble may exist in the excited state at 200 mK. Whether this change in magnetic environment meaningfully influences the qubits depends on the density and distance of unpaired spins which we currently cannot estimate.

The g-factor of an electron spin in a silicon quantum dot is renormalized by many factors including interface-induced spin-orbit coupling, micromagnet-induced spin-orbit coupling, the shape of the confinement potential, and crystal composition and strain. The renormalization from the micromagnet-induced spin-orbit coupling is on the order of 10 kHz and therefore any micromagnet dynamics are too small to account for the frequency shift via the g-factor. A g-factor change arising from a change in confinement potential can be seen as a general Stark shift effect, which we discuss below. It is possible that some degree of thermal expansion in the device, affecting both strain and spin-orbit

[3] The Overhauser field is given by $B_N = \sum_i \frac{A_i I_{z,i}}{g\mu_B} < 0$, where $g = +2$ for the electron spin, and $A_i \propto \gamma_e \gamma_n > 0$ is the hyperfine coupling constant. The gyromagnetic ratios of the relevant electron and nuclear spins $\gamma_e < 0$ and $\gamma_n < 0$ are both negative, and $\langle I \rangle < 0$ averaged over all nuclear spins in their thermal ground state [30].

coupling, may play a role in explaining the temperature-dependence of the Larmor frequency, although a rigorous estimate is extremely challenging to carry out given the scope of the microscopic details that must be accounted for. We note that [17] put forward a similar hypothetical origin by estimating the change in effective mass of the confined electron as a function of temperature [32]. This estimate relies on the validity of $\mathbf{k}\cdot\mathbf{p}$ model parameters at sub-Kelvin temperature scales.

The g-factor difference between valley-orbit states is worth consideration, since increased thermal energy may cause the excited valley state to become populated with greater probability during initialization [33, 34]. However, we see no additional evidence, such as a second resonance peak, that such a valley state is being populated. Rather, the single resonance smoothly moves as temperature is increased.

It is well-known that electric fields may induce a Stark shift due to the spatial dependence of both the magnetic field $B_{\mathrm{tot},i}$ and g-factor g_i. A temperature-dependent electric field could thus indirectly cause a frequency shift. In our system, we could expect such a shift to be dominated by the micromagnet gradient particularly for an in-plane electric field that laterally displaces the electron. By this logic, it is reasonable that the frequency shifts we observe are generally larger than in other devices [15, 19, 21] where intrinsic spin-orbit coupling dominates. However, an electric field oriented perpendicular to the quantum well may also result in a frequency shift, depending on its magnitude. Where may the electric field inducing the Stark shift originate? Transport experiments through various quantum wells (similar to experiments in Si-MOS [35]) record an increased percolation density as a function of temperature which is believed to correspond to thermally activated defects causing electrostatic "roughness" (see Appendix 3.8.2). We observe the Larmor frequency shift over similar temperature scales, such that a thermally-activated electric field caused by rearranging environmental fluctuators may be a contributing factor. A recent in-depth theoretical study explores this possibility [36].

We have not, however, been able to detect such a temperature-dependent electric field directly with the on-chip charge sensors. That is, Coulomb peak position and charge transitions within the quantum dot array move much less than 1 mV with respect to their associated plunger gates as the temperature is raised from 20 mK to 250 mK. For a rough comparison, we may expect electric fields on the order of 10 kV/m, or equivalently plunger gate voltages of several millivolts, to lead to 1 MHz shifts in the qubit frequency. We also find that temperature changes do not affect where Pauli spin blockade occurs in gate voltage space, a window of about 2 mV along the interdot detuning axis. An electric field that simultaneously Stark shifts qubits while preserving these other charge-sensitive features is peculiar. We extend this discussion in

Appendix 3.8.2. We also note that we do not observe any hysteresis in the temperature-dependence of the Larmor frequencies (see Fig. 3.10).

In summary, temperature-dependence in the micromagnet may contribute to our observations, but observations of the heating effect in devices that do not contain a micromagnet suggest its role is not fundamental. A change in the magnetic environment of each spin due to residual hyperfine interaction is expected to be discrete and monotonic, unlike our observations, and likely smaller than the frequency shifts we report. Thermally-induced strain may also play a role, but it is very difficult to make an accurate numeric estimate. A temperature-dependent electric field which Stark-shifts the Larmor frequencies is compelling, given the thermal sensitivity of charge defects in the heterostructure. Our experiments do not reveal "smoking gun" evidence of such an electric field, but it is possible that a field manifests in a way such that our charge sensing apparatus is insensitive to it.

Lastly, we remark that it is difficult to conceive of a single mechanism that yields a nonmonotonous frequency shift. This perhaps points to an interplay between more than one relevant effect. Data from additional devices, especially those without a micromagnet, may help elucidate the dominant physics at play. The ability to probe the g-tensor with vector magnet control, which we were unable to use for this study, may also provide additional insight into the microscopic nature of the temperature dependence [37].

3.7. CONCLUSION

In summary, we have documented for the first time an explicit temperature-dependence in silicon spin qubit Larmor frequencies. The magnitude of the observed frequency shift is consistent with the heating effect that has long been associated with microwave control of individual spin states but may also be induced by baseband control signals. We find that this effect becomes substantially smaller as the temperature of the device is modestly increased, leading to reduced crosstalk and simpler calibration routines for achieving high-fidelity single-qubit control at 200 mK without compromising coherence times. This makes microwave control of spins a viable means to continue scaling spin-based quantum processors in the near-term. While the microscopic origin of the temperature dependence remains elusive, we have highlighted some mechanisms that are consistent with our experiments.

3.8. SUPPLEMENTARY MATERIAL

3.8.1. TEMPERATURE DEPENDENCE OF RF-REFLECTOMETRY MEASUREMENTS

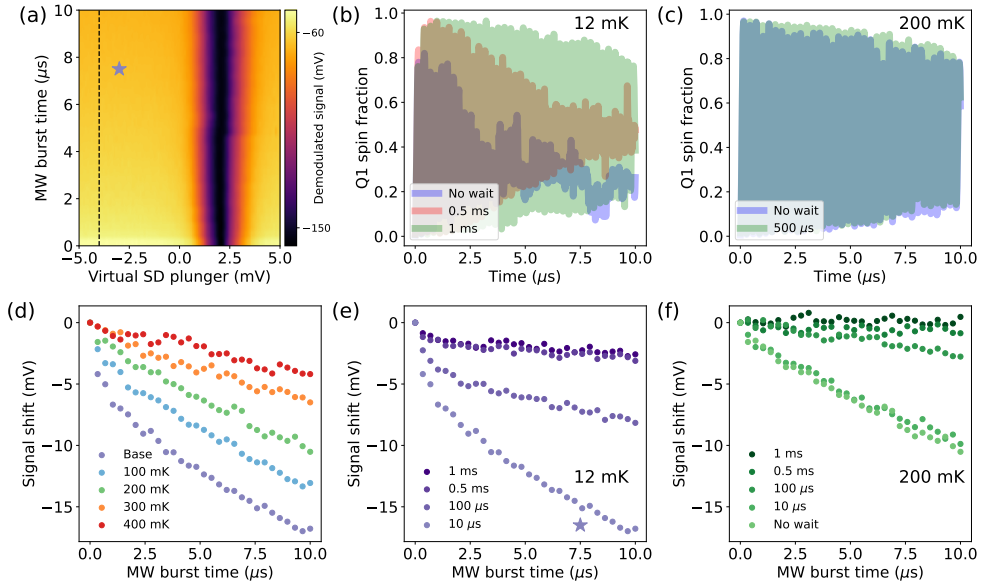


Figure 3.8: (a) A Coulomb conductance peak and its adjacent blockaded region measured using rf reflectometry at 12 mK as a function of the virtualized sensing dot plunger voltage and a microwave burst of swept duration. The burst amplitude corresponds to $f_{\text{Rabi}} \approx 1.3$ MHz. Due to the demodulation parameters used, the scalar signal at the conductance peak is invariant to microwaves up to ± 2 mV. (b-c) Rabi oscillations with $f_{\text{Rabi}} \approx 3$ MHz plotted to emphasize the apparent decay envelopes at 12 mK and 200 mK. The wait time indicates the idling duration between applying the resonant microwave tone and pulsing to the Pauli spin blockade region. (d) The integrated background signal along the line cut indicated in (a) taken at different mixing chamber temperatures. No wait time between microwave pulse and measurement is used, except at base temperature where a 10 μs pulse is employed. (e-f) The integrated background signal along the same line cut at 12 mK and 200 mK while different wait times between microwave pulse and readout were used.

While performing the experiments detailed in the main text, we observed that the rf reflectometry apparatus used to measure qubit spin states in this particular device also exhibits temperature dependence. While this dependence is not related to the qubit heating effects of primary focus in the main text, separating these two changes is not immediately trivial. Furthermore, as rf reflectometry has become a standard laboratory practice for measuring semiconductor spin qubits and quantum dot charge states more generally, we believe that careful consideration of its dependence on temperature will become an essential

engineering consideration in more advanced devices.

The implementation of rf reflectometry in our device closely follows the "Ohmic Approach" documented in [38]. We find that both the inductance L, which is implemented as an off-chip NbTiN high-kinetic inductance inductor, and the lead resistance R_{lead}, which includes the bond wire to the sample, the ohmic contact, and the electron reservoir coupled to the sensing dot in series, are temperature-dependent. The reason for the inductor's temperature dependence was not studied in detail, but it was found to be a general property of inductors from the particular fabrication batch. Subsequent devices do not replicate this behaviour, so here we focus only on the consequences of the temperature dependence and not its origin. As discussed in the main text, some degree of temperature dependence in the lead resistance may be expected as a result of thermally-activated electrostatic disorder in the quantum well, but the series resistance through the ohmic contact may also be a factor.

One of the two charge sensors is measured by demodulating a 10-20 µs pulse of frequency f_{res} and digitizing the resulting in-phase (I) and quadrature (Q) components of the signal. These two channels are converted into a single scalar value by rotating the IQ plane by an angle θ_{mod} such that the contrast between the two charge states of interest is maximized. A signal threshold V_{th} is then set to enable single-shot spin readout.

Temperature dependence in the rf reflectometry circuit is important because the probe frequency f_{res}, demodulating phase θ_{mod} and threshold V_{th} are constant during a predefined experiment (e.g. measuring Rabi oscillations). However, a temperature dependence in L and R_{lead} would affect the optimal f_{res}, θ_{mod}, and V_{th} as microwaves and other control signals dissipate in the device. At best, this results in poorer readout fidelity and at worst can completely eliminate all readout visibility.

Fig. 3.8(a) illustrates the consequences of microwave-induced heating at base (approx. 12 mK) mixing chamber temperature on a Coulomb peak measurement. A long wait time of 500 µs is implemented between shots to maintain independence between measurements. Figs. 3.8(d-f) show how the scalar background signal varies after a combination of microwave pulsing and waiting prior to signal integration at a variety of mixing chamber temperatures. The particular demodulation settings used during this set of experiments meant that the conductance peak signal was robust to microwave prepulsing within ±2 mV while the background signal was sensitive to changes in θ_{mod}. In this case, the change in background signal directly corresponds to a lower charge state distinguishability.

Similar to the microwave-induced heating effect, we observe that the rf reflectometry signal is more robust as the device temperature is increased. However, we do not find that this effect becomes negligible, meaning that readout heating must still be controlled even at warmer

device operation in order to maintain spin state visibility. The recovery of the original background signal amplitude as a function of wait time also illustrates how the cooling timescale becomes shorter when the mixing chamber temperature is increased. Although the signal at 200 mK is modified by the microwave pulse, only 100 µs is required for the signal to recover. However, over 0.5 ms of waiting is necessary for the signal to recover at 12 mK.

Fig. 3.8(b) illustrates the effect of rf reflectometry heating on spin experiments. During a 10 µs single qubit Rabi oscillation experiment, some visibility is lost as the constant readout threshold no longer optimally distinguishes between charge states. In [20], a wait time was placed between qubit operation and measurement in anticipation of this readout heating effect. Otherwise, the loss of spin visibility gives the illusion of T_2^{Rabi} decay. However, as the results in the main text illustrate, we find that this loss of visibility is also caused by the qubit frequencies shifting due to heat accumulated between shots.

Once again, we find that the most pragmatic solution is to work at an elevated temperature. At 200 mK, the RLC resonator peaks are not majorly degraded but the qubit frequencies are much more stable throughout experiments. As such, maintaining readout visibility throughout experiments containing repeated microwave pulses is possible with no addition of intra-sequence wait-times whatsoever (see Fig. 3.8(c)). The calibrated values of f_{res}, θ_{mod} and V_{th} are more robust to signal dissipation during experiments as well. Ultimately, heating in the rf reflectometry circuit becomes the limiting experimental factor. During microwave-intensive experiments, such as single-qubit randomized benchmarking, where driving tones totaling tens of microseconds may be applied, a wait time between shots must be used or else the readout threshold V_{th} will be so misaligned as to not provide any meaningful information due to steady heat accumulation.

We anticipate that a) using surface-mount inductors which exhibit less temperature dependence, and b) routing the rf reflectometry signal through a capacitively coupled gate as opposed to the galvanically connected ohmic contacts (see the “Split-gate approach” of [38]) will lead to better thermal insulation between the RLC circuit and the quantum well. Ultimately, eliminating wait-times for “cooling” altogether will be essential for interleaving qubit measurement and control in future quantum error correction implementations.

3.8.2. PROBING CHARGE DEFECTS AND TEMPERATURE-DEPENDENT STARK SHIFTS

Charge defects, or two-level fluctuators (TLFs), are ubiquitous in many solid state systems and are also expected to occupy the heterostructure

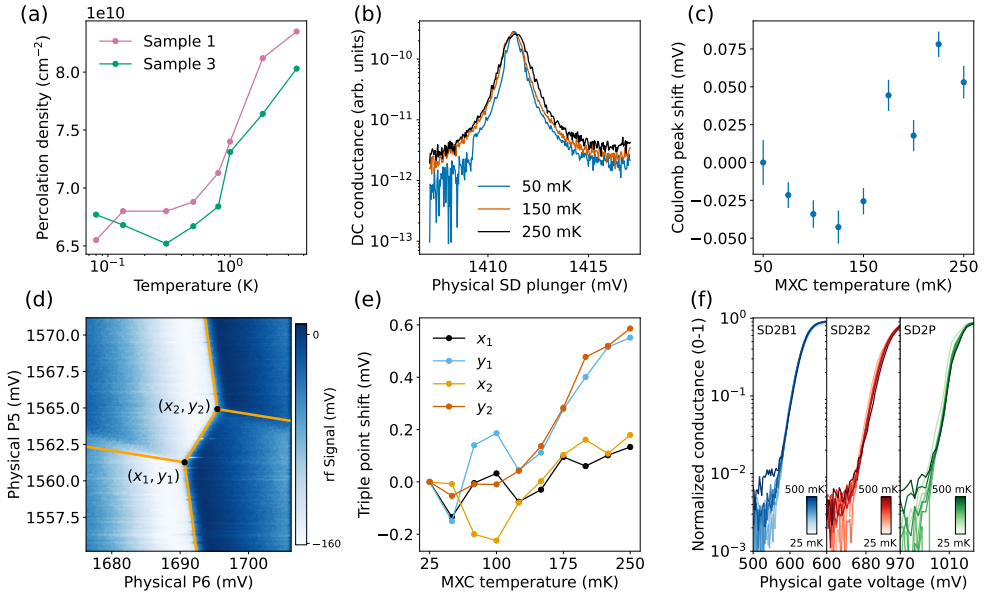


Figure 3.9: (a) Percolation density measurements as a function of temperature carried out on two ^{28}Si/SiGe heterostructures nominally equivalent to that used for the qubit device studied here. (b) A selection of Coulomb peaks formed in SD2 measured in DC as a function of the physical sensing dot plunger voltage. These measurements were qualitatively unchanged when rf reflectometry was used instead. (c) Shifts in the Coulomb peak position in plunger gate voltage space (V_G) when fitted to $dI/dV = A\cosh^{-2}[B(V_G - V_0)] + C$ where V_0 is the location of the peak at 50 mK, and A, B, and C are other fitting constants. (d) A sample charge stability diagram of the $(1,3)-(0,4)$ interdot transition between quantum dots 5 and 6 taken at 100 mK. An algorithm is used to extract the triple point coordinates plotted in (e). (e) The location of the two triple points labeled in (d) as a function of mixing chamber temperature. Charge stability diagrams were measured using rf reflectometry. (f) Comparison of threshold voltages in SD2 as a function of mixing chamber temperature, when using both sensing dot barriers (SD2B1, SD2B2) and the plunger (SD2P) to pinch off the accumulated channel. Measurements were taken using rf reflectometry to maximize sensitivity to any changes near the threshold.

in which the spin qubits studied here reside, as well as the dielectrics in the gate stack fabricated on top of the heterostructure. Although heavily researched for decades [39], much about their microscopic details remains unclear. It is generally well accepted that an ensemble of TLFs, each with a Lorentzian power spectral density, will cumulatively generate a $S(\omega) \propto 1/f^{\alpha}$ power spectral density with $\alpha \approx 1$ that is commonly cited as the origin of measured charge noise spectra [40]. Furthermore, the microscopic details of the TLFs may result in a variety of temperature dependencies at sub-Kelvin conditions [24, 41, 42].

Hall bar measurements shown in Fig. 3.9(a) were carried out on the same ^{28}Si/SiGe heterostructure as the six qubit device studied here

and demonstrate that the percolation density increases as the device temperature is raised, particularly in the few-hundred millikelvin regime. This is believed to be the result of thermally-sensitive charge defects increasing the electrostatic disorder within the quantum well [35]. If this thermal activation of TLFs is correlated with the temperature-dependent Larmor frequencies we measure, we believe it is reasonable that an electric field-spin coupling facilitates this dependence.

It is well known that electric fields are able to shift electron spin Larmor frequencies in silicon quantum dots. Though often generically referred to as a Stark shift, the coupling may take place due to a spatially varying magnetic field, as in the case of an on-chip micromagnet, and a spatially varying g-factor dominated by interface-induced spin-orbit coupling. As these frequency shifts can be on the MHz scale, it is reasonable to question whether a similar coupling may facilitate a temperature-dependent Stark shift.

Here we highlight three measurements that aim to uncover any correlation between the mixing chamber temperature and a change in electrostatic environment that may mediate the frequency shift and, consequently, motivate a microscopic origin of the "heating effect". First, we measure a Coulomb peak of Sensing Dot 2 (SD2) as a function of mixing chamber temperature by using a DC current. Figs. 3.9(b-c) respectively show the Coulomb peaks and a fit of the peak locations along the sensing dot plunger axis versus temperature. During qubit readout, the peak location will move by about 1 mV along this axis in the presence of a single electron transition between two dots in a radius of about 200 nm around the sensing dot. The fact that we see no systematic peak movement of more than 0.1 mV in the temperature range where the qubit frequencies shift by 1 MHz implies there is little environmental charge rearrangement occurring in the vicinity of the sensing dot. This is consistent with Fig. 3.8(a), measured via rf reflectometry, which also shows no Coulomb peak movement during microwave-induced heating.

Second, we measure the interdot charge transition between quantom dots 5 and 6 as a function of mixing chamber temperature. Figs. 3.9(d-e) illustrate the fitted triple points and their movement in physical gate space as a function of temperature. A total movement of much less than 1 mV is observed over the 250 mK temperature range studied. This change is less than the width of the charge transitions themselves, and we remark that it is necessary to modify the plunger voltages by at least several millivolts in order to observe 1 MHz Stark shifts in the qubit Larmor frequencies at a constant temperature. While this gives some evidence that the electrostatic environment near the quantum dots changes as a function of temperature, it does not form a convincing connection to the temperature-dependent frequency shift.

Third, we probe whether we can detect a change in the electrostatic

roughness of the 2DEG reservoirs as a function of temperature which may provide a more global indication of the presence of TLFs near the quantum well. To do this, we use rf reflectometry to measure the conduction turn-on through SD2 as a function of all three gate voltages along the channel (2 barrier gates and 1 plunger gate). Temperature dependence in this turn-on characteristic may indicate that charge defects in the oxide between the gate and the ^{28}Si/SiGe heterostructure activate and contribute to the net electric field at the quantum well. The rf measurement should be more sensitive than a dc current measurement since it may show a finite conductance before the 2DEG is fully accumulated. As shown in Fig. 3.9(f), very little change in the threshold voltage is observed as a function of temperature, and no clear correlation emerged between this behaviour and the Larmor frequency shifts.

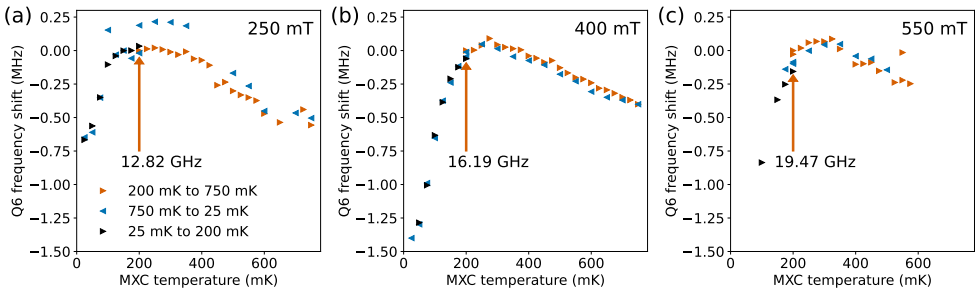


Figure 3.10: Tests for hysteresis in the temperature-dependent frequency shift of qubit 6 carried out at external magnetic field settings of (a) 250 mT, (b) 400 mT, and (c) 550 mT. In each case, the absolute qubit resonance frequency is indicated at 200 mK which also serves as a reference for the magnitude of the frequency shift. The device is positioned such that it experiences approximately 80% of the nominal external field quoted. Accordingly, the Larmor frequency scales linearly with the external field at a rate of 22.2 GHz/T, indicating that the micromagnet stray field is approximately constant for all experiments. To test for hysteresis, the temperature is swept from 200 mK to 750 mK in 25 mK steps, then down to 200 mK in 50 mK steps, then down to 25 mK in 25 mK steps, and finally back up to 200 mK in 25 mK steps. In (a) and (c), a low-frequency electrical TLF coupled to both the qubit and adjacent charge sensor. Experiments where readout quality is compromised entirely are omitted for clarity.

A final series of tests were carried out to detect whether the qubit frequency shifts exhibited a hysteresis effect with respect to temperature. As microscopic models of TLFs commonly include asymmetry in the constituent bi-stable states, hysteresis of the frequency shift with respect to temperature could provide an indication of this structure. Repeated experiments at three different external field settings, of which a few are included in Fig. 3.10 yield no systematic hysteresis effect. Although jumps in the qubit frequency and Coulomb peak tuning occur occasionally, the underlying temperature dependence remains robust, and repeated

experiments generally do not reproduce the frequency shifts originating from bi-stable behaviour. Simultaneous jumps of both the Coulomb peak and qubit frequencies are likely the result of nearby charge jumps in the system, whereas jumps in qubit frequency without an associated Coulomb peak shift may arise due to nuclear spin flips [31]. The characteristic temperature dependence of the qubit frequencies is observed regardless of whether these discrete jumps occur during an experiment. We remark that the magnitude of the temperature-dependent frequency shift is relatively larger at higher magnetic fields which is consistent with the hypothesis that the temperature-dependence originates with the electron g-factor. However, potential changes in the micromagnet magnetization do not let us make conclusive statements from this data. The reported microwave-induced frequency shifts in devices without a micromagnet provide the most compelling evidence that the g-factor itself is the fundamentally temperature-dependent quantity [15, 19, 21].

In summary, our experiments do not rule out an electrostatic or TLF contribution to the Larmor frequency temperature dependence. However, the exploratory results presented here certainly do not uncover a "smoking gun" of a significant effect. Ongoing research into the concentration and microscopic details of the dominant charge defects in semiconductor quantum wells will help contextualize their possible role in the "heating effect".

3.8.3. ELECTRON TEMPERATURE MEASUREMENTS

The equilibrium electron temperature of the accumulated charge carriers will be determined by (a) the rate at which ambient energy is incident on the chip, (b) the heat capacity of the systems into which it is deposited and their coupling to the 2DEG, and (c) the rate whereby heat diffuses to the cold sink (i.e. mixing chamber). (a) is primarily due to the thermalized flux of photons propagating through fast control lines. In general, we observe that devices with a greater number of connected fast control lines will exhibit a higher electron temperature. (b) will, at sub-Kelvin temperatures, likely be dominated by the amorphous oxide and TLF-type defects present in the heterostructure, as these systems exhibit a larger specific heat than would otherwise be predicted by the Debye model for crystalline solids [43]. Many of these systems will be in thermal contact with the conduction electrons and provide a heat bath which warms the electron gas above the nominal mixing chamber temperature. (c) will take place through a combination of phononic and electronic thermal transport as described in Fig. 3.1 and the main text.

We measure estimates for the electron temperature on both sides of the device by measuring Coulomb diamonds through the two sensing dots at base mixing chamber temperature. These yield estimates of

180 ± 10 mK and 200 ± 10 mK for the 2DEG reservoirs surrounding sensing dots 1 and 2 respectively. Estimates of electron temperature made via reservoir-dot charge transitions yield similar, but somewhat higher, estimates of 232 mK and 214 mK for sensing dots 1 and 2 respectively.

Although these temperatures are similar to the "sweet spot" appearing in Fig. 3.2, it is unclear whether this is a meaningful or coincidental correlation. However, it does seem reasonable that raising the mixing chamber temperature to at least the electron temperature facilitates faster device thermalization as various dissipative control signals are sent to the device, because electron diffusion may facilitate thermalization of the quantum dot environment when the phononic and electronic environments share a similar temperature. This may, in part, explain the observations in Fig. 3.6 where microwave induced heating is greatly reduced at temperatures similar to (or above) the electron temperature floor.

3.8.4. SPIN COHERENCE AT 200 MK

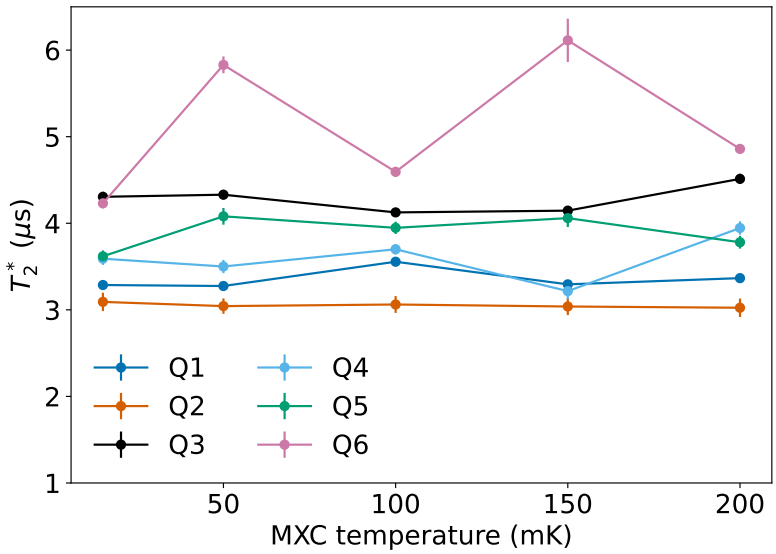


Figure 3.11: T_2^* measurements extracted from the same Ramsey experiments used to measure Larmor frequency temperature dependence in Fig. 3.2. Each single-qubit Ramsey measurement is averaged for approximately 8 minutes.

Fig. 3.11 illustrates how increasing the mixing chamber temperature from base to 200 mK has virtually no impact on the T_2^* values for all six qubits. The values reported here are directly comparable to previous measurements on the same device when no prepulsing was used prior to

qubit control [20]. In contrast, when a 4 µs microwave prepulse of normal gate-operation amplitude was applied prior to the measurement, T_2^* values fell to 1-3 µs across the array. From this, we conclude that directly raising the mixing chamber temperature to overcome the heating effect is superior to prepulsing. We emphasize that the modest increase in device temperature to 200 mK used to overcome contextual operation does not come at the cost of compromising coherence times or single-qubit gate fidelities.

3.8.5. EXCHANGE INTERACTION AND TEMPERATURE

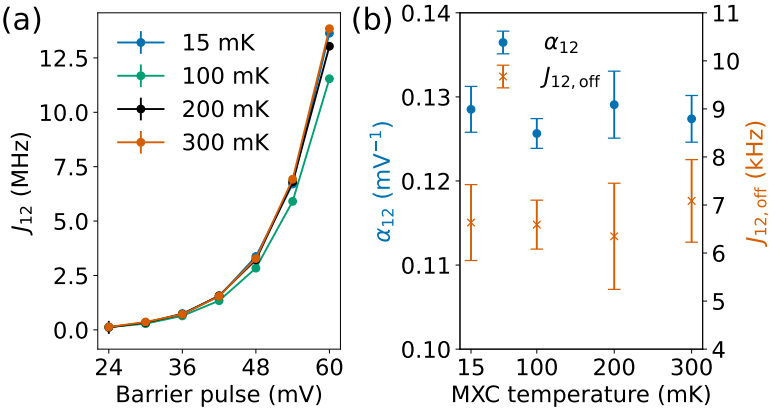


Figure 3.12: (a) Exchange strength J_{12} as a function of barrier voltage vB_1 at different mixing chamber temperatures. Oscillations are fit by performing a decoupled CZ sequence as described in [20] and fitting to the Ising Hamiltonian $H = J_{12} S_1^z \otimes S_2^z$ where S_i^z is the spin operator for qubit i projected along the quantization axis z. (b) The barrier-exchange coefficient α_{12} and extrapolated residual exchange coupling $J_{12,\text{off}}$ as measured at various mixing chamber temperatures. Fits assume a phenomenological relationship $J_{12} = J_{12,\text{off}} \exp(\alpha_{12} vB_1)$.

We carried out a preliminary investigation into the exchange interaction between qubits 1 and 2 as a function of temperature. In contrast to the qubit frequencies, the exchange interaction is far more sensitive to the electronic wavefunction position than the spins' magnetic environment and is therefore a good probe of changes in the electrical environment of the quantum dots. Fig. 3.12 summarizes the findings and provides no obvious evidence that temperature influences the exchange interaction. This is true both for how the barrier voltage modulates the exchange strength J_{12}, quantified by α_{12}, as well as the extrapolated residual exchange strength $J_{12,\text{off}}$. Both fitted parameters are constant within measurement uncertainty, and neither suggest a temperature dependence that resembles that of the Larmor frequency shifts. Although

the set of operating voltages was held constant, the experiments were conducted over a span of 4 days, and very low frequency device drift may account for some variation between temperature set points.

REFERENCES

[1] B. Undseth *et al.* “Hotter is Easier: Unexpected Temperature Dependence of Spin Qubit Frequencies”. In: *Phys. Rev. X* 13 (4 Oct. 2023), p. 041015. doi: 10.1103/PhysRevX.13.041015. url: https://link.aps.org/doi/10.1103/PhysRevX.13.041015.

[2] C. H. Yang *et al.* “Operation of a silicon quantum processor unit cell above one kelvin”. In: *Nature* 580.7803 (Apr. 2020), pp. 350–354. issn: 1476-4687. doi: 10.1038/s41586-020-2171-6. url: http://dx.doi.org/10.1038/s41586-020-2171-6.

[3] L. Petit *et al.* “Universal quantum logic in hot silicon qubits”. In: *Nature* 580.7803 (Apr. 2020), pp. 355–359. issn: 1476-4687. doi: 10.1038/s41586-020-2170-7. url: http://dx.doi.org/10.1038/s41586-020-2170-7.

[4] L. C. Camenzind *et al.* “A hole spin qubit in a fin field-effect transistor above 4 kelvin”. In: *Nature Electronics* 5.3 (Mar. 2022), pp. 178–183. doi: 10.1038/s41928-022-00722-0. url: https://doi.org/10.1038%5C%2Fs41928-022-00722-0.

[5] L. Petit *et al.* “Spin Lifetime and Charge Noise in Hot Silicon Quantum Dot Qubits”. In: *Phys. Rev. Lett.* 121 (7 Aug. 2018), p. 076801. doi: 10.1103/PhysRevLett.121.076801. url: https://link.aps.org/doi/10.1103/PhysRevLett.121.076801.

[6] A. R. Mills *et al.* “High-Fidelity State Preparation, Quantum Control, and Readout of an Isotopically Enriched Silicon Spin Qubit”. In: *Phys. Rev. Appl.* 18 (6 Dec. 2022), p. 064028. doi: 10.1103/PhysRevApplied.18.064028. url: https://link.aps.org/doi/10.1103/PhysRevApplied.18.064028.

[7] J. Yoneda *et al.* “A quantum-dot spin qubit with coherence limited by charge noise and fidelity higher than 99.9%”. In: *Nature Nanotechnology* 13.2 (Dec. 2017), pp. 102–106. issn: 1748-3395. doi: 10.1038/s41565-017-0014-x. url: http://dx.doi.org/10.1038/s41565-017-0014-x.

[8] W. I. L. Lawrie *et al.* “Simultaneous single-qubit driving of semiconductor spin qubits at the fault-tolerant threshold”. In: *Nature Communications* 14.1 (June 2023). issn: 2041-1723. doi: 10.1038/s41467-023-39334-3. url: http://dx.doi.org/10.1038/s41467-023-39334-3.

[9] A. Noiri *et al.* “Fast universal quantum gate above the fault-tolerance threshold in silicon”. In: *Nature* 601.7893 (Jan. 2022), pp. 338–342. issn: 1476-4687. doi: 10.1038/s41586-021-04182-y. url: http://dx.doi.org/10.1038/s41586-021-04182-y.

[10] X. Xue *et al.* “Quantum logic with spin qubits crossing the surface code threshold”. In: *Nature* 601.7893 (Jan. 2022), pp. 343–347. issn: 1476-4687. doi: 10.1038/s41586-021-04273-w. url: http://dx.doi.org/10.1038/s41586-021-04273-w.

[11] M. T. Mądzik *et al.* “Precision tomography of a three-qubit donor quantum processor in silicon”. In: *Nature* 601.7893 (Jan. 2022), pp. 348–353. doi: 10.1038/s41586-021-04292-7. url: https://doi.org/10.1038%5C%2Fs41586-021-04292-7.

[12] A. R. Mills *et al.* “Two-qubit silicon quantum processor with operation fidelity exceeding 99%”. In: *Science Advances* 8.14 (Apr. 2022). issn: 2375-2548. doi: 10.1126/sciadv.abn5130. url: http://dx.doi.org/10.1126/sciadv.abn5130.

[13] J. M. Nichol *et al.* “High-fidelity entangling gate for double-quantum-dot spin qubits”. In: *npj Quantum Information* 3.1 (2017), pp. 1–5.

[14] A. J. Weinstein *et al.* “Universal logic with encoded spin qubits in silicon”. In: *Nature* 615.7954 (Feb. 2023), pp. 817–822. issn: 1476-4687. doi: 10.1038/s41586-023-05777-3. url: http://dx.doi.org/10.1038/s41586-023-05777-3.

[15] S. Freer *et al.* “A single-atom quantum memory in silicon”. In: *Quantum Science and Technology* 2.1 (2017), p. 015009.

[16] T. F. Watson *et al.* “A programmable two-qubit quantum processor in silicon”. In: *Nature* 555.7698 (Feb. 2018), pp. 633–637. issn: 1476-4687. doi: 10.1038/nature25766. url: http://dx.doi.org/10.1038/nature25766.

[17] K. Takeda *et al.* “Optimized electrical control of a Si/SiGe spin qubit in the presence of an induced frequency shift”. In: *npj Quantum Inf.* 4 (2018), p. 54. issn: 2056-6387. url: https://doi.org/10.1038/s41534-018-0105-z.

[18] N. Hendrickx *et al.* “Fast two-qubit logic with holes in germanium”. In: *Nature* 577 (Jan. 2020). url: https://doi.org/10.1038/s41586-019-1919-3.

[19] A. Zwerver *et al.* “Qubits made by advanced semiconductor manufacturing”. In: *Nature Electronics* 5.3 (2022), pp. 184–190.

[20] S. G. J. Philips *et al.* “Universal control of a six-qubit quantum processor in silicon”. In: *Nature* 609.7929 (Sept. 2022), pp. 919–924. issn: 1476-4687. doi: 10.1038/s41586-022-05117-x. url: http://dx.doi.org/10.1038/s41586-022-05117-x.

[21] R. Savytskyy *et al.* “An electrically driven single-atom ‘flip-flop’ qubit”. In: *Science Advances* 9.6 (2023), eadd9408. doi: 10.1126/sciadv.add9408. url: https://www.science.org/doi/abs/10.1126/sciadv.add9408.

[22] F. Mueller *et al.* “Printed circuit board metal powder filters for low electron temperatures”. In: *Review of Scientific Instruments* 84.4 (Apr. 2013), p. 044706. doi: 10.1063/1.4802875. url: https://doi.org/10.1063%5C%2F1.4802875.

[23] R. L. Kautz, G. Zimmerli, and J. M. Martinis. “Self-heating in the Coulomb-blockade electrometer”. In: *Journal of Applied Physics* 73.5 (1993), pp. 2386–2396. doi: 10.1063/1.353092. url: https://doi.org/10.1063/1.353092.

[24] M. V. Gustafsson *et al.* “Thermal properties of charge noise sources”. In: *Phys. Rev. B* 88 (24 Dec. 2013), p. 245410. doi: 10.1103/PhysRevB.88.245410. url: https://link.aps.org/doi/10.1103/PhysRevB.88.245410.

[25] M. Reed *et al.* “Reduced Sensitivity to Charge Noise in Semiconductor Spin Qubits via Symmetric Operation”. In: *Physical Review Letters* 116.11 (Mar. 2016). issn: 1079-7114. doi: 10.1103/physrevlett.116.110402. url: http://dx.doi.org/10.1103/PhysRevLett.116.110402.

[26] X. Xue *et al.* “Benchmarking Gate Fidelities in a Si/SiGe Two-Qubit Device”. In: *Phys. Rev. X* 9 (2 Apr. 2019), p. 021011. url: https://link.aps.org/doi/10.1103/PhysRevX.9.021011.

[27] D. M. Pozar. *Microwave engineering*. John Wiley & Sons, 2012. url: https://search.library.wisc.edu/catalog/9910153599402121.

[28] C. H. Yang *et al.* “Silicon qubit fidelities approaching incoherent noise limits via pulse engineering”. In: *Nature Electronics* 2.4 (Apr. 2019), pp. 151–158. issn: 2520-1131. doi: 10.1038/s41928-019-0234-1. url: http://dx.doi.org/10.1038/s41928-019-0234-1.

[29] R. Blume-Kohout *et al. Wildcard error: Quantifying unmodeled errors in quantum processors*. 2020. arXiv: 2012.12231 [quant-ph]. url: https://arxiv.org/abs/2012.12231.

[30] R. Hanson *et al.* “Spins in few-electron quantum dots”. In: *Reviews of Modern Physics* 79.4 (Oct. 2007), pp. 1217–1265. issn: 1539-0756. url: http://dx.doi.org/10.1103/RevModPhys.79.1217.

[31] R. Zhao *et al.* “Single-spin qubits in isotopically enriched silicon at low magnetic field”. In: *Nat. Commun.* 10.1 (Dec. 2019). issn: 2041-1723. url: http://dx.doi.org/10.1038/s41467-019-13416-7.

[32] S. Richard *et al.* “Strained silicon on SiGe: Temperature dependence of carrier effective masses”. In: *Journal of Applied Physics* 94.8 (2003), pp. 5088–5094. eprint: https://aip.scitation.org/doi/pdf/10.1063/1.1609051. url: https://aip.scitation.org/doi/abs/10.1063/1.1609051.

[33] E. Kawakami *et al.* “Electrical control of a long-lived spin qubit in a Si/SiGe quantum dot”. In: *Nature Nanotechnology* 9.9 (Aug. 2014), pp. 666–670. issn: 1748-3395. doi: 10.1038/nnano.2014.153. url: http://dx.doi.org/10.1038/nnano.2014.153.

[34] R. Ferdous *et al.* “Valley dependent anisotropic spin splitting in silicon quantum dots”. In: *npj Quantum Information* 4.1 (June 2018). issn: 2056-6387. doi: 10.1038/s41534-018-0075-1. url: http://dx.doi.org/10.1038/s41534-018-0075-1.

[35] L. A. Tracy *et al.* “Observation of percolation-induced two-dimensional metal-insulator transition in a Si MOSFET”. In: *Phys. Rev. B* 79 (23 June 2009), p. 235307. doi: 10.1103/PhysRevB.79.235307. url: https://link.aps.org/doi/10.1103/PhysRevB.79.235307.

[36] Y. Choi and R. Joynt. “Interacting random-field dipole defect model for heating in semiconductor-based qubit devices”. In: *Phys. Rev. Res.* 6 (1 Feb. 2024), p. 013168. doi: 10.1103/PhysRevResearch.6.013168. url: https://link.aps.org/doi/10.1103/PhysRevResearch.6.013168.

[37] T. Tanttu *et al.* “Controlling Spin-Orbit Interactions in Silicon Quantum Dots Using Magnetic Field Direction”. In: *Phys. Rev. X* 9 (2 May 2019), p. 021028. doi: 10.1103/PhysRevX.9.021028. url: https://link.aps.org/doi/10.1103/PhysRevX.9.021028.

[38] Y.-Y. Liu *et al.* “Radio-Frequency Reflectometry in Silicon-Based Quantum Dots”. In: *Physical Review Applied* 16.1 (July 2021). issn: 2331-7019. doi: 10.1103/physrevapplied.16.014057. url: http://dx.doi.org/10.1103/PhysRevApplied.16.014057.

[39] E. Paladino *et al.* “1/*f* noise: Implications for solid-state quantum information”. In: *Reviews of Modern Physics* 86.2 (Apr. 2014), pp. 361–418. doi: 10.1103/revmodphys.86.361. url: https://doi.org/10.1103%5C%2Frevmodphys.86.361.

[40] P. Dutta and P. M. Horn. “Low-frequency fluctuations in solids: $\frac{1}{f}$ noise”. In: *Rev. Mod. Phys.* 53 (3 July 1981), pp. 497–516. doi: 10.1103/RevModPhys.53.497. url: https://link.aps.org/doi/10.1103/RevModPhys.53.497.

[41] W. A. Phillips. “Two-level states in glasses”. In: *Reports on Progress in Physics* 50.12 (Dec. 1987), p. 1657. doi: 10.1088/0034-4885/50/12/003. url: https://dx.doi.org/10.1088/0034-4885/50/12/003.

[42] F. Beaudoin and W. A. Coish. “Microscopic models for charge-noise-induced dephasing of solid-state qubits”. In: *Phys. Rev. B* 91 (16 Apr. 2015), p. 165432. doi: 10.1103/PhysRevB.91.165432. url: https://link.aps.org/doi/10.1103/PhysRevB.91.165432.

[43] W. A. Phillips. *Amorphous Solids*. Springer Berlin, Heidelberg, 1981.

4

BASEBAND CONTROL OF SINGLE-ELECTRON SILICON SPIN QUBITS IN TWO-DIMENSIONS

It is widely accepted that in order to make a useful quantum processor, it must have sufficient connectivity. Prior to this study, all silicon-based spin qubit devices had been one-dimensional. One of the key motivations for this is that Hamiltonian engineering with micromagnets had only been established to work in 1D. In the background, researchers with hole spins in germanium were finding exciting new ways to control spins in two-dimensions with only baseband control signals. This all begged 2 important questions. First, can we scale Hamiltonian engineering in silicon? Second, can we avoid some of the problems with established EDSR, like the heating effect discussed in Chapter 3, by working at baseband frequencies? In a serendipitous way, the work on a 2x2 silicon quantum dot device presented in this chapter addresses both of these questions with a confident "yes". Armed with a bigger toolbox to engineer single-spin control, we also propose a new way to think about designing two-dimensional spin qubit arrays.

Parts of this chapter have been published in Nat Commun **16**, 5605 (2025) [1].

4.1. INTRODUCTION

Industrial fabrication compatibility is a flagship argument for semiconductor spin qubits in gate-defined quantum dots as a candidate for large-scale quantum computation and simulation [2–6], but this promise can only be fully realized if the spin physics utilized to control qubits is also extensible. Currently, on-chip micromagnets have enabled state-of-the-art devices to exhibit powerful primitives including high-fidelity universal gate sets [7–9], high-fidelity initialization and readout of multiple qubits [10, 11], and coherent spin shuttling [12, 13].

The micromagnet typically serves two purposes. It produces a longitudinal gradient parallel to the quantization axes to give each spin a unique frequency and a transversal gradient that allows microwave electric fields to drive single-qubit gates via electric-dipole spin resonance (EDSR) [14–16]. While this method of operation has been extended to 12 qubits [17], the linear charge-noise sweet spot of present magnet designs has motivated scaling in only one dimension. The limited connectivity and stringent fault tolerance thresholds of linear arrays imply that entering the second dimension is all but essential [18]. Although proposals exist for scaling EDSR control into two-dimensional arrays using on-chip magnets [19, 20], an experimental demonstration beyond 1D has, until now, been lacking.

Even in 1D arrays the dissipation of microwaves used for EDSR control is known to produce heating effects that complicate multi-qubit operation [21–24]. Typically, this manifests as qubit frequency shifts that are contextual upon the magnitude and duration of preceding microwave bursts. Circumventing this issue by working at warmer device temperatures is possible, but microwaves may be bypassed altogether. Whereas singlet-triplet and exchange-only encoded qubits allow for universal baseband control, aspects like state leakage and gate complexity have limited error rates to higher levels than for the single-spin encoding. Recently, single-hole spins in a 2D germanium array have been manipulated with high fidelity using baseband hopping control exploiting large differences in the quantization axis arising from dot-to-dot variations in the g-tensor [25, 26]. It is therefore intriguing whether such control can be engineered with on-chip magnets and, if so, what implications this poses for future architectures.

Here, we commission a 2x2 silicon quantum dot device for qubit control in two distinct regimes. First, we demonstrate that conventional micromagnet-based EDSR control of all four spins is possible in the 2D array, and we also demonstrate nearest-neighbor exchange control. We benchmark the performance of the four-qubit system with a particular emphasis on the crosstalk caused by off-resonant driving. Next, we lower the external magnetic field of the half-filled array to demonstrate qubit operation via hopping gates, whereby the tip in quantization axis is

induced by the engineered magnetic stray field. We further analyze the qubit coherence, fidelity, and crosstalk properties of the hopping gate. Finally, we propose how a repeated nanomagnet pattern can be used to engineer hopping control across an arbitrarily large 2D array, thereby illustrating how baseband control of single-electron spins in silicon may be a compelling control method for future devices.

4.2. A 2x2 SILICON QUANTUM PROCESSOR BASED ON EDSR

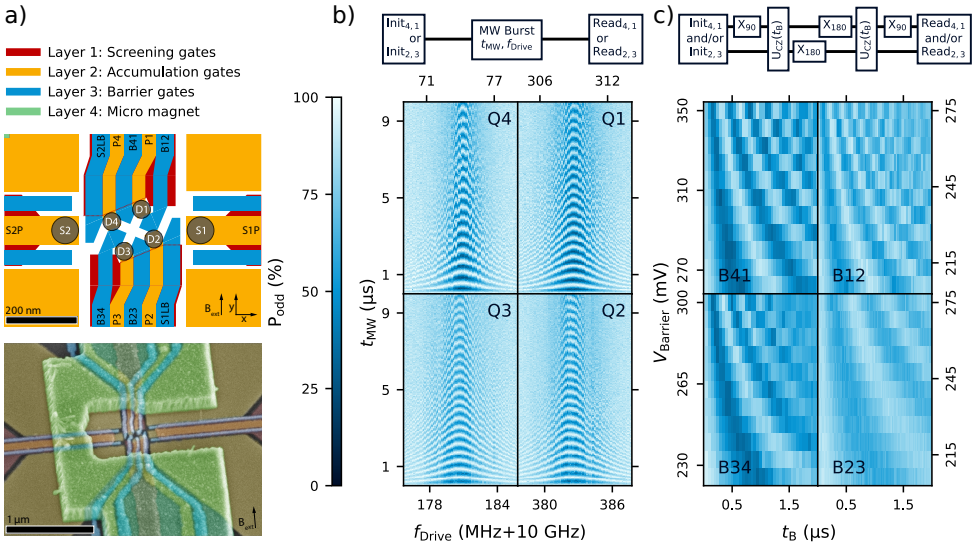


Figure 4.1: **A 2x2 Silicon Spin Qubit Array** a) Design schematic and false coloured SEM image of a device nominally identical to the one measured. In the schematic, single-electron transistor (SET) sensor positions are marked with S1 and S2, and the quantum dots are labeled clockwise with D1 through D4. We refer to each qubit as Q1 through Q4 according to the dot it primarily inhabits. The SEM image includes the micromagnet on top of the gate stack (not shown in the schematic). b) Odd parity probability after driving the qubit with a microwave burst as indicated by the block diagram. The respective chevron patterns of all qubits are arranged according to their physical position. The drive power and modulation amplitude were adjusted per qubit to achieve a Rabi frequency around 2 MHz. c) Decoupled controlled phase oscillations of adjacent qubit pairs using the pulse sequence indicated in the block diagram. The Ising-like interaction U_{CZ} is controlled by the voltage $V_{Barrier}$ on the barrier gate located between the respective plunger gates. We chose a static operating point such that the extrapolated exchange strength $J_{off} < 20$ kHz and apply a pulse on the barriers large enough such that $J_{on} > 1$ MHz. The large amplitudes for these barrier pulses as well as the particular fanout of gates B34, P3, and B23 often caused substantial degradation of the readout signal (see Section 4.6).

The most straightforward progression from a one-dimensional silicon spin-qubit array to a two-dimensional array is the adoption of existing

control strategies with only minor accommodations [10]. A 2x2 quantum dot array as shown in Fig. 4.1a) was fabricated on a ^{28}Si/SiGe heterostructure (residual nuclear spins of 800 ppm) and is used to accumulate four single electrons under each plunger gate as has been previously demonstrated [27]. After magnetizing the micromagnet at a field of 2 T along the positive y-axis as indicated in the SEM and schematic of Fig. 4.1a), the external field is reduced to 200 mT. We use Pauli-spin blockade (PSB) for initialization and measurement on the horizontal pairs (Q_1Q_4 and Q_2Q_3) along with electric-dipole spin resonance (EDSR) to perform addressable single-qubit rotations. The 22.5° rotation of the 2x2 array combined with the longitudinal field gradient gives good spectral separation of the spins with a minimum frequency difference of 74 MHz. Using adequate parameters we find reasonable agreement with micromagnet simulations (see Fig. 4.6 for details). The Rabi frequency of all four spins was tuned to 2 MHz to stay within the linear amplitude scaling regime (see Fig. 4.13) to observe the Chevron patterns in Fig. 4.1 b).

Despite the qubits not lying along the decoherence sweet axis of the micromagnet, we observe coherence metrics similar to [10]. The measured Ramsey decay times are $T_2^* = \{3.31(9),\ 2.03(2),\ 3.57(8),\ 2.90(5)\}$ µs for qubits Q_1 through Q_4 respectively with integration times of around 30 min. Similarly, we measured Hahn-echo decay times of $T_2^{\mathrm{H}} = \{30.21(24),\ 16.22(18),\ 40.38(21),\ 21.77(38)\}$ µs. Notably, the trend of coherence times is not strictly correlated to the designed decoherence gradients at each dot location (see Fig. 4.6). There are three possible reasons for such discrepancies. First, the decoherence gradient is not isotropic in the plane of the quantum well, and the observed coherence times will depend on the microscopic orientation of the local charge noise fluctuators for each qubit. Second, large variations in coherence may occur for sufficiently sparse charge noise baths depending on the nature of the constituent fluctuators [28]. Third, hyperfine noise due to residual nuclear spins in the heterostructure may also contribute to decoherence that does not couple to the spins via the micromagnet gradient [29].

Two-qubit interactions are controlled using the barrier gates located between neighboring plunger gate pairs to modulate the Ising-like exchange interaction. We observe the characteristic CPhase oscillations for all four nearest-neighbor pairs of qubits as a function of time and barrier pulse height as depicted in Fig. 4.1 c). Although we operate at the symmetry point to minimize the sensitivity to charge noise, the quality factor $T_2^{\mathrm{DCZ}}/t_{\mathrm{CZ}}$ of the oscillations for all pairs is limited to $Q_{2Q} = \{17(2),\ 7.5(7),\ 7.1(4),\ 12.2(7)\}$ for B12, B23, B34, and B41 respectively, which bounds the achievable two-qubit gate fidelities to modest values. Fig. 4.12 shows state tomography results before and after applying a calibrated CZ gate for qubit pairs Q_4Q_1 and Q_2Q_3, highlighting the universal capability

of this processor.

One reason for the suboptimal two-qubit performance may be the magnitude of pulses, ranging from 275 mV to 350 mV, required to achieve a satisfactory on/off exchange ratio as a result of the small barrier lever arms. Such large pulses jeopardize device stability and, in some cases, degrade readout visibility (see Fig. 4.11). Although we apply large pulse amplitudes, the maximum achievable exchange couplings of 1 MHz–4 MHz are small with respect to the dephasing times of the qubits.

Despite this shortcoming, we can still draw valuable insights about multi-qubit control with such an EDSR-based architecture. The quality factors $T_2^{\mathrm{Rabi}}/t_{180}$ of the four qubits are measured to be $Q_{1Q} = \{64(4), 67(6), 65(5), 64(7)\}$, and we estimate the resonant X_{90} fidelity averaged across all four qubits to be 99.54(4)% using randomized benchmarking (RB) as displayed in Fig. 4.2a). By comparing the infidelity expected from both quasi-static qubit frequency fluctuations (T_2^*) and decoherence of the spins subject to driving (T_2^{Rabi}), we conclude that it is the latter that predominantly limits the resonant single-qubit gate fidelity we observe from randomized benchmarking (see Sec 4.7.4 for details). It is possible that higher fidelities could be achieved by taking advantage of the higher possible Rabi frequencies on some of the qubits (see Fig. 4.13).

Having established a good single-qubit gate set for each qubit, we can probe the crosstalk such gates impart on neighboring qubits. Controlling crosstalk is critical for multi-qubit operation, and while the absolute amount of crosstalk is relevant for calibration, its contextuality in time and number of gates is particularly indicative of how difficult this calibration becomes in practice. For EDSR, crosstalk commonly manifests as a spurious pulse-induced resonance shift (PIRS). We probe this “heating effect” on idling qubits using a modified Hahn echo sequence as depicted in Fig. 4.2b) [22]. The sequence includes an off-resonant microwave burst that simulates the drive of another qubit, and we quantify the magnitude of this burst in relation to the average power required to perform single-qubit rotations across all four qubits in this device.

A nontrivial transient phase pickup is observed for all qubits for off-resonant bursts that are energetically comparable to those used for single-qubit gates. A particular instance is shown in Fig. 4.2c), though all qubits exhibit the same qualitative behavior (see Fig. 4.14). With increasing delay time and amplitude, more phase is picked up until an apparent saturation is reached. This transient response has been documented in previous studies [22]. However, when the off-resonant burst occurs closer in time to the resonant echo pulse, less phase is picked up. The most likely origin of this counterintuitive behavior is the transient heating caused by the resonant echo pulse: the heating induced by the decoupling pulse reduces the transient effect of the off-resonant burst. The nonlinear combination of the two transients has severe

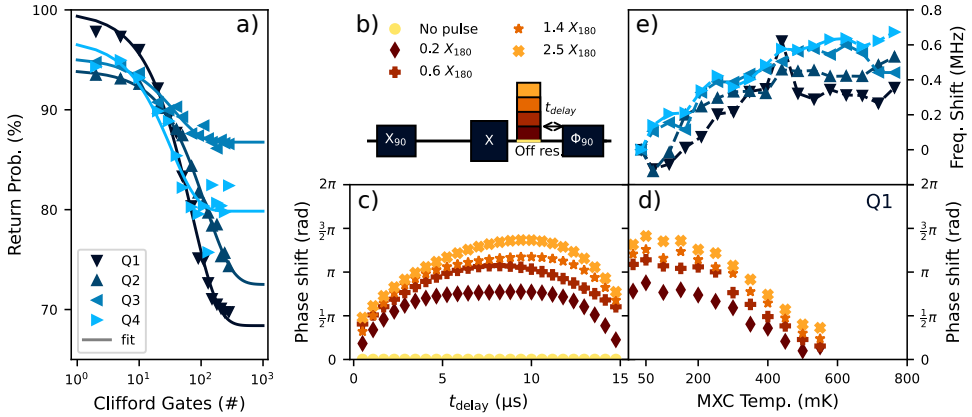


Figure 4.2: **EDSR Operation and PIRS Effects** a) Return probability as a function of the number of applied Clifford gates averaged over twenty different gate sequences for all four qubits. As each qubit readout has a different visibility, the curves decay to different values. The fitted Clifford gate fidelities are $F^{\text{res}}_{\text{Clif}} = \{99.28(5)\,\%,\ 99.58(4)\,\%,\ 98.7(2)\,\%,\ 98.5(3)\,\%\}$ for Q_1 through Q_4 respectively. The Clifford gate set is compiled using only $X_{\pm 90}$ and $Y_{\pm 90}$ primitive gates (see Sec 4.6), and the corresponding average physical gate fidelities are, respectively, $F^{\text{res}}_{\text{avg}} = \{99.67(2)\,\%,\ 99.80(2)\,\%,\ 99.39(8)\,\%,\ 99.31(15)\,\%\}$. b) Adapted Hahn Echo sequence to measure crosstalk effects as introduced in [22]. The off-resonant burst simulates the drive of a different qubit. By substituting the last X_{90} with a $\Phi_{90} = X_{90}Z(\Phi)$ operation in the echo sequence and sweeping the phase Φ, the relative phase pickup due to the off-resonant burst can be inferred. The transient behaviour is detected by varying the temporal position t_{delay} of the off-resonant burst with respect to Φ_{90}. c) Example of phase pickup as a function of t_{delay} for Q_1 at 100 mK for different amplitudes of the off-resonant burst (see panel b) for legend). We use a standard Hahn-echo sequence (yellow data points) as a reference to remove constant artifacts introduced by the echo pulse sequence. d) The maximum phase shift extracted from measurements as in panel c) as a function of mixing chamber temperature for qubit Q_1 for four different off-resonance bursts (see panel b) for legend). All qubits exhibit similar behaviour (see Fig. 4.14). e) Temperature dependence of the bare qubit frequencies as measured by a Ramsey experiment relative to the frequency at base temperature. Symbols refer to different qubits as in panel a)

consequences for crosstalk calibration, as the required compensation will be sensitive to both pulse scheduling and amplitude.

It has previously been observed that PIRS is dependent on the temperature of the device [23]. To verify this, we repeat the above experiment on all qubits for different mixing chamber temperatures. From the fitted data (e.g. Fig. 4.2c)) we extract and compare the maximum phase pickup as a function of temperature. Fig. 4.2d) shows how increasing the mixing chamber temperature reduces the magnitude of the PIRS effect for Q1 (see Fig. 4.14 for Q2-Q4). This substantial temperature increase, however, also has an impact on qubit coherence. Although the

T_2^* of all qubits is relatively unaffected by temperature, the T_2^H generally decreases monotonically as the mixing chamber temperature is raised (see Fig. 4.16). Additionally, an increase in spin Larmor frequency as a function of temperature is observed for all quantum dots as seen in Fig. 4.2e).

While these results are qualitatively in agreement with a previous study of a six-spin array [23], there are three notable differences. First, the generally monotonic increase in frequency of all four qubits studied here contrasts with the previous measurement of a non-monotonic trend across the six-qubit array. Second, the heating effect is more moderate than the 1 MHz frequency shifts observed by Undseth et al. when using similar microwave bursts [23]. In this work, PIRS was observed through residual phase pick-up corresponding to a frequency shift on the order of 10-100 kHz. Last, the measured PIRS phase pickup is consistent with a negative Larmor frequency shift opposite to the frequency shift seen when raising the device temperature. This suggests that although the device temperature clearly plays a meaningful role in how PIRS manifests, the dissipated heat of the microwave burst may not be the only PIRS mechanism in this device. It has been proposed that thermally-sensitive environmental fluctuators can significantly contribute to the temperature dependence of the qubit frequencies [30]. Our observations underscore the difficulty of predicting and compensating multi-qubit crosstalk with resonant control.

4.3. BASEBAND OPERATION

In light of the crosstalk challenges arising from microwave control, the operation of spin qubits using exclusively baseband pulses makes for a compelling alternative while retaining the Loss-DiVincenzo qubit encoding. Such control was recently demonstrated by hopping a hole spin qubit between germanium quantum dots with different quantization axes [26] and bears resemblance to the strong-driving flopping mode regime proposed by [31]. Similarly, the 2x2 silicon array allows us to take advantage of quantization axis variation originating from the inhomogeneous magnetic field introduced by the micromagnet. However, even in the 2x2 array a large external field forces the spins' quantization axes to be nearly colinear. In order to accentuate the inhomogeneous magnetic field and limit Larmor frequencies for baseband control, the external field is reduced.

First, the micromagnet is magnetized in a 0.8 T external field. We populate the array with a single electron in dots 1 and 4, allowing us to keep PSB readout on the pair Q_4Q_1 while dots 2 and 3 remain empty. We track the qubit frequencies of Q_1 and Q_4 using adiabatic inversion pulses as the external field is reduced step-by-step as shown in Fig. 4.3a).

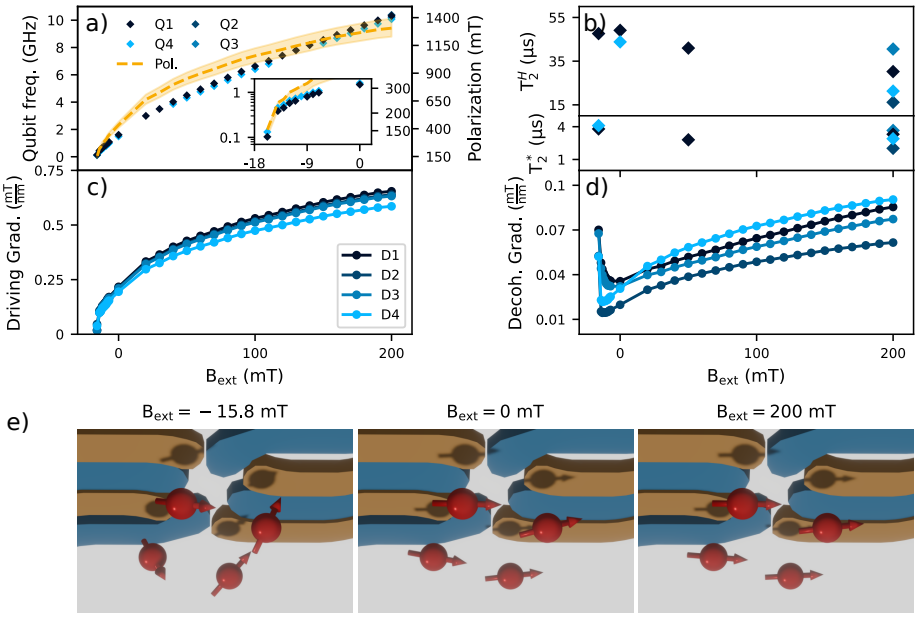


Figure 4.3: **Magnetic Field Dependence of Device and Qubit Properties** a) Dependence of the qubit frequencies on the external magnetic field. Adiabatic inversion pulses are used for external fields above $B_{\text{ext}} = -15\,\text{mT}$ (qubit frequencies above 400 MHz) while Ramsey experiments with hopping control are used for lower fields. The dashed line shows the predicted homogeneous polarization of the micromagnet as extracted by fitting the measured qubit frequencies to a simplified micromagnet model (see Sec 4.7.1). The shaded area provides a generous estimate of uncertainty by displacing the micromagnet model $\pm 15\,\text{nm}$ out-of-plane and repeating the fits. The inset zooms in onto the behavior below $B_{\text{ext}} = 0\,\text{mT}$ with the qubit frequencies and polarization plotted on a logarithmic scale. b) (lower) T_2^* integrated for 30 minutes at various external field settings. Ramsey decay times are relatively unchanged by the magnitude of the external field and, consequently, the decoherence gradient. Symbols as in panel a). b) (upper) T_2^{H} integrated for 30 minutes at various external field settings showing an inverse relation to external field and decoherence gradient. (Continued on next page)

Figure 4.3: (Continued) From the extracted micromagnet polarization in panel a) we extract c) the driving gradient along the y-axis and d) the decoherence gradient magnitude at the center of the plunger gates. The driving gradient decreases monotonically while the decoherence gradient shows a sweet spot close to $B_{\text{ext}} = 0\,\text{mT}$. e) Renders of the plunger and barrier gates (yellow, blue) from below with the four electron spins (red, from left-to-right: Q3, Q2, Q4, Q1) for three different external field settings. The arrows indicate the quantization axes at the dot location which, approximating an isotropic g-factor of 2 in the silicon quantum well, is effectively assumed to be colinear with the total magnetic field vector. At $B_{\text{ext}} = 200\,\text{mT}$ the quantization axes are almost perfectly aligned with each other within a few degrees. At $B_{\text{ext}} = 0\,\text{mT}$, some deviation becomes evident. At $B_{\text{ext}} = -15.8\,\text{mT}$ the differences in quantization axes are very pronounced. Based on the micromagnet simulation, the tips are estimated to be between about 30° and 60° depending on the exact locations of the quantum dot in the micromagnet stray field.

We observe the qubit frequencies dropping both as a result of the lower external field as well as the demagnetization of the micromagnet. The polarization of the micromagnet is inferred by fitting the measured frequencies to a simplified magnet model where the magnetization is assumed to be homogeneous with no crystalline domains or shape anisotropy coming into consideration (see Sec 4.7.1). Even so, this model provides a firm basis for understanding the qualitative qubit properties across a wide range of external field settings.

Even at zero external field, the remanence of the micromagnet forces the quantization axes to be reasonably colinear and provides a driving gradient large enough for conventional EDSR operation. Notably, the Hahn-echo coherence times of Q_1 and Q_4 nearly double from 30.2 µs and 21.3 µs to 49.1 µs and 43.8 µs respectively as shown in Fig. 4.3b). Curiously, the T_2^* coherence times do not change significantly with the magnetic field and decoherence gradient. This suggests the limiting low-frequency noise may be different than the noise inducing Hahn-echo decay. The amplitude with which these spins are driven with $f_{\text{Rabi}} \approx 2\,\text{MHz}$ also increases by about a factor of 3. These observations are compatible with the estimated change in decoherence and driving gradients at the dot locations: Fig. 4.3c) shows that the decoherence gradient permitting charge noise to couple to the spins has approximately halved while Fig. 4.3d) shows the driving gradient has been reduced by a factor of 3. As predicted by simulations, the 100 MHz frequency separation between Q_1 and Q_4 is retained and becomes the main contribution to the decoherence gradient. This suggests that EDSR operation in the absence of an external solenoid, a mundane but material obstacle for the near-term scalability of semiconductor spin qubits, is a realistic possibility.

Decreasing the external field further, we reach a regime where the local magnetic field in the dot region is increasingly inhomogeneous owing to the competition between the remaining micromagnet polarization and

the opposed external field. The spin quantization axes at the quantum dots will no longer align but instead point in different directions. This is most clearly illustrated by rendering the quantization axes at each dot location as shown in Fig. 4.3e). Despite the extreme inhomogeneity and low effective polarization of the micromagnet, we observe no pronounced instability of the spin frequencies. On the contrary, the measured Ramsey and Hahn-echo decay times universally improve upon the coherence measured at $B_{\text{ext}} = 200\,\text{mT}$ with EDSR control (Fig. 4.3b)). However, at a nominal external field setting of $B_{\text{ext}} = -15.8\,\text{mT}$ the driving gradient is too small for resonant control. Fortunately, the large quantization axis tips enable coherent control by hopping the electrons from dots D_1 and D_4 to the vacant dots D_2 and D_3. Furthermore, the Q_1 and Q_4 Larmor frequencies of 131 MHz and 103 MHz respectively are practical for AWG control.

Fig. 4.4a) illustrates the pulse sequence required for a hopping gate between dots D_1 and D_2. During each ramp, the charge transfer between dots should be adiabatic (see Fig. 4.4b)), hence a sufficiently large tunnel coupling t_c should be maintained between dots. A fast detuning ramp $\nu = \epsilon/t_{\text{ramp}}$ is desirable to minimize dephasing while the spin is most strongly hybridized with the charge at $\epsilon = 0\,\mu\text{eV}$. Within the subspace of the adiabatic charge transition, the spin state transfer should be diabatic (see Fig. 4.4c)) which is ensured by traversing the Hamiltonian "step" sufficiently fast. Provided these conditions are met (see Sec. 4.7.5), a universal gate set may be calibrated with the appropriate choice of parameters t_1, t_2, and t_{add} [26]. One repetition of two cycles as drawn is sufficient to calibrate an X_{90} provided the quantization axis tip between dots lies between 22.5° and 157.5°. For quantization axis tips between 45° and 135°, one repetition of a single cycle suffices. The additional idling time parameter t_{add} between subsequent repetitions ensures the axis of rotation is consistent when concatenating multiple X_{90} gates.

To quantify the quantization axis tip experimentally, we apply multiple repetitions of spin hopping for varying times t_1 and t_2 and measure the resulting spin fraction. For the presented data the ramp time between t_1 and t_2 was set to be 2 ns. This is comparable to the minimum rise time of the AWG output signal and was chosen to minimize decoherence during the shuttling process. The tunnel coupling was estimated to be roughly 48 µeV for all hopping gate experiments unless otherwise noted (see Fig. 4.17). The measured pattern sensitively depends on the tip angle and may be fit numerically to the expected unitary evolution of the spin (see Sec. 4.6). An example of a 2-cycle-4-repetition-protocol measurement and fit is shown in Fig 4.4d) and yields a tip angle of $\theta_{1,2} = 37.3(2)°$. Similarly, we measure $\theta_{4,3} = 47.5(2)°$ (see Fig. 4.8). In the latter case, we observe that pulsing on P3 causes severe degradation to the readout signal (as was also the case for probing two-qubit interactions in Fig 4.1).

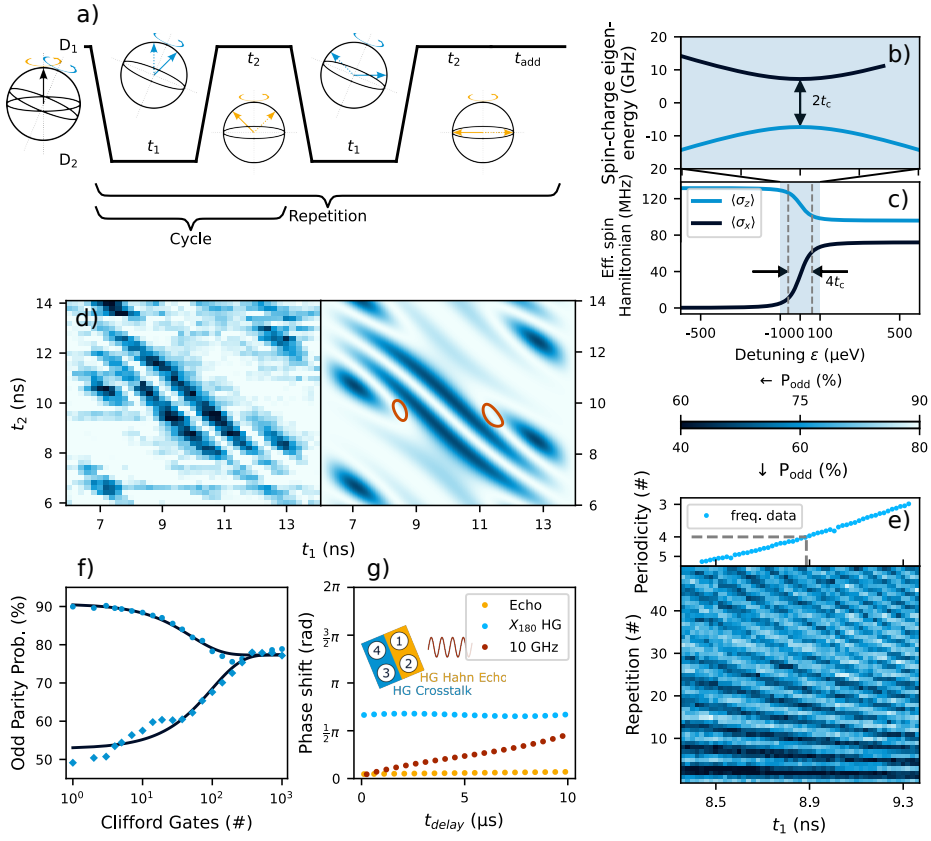


Figure 4.4: **Implementation and Characterization of a Hopping Gate** a) Hopping sequence and sketched evolution of the spin state vector. The dashed (solid) arrow indicates the initial (final) vector at each step while yellow (blue) correspond to the original (secondary) quantum dot. The sequence results in a 90 degree rotation around the x-axis in D_1. b) Spin-charge energy level diagram for the $D_{1,2}$ double-dot system illustrating the charge avoided-crossing. c) Components of the effective spin qubit Hamiltonian H' with respect to the quantization axis of D_1 in the subspace of the charge ground state given by $\langle\sigma_i\rangle = \mathrm{Tr}(\sigma_i H')$ for the $D_{1,2}$ double-dot system (see Sec 4.7.5). (Continued on next page)

Figure 4.4: (Continued) d) Experimental (left) and fitted (right) odd-parity probability using two cycles and four repetitions [refer to (a)] while sweeping t_1 and t_2 for the $D_{1,2}$ system with t_{add} fixed to 3.6 ns. The quantization axis tip is fit to 37.3(2)° (see Sec 4.6 for details). The red regions highlight the t_1 and t_2 where each one of the four repetitions achieves a high fidelity X_{90} gate. The tunnel coupling for this measurement was estimated to be roughly 18 µeV. Additional data, fits and fidelity contours for qubits Q_1 and Q_4 are shown in Fig. 4.8. e) Fine calibration of t_1 by repeating the roughly calibrated gate many times with minor adjustments to one of the timing parameters. We extract the periodicity of the pattern and select the t_1 that matches a periodicity of four for the benchmarked gate. The difference in t_1 with respect to the data in c) is due to adjustments in t_{add}. f) Randomized benchmarking using both initial basis states. The Clifford set is compiled using only X_{90} hopping gates and physical Z-rotations (see Sec. 4.6). The fitted Clifford gate fidelities are $F_{Clif}^{hop,odd} = 99.01(11)\%$ and $F_{Clif}^{hop,even} = 99.49(7)\%$ for the odd and even parity inputs respectively (see Sec. 4.6). g) PIRS-like measurements showing the phase accumulation after a hopping gate and a 10 GHz burst when included in adn echo sequence as depicted in Fig. 4.2b). The hopping gate is implemented as an X_{180} gate on Q_4. The microwave burst carries the same energy as an average X_{90} gate in this device during EDSR operation. Raw data is shown in Fig. 4.15.

We therefore opt to only benchmark the Q_1 hopping gate.

To coarsely calibrate the t_1, t_2 and t_{add} idling times for a high-fidelity single-qubit gate, we select parameters where the X_{90} fidelity is theoretically maximized as shown in Fig. 4.4d). We then fine tune the parameters by running a sequence of X_{90} gates and select the precession times that produce a periodicity of 4 as exemplified for t_1 in Fig. 4.4e). Consequently, we observe discretized Rabi oscillations of around 5 MHz. By padding idling times with 2π rotations, we intentionally do not operate the gates as fast as is theoretically possible in order to minimize artifacts that occur at the limit of the AWG time resolution. Z-rotations are implemented with a physical wait time calibrated by a Ramsey measurement of the spin Larmor frequency. Constructing a Clifford gate set comprised of X_{90} hopping gates and physical Z-rotations, single-qubit randomized benchmarking of Q_1 yields an average Clifford gate fidelity of about $F_{Clif,odd}^{hop} = 99.01(11)\%$ and $F_{Clif,even}^{hop} = 99.49(7)\%$ as shown in Fig. 4.4f). By attributing all errors to the X_{90} hopping gate we can provide a lower bound on its fidelity $F_{X_{90}}^{hop} = 99.50(6)\%$ (see Sec. 4.6). This is directly comparable to the physical resonant gate fidelities achieved with EDSR control at high field. Using blind randomized benchmarking, we estimate that the hopping gate fidelity is bounded by the tunnel coupling tunability in this device leading to non-adiabatic charge shuttling and state leakage (see Sec. 4.7.5 and 4.7.6 for further discussion) [32]. When applied to the data of Figure 4.4f), we obtain a leakage rate of 0.13(5) % and a corresponding Clifford gate fidelity of 99.26(5) %.

We may also compare the performance of the EDSR and hopping

mechanisms with regards to crosstalk (Fig. 4.4g)). We employ the same PIRS methodology as in Fig. 4.2 and perform a Hahn echo sequence on qubit Q_1 using hopping gates. As Q_4 is used for parity readout, we calibrate an X_{180} hopping gate on this qubit and embed it within the echo sequence (in place of the off-resonant burst) to measure the resulting phase pickup from the physical shuttling. In contrast to the EDSR-based gates, the hopping mechanism imparts a constant phase pick-up regardless of its temporal position in the echo sequence. We attribute this shift to the change in electrostatic conditions caused by both the gate voltage pulses and movement of the Q_4 electron in the quantum well which shifts the position of Q_1 in the magnetic field gradient. The qubit pair is maintained with very little residual exchange, hence negligible conditional phase is acquired during the sequence.

We also introduce a 10 GHz burst commensurate with an X_{90} gate in the standard EDSR regime. We observe a transient phase pickup analogous to the experiments executed at high-field. Notably, the nonlinear "masking" due to the resonant echo pulse is not observed here as the decoupling is performed with a hopping gate. The total transient phase pickup due to PIRS is reduced compared to Fig. 4.2. This is likely a consequence of the low magnetic field environment, as either a g-factor change or electron displacement in the gradient will result in a smaller shift in qubit Larmor frequency. In any case, the shuttling gate avoids the transient effect of the microwave burst, and the magnitude of the effect would decrease as the distance between local operations is increased, making a low-field shuttling implementation of single-qubit gates an appealing approach to reduce crosstalk and improve multi-qubit control.

4.4. ARCHITECTURE PROPOSAL

The design of on-chip magnets for EDSR control of extensible 2D spin arrays presents a design challenge: engineering controllability and spectral addressability with a small pitch requires nanoscale magnetic variation. With magnets or current-carrying wires that are an order-of-magnitude larger than the quantum dots themselves, this is difficult to achieve. Proposals making use of nanomagnets, with features similar in size to a ≈ 100 nm dot pitch, are a promising solution [19, 20, 33–36].

Inspired by these ideas, nanomagnets may also be used for hopping control. Compared to the microscopic g-tensor variations in germanium quantum dot arrays and similar platforms, local magnetic field variations could be engineered more deterministically. It is therefore worthwhile to revisit the design requirements for on-chip nanomagnets with hopping control in mind. Two specifications stand out compared to EDSR. First, qubit addressability with hopping gates is more localized and does not rely on the spectral separation of qubit frequencies. Second, the

transverse gradient required for EDSR control effectively mandates a total magnetic field magnitude on the order of tens of mT, whereas tips in the quantization axis for hopping control (i.e. inhomogeneity of the magnetic field vector) are possible at more modest magnetic fields as illustrated by this work.

Exploiting these features of hopping control, we propose a periodic nanomagnet design as depicted in Fig. 4.5a). After applying an external magnetic field along the y-axis, the shape anisotropy imposed by the 40 nm × 120 nm × 50 nm iron magnet geometry causes the magnetization to persist even at ambient conditions [33]. The relaxed magnetization, simulated by the OOMMF software package [37] (see Sec. 4.7.2), generates an inhomogeneous magnetic field that enables hopping conditions in a quantum well situated about 100 nm below the magnetic layer. Owing to the inhomogeneous magnetic vector field, a predictable pattern of quantization axis tips (relative to a fixed reference point) of around 90° occurs with a periodicity of 200 nm as shown in Fig. 4.5b). Fig. 4.5c) shows this smoothly-varying tip along two shuttling axes in which hopping gates may be implemented between adjacent sites with a pitch of about 100 nm.

A sparse 2D array of silicon quantum dots may therefore be populated with flexible occupancy to realize different spin connectivity within the magnetic landscape. Fig. 4.5d) (upper) illustrates an instance where many dots may be left vacant to facilitate not only hopping gates but also shuttling to peripheral sensing regions or to implement two-qubit gates between distant spins. Fig. 4.5d) (lower) depicts a denser array where all qubits still have access to single-qubit logic via hopping. As any quantization axis tip between 45° and 135° allows Hadamard gates to be performed with a single shuttling cycle, this architecture is robust to some variation in both the placement/shape of the magnets and formation of the dots. As the nanomagnets can be fabricated over a large area, edge effects are relegated far beyond the extent of any finite quantum dot array. Of course, such a periodic array would also have to grapple with gate patterning and fanout as any other dense 2D array of dots would, but the issue of qubit controllability would not compound the difficulties. Provided such a fanout can accommodate the sparse magnetic layer, the design space for potential architectures becomes very large.

The nanomagnet array presented here confers two additional benefits beyond enabling hopping control that can also be leveraged in other potential designs. First, the qubit frequencies are distributed in a range below 400 MHz without any applied external field. This removes the need for a solenoid in the cryogenic setup provided the magnets can be polarized at room temperature. Second, a periodic pattern of decoherence sweet spots also emerges to form a natural template upon which to place idling spins as seen in Fig. 4.5e). The proposed shuttling

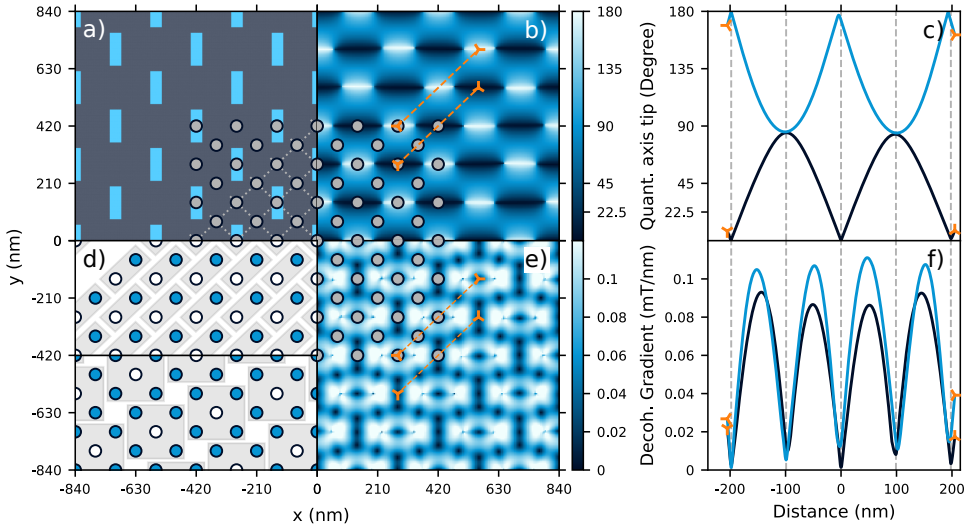


Figure 4.5: **Nanomagnet Based Tileable Architecture Utilizing Hopping Gates** a) Zoomed in section of the proposed nanomagnet pattern with the magnetic material shown in bright blue. Each iron nanomagnet is 40 nm × 120 nm in area and 50 nm in out-of-plane height. In the lower right corner we show the envisioned quantum dot positions and their connectivity. These patterns extend across the contiguous panels a), b), d), e) and pertain to the data contained within them. b) The relative change in quantization axis, assuming an isotropic *g*-factor, with respect to the central dot of the panel. The quantum well is located 100 nm below the bottom surface of the nanomagnet layer. The magnetic field is computed at zero external magnetic field after having allowed the nanomagnet magnetization to relax according to their shape anisotropy and material properties. c) Line cuts corresponding to the orange markings in panel b) illustrating the relative change in quantization axis tips along two potential hopping axes. The observed asymmetries are a consequence of the finite mesh size used for simulation and interpolation artifacts. The grey dashed lines indicate the quantum dot positions. d) Versatile filling of the quantum dot array: the bright blue filled dots indicate a quantum dot with an electron, the white markers indicate an empty quantum dot. The upper section shows a 50% filling, the lower section a denser filling with 80% occupancy. The gray shaded areas indicate the repeated unit cell. e) The calculated decoherence gradient resulting from the nanomagnet stray field as described in b). f) Line cuts corresponding to the orange markings in panel e) illustrating the decoherence gradient along two potential hopping axes. Minor artifacts from the finite mesh size and field interpolation are visible. Additional data is shown in Fig. 4.7.

channels plotted in Fig. 4.5f) show that even the maximum decoherence gradient encountered in the quantum well is not substantially larger than typical EDSR addressability gradients that range from 0.05 mT/nm to 0.1 mT/nm. We note that different combinations of ferromagnetic materials and nanomagnet geometries may be used to achieve similar outcomes.

The hopping approach is not without drawbacks. High fidelity hopping control requires voltage pulses with very precise timing on the order of tens of picoseconds and mandates working with physical phase gates as opposed to virtualized phase tracking in a rotating frame. In the case of silicon, the microscopic valley degree of freedom may interfere with charge shuttling in cases where the valley phase difference between dots modifies the effective tunnel coupling[31, 38–40]. Also, the nanomagnets compete for space with the fanout of the gate electrodes that define the dots. Beyond engineering for single-qubit control, considering Zeeman energy differences for high-fidelity two-qubit gates [41] and Pauli spin blockade readout [11] would be necessary to demonstrate a viable architecture. Engineering locations with zero magnetic field could also be useful for parking spins to alleviate the task of phase-tracking while idling qubits. Although we do not anticipate anything inhibiting these features with nanomagnet designs, we leave their details for future studies.

4.5. CONCLUSION

We have used a 2x2 ^{28}Si/SiGe quantum dot device to explore two ways in which future 2D arrays of single-electron spins in silicon may be controlled. Using microwave driving and barrier gate voltage pulses, we demonstrated universal control over a four-qubit system using conventional strategies from 1D arrays with only mild alterations. The performance was primarily limited by poor exchange control owing to the weak tunability of nearest-neighbour tunnel couplings. One potential remedy would be to modify the geometry of the barriers and invert the gate layers in fabrication to increase the lever arm controlling exchange. Another possibility would be the inclusion of a central gate to facilitate the decoupling of spins without requiring such large pulse amplitudes. Regardless, this demonstration of a 2D silicon spin array shows that established qubit control methods are sufficient for scaling beyond linear architectures. Longer bilinear arrays and perhaps trilinear devices ought to be compatible with established micromagnet designs. However, we also found that resonant single-qubit control causes crosstalk that complicates multi-qubit operation.

By opposing the polarization of the micromagnet with the external field to create a net vector field that varies over the scale of the array, we implement hopping gates that allow for baseband control of single spin qubits. Our initial characterization indicates several advantages of this operating regime. First, the baseband control pulses do not impart the transient phase crosstalk that was observed with resonant control. This may be attributed to the reduced power dissipation per logical operation which in turn reduces local heating effects [26]. Second, the reduced magnetic field reduces the coupling strength to charge noise thus

increasing the Hahn echo coherence substantially. Whereas the device was not optimized for hopping gate operation, we already demonstrate a hopping gate that is competitive with the EDSR control demonstrated in this device both in terms of speed and fidelity. We believe the same aforementioned improvements in tunnel coupling control would permit better fidelities in future implementations, and the gate speed would effectively double by increasing the tip of the quantization axis between dots to above 45°.

Finally, we explore how engineering on-chip magnets for hopping spins alleviates many of the challenges that impede scaling EDSR control. We put forward an illustrative example of a periodic nanomagnet pattern that creates a deterministic pattern of decoherence sweet spots and nearest-neighbour tip angles for implementing hopping spins in an arbitrarily large 2D array. These conditions can further enhance coherence times, increase the single-qubit gate speed, and do not require a superconducting solenoid to provide an external field. We believe further investigation into nanomagnet designs for hopping spin control would be very fruitful.

4.6. METHODS

4.6.1. DEVICE DESIGN AND FABRICATION

The device layout used in this work are similar to the ones used in our previous work [27]. The heterostructure comprises a $Si_{0.69}Ge_{0.31}$ strained relaxed buffer (SRB), a 7 nm tensile-strained ^{28}Si quantum well (isotopic enrichment 800ppm), and a 30 nm $Si_{0.69}Ge_{0.31}$ barrier passivated by an amorphous Si-rich layer [42]. Substantial noise from the magnet power supply in driven mode prevented a reliable magnetospectroscopic measurement of the valley splittings in this device. The average valley splittings of 240 µeV measured in [42] are representative of what we would expect in this device, though it is possible that local microscopic disorder may yield outliers for particular quantum dots.

On top of the heterostructure we fabricate a multilayer gate stack isolated by a native SiOx layer and a 10 nm thick layer of AlOx deposited using atomic layer deposition (ALD). The first metallic layer (3:17 nm Ti:Pd) connects to the ohmic contacts and defines screening gates. The screening gates define the area that will host the four quantum dots and two SETs and prevent electron accumulation or spurious dot formation in the fan out. Furthermore, the screening gates confining the 2x2 array are designed as coplanar waveguides to effectively deliver microwave signals for EDSR control. The second layer (3:27 nm Ti:Pd) includes all plunger and accumulation gates, while the third layer (3:27 nm Ti:Pd) contains all barrier gates. The top layer of the gate stack (3:200 nm Ti:Co) contains

only the micromagnet. Each layer is electrically isolated from the ones before by 5 nm AlOx grown with ALD.

The SETs are measured using RF reflectometry implemented using the split-gate approach [43]. The size of the accumulation gates was substantially increased compared to [27] to increase the capacitance to the 2D electron gas (2DEG). The split accumulation gate could be depleted to create a high-resistance path from the 2DEG to the ohmic to prevent signal leakage.

The fan out of the barrier and plunger gates is shown in Fig. 4.11. The starred connections indicate the bond pads corresponding to B43, P3 and B23 which have uniquely circuitous traces to adapt to the distribution of fast-lines on the sample PCB. We consistently observe readout degradation on a timescale at least as long as a 10 µs single-shot measurement when applying baseband pulses to these gates. As the cross-capacitance between these traces and adjacent bondpads (many of which connect to unvirtualized gates) is much larger in the fan out than at the scale of the quantum dot array, we suspect their suboptimal routing is correlated with the drop in readout quality and that these problems can be alleviated in future designs.

4.6.2. INITIALIZATION, CONTROL, AND READOUT

A single-shot measurement includes initialization, manipulation and readout. Initialization and readout are performed using Pauli spin blockade and post-selection similar to [10]. While PSB could be achieved in 4 qubit pairs in this device, we focus on pairs (4,1) and (2,3) as they offered superior performance. All shots begin with a round of parity-mode PSB measurement where parallel spin states are blockaded in the (1,1) charge state and antiparallel spin states are permitted to tunnel to the doubly-occupied singlet state S(2,0). A fast diabatic ramp is used to pulse from the readout point to the (1,1) charge state. When the post-selected initial state is S(2,0), the fast ramp yields a mostly-entangled state (see Fig. 4.12) with consistently higher single-qubit visibility than what is obtained with an adiabatic ramp to the (1,1) charge state. Prior to measurement, a wait-time of 1 µs to 5 µs is included to permit both antiparallel spin states to decay to the S(2,0) state. The charge sensor signal is integrated for 1 µs to 20 µs. Some datasets are post-processed to shift the readout threshold to an optimal point.

While a longer integration time improves readout quality somewhat, there appear to be other fundamental limits to the qubit visibilities we can achieve. One factor is the limited tunnel coupling tunability in this particular device upon which the PSB mechanism depends very sensitively. At the high-field operating condition, the spins' quantization axes are estimated to be aligned within a few degrees. However, at

low-field operation the expected tip between quantization axes in the PSB pair is estimated to be about 20 degrees. This causes an opening of the S(2,0)-$|\downarrow\downarrow\rangle$ avoided crossing which may impede a linear adiabatic ramp from the S(2,0) state to the $|\downarrow\uparrow\rangle$ for high-fidelity initialization. Pulse-shaping and active feedback may be used to mitigate this, but these were not investigated in this work. Alternatively, an adiabatic ramp through a sizeable S(2,0)-$|\downarrow\downarrow\rangle$ avoided crossing may permit initialization directly into the $|\downarrow\downarrow\rangle$ state as is often done with hole spin qubits. In the future, spin qubit designs could make use of separate zones for readout and control, which are individually optimized by local nanomagnets, for example.

Qubit manipulation includes resonant drive and diabatic spin shuttling for single-qubit gates. The Hamiltonian for the single-qubit gates are discussed in Sec. 2.3.1 and 2.4.2 respectively. All microwave pulses are padded with 5 ns wait times to allow for a transient ring-down of the microwave source. Furthermore, the IQ amplitudes and phases are adjusted for each qubit at its center-frequency to suppress LO-leakage, unwanted sidebands and other spurious tones during IQ modulation. In all cases, a square pulse shape is used for the I and Q waveforms.

The exchange interaction, given by $H_{\text{exch}} = 2\pi\hbar J\mathbf{S}\cdot\mathbf{S}$, is turned on and off via square barrier pulses for the DCZ oscillations shown in Fig. 4.1c). Due to the large Zeeman energy difference present between all qubit pairs, we take the two-qubit unitary evolution to be $U_{\text{CZ}}(t) = \text{diag}(1, \exp(i\pi Jt), \exp(i\pi Jt), 1)$.

The presented single- and two-qubit experiments were run at a wide variety of temperatures and fields. The chevron patterns in Fig. 4.1 b) and the randomized benchmarking in Fig. 4.4 a) were run at 250 mK and 200 mT to prevent heating effects. The decoupled CZ oscillations were measured at the same field but at base temperature (around 20 mK). All external field sweeps and shuttling gate experiments were conducted at base temperature.

4.6.3. RANDOMIZED BENCHMARKING

In this work, we benchmark single-qubit gates implemented via resonant control and hopping control. Here we discuss the implementation of the Clifford gate sets in greater detail to interpret the average gate fidelities that are extracted for both gate flavors. For standard randomized benchmarking, we extract fidelities by fitting the decay curve to:

$$y(N) = A + B(1-p)^N, \tag{4.1}$$

where N is the number of Clifford gates in the RB sequence, and A, B, and p are fitting parameters. The estimated Clifford gate fidelity is then

estimated as $1-p/2$. The reported error bars correspond to the standard deviations acquired from curve fitting.

When using resonant control, the X/Y compilation is used (see Table II of [44]) whereby all Clifford gates are compiled into ± 90 degree rotations about the X and Y axes of the Bloch sphere. A single microwave burst operation is calibrated: it has a constant amplitude, frequency, duration, and a post-burst padding of 5 ns to allow for the microwave source to ring down. The only difference between pulses is the relative phase with which the I and Q modulation channels begin. For a given sequence of Clifford operations, the error contributed by each physical gate should be nominally identical in the absence of any non-Markovian effects. As the X/Y compilation of the 24 Cliffords contains 52 primitive gates in total, the average resonant gate fidelity $F_{\text{avg}}^{\text{res}}$ from the set $\{X_{\pm 90}, Y_{\pm 90}\}$ is estimated to relate to the resonant Clifford gate fidelity $F_{\text{Clif}}^{\text{res}}$ as $F_{\text{avg}}^{\text{res}} = 1-(1-F_{\text{Clif}}^{\text{res}})\cdot\frac{24}{52}$. For Q_1 to Q_4 respectively, the Clifford gate fidelities are measured to be $F_{\text{Clif}}^{\text{res}} = \{99.28(5)\,\%, 99.58(4)\,\%, 98.7(2)\,\%, 98.5(3)\,\%\}$. We use 20 random Clifford circuits per data point, and average the result of about 1200 post-selected single shot measurements per circuit. The corresponding average resonant gate fidelities are, respectively, $F_{\text{avg}}^{\text{res}} = \{99.67(2)\,\%, 99.80(2)\,\%, 99.39(8)\,\%, 99.3(2)\,\%\}$.

When using hopping control, the X/Z compilation is used (see again Table II of [44]) as the gate set is comprised of a unique X_{90} hopping operation as well as Z rotations implemented with physical idling times. Negative rotation about the X axis is implemented by a Z_{180} prior to a X_{90} hopping gate. In contrast to the resonant gate compilation, the X and Z operations are of a fundamentally different nature and therefore contribute to the error rate in distinct ways. First, X_{90} operations require more time than Z rotations and therefore pick up more error through dephasing. Second, X_{90} operations require four precise intervals of Larmor precession whereas Z rotations require only one. This means that any uncorrelated jitter in the AWG ramps will cause more error in the X_{90} operations. Third, as X_{90} operations involve shuttling, errors may arise due to imperfect charge or spin transfer between dots. Therefore, X_{90} gates should be more prone to error than any Z rotation.

Interleaved randomized benchmarking data was not taken to directly estimate individual gate fidelities, so we propose two ways of interpreting the fidelity of the individual physical operations. From randomized benchmarking, we obtain a Clifford gate fidelity $F_{\text{Clif}}^{\text{hop}}$. We use 250 random Clifford circuits per data point, and average the result of about 1500 (200 circuits) and 750 (50 circuits) post-selected single- shot measurements per circuit. The X/Z Clifford set is compiled from 89 physical gates in the set $\{X_{\pm 90}, Z_{\pm 90}, Z_{180}\}$, so one may estimate the average gate fidelity of this set as $F_{\text{avg}}^{\text{hop}} = 1-(1-F_{\text{Clif}}^{\text{hop}})\cdot\frac{24}{89}$. Alternatively, one may estimate

a lower bound of the X_{90} gate fidelity by attributing all of the error to the X_{90} operations on the basis that all Z operations are effectively brief extensions to the preceding X_{90} sequence. As each Clifford gate in the X/Z compilation contains exactly 2 X_{90} gates, the X_{90} fidelity may be bounded as $F^{\text{hop}}_{X_{90}} = 1-(1-F^{\text{hop}}_{\text{Clif}})\cdot\frac{1}{2}$. We run standard randomized benchmarking of the baseband gate set after initializing both in the odd and even parity states as shown in Fig. 4.4(f). To be conservative in our evaluation of the X90 hopping gate quality, we extract the Clifford gate fidelity of $F^{\text{hop}}_{\text{Clif,odd}} = 99.01(11)\%$ for Q_1 from the odd parity decay. It follows that $F^{\text{hop}}_{\text{avg,odd}} = 99.73(3)\%$ and $F^{\text{hop}}_{X_{90},\text{odd}} = 99.50(6)\%$. This latter value is the estimated fidelity bound reported in the abstract. For the even parity branch we fit $F^{\text{hop}}_{\text{Clif,even}} = 99.49(7)\%$, $F^{\text{hop}}_{\text{avg,even}} = 99.86(2)\%$ and $F^{\text{hop}}_{X_{90},\text{even}} = 99.74(4)\%$. The even parity branch contains a small oscillatory artifact that persists even with substantial averaging, and we are unsure of the origin of this artifact.

To gain insight about possible state leakage during hopping operation, we also employ the fitting method of blind randomized benchmarking (blind RB) [32]. Blind RB was developed to estimate the influence of leakage on the operation fidelity within an encoded subspace. We can use a similar interpretation here to estimate the role of leakage for the hopping gate. Blind RB makes use of two separate RB decay curves: one, $y_0(N)$, where the inverting Clifford is calculated to return the qubit to the initial state, and another, $y_1(N)$, where the inverting Clifford is modified to result in a net qubit-flip. Our implementation is imperfect in the sense that the even-parity decay curve was prepared with a physical X_{180} gate that introduces additional SPAM errors compared to the odd-parity decay curve, but this effect should be small. The two RB curves can be fit to the following system of equations:

$$y_0(N) = A + B(1-p)^N + C(1-q)^N \tag{4.2}$$

$$y_1(N) = A - B(1-p)^N + C(1-q)^N, \tag{4.3}$$

where N is the number of Clifford gates in the RB sequence, and A, B, C, p, and q are fitting parameters. The estimated SPAM-normalized leakage rate per Clifford operation is estimated as:

$$\Gamma = -Cq/B, \tag{4.4}$$

the total SPAM-normalized error rate per Clifford operation is estimated as:

$$\epsilon = p/2 - Cq/2B, \tag{4.5}$$

and the error rate within the qubit subspace is inferred to be $\epsilon_q = \epsilon - \Gamma$ (see [32] for derivations). For the hopping gate benchmarking data shown in Figure 4.4f), blind RB yields a leakage rate of $\Gamma = 0.13(5)\%$, a total error rate of $\epsilon = 0.74(5)\%$, and a qubit error rate of $\epsilon_q = 0.61(5)\%$ for a Clifford gate fidelity estimate of $1-\epsilon = 99.26(5)\%$ which is comparable to the estimates of the standard RB fits. We discuss this observed leakage in Sec. 4.7.6.

We note that neither the X/Y or X/Z compilations used are maximally efficient at compiling Clifford operations from primitive operations. Therefore, the Clifford gate fidelities extracted from randomized benchmarking could themselves be improved by tailoring the gate set to the physical gates. The average gate fidelity estimates should therefore be the most reasonable quantitative benchmark with which to compare the gate performance.

4.6.4. TIP ANGLE FITTING

There are multiple strategies to estimate the quantization axis tip θ between two dots. The visibility of oscillations observed after diabatically shuttling from one dot to another can be directly related to the tip in quantization axis [25]. This provides a reasonable estimate if the maximum visibility of oscillations can be established and provides good contrast. Alternatively, the Larmor frequency as a function of detuning across the hopping double-dot pair can be measured and fit to Eq. 2.37[25, 26]. Both of these methods are made difficult in our case by not having EDSR control at the magnetic field condition at which hopping gates are possible.

Here, we take advantage of the fact that a number of repetitions r of the shuttling sequence as drawn in Fig. 4.4a) will result in a unique 2D "fingerprint" as a function of the timing parameters t_1 and t_2. Generally, the pattern will depend more sensitively on the tip θ as r increases. Exemplary patterns for both dot pairs are shown in Fig. 4.8.

We may model the pattern using the two-level Hamiltonian given in Eq. 2.41 and make the approximation that the change in the Hamiltonian as a function of interdot detuning is perfectly sharp given the nanosecond-scale detuning ramp times [26]. The time evolution is therefore a product of unitary Larmor precessions. In the initial dot, this precession occurs at an angular frequency of ω_{init} about a quantization axis $\hat{z} = (0, 0, 1)^T$. In the tipped dot, this precession occurs at an angular frequency of ω_{tip} about a quantization axis $\hat{\theta} = (\sin\theta, 0, \cos\theta)^T$. Since the detuning ramp times are still finite, precession occurs during the ramps and can be accounted for by adjusting the nominal precession time such that $t_1' = t_1 - t_{1,\text{offset}}$ and $t_2' = t_2 - t_{2,\text{offset}}$. The unitary evolution for r repetitions of the sequence shown in Fig. 4.4a) is therefore given by:

$$U(t_1', t_2', t_{\text{add}}, \omega_{\text{init}}, \omega_{\text{tip}}, \theta) = \left(R_z(\omega_{\text{init}}(t_2' + t_{\text{add}}))R_\theta(\omega_{\text{tip}}t_1')R_z(\omega_{\text{init}}t_2')R_\theta(\omega_{\text{tip}}t_1')\right)^r \quad (4.6)$$

where $R_n(\alpha) = \exp(-i\alpha\hat{n}\cdot\vec{\sigma}/2)$ indicates a positive rotation about the unit vector $\hat{n}$ by an angle α. The measured pattern is given by:

$$p_{\text{odd}}(t_1', t_2', t_{\text{add}}, \omega_{\text{init}}, \omega_{\text{tip}}, \theta, A, B) = A\text{Tr}\left(OU\rho_{\text{odd}}U^\dagger\right) + B, \quad (4.7)$$

where ρ_{odd} is the initialized odd-parity state, $O = (\mathbb{1} - \sigma_z \otimes \sigma_z)/2$ is the odd-parity observable, and A and B are visibility and offset corrections due to SPAM errors.

We fit the experimental data to Eq. 4.7 with a pixel-by-pixel least-squares optimization over the parameters $t_{1,\text{offset}}$, $t_{2,\text{offset}}$, ω_{init}, ω_{tip}, A, B, and θ. t_{add} is known exactly from the experiment definition. As the qubit frequencies, offset times, and visibilities are well-estimated from other experiments, they are optimized within narrow bounds. For $r = 4$, the optimized value for θ is accurate within a degree. For fewer repetitions, the fit is less accurate, and we instead simulate using the $r = 4$ fit directly.

4.7. SUPPLEMENTARY MATERIAL

Content originally included in Supplementary Notes 1, 5, and 6 of the published manuscript appears in Sec. 2.4.1, 2.3.3, and 2.4.2 respectively.

4.7.1. MICROMAGNET SIMULATIONS

For micromagnet simulations where the ferromagnetic material can be approximated as a bulk material, we leverage the efficient magnetic field calculations of the Python package magpylib [45]. Such simulations treat the micromagnet as having a homogeneous polarization with no microscopic crystal structure such that the analytic form of the stray field for constituent magnet shapes can be used to calculate the relevant total magnetic vector field.

There are several sources of uncertainty in such a simulation in our context. At a fundamental level, no time-dynamics or domain wall formation is accounted for in the simulations. See [20] for a detailed discussion of magnet simulation approaches and their limitations. Independent of the simulation method, the accuracy is limited to the level of detail included in the magnet model itself as well as knowledge of the precise location of the accumulated quantum dots.

We therefore aim to extract a useful qualitative picture. First, we model the micromagnet using the nominal design. This excludes roughness due

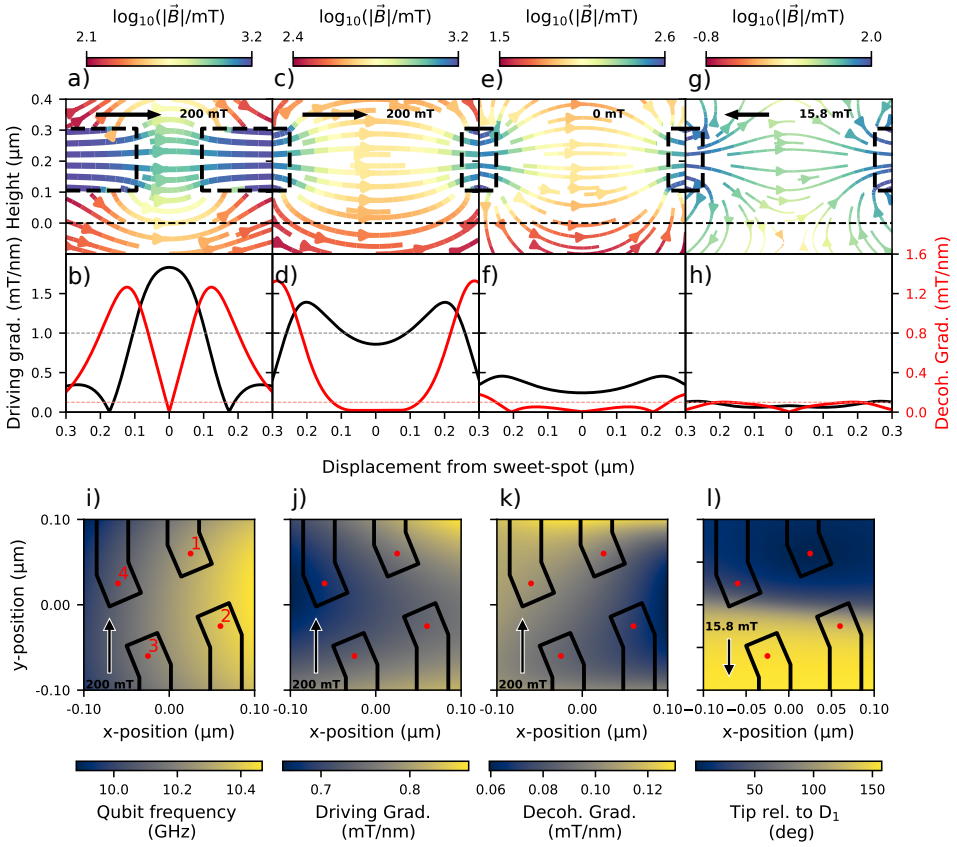


Figure 4.6: **Micromagnet Simulations** a) Magnetic field lines forming in a micromagnet gap of 190 nm as used in [10] when an external field of 200 mT is applied as indicated. No addressability features along the x-axis are included in the magnet design, so the field lines only exist in the y-z plane. The dashed line indicates the level at which the 2DEG and quantum dots would be formed below the magnet. b) The simulated driving gradient (black) along the y-axis and estimated decoherence gradient (red) corresponding to the magnet design in a). The black dashed line indicates the 1 mT/nm minimum threshold for good EDSR control, and the red dashed line indicates the 0.1 mT/nm maximum threshold for good charge-noise resilience. Although a good driving gradient is present, the decoherence sweet spot is only wide enough to support a linear qubit array. (Continued on next page)

Figure 4.6: (Continued) c) Magnetic field lines forming in a micromagnet gap of 500 nm similar to the design used in this work when an external field of 200 mT is applied as indicated. d) The simulated driving and decoherence gradients corresponding to the magnet design in c). Good EDSR is generally possible, and the decoherence sweet spot is wider than in a-b). e) Magnetic field lines forming in a micromagnet gap of 500 nm when no external field is applied. f) The simulated driving and decoherence gradients corresponding to the magnet design in e). EDSR is only possible with a stronger driving field, but the sweet spot in which to form good qubits is substantially wider. g) Magnetic field lines forming in a micromagnet gap of 500 nm when an external field of 15.8 mT is applied as indicated. h) The simulated driving and decoherence gradients corresponding to the magnet design in g). EDSR is effectively impossible due to the small gradient, but qubits may be controlled via shuttling. The decoherence sweet spot is still wide. i) Simulated qubit frequencies using the nominal micromagnet design used in this work and an external field of 200 mT. The polarization of the micromagnet used in simulation is inferred based on the measured qubit frequencies. The gate overlay indicates the approximate locations where Qubits 1-4 are formed in the magnetic field. j) The simulated driving gradient along the y-axis with an external field of 200 mT. k) The simulated decoherence gradient with an external field of 200 mT. l) The simulated tip in quantization axis relative to Dot 1 with an external field of 15.8 mT oriented opposite the micromagnet polarization illustrating the substantial tips formed between dots D_1D_2 and D_3D_4.

to the underlying gate structure, finite rounding of the magnet edges, and other small misalignments from the fabrication procedure. Second, we use the experimentally measured qubit frequencies to fit the effective homogeneous polarization of the model at a particular external field setting using a least-squares optimization (see Fig. 4.3). This requires making an assumption about the location of the spins. We take the center coordinate of the plunger gates as the point-like dot location (as indicated by the red dots in the bottom row of Fig. 4.6). A more detailed electrostatic simulation could be leveraged to predict the dot locations with more precision, but it is unclear if this confers any benefit due to the approximate nature of the magnetic simulation itself. With a fitted magnet polarization, a field can be simulated from which relevant parameters may be extracted per Sec. 2.4.1.

The trends predicted in terms of addressability, driving gradient and decoherence gradient all qualitatively match our experimental observations. While the model also predicts when quantization axis tips become substantial, a quantitative estimate becomes very sensitive to the estimated dot locations and the microscopic demagnetization of the micromagnets. Leveraging hopping spins through a larger array could be a powerful *in situ* method of characterizing micromagnet behaviour. Direct cryogenic magnetic imaging of patterned micromagnets would be another straightforward means of verifying magnet behavior.

4.7.2. NANOMAGNET SIMULATIONS

To obtain an accurate picture of the periodic stray fields produced by the nanomagnets in the 2D array (see Fig. 4.7), we use the OOMMF package [37]. We set the nanomagnets' initial magnetization along the y-axis (their longest axis), which we would perform experimentally by applying an external B-field along the y-axis. We employ an energy minimization evolver/driver (MinDriver) to find the energy-relaxed state of the entire 2D array. The relaxed magnetization will be defined by the nanomagnets' material parameters, as well as their geometry (shape anisotropy), pitch and initial magnetization direction. For the results presented in the main text, we choose Fe with material parameters similar to those in [33], i.e. saturation magnetization M_s = 1700 kA/m, exchange stiffness A_{ex} = 21 pJ/m, and 0 K temperature. We aim for a quantum dot pitch of 100 nm, which requires a nanomagnet pitch of about 280 nm in both the vertical and horizontal direction (this is the pitch within the same row or column). To minimize edge effects, we simulate a rather large volume of 3990 nm x 3815 nm x 200 nm with a cell size of 5 nm in all directions. The nanomagnet sizes are 40 nm x 120 nm x 50 nm. The results in the main text present stray fields at a distance of 100 nm below the nanomagnets, mimicking a quantum well positioned 100 nm below the nanomagnet array. Additional simulations suggest that the exact distance is not critical, as favorable conditions for hopping occur at a range of 90 to 140 nm for the specific sizes of the Fe nanomagnets shown here. Moreover, we find that by decreasing the thickness of the Fe nanomagnet to 30 nm, we can decrease the qubit frequency and decoherence gradient further while maintaining the same tip angles. Finally, we note that we are not limited to Fe, as we further varied ferromagnetic materials and nanomagnet geometries and could obtain similar outcomes. We leave these optimizations for future studies.

4.7.3. SIGN EXTRACTION FROM CROSSTALK EXPERIMENTS

The effective Hamiltonian for EDSR used in this work is given by Eq. 2.10 and is consistent with the notation of Sec. 2.3.1. We use parity-mode Pauli spin blockade for measurement and take our observable as $O = (\mathbb{1} - \sigma_z \otimes \sigma_z)/2$ in all cases where $\mathbb{1}$ is the identity operator. We initialize using post-selection into the subspace spanned by $\{|01\rangle, |10\rangle\}$ (see Fig. 4.12 for further discussion). Regardless of whether the initial pair is entangled, mixed, or a product state, the following expectation values hold.

We can use a modified Ramsey sequence with a virtual detuning in order to precisely estimate the qubit frequency. After preparation of a superposition state via a gate applied to qubit i, an $R_z^i(\omega_{\text{virtual}} t)$ operation is performed via a reference frame update (in the case of resonant

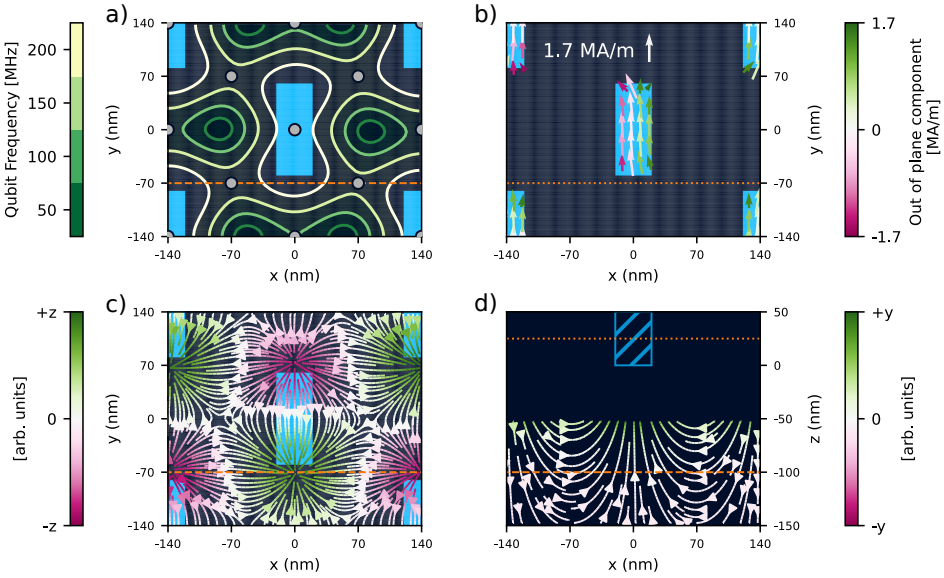


Figure 4.7: **Nanomagnet Simulations** a) Zoomed-in nanomagnet pattern as introduced in Fig. 4.5. The magnets are shown in bright blue. The bottom surface of the magnets is defined as $z = 0$. For the simulations, we choose Fe as the magnetic material [33] with saturation magnetization $M_s = 1.7\,\mathrm{MA/m}$, exchange stiffness $A_{ex} = 21\,\mathrm{pJ/m^3}$, nanomagnet size $\{l_x, l_y, l_z\} = \{40\,\mathrm{nm}, 120\,\mathrm{nm}, 50\,\mathrm{nm}\}$, cell size $x, y, z = 5\,\mathrm{nm}$ and simulated volume $\{L_x, L_y, L_z\} = \{3990\,\mathrm{nm}, 3815\,\mathrm{nm}, 200\,\mathrm{nm}\}$. The grey dots mark quantum dot locations, and the orange dashed line marks the intersection with the plot shown in panel d). The contour lines show the estimated qubit frequency distribution in a quantum well at $z = -100\,\mathrm{nm}$ assuming a g-factor of 2 for silicon. No external magnetic field is present. b) Magnetization of the nanomagnets at $z = 25\,\mathrm{nm}$. The dotted orange line marks the intersection with the plot shown in panel d). The color of the quiver arrows shows the z-component of the magnetization. The nanomagnets are originally magnetized along the positive y-axis. After the external field is removed, the shape anisotropy maintains the magnetization predominantly in the y-direction. c) Magnetic field lines in the x-y quantum dot plane at $z = -100\,\mathrm{nm}$. The stray field causes the relative quantization axis tips between the dot locations indicated in a) to be about 90°. The dashed line indicates the intersection with panel d). (Continued on next page)

Figure 4.7: (Continued) d) Stray field lines in the x-z plane at $y = -70\,\text{nm}$. The dashed and dotted orange lines mark the intersections with the planes shown a), b) and c). To maintain good visibility, only the region up to $z = -50\,\text{nm}$ is depicted. The crosshatched blue square indicates the position of the magnetic layer, though there is no nanomagnet present in this plane. The inhomogeneity of the stray field extends relatively far below the magnetic layer allowing ample space for independent gate electrodes.

control) or a physical wait (in the case of baseband control) prior to measurement:

$$\text{Init} \rightarrow R_x^i(\pi/2) \rightarrow \text{Wait } t \rightarrow R_z^i(\omega_{\text{virtual}} t) \rightarrow R_x^i(-\pi/2) \rightarrow \text{Measure } O. \quad (4.8)$$

The expectation value of the time-ordered sequence is:

$$p_{\text{odd}}(t) = A\cos((\Delta + \omega_{\text{virtual}})t)\exp(-(t/T_2^*)^a) + B, \quad (4.9)$$

where $p_{\text{odd}}(t)$ is the probability of measuring a state in the $\{|01\rangle, |10\rangle\}$ subspace. A and B are visibility and offset corrections due to constant state preparation and measurement (SPAM) errors, a is a decay constant and T_2^* is the decay time. The frequency of the fitted oscillations ω_{fit}^* can be related to the Larmor frequency as:

$$\omega_0 = \omega_{\text{MW}} - (\omega_{\text{fit}}^* - \omega_{\text{virtual}}). \quad (4.10)$$

A similar analysis holds for a Hahn echo pulse sequence:

$$\text{Init} \rightarrow R_x^i(\pi/2) \rightarrow \text{Wait } t/2 \rightarrow R_x^i(\pi) \rightarrow \text{Wait } t/2 \rightarrow R_z^i(\omega_{\text{virtual}} t) \rightarrow R_x^i(-\pi/2) \rightarrow \text{Measure } O. \quad (4.11)$$

The expectation value is given as:

$$p_{\text{odd}}(t) = C\cos((\Delta_2 - \Delta_1)/2 + \omega_{\text{virtual}})t)\exp(-(t/T_2^{\text{H}})^b) + D, \quad (4.12)$$

where C and D are once again due to SPAM errors, b is a decay constant and T_2^H is the extracted decay time. Here we observe that, contrary to expectation, the free evolution in the rotating frame with frequency $\Delta_1 = \omega_{\text{MW}} - \omega_{01}$ before the decoupling pulse may be measurably different than the free evolution with frequency $\Delta_2 = \omega_{\text{MW}} - \omega_{02}$ after the pulse. Fitting the decaying oscillations to a frequency ω_{fit}^H offers information about this systematic difference in Larmor frequency after the echo pulse, as any quasistatic fluctuations are eliminated by the echo pulse:

$$\omega_{01} - \omega_{02} = 2(\omega_{\text{fit}}^H - \omega_{\text{virtual}}). \quad (4.13)$$

An off-resonant pulse may be embedded into the second half of an echo sequence of fixed duration T to probe the transient phase pickup $\theta_t(t_{\text{delay}})$ over time t_{delay} as in Fig. 4.2. In this case, a gate $R_z^i(\theta)$ is swept prior to measurement:

$$\text{Init} \rightarrow R_x^i(\pi/2) \rightarrow \text{Wait } T/2 \rightarrow R_x^i(\pi) \rightarrow \text{Wait } T/2 - t_{\text{delay}} \rightarrow \text{Burst} \rightarrow \text{Wait } t_{\text{delay}} \rightarrow R_z^i(\theta) \rightarrow R_x^i(\pi/2) \rightarrow \text{Measure } O. \quad (4.14)$$

The expectation value is given as:

$$p_{\text{odd}}(\theta, t_{\text{delay}}) = E\cos(T(\Delta_2 - \Delta_1)/2 + \theta_t(t_{\text{delay}}) + \theta) + F, \quad (4.15)$$

where E and F account for the loss of visibility due to the echo decay as well as SPAM errors. As the difference $\Delta_2 - \Delta_1$ is known from the unmodified echo experiment, fitting the oscillation permits extracting θ_t. In the rotating frame, $\theta_t = \int dt_{\text{delay}}\Delta(t_{\text{delay}})$, and it follows that $\omega_0(t_{\text{delay}}) = \omega_{\text{MW}} - d\theta_t/dt_{\text{delay}}$.

4.7.4. ESTIMATING THE INFIDELITY OF RESONANT QUBIT CONTROL

Table 4.1: Comparing the Rabi frequency, T_2^*, T_2^{Rabi}, measured X90 gate error $\epsilon_{X90,\text{RB}}$, estimated X90 gate error due to quasi-static noise ϵ^*_{X90}, and estimated X90 gate due to decoherence of the dressed qubit $\epsilon^{\text{R}}_{X90}$ as defined in Sec. 2.3.3.

Qubit	f_{Rabi} (MHz)	T_2^* (μs)	T_2^{Rabi} (μs)	$\epsilon_{X90,\text{RB}}$ (%)	ϵ^*_{X90} (%)	$\epsilon^{\text{R}}_{X90}$ (%)
Q1	2.0412(7)	3.31(9)	16(1)	0.33(2)	0.037(2)	0.78(5)
Q2	2.2413(9)	2.02(2)	15(1)	0.20(2)	0.082(2)	0.74(7)
Q3	2.2685(9)	3.57(8)	14(1)	0.61(8)	0.026(1)	0.77(6)
Q4	1.752(1)	2.90(5)	18(2)	0.7(1)	0.065(2)	0.78(8)

Table 4.1 shows the error estimates from fitting all 4 qubit properties including the measured error $\epsilon_{X90,\text{RB}} = 1 - F^{\text{res}}_{\text{avg}}$ of the primitive X_{90} gate extracted from randomized benchmarking. We can see that the error estimate due to T_2^{Rabi} decay is about an order of magnitude larger than that originating from quasi-static frequency fluctuations and of the same order as the error measured with randomized benchmarking. We therefore conclude that the T_2^{Rabi} decay dominates the resonant single-qubit gate infidelity.

We note that these estimates can change meaningfully depending on the exponents of the decay curves and the nature of the microscopic noise. Additionally, the qubit coherence properties were extracted at different points in time than the randomized benchmarking data, so some electrostatic drift could be anticipated. This likely accounts for why

there is a discrepancy between the measured and estimated error rates, particularly for Q1 and Q2.

4.7.5. HOPPING CONTROL AND THE DIABATICITY CONDITION

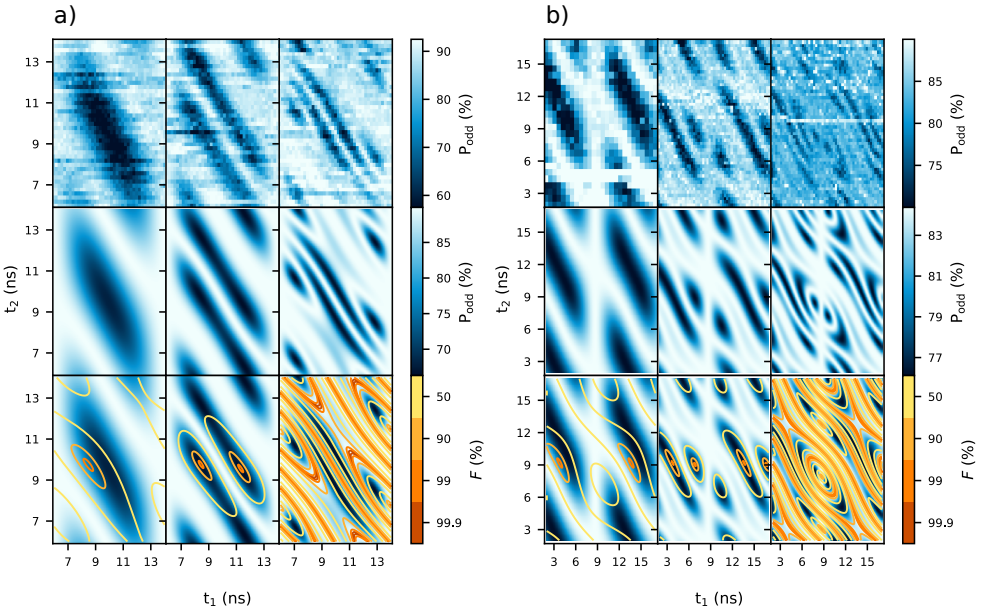


Figure 4.8: **Hopping gate characterisation of D1D2 and D4D3** Raw data (row 1), simulated data (row 2) and estimated gate fidelity (row 3) of one (column 1), two (column 2) and four (column 3) shuttle repetitions for the qubit in D1 (a) and the qubit in D4 (b). In both cases we used two shuttle cycles per repetition. The tunnel coupling for the D_1,D_2 data was fitted to be roughly 18 µeV. For D_4,D_3 the tunnel coupling was not measured. To generate the simulated data sets we fit the four-repetition pattern and extract parameters such as the quantisation axis tip and timing offsets due to finite ramp times. Using the simulated data we calculate the gate fidelity as indicated by the contour plots: for one repetition, we calculate the X_{90} fidelity; for two repetitions, we calculate the X_{180} fidelity; and for four repetitions, we calculate the X_{360} fidelity. The fidelity is calculated by assuming instantaneous shuttling between dots and considering only unitary spin state evolution. In the case of shuttling with Qubit 4, we observe the degradation of the readout signal due to the repeated pulsing on gate P3 (see Sec. 4.6)

.

The model of Eq. 2.37 can be used to understand the physics of the hopping gate as described in Sec. 2.4.2. When the detuning is linearly swept $\epsilon(t) = \nu t$, the Landau-Zener formula provides a means to estimate the condition for which charge transfer between the two dots is is not adiabatic:

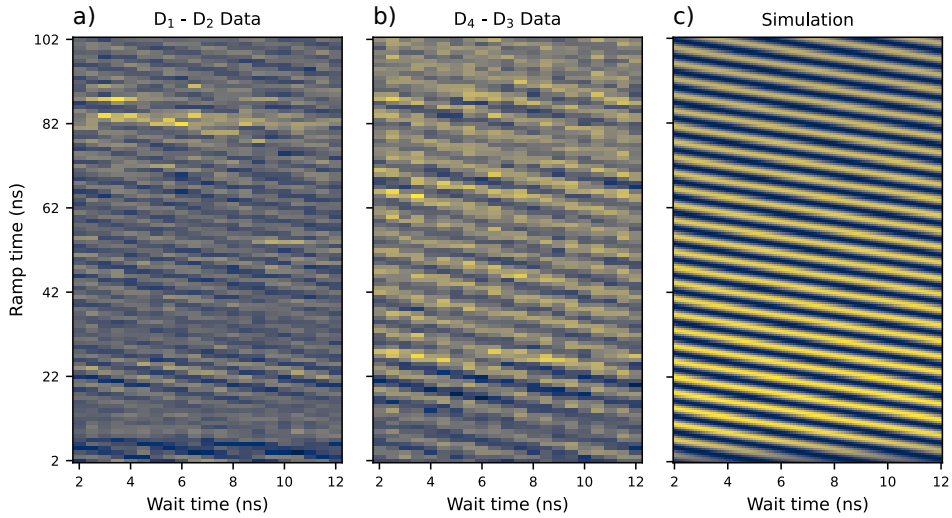


Figure 4.9: **Spin shuttling versus ramp time** Observed spin fraction oscillations when shuttling between a) Dots D_1 and D_2 and b) Dots D_4 and D_3 with a varying ramp time. c) Simulation using parameters extracted from Pair 1-2 in experiment. A total detuning ramp of 300 mV is converted to 10 500 µeV with a combined lever arm of 0.07 meV/mV, and a tunnel coupling of 30 µeV is estimated. The measured qubit frequencies of 240 MHz and 270 MHz are used for the two dot positions along with a measured tip angle of 22°. The data in a-b) was collected with an external field of −15 mT. The simulations show that the sudden approximation for spin-state preservation during shuttling is reasonably met in our experiments over a large range of ramp times owing to the very large detuning sweep.

$$P_{\mathrm{LZ}} = \exp\left(\frac{-2\pi t_c^2}{\hbar v}\right). \tag{4.16}$$

Based on a combined vP1+vP2 lever arm of about 0.07 meV/mV and a ramp time of 5 ns, we estimate a detuning ramp speed of about $v = 3000$ µeV/ns. With an estimated tunnel coupling of 40 µeV, we roughly estimate that $0.001 < P_{\mathrm{LZ}} \approx 0.01$. We discuss the implications of this shortly.

The sudden approximation quantifies how quickly the Hamiltonian step of Eq. 2.41 (shown in Fig. 4.4c)) needs to be traversed in order for the initial quantum state to be preserved:

$$t \ll \frac{2\pi\hbar}{\Delta E}, \tag{4.17}$$

where $\Delta E \approx 0.1$ µeV is the difference between the relevant eigenvalues of H'. This suggests the time interval needs to be less than 1 ns.

As the energetic width of the step is about $4t_c$ for the case of our linear detuning ramp, the step is crossed in about 60 ps. In fact, even a total ramp time much longer than was used for the logical gate implementation may be sufficient. This is observed in Fig. 4.9 where ramp times extending to several tens of nanoseconds were used while still observing evidence of sudden spin state transfer between both dot pairs 1-2 and 3-4. Simulations of the time-dependent Schrodinger equation with estimates of experimental parameters corroborate this. We remark that certain ramp times are nontrivially associated with oscillations of different visibility. For example 12 µs ramps consistently resulted in poor visibility despite longer ramps of 22 µs showing higher visibility. The origin of this effect is unknown to us, but it may be related to the microscopic valley-orbit structure of the double-dot system.

The estimated 0.1-1% probability of a diabatic transition at the charge anticrossing is one of the main limitations for the maximum single-qubit gate fidelity that we achieved via hopping spins. This was due to a particularly limited window of device stability within which DC voltages could be tuned to either increase the tunnel coupling or decrease the detuning range necessary to shuttle the electron. The conditions imposed by the Landau-Zener formula and sudden approximation represent a fundamental trade-off, as we desire an adiabatic charge transition with a diabatic spin transition. However, the exponential dependence of the Landau-Zener formula implies that even a modest increase of tunnel coupling greatly enhances the quality of charge transfer while still safely satisfying the sudden approximation. Furthermore, the increased susceptibility to charge noise that occurs when the spin and charge are maximally hybridized means that a fast shuttling time is preferable.

As the micromagnet design and gate layout in the present device was not intended for electron shuttling, there is almost certainly substantial room for improved fidelities by tailoring device design to the conditions for performing shuttling gates. Building upon the understanding of the depolarization of the micromagnet under low-field conditions, engineering quantum axis tips well above 45 degrees between adjacent dots should be easily achievable while keeping qubit frequencies on the order of 100 MHz. Furthermore, being able to modulate the tunnel coupling to the range of 50-100 µeV would substantially improve the quality of adiabatic charge shuttling and should lead to enhanced gate operation.

4.7.6. ESTIMATING LEAKAGE WITH BLIND RANDOMIZED BENCHMARKING

In Figure 4.10, we present two examples of the blind RB fitting protocol described in Sec. 4.6. The two datasets used were calibrated when different Larmor frequencies and tip angles were implemented in the

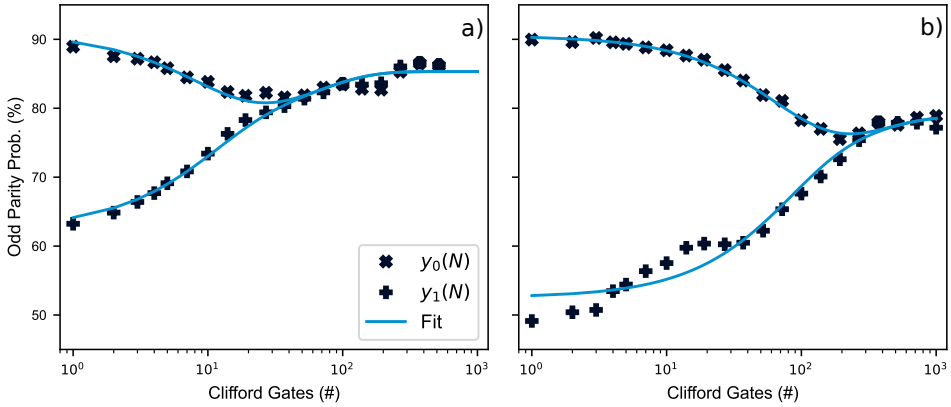


Figure 4.10: **Blind randomized benchmarking** a) Randomized benchmarking performed when the tunnel coupling is estimated to be approximately 18 μeV. Fitting to the blind RB theory results in $A = 0.853$, $B = 0.141$, $C = -0.086$, $p = 0.098$ and $q = 0.017$ and yields a leakage rate of $\Gamma = 1.0(2)\%$, a total error rate of $\epsilon = 5.4(2)\%$, and a qubit error rate of $\epsilon = 4.4(2)\%$ for a Clifford gate fidelity estimate of 94.6(2)%. Each decay curve is the average of 250 random Clifford circuits. (b) Randomized benchmarking performed when the tunnel coupling is estimated to be approximately 48 μeV. Fitting to the blind RB theory results in $A = 0.788$, $B = 0.190$, $C = -0.073$, $p = 0.013$ and $q = 0.003$ and yields a leakage rate of $\Gamma = 0.13(5)\%$, a total error rate of $\epsilon = 0.74(5)\%$, and a qubit error rate of $\epsilon = 0.61(5)\%$ for a Clifford gate fidelity estimate of 99.26(5)%. Each decay curve is the average of 250 random Clifford circuits.

dots, so the two results cannot be compared directly. However, the hopping gate tune-up procedure was the same in both cases. The data in Figure 4.10a) was taken when the virtual barrier $vB12$ was approximately 100 mV lower than in Figure 4.10b), which is the same data presented in Figure 4f) of the main text, and we estimate the tunnel coupling between dots to be 18 μeV and 48 μeV in the two cases respectively. The hopping gate suffers from substantially worse leakage when the tunnel coupling is lower, and the blind RB protocol estimates this error to be an order of magnitude lower when the tunnel coupling is raised to the condition where the best hopping gate fidelity was achieved in this device. The Clifford gate fidelity extracted from Figure 4.10b) is estimated to be 99.52(9)%, which is comparable to the values of 99.01(11)% and 99.49(7)% obtained from standard RB fits for the odd and even parity decay curves respectively.

Blind RB offers limited information about where the state is leaking. In all instances of randomized benchmarking that exhibited signs of leakage, the trend converges towards the odd spin parity signal (i.e. a (2,0) charge state measurement). One explanation consistent with this observation is leakage to excited valley-orbit states. In the discussion in Sec. 4.7.5, we

did not discuss the role that the valley-orbit state plays in the shuttling physics. Although diabatic passage through the charge avoided crossing may impede charge transfer, it is also possible that the charge does tunnel between dots but excites into a higher valley-like state. If, at the end of the random Clifford circuit, the charge state is excited to a different valley-orbit state, it is possible that Pauli spin blockade is lifted, resulting in tunneling to the (2,0) charge state during readout.

4.7.7. SUPPLEMENTARY FIGURES

Table 4.2: Lever arms in the 2x2 array. Virtualized sensor dot plungers (vS1P and vS2P) and virtualized loading barriers (vS1LB and vS2LB) are extracted directly via Coulomb diamonds. Virtualized quantum dot plungers (vP1 - vP4) are inferred by propagating the slope of interdot transitions through the array. The uncertainty of the virtual plunger gates is dominated by the uncertainty of propagating the sensor lever arm into the 2x2 array.

Gate	Lever arm
vS1P	0.1542 ± 0.0017
vS1LB	0.0155 ± 0.0004
vS2P	0.1537 ± 0.0029
vS2LB	0.0151 ± 0.0002
vP1	0.0289 ± 0.0083
vP2	0.0455 ± 0.0131
vP3	0.0290 ± 0.0084
vP4	0.0349 ± 0.0101

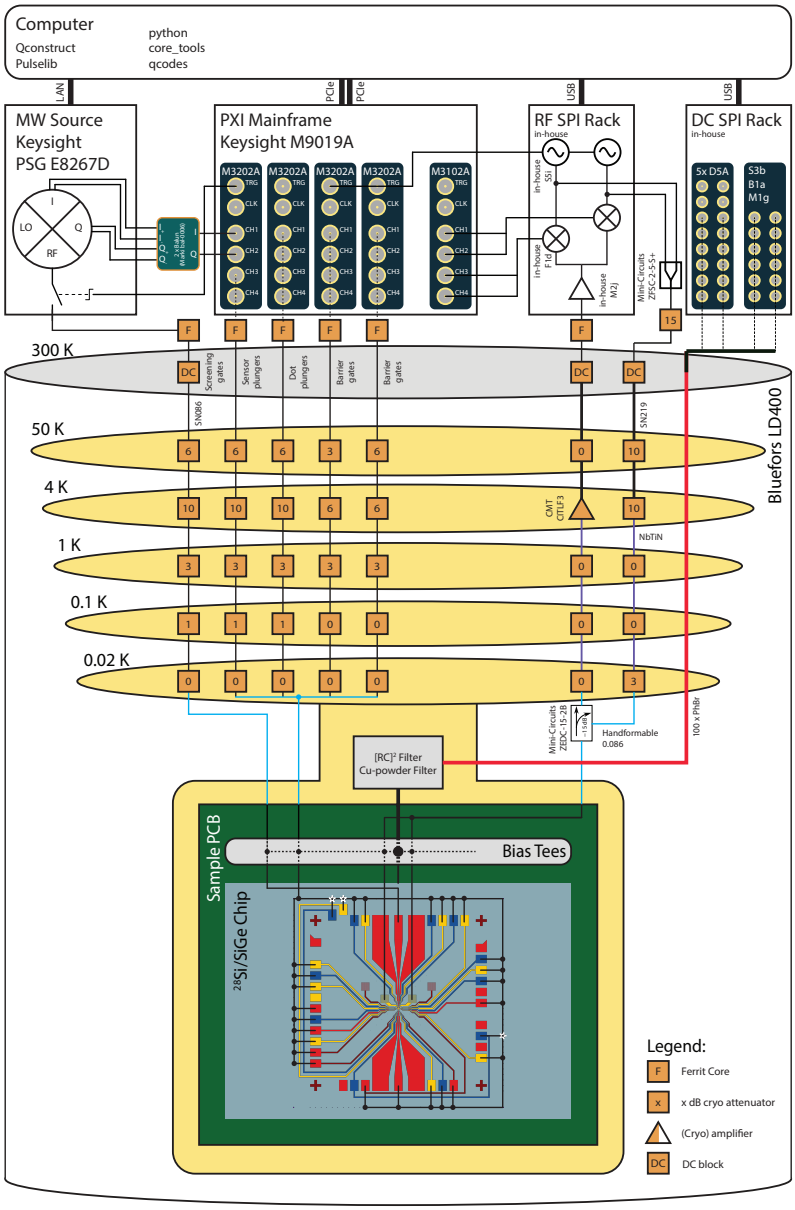


Figure 4.11: **Schematic of the experimental setup** (Continued on next page)

Figure 4.11: (Continued) Arbitrary Waveform Generators (AWG, Keysight M3202A) in a PXI chassis are used to generate baseband pulses as well as I/Q input signals for the microwave (MW) vector source (Keysight PSG E8267D). Baseband signals are supplied to all plunger and barrier gates comprising the 2x2 array along with both sensing dot plunger gates. Lines routed to barrier gates are attenuated less to allow for larger voltage pulses on these gates. Wideband modulation with differential I/Q inputs is implemented using Balun's (Marki bal-0006). Ferrite cores are used to reduce low-frequency noise. Double DC blocks (Pasternack PE8210) are used on the microwave drive line and rf-reflectometry readout lines. DC voltages are supplied by battery-powered low-noise voltage sources and are filtered with low-pass RC filters and copper-powder filters before being combined on the sample PCB using bias tees with RC time constants of 100 ms. Two carrier frequencies are generated using homemade sources that are triggered by AWG marker channels and routed via bias tees to two readout tank circuits which are connected to accumulation gates adjacent to the two sensing dots using the split-gate method [43]. The tank circuit consists of a series NbTiN inductor wirebonded on the PCB, the capacitance between the accumulation gate and the underlying 2DEG, as well as the resistive SET. The path from the 2DEG to the ohmic contact is depleted to minimize resistive leakage to ground. The reflected signal is separated from the incoming carrier with a directional coupler (Mini-Circuits ZEDC-15-2B), amplified at 4 Kelvin (CMT CITLF3) and room temperature before being demodulated and digitized (Keysight M3102A).

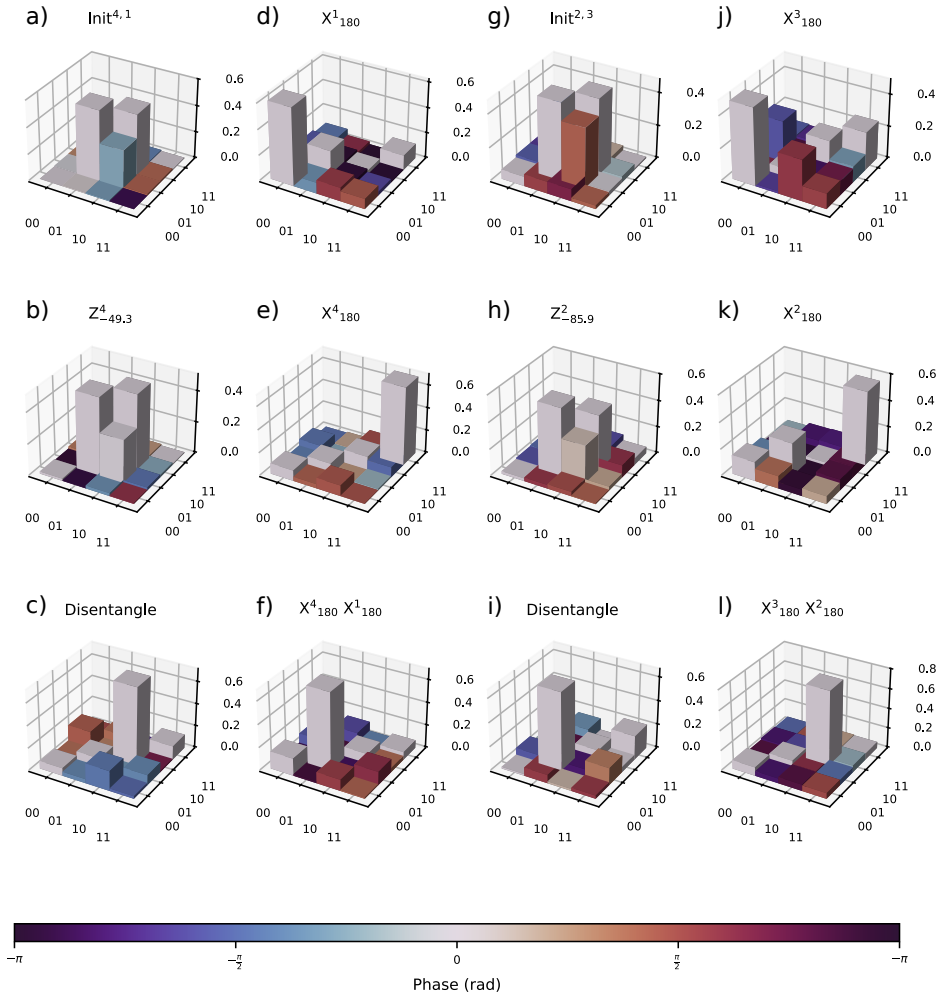


Figure 4.12: **Quantum State Tomography of Qubit Pairs Q4Q1 (a-f) and Q2Q3 (g-l) obtained using EDSR and CZ operations** a)/g) Tomography of the initial state. As we transition quickly out of the (0,2)/(2,0) charge state to the (1,1) charge state, we initialise predominantly in an entangled state in the $\{|01\rangle, |10\rangle\}$ subspace. This diabatic initialization offers more consistent state preparation compared to slow adiabatic ramping. In both cases we still observe a significant classical mixture of the two odd-parity states. (Continued on next page)

Figure 4.12: (Continued) For the single-qubit measurement protocols used in this work, a mixed initial state has no impact on the final result. However, such poor initialization has a large impact on most multi-qubit experiments. b)/h) The initialized state after applying a phase operation to produce a $|T_0\rangle$ state. c)/i) The initialized state after disentangling the qubits with a CZ and H gate. d)-f)/j)-l) The disentangled initial state after various X_{180} gates to transform between the product states. A full two-qubit gate set is required to implement quantum state tomography on both Pauli spin blockade pairs illustrating full quantum logic on this device. The poor fidelity of the initial state as well as the poor quality factors of the two-qubit interactions limit the quality of further multi-qubit characterization on this particular device.

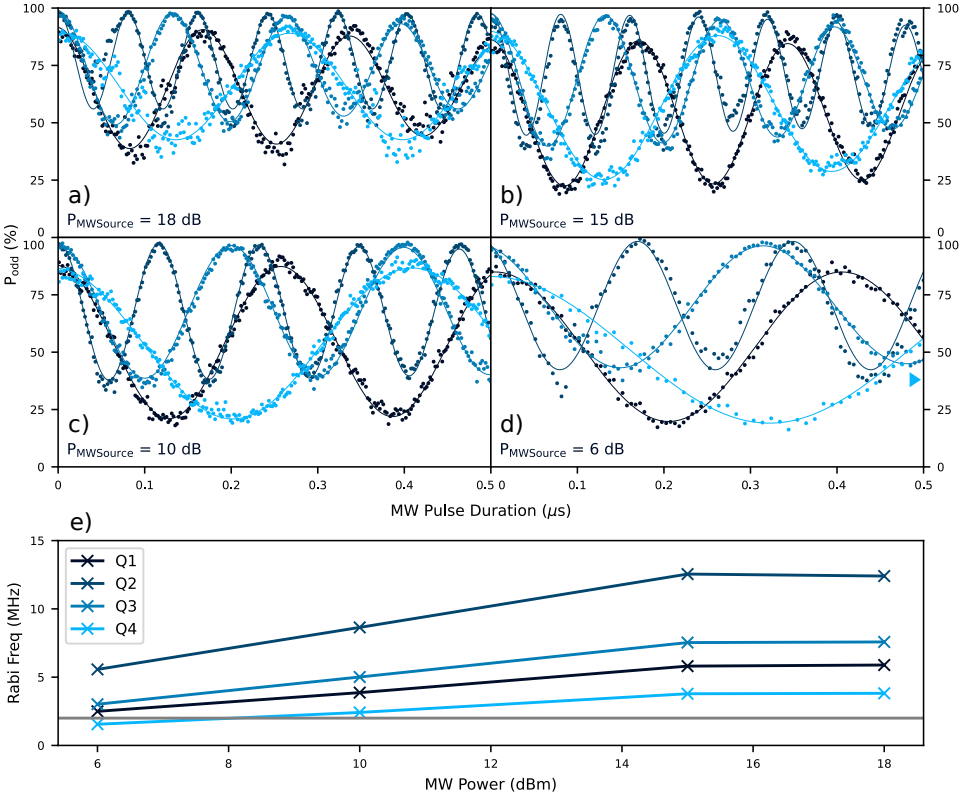


Figure 4.13: **Rabi oscillations at various MW powers** a)-d) Measured (data points) and fitted (solid lines) Rabi oscillations for all four qubits at various powers of the MW-source as annotated in the figures. We point out that the data of Q_4 in panel d) was cropped as indicated by the marker. The fit was performed with the full oscillation. Visibility differences between panel a) and panels b) through d) can be attributed to a retuning of initialization and read out parameters. e) Rabi frequencies plotted against the MW-source powers. Above 15 dBm we observe a saturation on all qubits that is caused by the limitations of the microwave source. For the experiments in the main text we used 6 dBm and adjusted the IQ input amplitudes to achieve a Rabi frequency of around 2 MHz (gray line) on all 4 qubits.

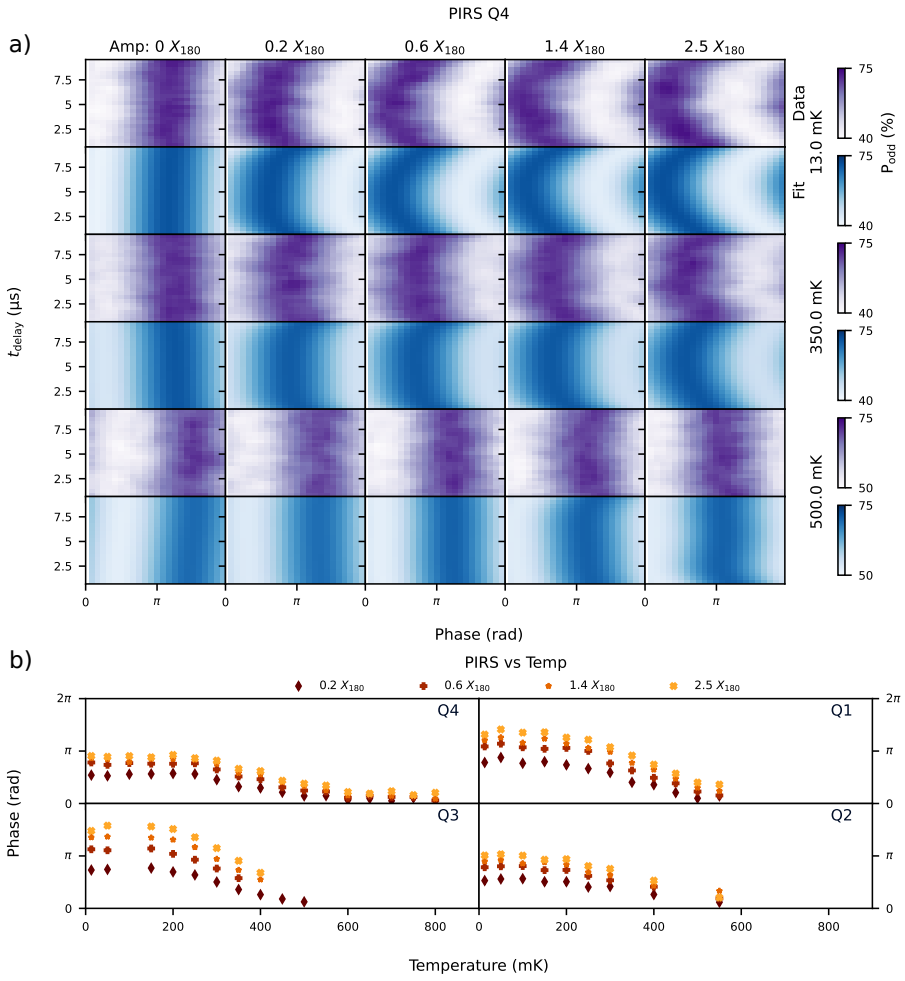


Figure 4.14: **PIRS during EDSR operation** a) Experimental data (purple) and respective fits (blue) for different off-resonant burst amplitudes at three exemplary mixing chamber temperatures for Qubit 4 (see Fig. 4.2 for the pulse sequence schematic). (Continued on next page)

Figure 4.14: (Continued) As the individual traces at constant t_{delay} are both low in visibility due to the long echo pulse sequence used and subject to small signal drifts over the course of the long experiments, we fit the 2D datasets to Eq. (4.15) using a quartic polynomial representation of $\theta_t(t_{\text{delay}}) = \sum_{k=0}^{4} c_k (t_{\text{delay}} - t_0)^k$ to extract the smooth transient phase accumulation from the off-resonant burst as a function of t_{delay}. In the left-most column, the experiment is a standard Hahn-echo sequence, and a constant phase offset is observed at the different temperature settings. We subtract this constant offset from the datasets plotted to the right which are collected at the same temperature in order to isolate the transient effect of the off-resonant burst. b) To quantify the relation between temperature and non-linear transient phase pick-up, we plot the maximum phase accumulation at as a function of mixing chamber temperature for all four qubits. All qubits exhibit the same behaviour whereby the maximum phase pickup is suppressed by operating at higher device temperatures. The positive phase accumulation is consistent with a negative qubit frequency shift given the definition of the rotating frame used in these experiments (see Sec. 4.7.3).

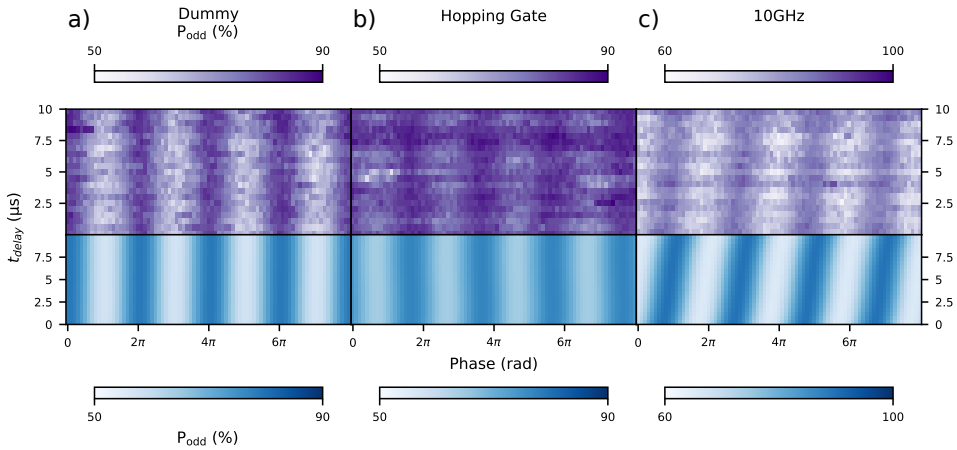


Figure 4.15: **PIRS during baseband operation** a-c) Experimental data (purple) and respective fits (blue) using three variants of the PIRS experiment. a) The Hahn-echo pulse template is implemented on Qubit 1 using hopping gates. The same fitting procedure as described in Fig. 4.14 is used. No off-resonant burst or pulse is applied. b) An X_{180} hopping gate is applied to Qubit 4 in place of the off-resonant burst. Qubit 1 experiences a non-transient phase pickup in addition to a 180° phase shift due to the change in measurement parity. The visibility is notably degraded compared to the other experiments due to the effect of baseband pulsing on gate P3. c) A 10 GHz burst is applied with an amplitude and duration energetically commensurate with $0.6X_{180}$ during standard EDSR operation. A transient phase pickup is observed, but no "saturation" effect as in Fig. 4.14 is seen. We believe this is due to the implementation of the decoupling pulse with a hopping gate rather than a resonant gate. The hopping gate itself does not impart a PIRS effect on the device.

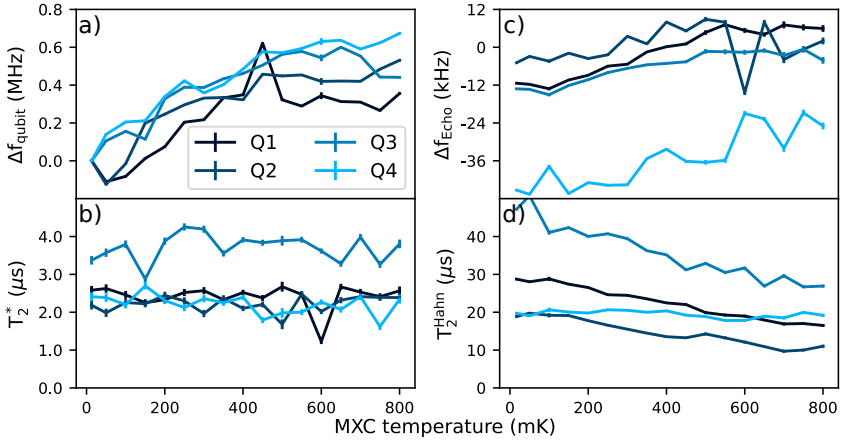


Figure 4.16: **Temperature dependence of T_2^*, T_2^H and qubit frequencies** a-b) Data extracted from Ramsey experiments (approx. 30 min) conducted using EDSR control as a function of mixing chamber temperature. The measured oscillations can be fit to extract (a) the qubit frequency and (b) the Ramsey decay time T_2^* per Sec. 4.7.3. Discounting spurious jumps in qubit frequency on the order of 100 kHz which we attribute to slow charge fluctuators, all qubit frequencies increase monotonically as a function of temperature within the range we are able to measure. The Ramsey decay times are notably unaffected by the device temperature for all four qubits. c-d) Hahn-echo experiments (approx. 30 min) conducted using EDSR control as a function of mixing chamber temperature. The measured oscillations can be fit to extract (c) the difference in qubit frequency before and after the decoupling pulse and (d) the Hahn-echo decay time T_2^H per Sec. 4.7.3. The systematic difference in qubit frequencies is predominantly attributed to the PIRS induced by the decoupling X_{180} pulse as it has a greater duration than the initial X_{90} pulse. This systematic frequency difference appears to converge to zero as the mixing chamber temperature is increases, which is consistent with the observation that an increased device temperature mitigates the PIRS effect (see Fig. 4.14). Hahn-echo decay times for all qubits except Qubit 4 monotonically decrease as a function of mixing chamber temperature. Qubit 4's coherence remains constant with the changing temperature. The plotted error bars in all panels represent the standard deviation of the fitted parameters.

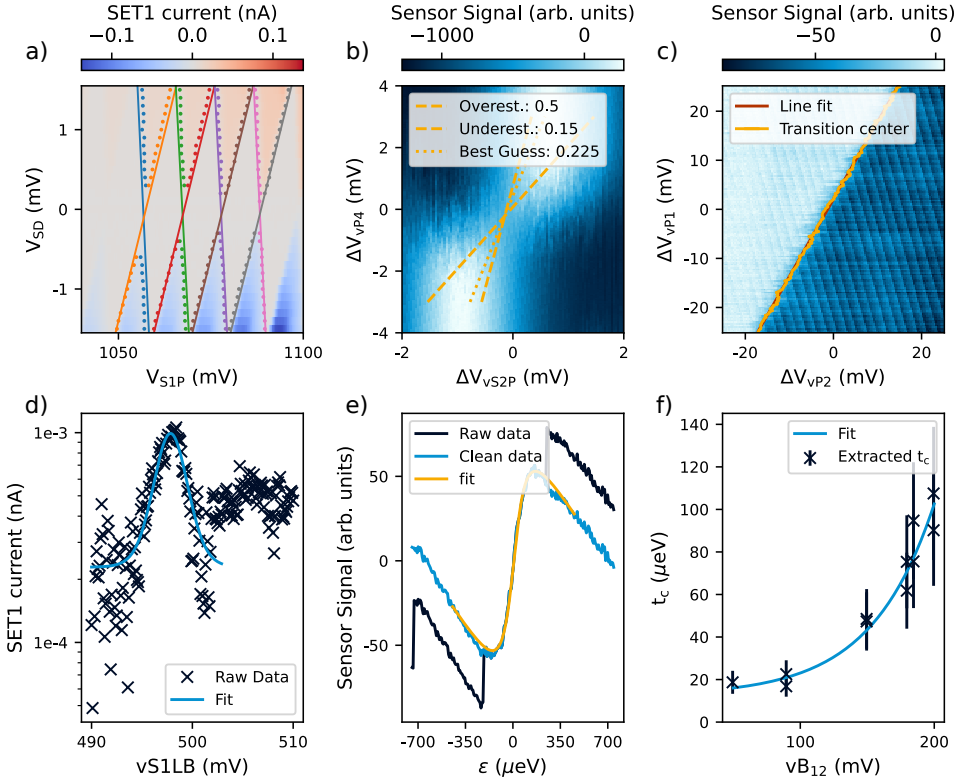


Figure 4.17: **Lever arm, electron temperature and tunnel coupling measurements** a) Coulomb diamonds of SET 1 showing the extracted slopes used to calculate the lever arm of the sensing dot plunger. b) An exemplaray interdot transition of sensing dot 2 and quantum dot 4. The shift of the coulomb peak (bright white line) due to the added charge on quantum do D_4 is used for determining the lever arm ratio between the sensing dot plunger and the quantum dot plunger. Dashed and dotted lines show the manual over- and under-estimation as well as the best fit. The latter takes into account that both lever arms for vS1P and vS2P have to be in an agreement when propagated through the array. c) An exemplary interdot transition between quantum dots 1 and 2 used for determining the lever arm ratio between the two plunger gates. We fit the interdot transition line-by-line to extract a consistent center point followed by a linear fit through all center points to determine the slope. (Continued on next page)

Figure 4.17: (Continued) d) Coulomb peak and fit to extract a bound on the electron temperature of about $T_e < 175\,mK$. e) Exemplary fit of an interdot transition to extract the tunnel coupling [46]. The detuning lever arm as computed in panels a-c) as well as the electron temperature from d) are used in this fitting procedure. The sensing dot plunger is virtualized with respect to the detuning, and discrete steps in the measured signal due to finite AWG resolution are extracted from the measured transition prior to fitting. f) Extracted tunnel couplings between dots 1 and 2 plotted against the respective barrier voltage showing the expected exponential dependency. The plotted error bars represent the standard deviation of the fit using the nominal value of the fitted lever arm and electron temperature.

REFERENCES

[1] F. K. Unseld *et al.* “Baseband control of single-electron silicon spin qubits in two dimensions”. In: *Nature Communications* 16 (July 2025), p. 5605. url: https://doi.org/10.1038/s41467-025-60351-x.

[2] R. Maurand *et al.* “A CMOS silicon spin qubit”. In: *Nature Communications* 7.1 (Nov. 2016). issn: 2041-1723. doi: 10.1038/ncomms13575. url: http://dx.doi.org/10.1038/ncomms13575.

[3] A. Zwerver *et al.* “Qubits made by advanced semiconductor manufacturing”. In: *Nature Electronics* 5.3 (2022), pp. 184–190.

[4] S. Neyens *et al.* “Probing single electrons across 300-mm spin qubit wafers”. en. In: *Nature* 629.8010 (May 2024), pp. 80–85. issn: 1476-4687. doi: 10.1038/s41586-024-07275-6.

[5] P. Steinacker *et al. A 300 mm foundry silicon spin qubit unit cell exceeding 99% fidelity in all operations*. 2024. arXiv: 2410.15590 [cond-mat.mes-hall]. url: https://arxiv.org/abs/2410.15590.

[6] T. Huckemann *et al. Industrially fabricated single-electron quantum dots in Si/Si-Ge heterostructures*. 2024. arXiv: 2410.16913 [cond-mat.mes-hall]. url: https://arxiv.org/abs/2410.16913.

[7] X. Xue *et al.* “Quantum logic with spin qubits crossing the surface code threshold”. In: *Nature* 601.7893 (Jan. 2022), pp. 343–347. issn: 1476-4687. doi: 10.1038/s41586-021-04273-w. url: http://dx.doi.org/10.1038/s41586-021-04273-w.

[8] A. Noiri *et al.* “Fast universal quantum gate above the fault-tolerance threshold in silicon”. In: *Nature* 601.7893 (Jan. 2022), pp. 338–342. issn: 1476-4687. doi: 10.1038/s41586-021-04182-y. url: http://dx.doi.org/10.1038/s41586-021-04182-y.

[9] A. R. Mills *et al.* “Two-qubit silicon quantum processor with operation fidelity exceeding 99%”. In: *Science Advances* 8.14 (Apr. 2022). issn: 2375-2548. doi: 10.1126/sciadv.abn5130. url: http://dx.doi.org/10.1126/sciadv.abn5130.

[10] S. G. J. Philips *et al.* “Universal control of a six-qubit quantum processor in silicon”. In: *Nature* 609.7929 (Sept. 2022), pp. 919–924. issn: 1476-4687. doi: 10.1038/s41586-022-05117-x. url: http://dx.doi.org/10.1038/s41586-022-05117-x.

[11] K. Takeda *et al.* “Rapid single-shot parity spin readout in a silicon double quantum dot with fidelity exceeding 99%”. In: *npj Quantum Information* 10.1 (Feb. 2024). issn: 2056-6387. doi: 10.1038/s41534-024-00813-0. url: http://dx.doi.org/10.1038/s41534-024-00813-0.

[12] A. Noiri *et al.* “A shuttling-based two-qubit logic gate for linking distant silicon quantum processors”. In: *Nature Communications* 13.1 (Sept. 2022). issn: 2041-1723. url: http://dx.doi.org/10.1038/s41467-022-33453-z.

[13] M. D. Smet *et al. High-fidelity single-spin shuttling in silicon*. 2024. arXiv: 2406.07267 [cond-mat.mes-hall]. url: https://arxiv.org/abs/2406.07267.

[14] R. Neumann and L. R. Schreiber. “Simulation of micro-magnet stray-field dynamics for spin qubit manipulation”. In: *Journal of Applied Physics* 117.19 (May 2015). issn: 10897550. doi: 10.1063/1.4921291.

[15] J. Yoneda *et al.* “Robust micromagnet design for fast electrical manipulations of single spins in quantum dots”. In: *Applied Physics Express* 8.8 (Aug. 2015). issn: 18820786. doi: 10.7567/APEX.8.084401.

[16] N. I. D. Stuyck *et al.* “Low dephasing and robust micromagnet designs for silicon spin qubits”. en. In: *Applied Physics Letters* 119.9 (Aug. 2021), p. 094001. issn: 0003-6951, 1077-3118. doi: 10.1063/5.0059939.

[17] H. C. George *et al.* “12-Spin-Qubit Arrays Fabricated on a 300 mm Semiconductor Manufacturing Line”. In: *Nano Letters* 25.2 (2025). PMID: 39721970, pp. 793–799. doi: 10.1021/acs.nanolett.4c05205. eprint: https://doi.org/10.1021/acs.nanolett.4c05205. url: https://doi.org/10.1021/acs.nanolett.4c05205.

[18] C. Jones *et al.* “Logical Qubit in a Linear Array of Semiconductor Quantum Dots”. In: *Phys. Rev. X* 8 (2 June 2018), p. 021058. doi: 10.1103/PhysRevX.8.021058. url: https://link.aps.org/doi/10.1103/PhysRevX.8.021058.

[19] M. Tadokoro *et al.* “Designs for a two-dimensional Si quantum dot array with spin qubit addressability”. en. In: *Scientific Reports* 11.11 (Sept. 2021), p. 19406. issn: 2045-2322. doi: 10.1038/s41598-021-98212-4.

[20] M. Aldeghi *et al.* “Simulation and Measurement of Stray Fields for the Manipulation of Spin Qubits in One- and Two-Dimensional Arrays”. In: *Nano Letters* 25.5 (Feb. 2025), pp. 1838–1844. issn: 1530-6984. doi: 10.1021/acs.nanolett.4c05037.

[21] S. Freer *et al.* “A single-atom quantum memory in silicon”. In: *Quantum Science and Technology* 2.1 (2017), p. 015009.

[22] K. Takeda *et al.* “Optimized electrical control of a Si/SiGe spin qubit in the presence of an induced frequency shift”. In: *npj Quantum Inf.* 4 (2018), p. 54. issn: 2056-6387. url: https://doi.org/10.1038/s41534-018-0105-z.

[23] B. Undseth *et al.* “Hotter is Easier: Unexpected Temperature Dependence of Spin Qubit Frequencies”. In: *Phys. Rev. X* 13 (4 Oct. 2023), p. 041015. doi: 10.1103/PhysRevX.13.041015. url: https://link.aps.org/doi/10.1103/PhysRevX.13.041015.

[24] T. Tanttu *et al.* “Assessment of the errors of high-fidelity two-qubit gates in silicon quantum dots”. In: *Nature Physics* 20.11 (Aug. 2024), pp. 1804–1809. issn: 1745-2481. doi: 10.1038/s41567-024-02614-w. url: http://dx.doi.org/10.1038/s41567-024-02614-w.

[25] F. van Riggelen-Doelman *et al.* “Coherent spin qubit shuttling through germanium quantum dots”. In: *Nature Communications* 15.1 (July 2024). issn: 2041-1723. doi: 10.1038/s41467-024-49358-y. url: http://dx.doi.org/10.1038/s41467-024-49358-y.

[26] C.-A. Wang *et al.* “Operating semiconductor quantum processors with hopping spins”. In: *Science* 385.6707 (July 2024), pp. 447–452. issn: 1095-9203. doi: 10.1126/science.ado5915. url: http://dx.doi.org/10.1126/science.ado5915.

[27] F. K. Unseld *et al.* “A 2D quantum dot array in planar 28Si/SiGe”. In: *Applied Physics Letters* 123.8 (Aug. 2023). issn: 1077-3118. doi: 10.1063/5.0160847. url: http://dx.doi.org/10.1063/5.0160847.

[28] M. Mehmandoost and V. V. Dobrovitski. “Decoherence induced by a sparse bath of two-level fluctuators: $1/f$ noise in high-quality qubits”. In: *Physical Review Research* 6.3 (Aug. 2024). issn: 2643-1564. doi: 10.1103/physrevresearch.6.033175. url:

http://dx.doi.org/10.1103/PhysRevResearch.6.033175.

[29] L. Cvitkovich *et al.* “Coherence limit due to hyperfine interaction with nuclei in the barrier material of Si spin qubits”. In: *Phys. Rev. Appl.* 22 (6 Dec. 2024), p. 064089. doi: 10.1103/PhysRevApplied.22.064089. url: https://link.aps.org/doi/10.1103/PhysRevApplied.22.064089.

[30] Y. Choi and R. Joynt. “Interacting random-field dipole defect model for heating in semiconductor-based qubit devices”. In: *Phys. Rev. Res.* 6 (1 Feb. 2024), p. 013168. doi: 10.1103/PhysRevResearch.6.013168. url: https://link.aps.org/doi/10.1103/PhysRevResearch.6.013168.

[31] J. D. Teske *et al.* “Flopping-mode electron dipole spin resonance in the strong-driving regime”. In: *Physical Review B* 107.3 (Jan. 2023). issn: 2469-9969. doi: 10.1103/physrevb.107.035302. url: http://dx.doi.org/10.1103/PhysRevB.107.035302.

[32] R. W. Andrews *et al.* “Quantifying error and leakage in an encoded Si/SiGe triple-dot qubit”. In: *Nature Nanotechnology* 14.8 (July 2019), pp. 747–750. issn: 1748-3395. doi: 10.1038/s41565-019-0500-4. url: http://dx.doi.org/10.1038/s41565-019-0500-4.

[33] M. Aldeghi, R. Allenspach, and G. Salis. “Modular nanomagnet design for spin qubits confined in a linear chain”. In: *Applied Physics Letters* 122.13 (Mar. 2023). issn: 1077-3118. doi: 10.1063/5.0139670. url: http://dx.doi.org/10.1063/5.0139670.

[34] F. Forster *et al.* “Electric-dipole-induced spin resonance in a lateral double quantum dot incorporating two single-domain nanomagnets”. In: *Physical Review B* 91.19 (May 2015), p. 195417. doi: 10.1103/PhysRevB.91.195417.

[35] F. Bersano *et al.* “Integration of Cobalt Ferromagnetic Control Gates for Electrical and Magnetic Manipulation of Semiconductor Quantum Dots”. In: *Advanced Functional Materials* 35.14 (Jan. 2025). issn: 1616-3028. doi: 10.1002/adfm.202419940. url: http://dx.doi.org/10.1002/adfm.202419940.

[36] W. Legrand *et al.* “Optimal design of nanomagnets for on-chip field gradients”. In: *Physical Review Applied* 20.4 (Oct. 2023), p. 044062. doi: 10.1103/PhysRevApplied.20.044062.

[37] M. J. Donahue and D. G. Porter. *OOMMF user’s guide, version 1.0*. National Institute of Standards and Technology, Gaithersburg, MD, 1999. doi: 10.6028/nist.ir.6376.

[38] F. Ginzel *et al.* “Spin shuttling in a silicon double quantum dot”. In: *Physical Review B* 102.19 (Nov. 2020). issn: 24699969. doi: 10.1103/PhysRevB.102.195418.

[39] X. Zhao and X. Hu. *Coherent electron transport in silicon quantum dots*. 2019. arXiv: 1803.00749 [cond-mat.mes-hall]. url: https://arxiv.org/abs/1803.00749.

[40] B. Buonacorsi, B. Shaw, and J. Baugh. “Simulated coherent electron shuttling in silicon quantum dots”. In: *Physical Review B* 102.12 (Sept. 2020). issn: 2469-9969. doi: 10.1103/physrevb.102.125406. url: http://dx.doi.org/10.1103/PhysRevB.102.125406.

[41] M. Rimbach-Russ *et al.* “Simple framework for systematic high-fidelity gate operations”. In: *Quantum Science and Technology* 8.4 (Sept. 2023), p. 045025. url: https://doi.org/10.1088/2058-9565/acf786.

[42] D. Degli Esposti *et al.* “Low disorder and high valley splitting in silicon”. In: *npj Quantum Information* 10.1 (Mar. 2024). issn: 2056-6387. url: http://dx.doi.org/10.1038/s41534-024-00826-9.

[43] Y.-Y. Liu *et al.* “Radio-Frequency Reflectometry in Silicon-Based Quantum Dots”. In: *Physical Review Applied* 16.1 (July 2021). issn: 2331-7019. doi: 10.1103/physrevapplied.16.014057. url: http://dx.doi.org/10.1103/PhysRevApplied.16.014057.

[44] X. Xue *et al.* “Benchmarking Gate Fidelities in a Si/SiGe Two-Qubit Device”. In: *Phys. Rev. X* 9 (2 Apr. 2019), p. 021011. url: https://link.aps.org/doi/10.1103/PhysRevX.9.021011.

[45] M. Ortner and L. G. C. Bandeira. “Magpylib: A free Python package for magnetic field computation”. In: *SoftwareX* 11 (2020), p. 100466. issn: 2352-7110. doi: https://doi.org/10.1016/j.softx.2020.100466. url: https://www.sciencedirect.com/science/article/pii/S2352711020300170.

[46] L. DiCarlo *et al.* “Differential Charge Sensing and Charge Delocalization in a Tunable Double Quantum Dot”. In: *Phys. Rev. Lett.* 92 (22 June 2004), p. 226801. doi: 10.1103/PhysRevLett.92.226801. url: https://link.aps.org/doi/10.1103/PhysRevLett.92.226801.

5

WEIGHT-FOUR PARITY CHECKS IN A SPIN-SHUTTLING ARCHITECTURE

This work forms the capstone of this dissertation and illustrates the full procedure of using the principles outlined in Chapter 2 to engineer a silicon quantum processor from the ground up. The lessons from other chapters in this thesis are also put to good use: following Chapter 3, we operate the device at 200 mK to avoid heating effects; using what was learned from the behaviour of partially demagnetized micromagnets in Chapter 4, we operate the device in zero external field. The result is, by a couple measures at least, the most advanced demonstration of a semiconductor-based quantum processor to date. This work opens immediate opportunities to pursue QEC experiments with spin qubits, and the protocols developed here lay the groundwork for the modular calibration and operation of sparse spin qubit arrays, including some of the more ambitious ideas explored in Chapter 6.

Parts of this chapter have been accepted for publication in *Nature* and are available as the preprint arXiv:2601.23267 [1].

5.1. INTRODUCTION

For semiconductor-based spin qubits to be a viable platform for fault-tolerant quantum computing, their physical advantages, including their small size, long coherence times, and high-fidelity operations [2], must be compatible with quantum error correction (QEC). Although previous demonstrations of phase-flip codes with spin qubits have made use of Toffoli-like primitives to implement conditional correction operations [3, 4], large-scale deployment of QEC requires the repeated extraction of stabilizer measurements to infer error syndromes in both space and time. A well-established error correction benchmark, the surface code, uses weight-four X- and Z-type parity checks to achieve quantum memories with reasonable error thresholds [5, 6]. Such operations require an ancillary qubit to interact with four data qubits, and the former must be measured without destroying the quantum state of the latter. This connectivity is challenging to realize in densely populated quantum dot arrays due to crosstalk and the co-integration of readout, but spin shuttling in sparsely-occupied arrays has long been recognized as a path forward [7].

The performance of semiconductor-based spin shuttling has progressed rapidly in recent years due to improvements in material uniformity and control techniques [8–18]. More recently, spin shuttling has also been used as a means of material characterization [19], qubit characterization [20], and implementing logical gates [21, 22]. These advancements have maintained substantial interest in sparse spin qubit architectures for fault-tolerant quantum information processing where the physical movement of spins enables the coupling of qubits at distances far greater than kinetic exchange or capacitive coupling and allows for the dynamic reconfiguration of qubit connectivity [7, 23–28].

Qubit shuttling in other quantum computing platforms, such as trapped ion systems [29] and neutral atom systems [30], enables zoned architectures and permits beyond-planar connectivity that is relevant for QEC codes with higher encoding rates [31]. For semiconductor-based spins in particular, the additional separation between shuttled qubits in sparse arrays offers advantages beyond higher connectivity. First, residual exchange between adjacent spins can be effectively eliminated during idling, greatly reducing the potential for entangling crosstalk [32]. Second, a lower qubit density eases the routing and localization of control signals, which consequently reduces the calibration overhead required to mitigate capacitive crosstalk [33, 34]. Finally, spin qubit readout becomes more flexible as the co-integration of charge sensing can require charge reservoirs, DC current paths [35] or rf resonators [36] that are bulkier than the individual qubits. However, to realize these advantages of sparser architectures, coherent spin shuttling must be integrated within a multi-qubit setting while maintaining universal control and efficient

measurement [37–42].

In this work, we commission a sparse five-qubit array in silicon that leverages spin shuttling to enable long-range connectivity. In contrast to previous demonstrations with semiconductor spins, we characterize the array and tune logical control using shuttling in the absence of direct charge sensing. The resulting protocol allows for modular calibration and optimization, and it illustrates a viable alternative to the challenges of experimentally realizing dense qubit arrays. After outlining the measurement framework used to initialize and readout the multi-qubit state of the device, we benchmark the quantum processor and report the successful implementation of parity checks up to weight-four as well as the creation of genuine entanglement between all qubit combinations in the array. These results highlight both the feasibility and the architectural benefits of incorporating shuttling into semiconductor quantum processors.

5.2. DEVICE CONCEPT

The sparse array, as shown in Fig. 5.1a, is electrostatically defined in the isotopically purified quantum well of a ^{28}Si/SiGe heterostructure (see Sec. 5.7.1) and consists of three zones: a readout zone, a spin shuttling bus, and an adjacent row of quantum dots we refer to as bus stops. At constant DC voltages, only the quantum dots formed under gates P1 and P2 are populated with 3 and 1 electrons, respectively, to form a qubit readout pair using parity-mode Pauli spin blockade (PSB) for spin-to-charge conversion [43]. The adjacent sensor S1 is a single-electron transistor (SET) connected to an off-chip tank circuit such that rf-reflectometry may be used to probe the charge state of the readout pair (see Sec. 5.7.4). The spin qubit R1, kept constantly below gate P1, is only used as a readout ancilla in this work, although it is fully controllable. The qubit A1, initialized below gate P2, functions as a mobile ancilla with which to characterize the sparse array and connect the qubits within it.

The overlapping gates C0-C14 in the top row of the array define the shuttling bus in the channel between the screening gates. The bottom row defines the bus stops with four individual plunger gates BP1-BP4 to accumulate four spin qubits, respectively D1-D4, and four adjacent barrier gates BB1-BB4 to control the tunnel couplings to the bus. The resulting connectivity graph, shown in Fig. 5.1b, corresponds to a weight-four stabilizer plaquette where each data qubit may directly interact with the ancilla qubit by coherently shuttling the latter to a position adjacent to the data qubit bus stop. The data qubits could also be shuttled and interact directly with one another for effective all-to-all connectivity [23], but we do not make use of these couplings in this work. It has been shown that extending such a bilinear architecture is conceptually sufficient to support

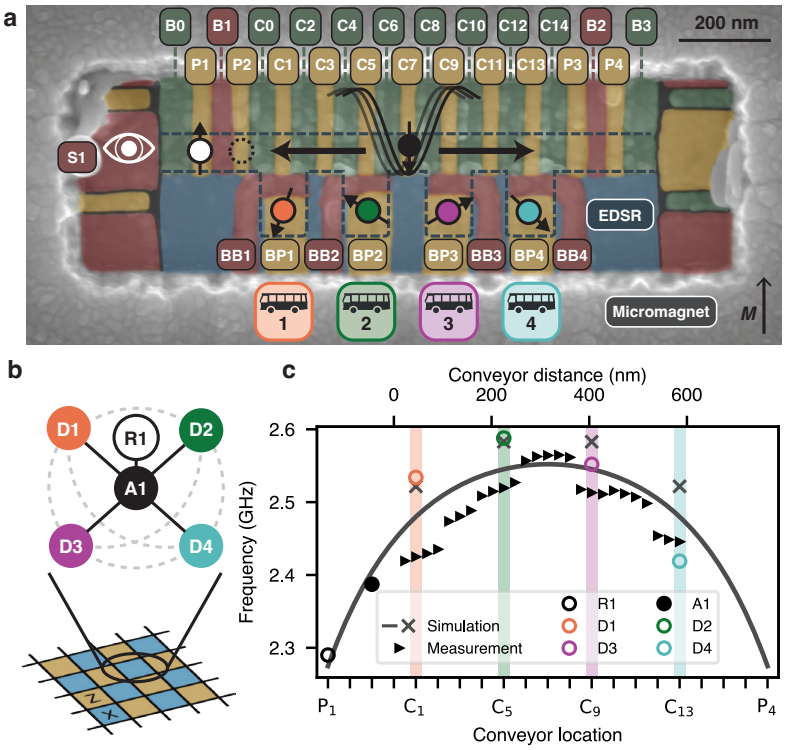


Figure 5.1: **Device concept and shuttling bus**. **a** False-colored scanning electron microscope image of a device nominally identical to that used in the experiments. Four metallization layers (from bottom to top: blue, red, yellow, green) are used to define a single-electron transistor charge sensor (S1), the readout zone (B0-P2), the shuttling bus (C0-C14), and four bus stops (BP1-BP4). The readout zone on the right side of the device (P3-B3) is functional but unused, and no electrons are accumulated beneath P3 or P4. A partially-magnetized cobalt micromagnet (gray) provides an inhomogeneous magnetic field profile to define and operate the qubits. No external magnetic field is present. The colored spins correspond to the qubit labels in **b**. **b** The qubit connectivity graph made possible via the shuttling bus. Solid lines indicate connections used in this work, whereby the shuttled ancilla qubit (A1) may interact with the four data qubits (D1-D4) as well as the readout ancilla (R1). This connectivity forms a surface code stabilizer plaquette in the context of a larger architecture. Dashed lines indicate connections that are physically available but unused in this work. **c** The simulated and measured Larmor frequency profile along the shuttling bus axis. Analogous values for a spin localized under the bus stop plungers (BP1-BP4) are plotted at the adjacent shuttling bus gates (C1-C13) and highlighted by the respective colors depicted in **a**.

the surface code [44], while the addition of more shuttling channels increases the architectural flexibility further [26].

The gate stack consists of four metallization layers and an on-chip micromagnet. The bottom screening gate is used as a microwave antenna

for driving resonant single-qubit gates and conditional rotations (CROT) via electric-dipole spin resonance (EDSR) [2]. The gate layer order is selected (refer to Fig. 5.1a) to maximize the tunnel coupling tunability for two-qubit interactions between the ancilla and data qubits as well as the interaction between the PSB pair, as gates in higher layers typically exhibit lower lever arms to the buried quantum well [45]. Each labeled finger gate is controlled individually, although the experiments presented here are conceptually compatible with shared control of the shuttling bus [12, 16].

The on-chip cobalt micromagnet is used to engineer the spin Hamiltonian of the array (see Sec. 5.7.17). After magnetizing the micromagnet in an external field of 1 T, the external field is turned off so that only the micromagnet remanence field remains. Fig. 5.1c shows the simulated parabolic trend in Larmor frequencies of spins located along the bus axis along with the estimated Larmor frequencies of spins localized in the adjacent bus stops. These frequencies are experimentally probed by shuttling the ancilla spin prepared in a superposition with a resonant burst and measuring the relative change in Larmor precession. We use a four-phase traveling-wave potential to propagate spins through the bus [15, 16, 46], at a speed of 1.8 m/s (see Sec. 5.7.5). The sudden steps in the measured trend indicate confinement potential roughness [47]. The shuttling operation is adiabatic, and the effective unitary acting on the spin is a phase pickup that can be calibrated explicitly or negated using a spin echo.

5.3. REMOTE TUNING

The conventional method of tuning spin qubit arrays begins with using a charge sensor to tune quantum dots into known charge states, followed by using spin physics to calibrate and refine qubit interactions. In this device, direct charge sensing with S1 is possible only up to bus stop 1, so we pioneer a remote tuning procedure that allows us to populate and virtualize control of the distant bus stops as well as tune single- and two-qubit operations without local charge sensing. Fig. 5.2a provides a conceptual illustration where a spin is placed in a superposition and shuttled to a bus stop out of charge sensing range. After pulsing the effective double-dot system to a particular balance of chemical potentials, the phase of the resulting superposition will depend on whether coherent tunneling between dots occurred. This phase is measured by shuttling the spin back to the readout zone. Fig. 5.2b depicts an instance of this tunneling, similar to measurements performed in Si-MOS and Ge/SiGe spin qubits while in range of charge sensing [11, 14].

By fixing the time of free evolution, single-electron charge stability diagrams are reconstructed from the shuttled spin phase as in Fig. 5.2c-f

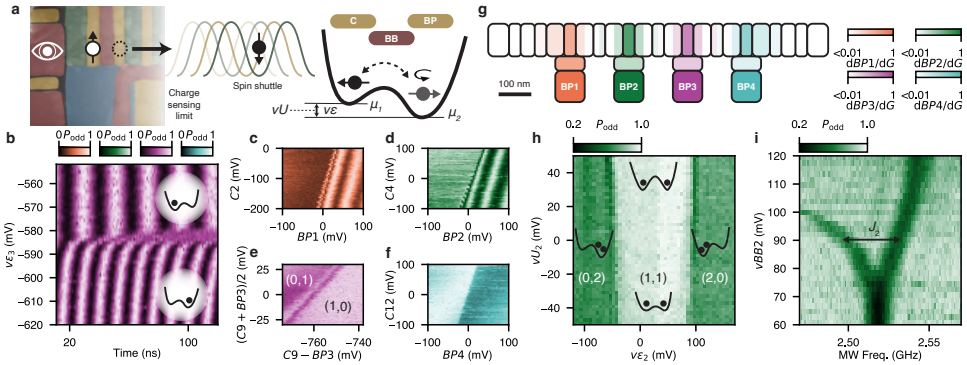


Figure 5.2: **Remote tuning protocols**. **a** Illustration of the remote tuning concept. The sensor has a limited charge sensing range and is therefore only used for qubit measurement of the ancilla spin. To probe control of the bus stops, the ancilla is shuttled beyond charge sensing range, and spin physics is used to calibrate the virtual detuning $v\epsilon \propto \mu_1 - \mu_2$ and average chemical potential $vU \propto (\mu_1 + \mu_2)/2$ for all four effective double-dot systems formed at the bus stops (see Sec. 5.7.6). **b** An example of a Ramsey tunneling experiment at bus stop 3. Coherent tunneling of the ancilla spin from the shuttling bus to the bus stop is recognized by the abrupt change in Larmor precession frequency. Colorbars are shared with **c**-**f**. **c**-**f** Examples of charge transitions identified via Ramsey tunneling experiments for bus stops 1-4 respectively with wait times on the order of tens of nanoseconds. The interdot charge transition between the shuttling bus and bus stop 3 which may be used to infer control of $v\epsilon$ and vU is shown in **e**, while the other scans are used to extract other virtual gate matrix elements. **g** Crosstalk heatmap with respect to the interdot charge transition between the bus and each bus stop extracted from scans analogous to those in **c**-**f** (see Fig. 5.8). Detectable crosstalk to multiple bus stops is indicated by split coloring. **h** An effective two-electron charge stability diagram of the isolated double dot system formed at bus stop 2 identified from the returned polarization of a shuttled spin. **i** Detection of the exchange interaction strength J_2 between a shuttled spin and a mixed spin state in bus stop 2 obtained by applying microwave bursts at the charge symmetry point as determined from **h**. See Fig. 5.7 for analogous calibrations of all four bus stops.

for all four bus stops. Based on the slope of the interdot transition, the relative capacitive coupling between all gates and the bus stop quantum dot can be inferred and compensated through gate virtualization (see Sec. 5.7.6). Fig. 5.2g illustrates a heatmap of all such electrostatic crosstalk and highlights one of the benefits of increased dot separation. While a few intermediate gates in the shuttling bus have a weak effect on two bus stops, the charge transition to each bus stop can be treated as effectively independent, allowing modular charge tuning of the array. Virtualization of the gates in the shuttling bus with respect to the bus stop plungers prevents the occurrence of unintended electron transitions to the bus stops during shuttling. However, the bus stop plunger gates are not virtualized with respect to the gates of the shuttling bus. We

therefore expect the electrostatic potential in the shuttling channel to change when gate voltages are pulsed to accumulate data qubits, and we use two different conveyor definitions for charge loading and multi-qubit operation to account for this (see Sec. 5.7.5).

After a spin has shuttled through the bus and tunneled into a bus stop, we can load a new spin into the array on-demand from the sensor S1, which doubles as an electron reservoir, in approximately 10 µs (see Sec. 5.7.7). To calibrate two-qubit logic between the ancilla qubit in the bus and a data qubit in a bus stop, the correct electrostatic balance in the effective double-dot system must be ensured. To do this, we initialize the ancilla to $|\downarrow\rangle$ after loading the bus stop with a mixed spin state. The ancilla spin is shuttled to be adjacent to the bus stop for 10 µs, and the polarization of the returned spin serves as a probe of whether tunneling to or from the bus stop and subsequent spin mixing occurred. The resulting spin signal can be used to infer two-electron charge stability diagrams as shown in Fig. 5.2h. We note that such a method could form the basis for more rigorous spectroscopy of excited valley-orbital states far from local charge sensing as well [48].

After identifying the approximate symmetry point ($v\epsilon = 0$) of the two-electron charge state in each bus stop (see Fig. 5.7i-l), the exchange splitting is probed by modulating the bus stop barrier gates to establish a suitable range for two-qubit interactions as shown in Fig. 5.2i. Exchange tunability on the order of 10 MHz is suitable for resonant controlled rotations (CROT) and adiabatic controlled-phase (CZ) operations [2], both of which provide a universal entangling gate. Verifying the tunability of all four unique exchange interactions after sequentially loading all four bus stops confirms that the loaded spins are robust to the interleaved shuttling operations and suitable for calibrating quantum logic (see Fig. 5.7m-p).

5.4. QPU CHARACTERIZATION

To operate the sparse spin qubit array as a five-qubit quantum processor, the protocol shown in Fig. 5.3a is used. First, all four data qubits are loaded into the bus stops in mixed states via shuttling the ancilla qubit and reloading as depicted in subcircuit Fig. 5.3b. After reloading the ancilla qubit for the final time, a QND protocol, expanded in Fig. 5.3c, is used to initialize both the ancilla and data qubits by measurement and using real-time feedback [42, 49]. Direct initialization of the data qubits at the readout zone prior to shuttling is possible, but the QND protocol generally permits higher measurement fidelities due to its repeatability. At the end of the initialization sequence, all spins are initialized in the ground state $|\downarrow\rangle \equiv |0\rangle$ with the exception of R1, which is initialized to $|\uparrow\rangle \equiv |1\rangle$. After universally controlling the spins with a combination of coherent shuttling, single-qubit EDSR, and two-qubit exchange, they are

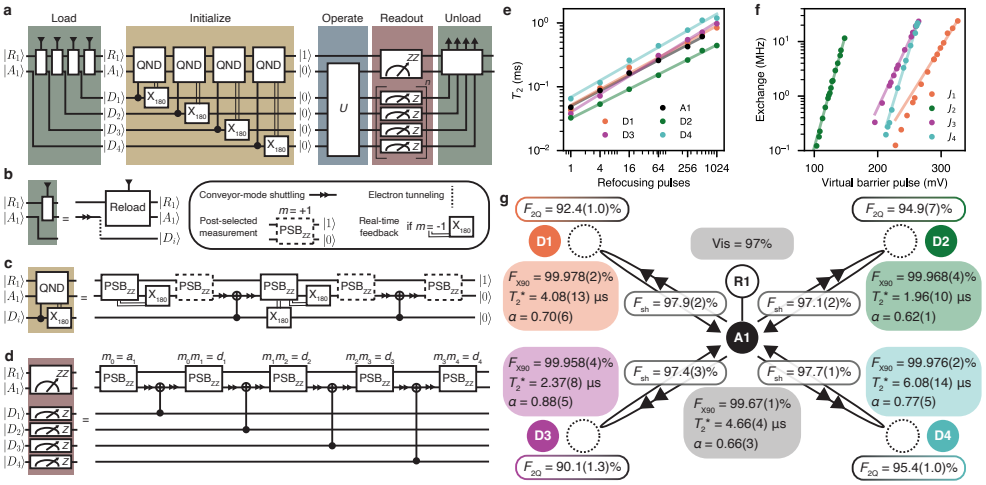


Figure 5.3: **QND measurement framework and QPU characterization**. **a** Schematic showing the overall protocol for loading, initializing, measuring, and unloading the sparse array when used as a quantum processor. **b** Building block of the loading protocol. The ancilla qubit is shuttled along the bus, tunnels into the selected bus stop, and is relabeled as a data qubit. A new ancilla is then reloaded from S1 as described in Sec. 5.7.7. **c** Building block of the initialization protocol. Two rounds of QND measurements are performed on the data qubit, with real-time feedback used to correct the measured state of both the ancilla and data qubits. Post-selection is used to further boost the initialization fidelity by filtering certain error modes, such as infidelity in the CROT. A variable number of data qubits can be initialized in any order using this fixed building block at the expense of some redundancy, but this does not cause a meaningful performance bottleneck. **d** Building block of the QND readout protocol. Extraction of the five-qubit computational-basis measurement is elaborated in Sec. 5.7.8. **e** CPMG coherence time measured for the ancilla qubit and four data qubits. Fits are according to an assumed $1/f^{\alpha}$ noise power spectral density (see Sec. 5.7.11). **f** Exchange tunability of all four interactions between data qubits and the ancilla. Fits assume an exponential relation between barrier voltage and exchange. **g** Overview of all benchmarked operations and qubit properties in the five-qubit processor (see Sec. 5.7.11 and 5.7.12).

measured using a generalized multi-qubit QND measurement, shown in Fig. 5.3d. The measurement yields up to five bits of information corresponding to the computational-basis measurement of the ancilla qubit and the four data qubits, and multiple rounds of QND measurement may be used to improve the readout fidelity of the data qubit states (see Sec. 5.7.8). After measurement, the pulsed gate voltages are returned to zero and the bus stop spins are unloaded before a next experimental cycle is initiated (see Sec. 5.7.7). The dominant timescale is the 10 µs integration time associated with each PSB measurement, and the minimal duration of an experimental cycle is about 300 µs.

We use the QND measurement framework to calibrate and characterize

all relevant operations for multi-qubit control using established methods (see Sec. 5.7.9 and 5.7.10). With dynamical decoupling, all qubits maintain coherence for hundreds of microseconds and exhibit behavior consistent with a $1/f^{\alpha}$ noise power spectral density as seen in Fig. 5.3e. We note that the data qubit coherence far exceeds the 10 µs readout time and permits coherence-preserving mid-circuit measurements in this device [50]. Fig. 5.3f illustrates the dynamic range of exchange tunability that is used to implement entangling two-qubit operations. Residual exchange between spins loaded in the bus stops is directly verified to be at least below 10 kHz, though it is likely much smaller, and therefore entangling crosstalk within the sparse array is negligible (see Fig. 5.14). We note that the residual exchange between data qubits and the ancilla is not relevant as the ancilla never idles adjacent to any bus stop.

Fig. 5.3g illustrates all benchmarks when the device is fully operational. Although the single-qubit fidelities F_{X90} are respectable when compared with the state-of-the-art [37], we find that the two-qubit gate fidelities F_{2Q} are limited by incoherent noise in the exchange interaction strength (see Fig. 5.15). Previous demonstrations in two-qubit devices show that the technology is capable of two-qubit gate fidelities well over 99% [38–40, 51, 52], and it will require ongoing work to routinely incorporate higher-fidelity two-qubit gates in a multi-qubit setting.

We characterize the 1.2 µm round-trip shuttling path to have a single-qubit fidelity of 97.7(1)% with respect to an identity operation when the array is operated as a five-qubit processor. The largest error contribution is associated with the charge transition from below P2 to C0. We estimate the remaining infidelity to be consistent with dephasing and discuss the possible role of valley excitations further in Sec. 5.7.11. Although higher shuttling fidelity has been reported over a larger cumulative distance [15], our results demonstrate the longest coherent spin shuttle over a real distance in silicon. While further refinement of the traveling-wave potential would likely enhance both the speed and fidelity of shuttling by reducing dephasing, the total error budget for operating all five qubits is dominated by the two-qubit interactions (see Sec. 5.7.13).

5.5. PARITY CHECKS

To demonstrate both phase-coherent two-qubit interactions and the utility of the shuttling-enabled connectivity across the full system, we demonstrate up to weight-four parity checks of the data qubits and five-qubit entanglement. A central consideration for operating multi-qubit registers with shuttling is that moved spins will accrue phase in the rotating frame in which they are being resonantly controlled. In this device, the ancilla qubit will pick up a phase as it travels in the inhomogeneous magnetic field. The data qubits, although stationary, also

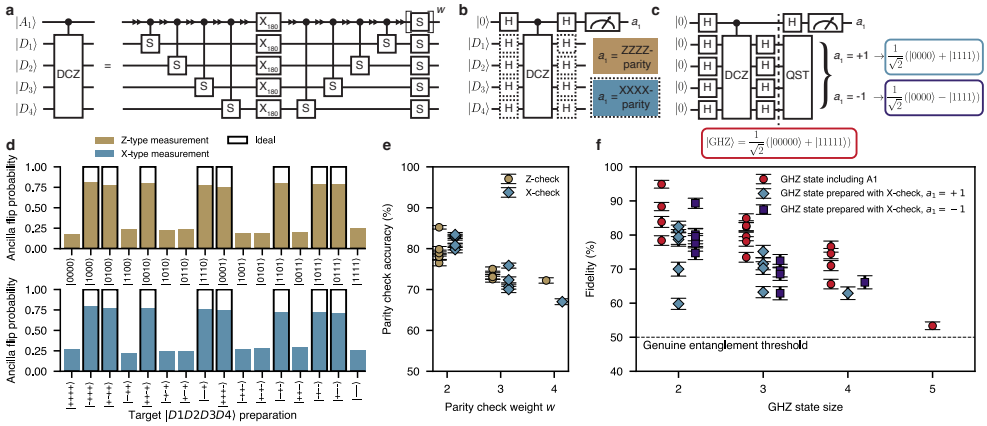


Figure 5.4: **Benchmarking parity checks and multi-qubit entanglement**. **a** Quantum circuit depicting the multi-qubit decoupled CZ used for coherent two-qubit operations. The circuit generalizes to any number w of data qubits by omitting or adding quantum wires of different data qubits. Single-qubit gates are parallelized pairwise when relevant, and the $2w$ S gates are applied virtually. **b** Quantum circuit depicting a weight-four Z-type parity check utilizing the multi-qubit decoupled CZ from **a**. The circuit generalizes to any number of data qubits by changing the weight w of the decoupled CZ. An X-type check is performed with the inclusion of the dashed Hadamard gates. **c** Quantum circuit depicting w-qubit GHZ state generation using an X-type parity check. The dashed line indicates when the ancilla forms a $w+1$-qubit GHZ state with the data qubits. The outcome of the ancilla measurement determines which of two GHZ states are realized in the data qubits. One of the two outcomes can be used as a logical state of a four-qubit quantum error correction code. **d** Outcomes of the weight-four Z-type (X-type) parity check obtained after preparing all Z-basis (X-basis) eigenstates of the data qubits. The black wireframes indicate the ideal result for each input state, and we estimate that data qubit initialization errors contribute a discrepancy of 2% in the observed ancilla outcome. All other parity checks are shown in Fig. 5.21. **e** The parity check accuracy for all Z- and X-type parity checks of weights two through four computed as the average probability that the ancilla measurement is correct and the data qubits are measured in the intended prepared state. Data qubit initialization and readout errors are removed by rescaling, and error bars signify $\pm 1\sigma$ as determined by Monte Carlo bootstrapping (see Sec. 5.7.15). **f** GHZ state fidelities for all combinations of two or more qubits in the five qubit processor (some overlap closely). State fidelities including the ancilla are calculated with respect to the GHZ state $\frac{1}{\sqrt{2}}(|0\rangle^{\otimes(w+1)} + |1\rangle^{\otimes(w+1)})$. For GHZ states initialized via a weight-w parity check, the state fidelities are calculated with respect to $\frac{1}{\sqrt{2}}(|0\rangle^{\otimes w} \pm |1\rangle^{\otimes w})$. Error bars signify $\pm 1\sigma$ as determined by Monte Carlo bootstrapping (see Sec. 5.7.14). All reconstructed density matrices are shown in Fig. 5.17, Fig. 5.18, Fig. 5.19 and Fig. 5.20 along with the estimated fidelities in the absence of initialization and readout error removal.

pick up a phase due to the stray electric fields from the shuttling pulses coupling to the spins via the magnetic field gradient. These phases depend on the shuttling path and the number of two-qubit interactions carried out on the way, and therefore may lead to a large overhead in the

number of calibrated parameters.

To avoid this, we perform two-qubit logic using a decoupled CZ gate shown in Fig. 5.4a. In addition to decoupling low-frequency noise, the X_{180} gates also refocus the single-qubit phase pickups acquired during both shuttling and two-qubit gates provided the operation is symmetric. The pairs of native conditional-S gates are implemented by adiabatically modulating the exchange interactions, which commute with the refocusing pulses, and enable a maximally entangling operation between the ancilla and any combination of the data qubits depending on which two-qubit interactions are enabled. The single-qubit operation on the ancilla has the highest quality when the spin is localized below gate P2, and therefore the implemented decoupled CZ operation employs two rounds of shuttling. However, this is not a fundamental requirement of the approach.

The parity of any multi-qubit Pauli operator acting on any subset of the data qubits can be extracted with the appropriate change in basis of the data qubits as shown in Fig. 5.4b. Fig. 5.4c shows how a weight-w X-type parity check acting on an input state $|0\rangle^{\otimes w}$ is used to probabilistically generate maximally entangled w-qubit states that differ by a single-qubit Pauli operation. In the case of a weight-four parity check, one of the post-selected states is the logical state of a $[[4,1,2]]$ surface code while the other state is outside of the code space. We can therefore benchmark the quality of the parity checks in two ways. First, we ensure that all eigenstates of Z- and X-type parity observables are detected and preserved properly. Second, we generate multi-qubit entanglement generated via the parity checks as a more stringent test of the parity check performance.

Fig. 5.4d shows the measured ancilla state when weight-four Z- and X-type parity checks act on all of the respective input eigenstates. Imperfections between the ideal ancilla outcome and the measured parity are a result of imperfect state preparation of ancilla and data qubits, finite ancilla measurement fidelity, finite ancilla shuttling fidelity, and finite single- and two-qubit gate fidelity. Additionally, we measure the data qubit state after the parity check and calculate the parity check accuracy as the probability that both the ancilla outcome is correct and the intended prepared state is observed. Fig. 5.4e tabulates this parity check accuracy for all data qubit combinations. The weight-four parity check accuracy of 72.2(6)% (67.0(7)%) therefore establishes the quality with which the parity of the $ZZZZ$ ($XXXX$) eigenbasis can be detected and conserved. The primary difference between X- and Z-type checks is the larger number of single-qubit rotations required in the former case. In Sec. 5.7.15, we show an example of performing 35 repeated weight-two parity checks with a retention rate above 93%.

When benchmarking the check performance on eigenstates, the data

qubits are ideally $|0\rangle$ or $|1\rangle$ throughout the decoupled CZ operation and, due to the long T_1 times of spin qubits, robust to decoherence. The generation of entanglement is therefore a stronger test of the parity check performance, as the quantum state of the system will be maximally sensitive to operational errors, including the error rates associated with spin shuttling and crosstalk. Fig. 5.4f tabulates the GHZ state fidelities of all combinations of entangled states possible in the five-qubit processor. After accounting for measurement errors, the observed fidelities are comparable to the best multi-qubit entangled states generated with gate-defined semiconductor spins [42, 53, 54], and we observe genuine five-qubit entanglement ($F_{\mathrm{GHZ}} > 50\%$) for the first time in the platform.

By postselecting the state of the ancilla measurement, we probabilistically initialize the data qubits into the logical state of a $[[4, 1, 2]]$ surface code with a state fidelity of 62.9(1.8)%. This central result highlights that our implementation of parity checks is suitable for more sophisticated QEC experiments [55]. We note that this procedure requires five-qubit entanglement, and we demonstrate higher four-qubit GHZ state fidelities up to 76.6(1.6)% with qubit combinations that include the ancilla. In Sec. 5.7.13, we formulate a budget of all characterized error sources and conclude that the majority of the error originates from infidelity in the two-qubit exchange interactions. Dephasing during shuttling and idling constitutes about a quarter of the total error, and increasing the speed of shuttling is the most direct means to lower this contribution.

5.6. CONCLUSION

The incorporation of spin shuttling into a multi-qubit setting has implications both for how semiconductor spin-based quantum processors are operated and the level of performance they can achieve. We have shown that shuttling can be used to tune universal multi-qubit control without the need for local charge sensing throughout an array. The presented tuning protocols are only limited by the distance over which the shuttling operation maintains spin coherence. With high-fidelity shuttling already demonstrated over a 10 µm length scale [15], we expect that the approach presented here is sufficient to tune on the order of 100 qubits using a single charge sensor and ohmic contact in prototype industrial layouts [56]. Due to the lower degree of electrostatic crosstalk in sparse arrays, this calibration would be modular and scale linearly with the number of qubits in the worst case. The addition of more shuttling channels further increases architectural flexibility and will be essential to avoid a measurement bottleneck.

Despite the finite fidelity of shuttling, we have shown that generating and preserving multi-qubit entanglement is not only versatile but was achieved over more spins than in past experiments. The connectivity

enabled by shuttling allows for QND parity check measurements to be performed on flexible combinations of nonlocal data qubits. The device studied here supports the necessary operations required to implement a minimal $[[4, 1, 2]]$ code with pipelined syndrome extraction of the three necessary checks [57]. The successful implementation of repeated parity checks will require further enhancement of the parity check quality. In particular, the low two-qubit gate quality observed in this device is limited by incoherent noise, but the methods used here are fully compatible with achieving error rates below 1%.

Utilizing the operational right side of the device as a second ancilla and readout zone, complete single-shot syndrome extraction of a $[[4, 2, 2]]$ toric code could be explored [58]. Zero-distance state-preservation protocols would also be possible [59, 60]. The non-planar connectivity possible in larger sparse devices would permit more exotic encodings as well. The success of future implementations of quantum memories with gate-defined semiconductor spins depends on systematically combining the high fidelities and long coherence times that are now routinely demonstrated in smaller and industrially-fabricated devices with the versatile and extensible control possible in sparse architectures.

5.7. SUPPLEMENTARY MATERIAL

Sec. 5.7.3 has been included to provide additional details on the commissioning of the device and does not appear in the preprint [1].

5.7.1. DEVICE FABRICATION

The device is fabricated on an isotopically purified ^{28}Si/SiGe heterostructure containing a 7 nm thick strained quantum well [18], 30 nm SiGe buffer passivated with an amorphous silicon cap, and a 10 nm atomic layer deposition of insulating Al_2O_3. The heterostructure is nominally equal to that in previous studies where large average valley splitting in excess of 200 µeV [18] and high fidelity shuttling [15] have been observed. The four proceeding Ti:Pd layers have thicknesses of 3:17, 3:27, 3:27, and 3:27 nm respectively and are each followed by 5 nm atomic layer deposition of Al_2O_3. Finally, a 3:150 nm Ti:Co micromagnet is evaporated.

5.7.2. EXPERIMENTAL SETUP

The experiments are performed in an Oxford Instruments ProteoxMX dilution refrigerator where the mixing chamber temperature is held at 200 mK to mitigate heating effects [61]. A driven superconducting vector magnet is used to magnetize the on-chip micromagnet in a field of 1 T and is otherwise unpowered. The device is glued with GE varnish to a

copper plate in direct thermal contact with the mixing chamber and is wirebonded to an in-house PCB. We apply DC bias voltages supplied by battery-powered home-built voltage source modules (D5a) and generate baseband control and readout pulses with a Qblox Cluster equipped with 8 4-channel QCM AWG modules and a QRM module for rf-reflectometry readout. DC channels are filtered with a combination of PI and RC filters with a nominal cutoff frequency of about 20 Hz. AC channels are filtered by ferrite chokes, pass through UT85 stainless steel semi-rigid coaxial cables, and are attenuated by 20 dB at 4 K to balance thermalization and having a large dynamic range for baseband pulsing. The ± 2.5 V output range of the AWG channels corresponds to a ± 500 mV available range at the device. The DC and AC signals are combined through bias tees with a time constant of 100 ms. Two channels of a QCM module are used for IQ modulation of a Rohde & Schwarz SGS100A vector source. We set the local oscillator of the vector source to 2.27 GHz to ensure that all target qubit frequencies fall on the same sideband within the 400 MHz bandwidth of the QCM. The output power of the vector source is set to 6 dBm.

The rf tone for readout is generated by the QRM, attenuated by 40 dB at room temperature and 20 dB at 4 K, and the input and output signals pass through a MiniCircuits ZEDC-15-2B directional coupler at the mixing chamber stage. The input power is set to optimize the signal-to-noise ratio (SNR) of charge sensing. The output signal is carried through a superconduting NbTi UT85 cable to a Cosmic Microwave Technologies CMT-BA1 cryogenic amplifier mounted at the 4 K stage which provides approximately 30 dB of amplification. The signal is further amplified at room-temperature with a home-built amplifier (standalone M2j) which provides an additional 45 dB of amplification before being filtered, digitized, and demodulated by the QRM. The demodulated signal is digitally rotated to the in-phase quadrature to make use of real-time feedback.

5.7.3. INITIAL DEVICE TESTING

A preliminary screening of fabricated devices is performed via atomic force microscopy (AFM) and scanning electron microscopy (SEM) of test structures on the fabricated coupon sharing the same layout with the devices. As good alignment of the coupon was verified, the devices were directly screened in the dilution refrigerator. The available alternative, dipping the bonded sample in liquid helium, poses a risk for the multi-layered PCBs unless thoroughly dessicated of moisture before. The slower cooldown in the dilution refrigerator while under vacuum provides more reliable results.

A preliminary test of the loaded sample at room temperature makes

use of a ohmmeter. As the insulating oxide beneath the active bondpads of the sample is etched prior to deposition of each gate layer, the direct contact to the room-temperature substrate provides a conductive path to all other bonded lines such that a 2-point measurement of resistance reads on the order of a few MΩ. Any discontinuities, such as a missing bond wire, would appear as open circuits. The conductive substrate also provides some protection against electrostatic discharge (ESD) at room temperature, as voltage transients dissipate through the substrate as opposed to the finger gates of the quantum dot region. When cooled to 4 K, carriers in the heterostructure are frozen out and all lines are measured as open circuits.

After cooling below 1 K, rf-reflectometry is verified by searching for LC circuit resonances with a spectrum analyzer. We then proceed to verifying DC transport through both SET structures as well as the conveyor channel. This is shown for the latter in Fig. 5.5. Although the adjacent bus stop gates cannot pinch off the channel entirely, their large effect on the conducted current is an indication that they operate normally as shown in Fig. 5.6. A −100 µV source-drain bias with negative polarity is used such that the desired I-V curve is distinguishable from leakage of the positively-biased gate electrodes. After verifying DC transport, we benefited from a complete thermal cycle to reset hysteresis before tuning up sensors with rf-reflectometry.

The pinch off voltages within the channel provide a first guideline for DC voltages that allow the device to be accessible by shuttling. We see that the channel gates pinch off with reasonable uniformity around 1 V. With the intention of avoiding unwanted static charge occupation, we set the preliminary DC voltages of the conveyor and bus stop gates to be in the range of 700 mV-800 mV. The DC tests on the bus stop gates do not provide such a quantitative guideline. Based on electrostatic simulations, we estimate that the bus stop plunger voltages need to be about a factor 1.5 larger than the conveyor gate voltages in order to create a balanced double-dot potential, and the bus stop barriers need to be on the order of the conveyor gate voltages in order to create a reasonable tunnel coupling between two localized charges. We therefore set the bus stop plungers to 1200 mV and the bus stop barriers to 750 mV as a reasonable starting point to tune the array.

5.7.4. ANCILLA READOUT

Charge sensing is achieved via an rf-SET measurement. The 2DEG leads of each SET are accumulated according to the split-gate method, whereby the rf signal is capacitively coupled to the 2DEG via an accumulation gate to miminimize series resistance and remove leakage pathways [62]. An LC tank circuit is formed with a NbTiN meandering superconducting

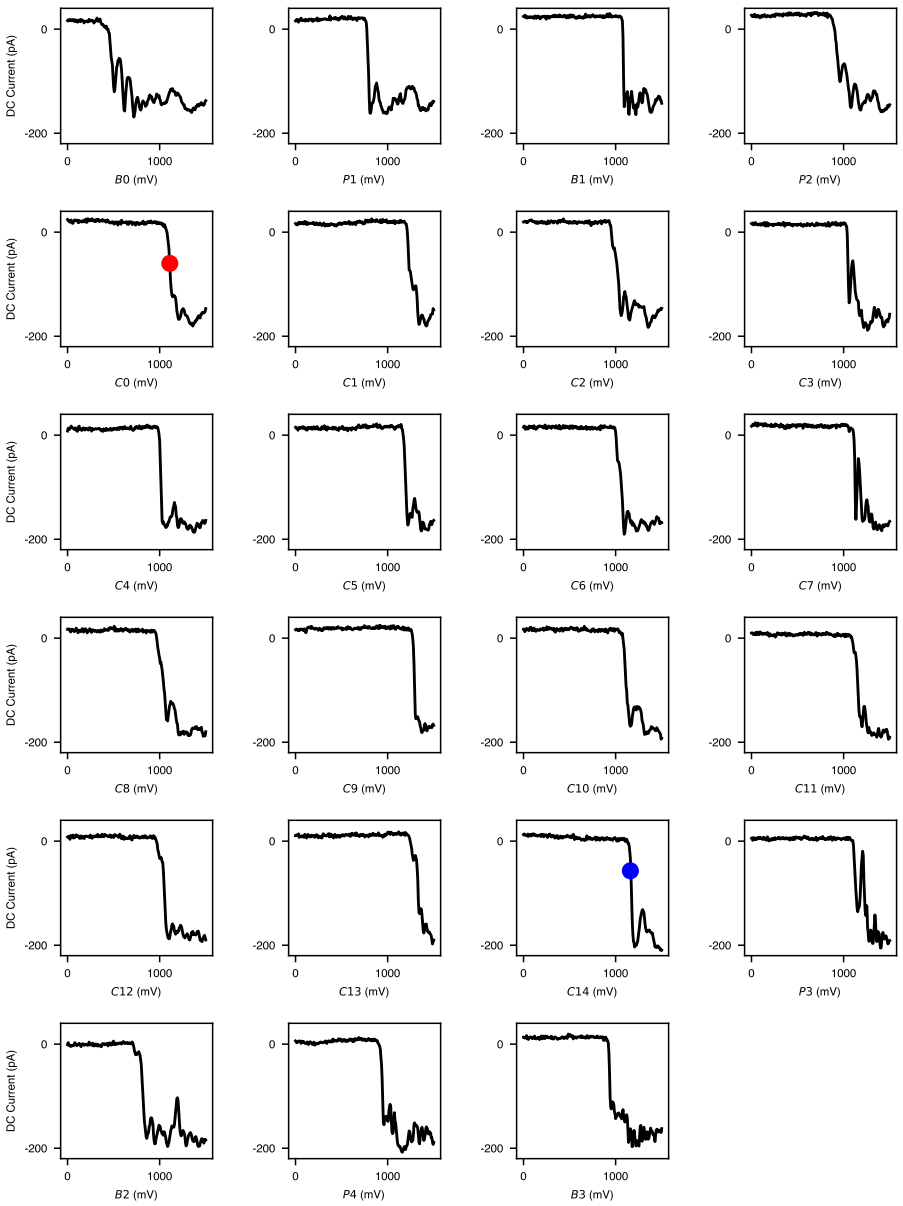


Figure 5.5: (Continued on next page)

Figure 5.5: (Continued) Collection of turn-on voltages measured during initial sample screening. We use a negative bias voltage from source to drain to differentiate the measured current from an undesired positive leakage current that passes through the swept gate. The colored points indicate the settings used to test bus stop gates. The data presented is from the sample which was subsequently used for all experiments in this work.

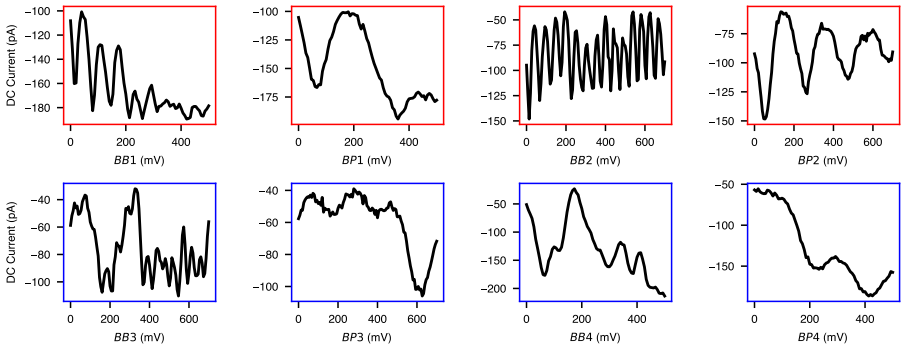


Figure 5.6: Collection of DC voltage sweeps for all 8 bus stop gates to test their effect on conduction through the conveyor channel. For bus stops 1 and 2, $C0$ is set to 1.15 V as shown in Fig. 5.5 while all other gates are accumulated in order to create an electrostatically sensitive channel near the tested gates. For bus stops 3 and 4, $C14$ is set to 1.18 V by the same reasoning.

nanowire with a nominal kinetic inductance on the order of a few μH, the series capacitance between the accumulation gate and the 2DEG, and the parasitic capacitance between the bond wires and the PCB ground plane, giving rise to a resonance frequency of 114.3 MHz.

Spin to charge conversion is achieved via parity-mode PSB. The Zeeman energy difference of about 100 MHz between the readout ancilla R1 and ancilla A1 lifts blockade of the $|T_0\rangle$ spin triplet, resulting in an effective $Z \otimes Z$ observable for the qubit pair [43]. The (4,0)-(3,1) interdot charge transition is used such that R1 occupies the dot where the lowest valley-orbit shell is filled, increasing the energy required to lift blockade. A charge stability diagram of this region can be seen in Fig. 5.9b.

PSB is first tuned in isolation-mode, where the tunnel barrier to the reservoir (S1) is completely closed, as this makes the visual characteristic easier to recognize during manual tuning with video-mode charge state measurements while sweeping the respective plunger gates of the PSB pair. After initial identification of the qubit resonances, PSB is retuned with a finite reservoir coupling to allow for efficient qubit reloading.

The tunnel coupling between the quantum dots of the readout pair is pulsed to be on the order of several GHz such that the singlet state $|S(4,0)\rangle$ evolves adiabatically to the $|\uparrow\downarrow\rangle$ spin state of the (3,1)

configuration with a 50 ns linear voltage ramp. This allows for the initialization of an unblockaded $|\uparrow\downarrow\rangle$ state via post-selection. Real-time feedback serves to enhance the fraction of post-selected measurement shots by flipping the state of A1 if blockade is detected during initialization. Although we conceptually identify the ancilla qubit as the single spin A1 that is shuttled through the device, it is technically correct to attribute the qubit to the parity of the $|R1\rangle \otimes |A1\rangle$ spin state. The initialization and readout protocols of Fig. 5.3 only require PSB to be parity-preserving to function correctly.

After achieving reasonable readout visibility with manual tuning, the visibility of Rabi oscillations is used as a cost function for a CMA-ES optimizer to maximize the quality of initialization and readout [63]. The optimizer takes as parameters the voltage pulse amplitudes on all gates immediately surrounding the double quantum dot system hosting the readout pair, as well as the durations of piecewise-linear voltage ramps defining the readout sequence. We routinely achieve ancilla qubit visibilities of about 97% with such an optimization, corresponding to initialization and readout error rates below 1%, while using an integration time of 10 µs.

5.7.5. CONVEYOR-MODE SHUTTLING

To generate the traveling-wave potential for the shuttling bus, we make use of a four-phase conveyor-mode pulse template as in [12, 15, 16, 46, 47]. During conveyor operation, every participating virtual gate $\mathrm{vG} \in \{\mathrm{vC0}, \ldots \mathrm{vC12}, \mathrm{vU}_1, \mathrm{v}\epsilon_1, \ldots, \mathrm{vU}_4, \mathrm{v}\epsilon_4\}$ is assigned a voltage vG such that:

$$vG(t) = vG^{\mathrm{offset}} + vG^{\mathrm{amp}} \sin(2\pi f_{\mathrm{conv}} t - \phi_G), \tag{5.1}$$

where $\phi_G = m\pi/2$ for integer $m = G \mod 4$ such that every fourth virtual gate is in-phase. vU_{1-4} and $\mathrm{v}\epsilon_{1-4}$ are used in place of vC1, vC5, vC9, and vC13 to avoid unwanted charge transitions at the bus stops during shuttling. All gate voltages oscillate with the conveyor frequency f_{conv}, and the constant offsets vG^{offset} and amplitudes vG^{amp} are unique to each individually-controlled gate. The set of parameters $\{f_{\mathrm{conv}}, vG^{\mathrm{offset}}, vG^{\mathrm{amp}}\}$ constitutes a conveyor definition. The pulses are applied in addition to the constant DC bias voltages vG^{DC}.

All shuttling experiments begin with the ancilla A1 located below P2. A linear voltage ramp to $\{vG(0)\}$ pulls the charge below C0, and the traveling-wave potential minimum progresses by four gate lengths for every conveyor cycle of duration $t_{\mathrm{conv}} = 1/f_{\mathrm{conv}}$. The ancilla is therefore localized adjacent to bus stops 1-4 at $t/t_{\mathrm{conv}} = 0.25, 1.25, 2.25, 3.25$ respectively. When the conveyor voltages are held constant at a fixed time, additional gate voltage pulses (e.g. for activating an exchange

interaction) are applied in linear combination with the paused conveyor. The direction of the traveling-wave potential is reversed by flipping the sign of f_{conv} and adding a time-dependent offset to ensure there is no sudden discontinuity in the conveyor. The charge returns from below C0 to below P2 by linearly ramping all conveyor voltages to zero.

Two conveyor definitions are used during operation of the array. The first is a coarse-tuned conveyor that is used to shuttle uninitialized spins past unpopulated bus stops during loading and unloading. This is achieved by manually tuning $\{vG^{\mathrm{amp}}\}$ and, if necessary, the DC gate voltages, to ensure good charge shuttling fidelity. Coherent spin shuttling fidelity is unimportant for this conveyor definition.

The second conveyor definition is used when the bus stops are loaded with single electrons, and therefore the electrostatic landscape of the bus is different than during loading (which is ordered from bus stop 4 to bus stop 1 to avoid this issue). Here, coherent spin transfer is relevant, and we make use of CMA-ES optimization to fine tune $\{vG^{\mathrm{offset}}, vG^{\mathrm{amp}}\}$. As a cost function, we use an echo-type experiment where the spin is shuttled 10 times back-and-forth in total from P2 to C13 [63]. The spin visibility serves as a proxy for the dephasing experienced during shuttling making it an easy-to-evaluate cost function for optimization.

The Larmor frequencies along the optimized conveyor as shown in Fig. 5.1c are extracted by preparing the shuttled spin in superposition and observing the precession frequency after transporting the spin to various points along the array.

5.7.6. SINGLE-SPIN REMOTE TUNING

After confirming the operation of the shuttling bus, the loading protocol of the bus stops can be tuned. For this, we leverage the availability of EDSR throughout the bus to perform Ramsey experiments with respect to various rotating frames, but we note that the strategy we use is compatible with not having single-spin control throughout the array. The minimum requirement is the ability to prepare a spin in a superposition state and shuttle it coherently.

During initial tuning, no gate virtualization has taken place beyond the readout zone, and the ability to load the bus stops is probed by applying a physical detuning pulse $\epsilon_i = Cj - BPi$ where Cj is the conveyor gate adjacent to bus stop i ($j = 1, 5, 9, 13$ for bus stops 1-4 respectively). Fig. 5.7a-d shows the first convincing experimental signatures of bus stop loading before any virtualization takes place. To verify that the bus stop is the most likely destination for the tunneled electron, we repeat the loading experiments while pulsing negatively on the surrounding conveyor gates. This provides evidence that tunneling is not taking place within the shuttling bus.

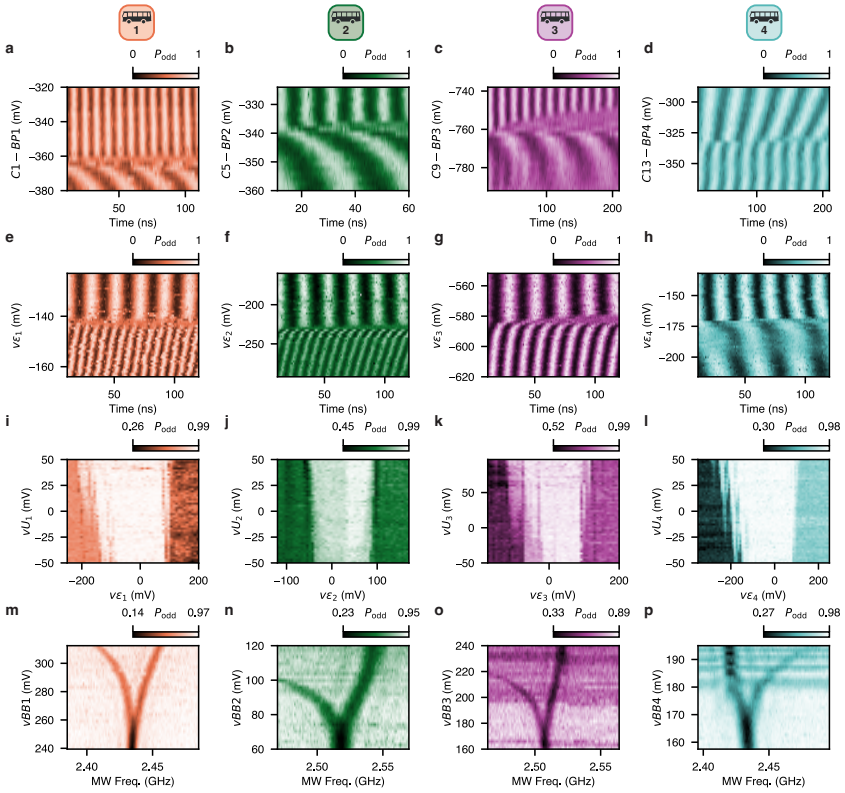


Figure 5.7: **a-d** First signatures of remote single-electron charge transitions measured within the four bus stops when exploring the empty array by shuttling a spin in superposition before gate virtualization or tunnel coupling tuning had taken place. **e-h** Remote single-electron charge transitions measured within the four bus stops after virtualizing control of each effective double-dot system and increasing the tunnel coupling. A fixed ramp time of 40 ns was used, therefore the tunneled spin picks up a phase that depends on the magnitude of the detuning pulse. The Larmor precession frequency in each dot is effectively constant. **i-l** Remote two-electron charge stability diagrams measured for all four bus stops when all other bus stops are populated with a single-electron. Multiple features parallel to the charge transition line likely indicate tunneling to excited orbital states. **m-p** Exchange splitting measured with EDSR for all four bus stops when all other bus stops are populated with a single electron. The four bus stops are color-coded for clarity, but the measured signal is the probability of an odd-parity PSB outcome P_{odd} in all cases.

The Larmor frequency difference between the spin when localized in the bus and in the bus stop encodes information about its position in the phase of the spin state. For each bus stop, we select a free induction time on the order of tens of nanoseconds to optimize contrast between

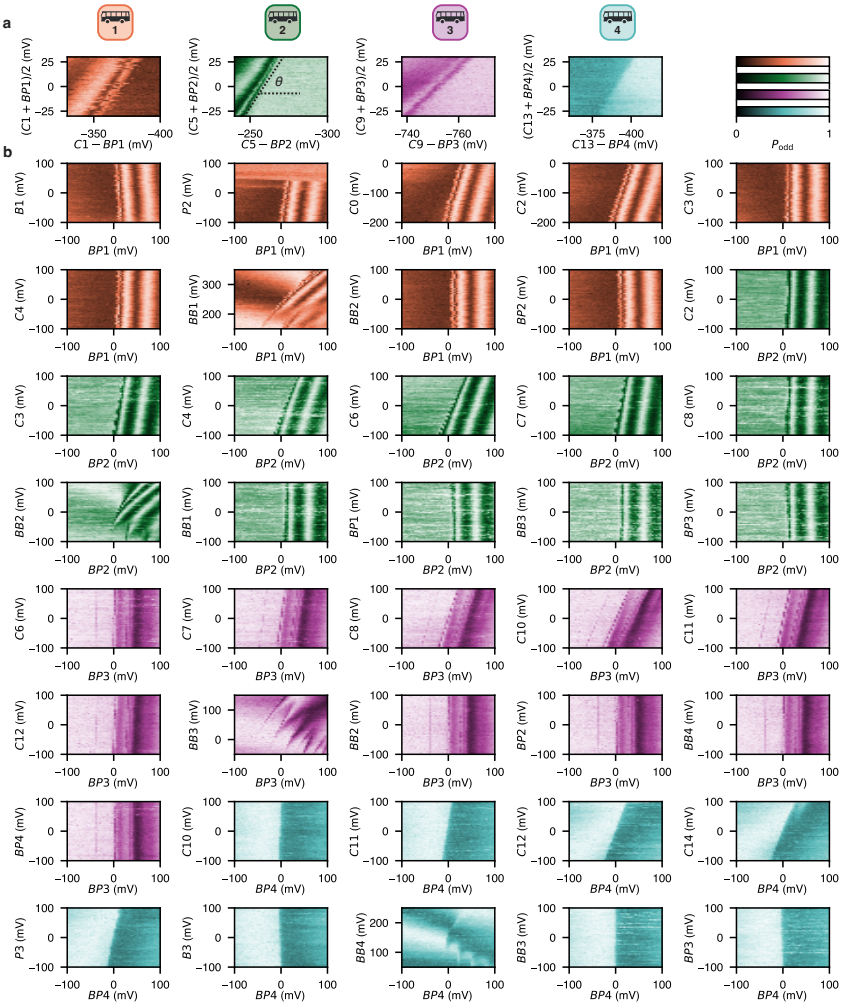


Figure 5.8: **a** Single-electron charge stability diagrams measured via the phase pick-up of a tunneled spin in superposition for each of the four bus stops. The four bus stops are color-coded for clarity, but the measured signal is the probability of an odd-parity PSB outcome P_{odd} in all cases. The angle θ, which allows for calibration of the virtual detuning and average potential as described in Sec. 5.7.6, is labeled. **b** Analogous gate-gate virtualization measurements for all gates G in the vicinity of each bus stop. The extracted slopes dBPi/dG from all scans are represented as a heat map in Fig. 5.2g.

the two cases, and we use this signal to virtualize control of the effective double-dot system as well as the surrounding conveyor gates. First, we focus on the gate voltage subspace consisting of the physical conveyor gate voltage C_j and physical bus stop plunger gate voltage BPi. In the case of bus stop 1, these gates are already virtualized with respect to the readout zone, but not to each other, and the following procedure is the same regardless of any pre-existing virtualization.

We define unvirtualized detuning and average potential parameters ϵ_i, U_i that relate to voltages Cj, BPi as $(\epsilon_i, U_i)^T = V\,(Cj, BPi)^T$ where:

$$V = \begin{pmatrix} 1 & -1 \\ 0.5 & 0.5 \end{pmatrix}. \tag{5.2}$$

We want to identify corresponding virtual gates vCj and $vBPi$, where $(vCj, vBPi)^T = M_i\,(Cj, BPi)^T$, such that the virtual detuning and average potential, defined as $(v\epsilon_i, vU_i)^T = V\,(vCj, vBPi)^T$, relate to the double-dot chemical potentials as sketched in Fig. 5.2a. Explicitly, this means $v\epsilon_i \propto \mu_{\mathrm{Cj}} - \mu_{\mathrm{BPi}}$ and $vU_i \propto (\mu_{\mathrm{Cj}} + \mu_{\mathrm{BPi}})/2$ where μ_{Cj} and μ_{BPi} are the chemical potentials of the dots formed below gates Cj and BPi respectively. An interdot charge transition to bus stop i should therefore only be modulated by $v\epsilon_i$.

The interdot charge transitions measured when sweeping the physical detuning and average potential parameters (see Fig. 5.8a) show a finite (positive) slope $\mathrm{d}\epsilon_i/\mathrm{d}U_i = \tan\theta_i$ from which it follows that $(v\epsilon_i, vU_i)^T = R(\theta_i)\,(\epsilon_i, U_i)^T$ where $R(\theta_i)$ is a counterclockwise rotation about the origin $(\epsilon_i = v\epsilon_i = 0, U_i = vU_i = 0)$ by an angle θ_i such that $\tan(\theta_i) = d\epsilon_{\mathrm{BS,i}}/dU_{\mathrm{BS,i}}$. We therefore have $M_i = V^{-1}R(\theta_i)V$. Applying the elements of M_i to the total virtual gate matrix permits direct control over the virtual detuning and average potential.

To virtualize any other gate G with respect to each bus stop plunger BPi, the same experiment definition is used where the slope $\mathrm{d}BPi/\mathrm{d}G$ of the interdot transition informs both the degree of influence of the gate voltage G on the chemical potential below gate BPi and therefore the virtual gate definition vG required to offset the effect (see Fig. 5.8b). The slope $\mathrm{d}BPi/\mathrm{d}Cj = (2 - \tan\theta_i)/(2 + \tan\theta_i)$. This provides all slopes plotted in the crosstalk heatmap of Fig. 5.2g.

Fig. 5.7e-f shows the loading experiments repeated after gate virtualization has taken place. In certain cases, the tunnel coupling between the bus and bus stop dots is pulsed during tunneling to smoothen the transition compared to the preliminary loading. The two-electron charge stability diagrams reconstructed from the shuttled spin polarization in Fig. 5.7i-l also show charge transitions that are effectively orthogonal to the virtualized detuning axis, confirming the validity of this approach.

5.7.7. SPIN RELOADING

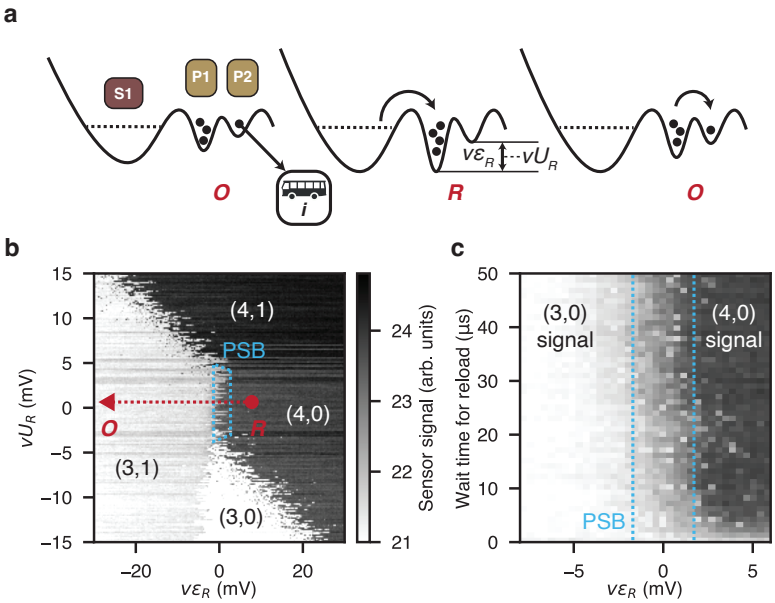


Figure 5.9: **a** Illustration of the reload protocol. After shuttling the ancilla spin to a bus stop, the charge state of the readout pair is blockaded in the metastable (3,0) charge state at the operation point *O*. When the detuning is pulsed to the reload point *R*, the blockade is lifted and a fourth electron quickly tunnels from S1 to the readout ancilla dot. The double-dot system returns to the (3,1) charge state upon ramping the detuning back to the point *O*. **b** rf-reflectometry measurement of the equilibrium charge stability diagram of the readout pair. The PSB region is highlighted by the blue dashed lines. The detuning axis followed to go from the operation point *O* to the reload point *R* is shown by the red dashed line. **c** Averaged rf-reflectometry time-traces after waiting at different reload points along the detuning axis of **b** after the system has been initialized in the metastable (3,0) charge state. Between *O* and the PSB region, blockade persists for at least 20 ms. Beyond the PSB region, the reload time scale is on the order of 10 μs. The colorbar is identical to that of **b**.

Fig. 5.9a illustrates the procedure used for reloading a new spin into the array after the original ancilla has been shuttled to occupy a bus stop. The sensor S1 doubles as an electron reservoir from which qubits can be loaded on-demand. It has a small but finite tunnel coupling to the dot below P1 where the readout ancilla R1 remains and a weaker coupling to the dot below P2 where the ancilla A1 is initialized as can be seen in the measured charge stability diagram of Fig. 5.9b.

After shuttling the ancilla, the voltage configuration in the readout zone remains at the operation point *O* in the quasi-equilibrium (3,0) charge state. As the direct tunnel rate to (3,1) is very slow, this charge configuration persists for at least 20 ms and is limited by the bias-tee

charging time of the sample PCB. No unwanted electrons tunnel into the empty dot during the experiments. To reload on-demand, the virtual detuning of the readout pair $v\epsilon_R$ is pulsed to the reload point R. The rate at which a new charge enters is evident from Fig. 5.9c. Pulsing beyond the PSB region of the interdot transition allows for a relatively fast loading to the (4,0) state in less than 10 µs, and ramping the detuning back to O returns the system to the equilibrium (3,1) charge state and restores the ancilla spin. No additional barrier pulse (i.e. on gate B0) is used to modulate the tunnel rate, and including one could increase the loading speed further. This reloading procedure repeats until all bus stops are occupied and the final ancilla spin is reloaded, after which the initialization protocol may begin.

The bus stop spins are unloaded in one of two ways. First, they may be shuttled back to the readout zone in a sequence inverse to the loading protocol. In this case, the five-electron charge state at the readout zone quickly equilibrates to the (3,1) charge state in about 1 µs, and no detuning pulse is necessary. Alternatively, we can simply ramp all pulsed voltages back to their DC condition without any traveling-wave potential used. Bias-tee compensation pulses are applied over a period of several tens of microseconds before the next experimental shot begins, and the free spins vacate the bus stops within this time scale, presumably to one of the 2DEG reservoirs on either side of sparse array. We observe no adverse consequences when unloading spins in this manner, and this approach is used for most experiments presented in this work.

The necessity for unloading and subsequent loading is set by the finite bias-tee time and amplitude range of the AWG modules. In future work, loading bus stops or other remote quantum dots with DC voltages would eliminate the need for spin reloading altogether.

5.7.8. QND MEASUREMENT

All qubits in the effective five-qubit processor can be measured in the computational basis as illustrated in Fig. 5.3d by a sequence of parity-mode PSB measurements $m_0, m_1, m_2, \ldots$. We use the convention that each projective measurement ideally yields $m_k = +1$ when an odd-parity spin state $|R_1\rangle \otimes |A1\rangle$ is present and $m_k = -1$ when an even-parity spin state is present.

The ancilla is always measured first. By assuming R1 remains in the prepared eigenstate $|1\rangle$ throughout all experiments, $m_0 = a_1$ gives the computational-basis measurement outcome of qubit A1. To perform a QND measurement on a data qubit Di, A1 is shuttled adjacent to the relevant bus stop and a calibrated CROT will flip the state of A1 conditional on the data qubit being in the $|1\rangle$ state (see Sec. 5.7.9). The next measurement m_k indicates whether an ancilla spin flip took place by considering the

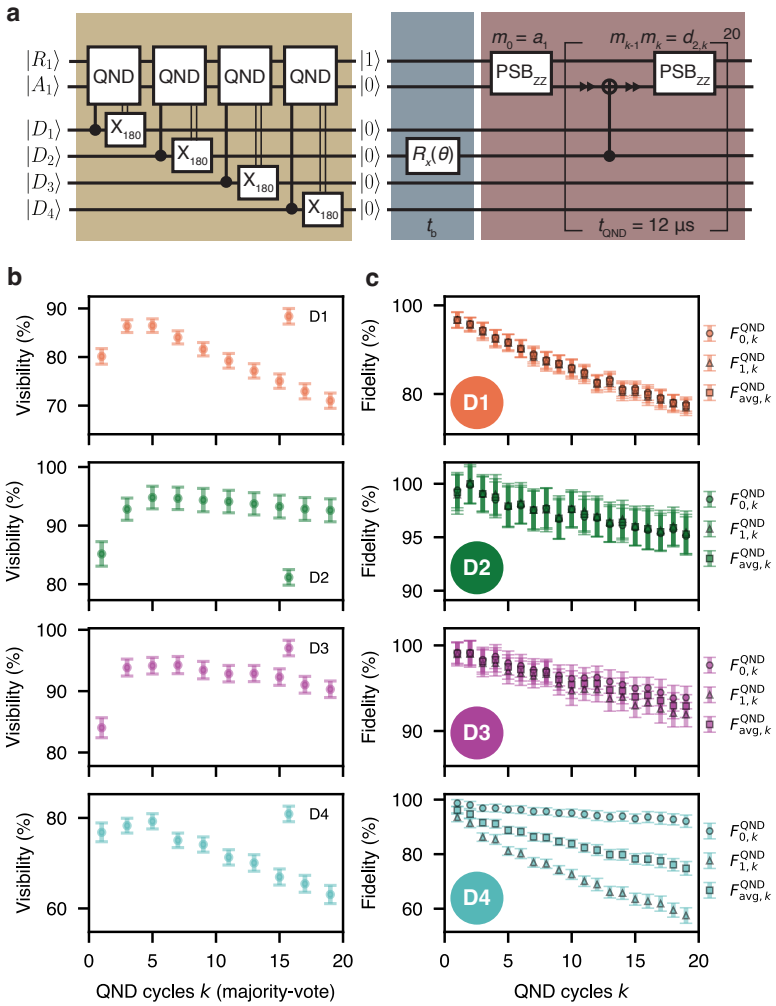


Figure 5.10: **a** Example of a repeated QND measurement circuit for D2. After the loading and initialization of all qubits, a resonant microwave burst is applied to one of the data qubits for a time t_b. This is followed by 20 successive QND measurement cycles on the data qubit. The single-shot computational-basis measurement for the k-th cycle is given by $d_{i,k} = m_{k-1}m_k$. Each QND measurement cycle requires about 12 µs. **b** Visibility of data qubit Rabi oscillations as a function of the number of successive QND measurement cycles used to conduct a majority-vote. **c** QND fidelities calculated as a function of the number of successive QND cycles.

previous measurement m_{k-1}. The k-th computational-basis readout $d_{i,k}$ of Di is therefore given by the product $m_{k-1}m_k$.

Unlike for the ancilla measurement, repeated QND measurements can

take place on the data qubits to improve the readout fidelity as indicated in Fig. 5.3a. To characterize the quality of the repeated QND readout, we perform Rabi oscillation measurements with 20 sequential QND readouts on the four data qubits individually. Fig. 5.10a gives an exemplary circuit for D2. The QND single-shot outcomes $\{d_i\} = \{d_{i,1}, d_{i,2}, \dots d_{i,20}\}$ are used to infer the data qubit Di $|1\rangle$ state probability $P_1(t_\mathrm{b})$ through a majority-vote scheme. The resulting oscillation is fit to $P_1(t_\mathrm{b}) = B - A\cos(2\pi f_\mathrm{R} t_\mathrm{b})\exp(-t_\mathrm{b}/T_2^\mathrm{R})$, where t_b is the MW burst time, f_R is the Rabi frequency, and T_2^R is the Rabi oscillation decay time. Fig. 5.10b shows the visibility, given by $2A$, of the Rabi oscillations as a function of the number of QND readout cycles used in the majority-vote. We use up to five QND repetitions in our experiments, as this yields the highest visibility for all data qubits.

We also characterize the QND fidelity of our readout, which quantifies the ability of the QND measurement to preserve the data qubit $|0\rangle$ and $|1\rangle$ states. We again utilize the 20 repetitive QND readouts but calculate the Rabi oscillation from each individual outcome $d_{i,k}$. This results in Rabi oscillations with decaying amplitudes and offsets as the data qubit state is disturbed by finite CROT fidelity and spin relaxation. The individual Rabi oscillations $P_{1,k}(t_\mathrm{b})$ are fitted to obtain the amplitude A_k and offset B_k for the k-th QND measurement repetition. The decay of these parameters is then fitted using the model [64]:

$$A_k = A_0\gamma^k, \tag{5.3}$$

$$B_k = \left(B_0 - \frac{1-\gamma_0}{1-\gamma}\right)\gamma^k + \frac{1-\gamma_0}{1-\gamma}, \tag{5.4}$$

where $\gamma_0 = \exp(-t_\mathrm{QND}/T_1^{(0)})$, $\gamma_1 = \exp(-t_\mathrm{QND}/T_1^{(1)})$, and $\gamma = \gamma_0 + \gamma_1 - 1$. t_QND is the time required for a cycle of QND measurement, which in our case is about 12 µs for all four data qubits, $T_1^{(0)}$ is the spin-flip time of the data qubit $|0\rangle$ state, and $T_1^{(1)}$ is the spin-flip time of the data qubit $|1\rangle$ state. We observed a decay in A_k for all data qubits. However, only data qubit D4 shows a decay in B_k; the remaining data qubits show no visible decay over the 20 QND repetitions. We conclude that the QND readouts of D1, D2, and D3 are mainly limited by unintentional data qubit spin flips due to the CROT infidelity, while the QND readout of D4 is affected by both the CROT infidelity and intrinsic spin relaxation. We are unsure of the reason for this unique spin relaxation effect. One possible explanation could be that the valley splitting of the dot containing D4 is nearly degenerate with the Zeeman splitting, as spin relaxation would be enhanced. This potential issue may be bypassed by changing the magnetic field to lift the degeneracy.

The fitted parameters A_k and B_k are related to the QND fidelities by the

following relation [64]:

$$P_{1,k}(t_b) = (1 - F_{0,k}^{QND})(1 - P_{1,0}(t_b)) + F_{1,k}^{QND} P_{1,0}(t_b), \tag{5.5}$$

which translates to:

$$F_{0,k}^{QND} = 1 - B_k + \frac{B_0}{A_0} A_k, \tag{5.6}$$

$$F_{1,k}^{QND} = B_k + \frac{1 - B_0}{A_0} A_k. \tag{5.7}$$

Figure 5.10c shows the extracted QND fidelities $F_{0,k}^{QND}$ and $F_{1,k}^{QND}$, along with the average fidelity $F_{avg,k}^{QND} = (F_{0,k}^{QND} + F_{1,k}^{QND})/2$. For one QND repetition, the $F_{avg,1}^{QND}$ for D1-D4 are 96.7(1.8)%, 99.2(1.7)%, 99.1(1.3)%, and 96.1(1.4)% respectively.

5.7.9. UNIVERSAL SPIN CONTROL

All primitive qubit operations can be derived from the Heisenberg Hamiltonian describing the sparse spin array. It can be expressed in terms of the Loss-DiVincenzo qubit operators as:

$$H = \sum_{ij} hJ_{ij} \left(\frac{\vec{\sigma}_i \cdot \vec{\sigma}_j}{4} - \frac{1}{4} \right) - \sum_i \frac{1}{2} g\mu_B \vec{B}_i \cdot \vec{\sigma}_i, \tag{5.8}$$

where $\vec{\sigma}_i = (X, Y, Z)^T$ is the vector of Pauli matrices acting on qubit i, $\vec{B}_i$ is the magnetic field vector at the location of qubit i, h is the Planck constant, $g \approx 2$ is the electron spin g-factor in silicon, and μ_B is the Bohr magneton. J_{ij} gives the magnitude of exchange interaction between spins. It is controllable via baseband pulses on the electrostatic gates and is effectively zero for non-adjacent spins.

When $J = 0$, single-qubit control is achieved via EDSR where an oscillating electric field $E_{ac}(t)\cos(2\pi f_{MW} t + \phi)$ with time-varying amplitude $E_{ac}(t)$, frequency f_{MW} and phase ϕ couples to the spin via a transverse gradient b_t originating from the micromagnet stray field. The single spin therefore experiences an effective magnetic field $\vec{B}(t) = (hf_R \cos(2\pi f_{MW} t + \phi), 0, hf_L)^T / g\mu_B$ where f_L is the Larmor frequency set by the total magnetic field at the qubit location and $f_R(t) = g\mu_B b_t e E_{ac}(t) a_0^2 / 2hE_{orb}$ is the on-resonance Rabi frequency, e is the electron charge, a_0 is the Fock-Darwin length scale of the quantum dot and E_{orb} is the orbital energy scale of the quantum dot.

In the rotating frame, the single-qubit Hamiltonian after application of the rotating wave approximation is:

$$H_{\mathrm{EDSR}} = \frac{h(f_{\mathrm{MW}} - f_{\mathrm{L}})}{2} Z + \frac{h f_{\mathrm{R}}(t)}{2} (\cos\phi X - \sin\phi Y), \tag{5.9}$$

When driven on-resonance such that $f_{\mathrm{MW}} = f_{\mathrm{L}}$, the single-qubit unitary evolution is given by

$$U_{1Q} = \exp\left(-i 2\pi f_{\mathrm{R}}(t) t (\cos\phi, -\sin\phi, 0)^T \cdot \vec{\sigma}/2\right), \tag{5.10}$$

which is a rotation $R_{\hat{n}}(\theta)$ about an axis $\hat{n} = (\cos\phi, -\sin\phi, 0)^T$ by an angle $\theta = 2\pi f_{\mathrm{R}}(t) t$. All single-qubit gates are derived from a single definition for an $X_{90} = \exp(-i\pi X/4)$ operation which consists of a microwave burst of duration t_{90}. Rotations around other axes are implemented by changing the phase ϕ of the microwave burst, and arbitrary rotations $R_z(\theta)$ about the z-axis of the Bloch sphere are similarly implemented by a phase update of the subsequent microwave bursts. X_{180} rotations are implemented with two concatenated X_{90} pulse definitions. The use of a unique single-gate primitive streamlines the calibration of crosstalk in the multi-qubit Hilbert space (see Sec. 5.7.10).

As all microwaves are delivered via a single antenna, we rely on spectral separation to address individual spins. To limit errors due to off-resonant coherent driving, we use a Hamming window for the microwave pulse amplitude $E_{\mathrm{ac}}(t)$ to limit the bandwidth of each microwave pulse to approximately $1/t_{90}$. For pulse durations of about 250 ns, the pulses therefore have a resolution of about 10 MHz. Remaining phase pickup due to the ac Stark shift and heating effects is calibrated experimentally and accounted for in the form of virtual phase updates.

A CROT operation is used for initialization and readout by applying a resonant pulse while the exchange J_{ij} between the shuttled ancilla and a data qubit is finite. In the limit where the exchange is much smaller than the Larmor frequency difference between spins ($J_{ij} \ll |f_{\mathrm{L},i} - f_{\mathrm{L},j}|$), it is appropriate to approximate the resonance frequency of qubit i as conditional on the state of qubit j with a separation of J_{ij}. Qubit i can therefore be conditionally rotated depending on the state of qubit j via EDSR. The exchange $J_{ij}(t)$ is ramped on and off adiabatically with a Tukey pulse shape, and a microwave burst with a rectangular window is applied for a duration t_{180} required for a complete flip of qubit i. The synchronization condition $1/2t_{180} = J_{ij}/\sqrt{4n^2 - 1}$ with integer n is used to drive a 2π rotation in the subspace of the undesired transition [65]. The operation therefore performs the mapping $\{|00\rangle \to |00\rangle, |01\rangle \to |01\rangle, |10\rangle \to |11\rangle, |11\rangle \to |10\rangle\}$ which is suitable for a projective QND measurement of the control qubit in the computational basis. Although the CROT may form a universal entangling gate, we do not use the CROT as a coherent two-qubit operation and therefore do not track the single-qubit phases picked up during the operation. We also

neglect the conditional phases in the CROT as they are unimportant for initialization and readout.

Coherent two-qubit operations are implemented by modulating the exchange J_{ij} adiabatically without any additional microwave burst. This ideally results in a unitary evolution $U_{2Q} = \mathrm{diag}\left(1, e^{-i\phi_{01}}, e^{-i\phi_{10}}, e^{-i\phi_{11}}\right)$. U_{2Q} can be transformed into a controlled-phase gate via commuting virtual single-qubit z-rotations such that $R_z(\phi_{10}) \otimes R_z(\phi_{01}) U_{2Q} = \mathrm{diag}\left(1, 1, 1, e^{i(\phi_{01}+\phi_{10}-\phi_{11})}\right)$. A controlled-$S$ gate between qubits i and j is achieved when $J_{ij}(t)$ is modulated such that $\phi_{01} + \phi_{10} - \phi_{11} = \pi/2$. The duration for the gate is bounded by $t_{CS} > 1/4J_{ij,\max}$, where $J_{ij,\max}$ is the maximum exchange strength during the operation, and is necessarily longer to maintain adiabaticity.

The CS gate is used as the two-qubit entangling primitive as illustrated in Fig. 5.4a where the single-qubit z-rotations are obviated by the refocusing pulses. The multi-qubit decoupled CZ operation can be expressed in terms of controlled-phase gates CZ^i_{00} acting on the ancilla qubit and data qubit i, where $CZ_{xy}|m,n\rangle = (-1)^{\delta(x,m)\delta(y,n)}|m,n\rangle$. The circuit of Fig. 5.4a implements the unitary $X^{\otimes(w+1)}_{180}\Pi^w_{i=1}CZ^i_{00}$ acting on the ancilla qubit and w data qubits. With a universal single-qubit gate set, this operation is sufficient to apply any Pauli operation on the data qubits conditional on the state of the ancilla qubit.

5.7.10. GATE CALIBRATION PROTOCOLS

Periodic calibration of the five-qubit processor is necessary to compensate for slow drifts in the solid-state environment in order to maintain the gate fidelities required for the results presented in this work. We use a semi-automated calibration procedure that efficiently updates the control parameters for resonant gates (Fig. 5.11), crosstalk compensation (Fig. 5.12), and adiabatic two-qubit gates (Fig. 5.13). The following protocols may be carried out once all bus stops can be populated, the ancilla can be shuttled with reasonable fidelity (specifically, the visibility of QND measurement of the data qubits will be bounded by how well spin polarization is preserved during shuttling), and all four exchange interactions are tunable over a workable range (e.g. $100\,\mathrm{kHz} < J < 10\,\mathrm{MHz}$).

SINGLE-QUBIT GATE AND CROT CALIBRATION

Each resonant gate calibration begins with a coarse calibration followed by a finer one. We coarsely calibrate the Larmor frequency of the ancilla qubit A1 using microwave spectroscopy. The dip in the measured odd-state return probability is isolated and the resonance frequency is estimated via a quadratic fit. We then drive A1 with a microwave burst

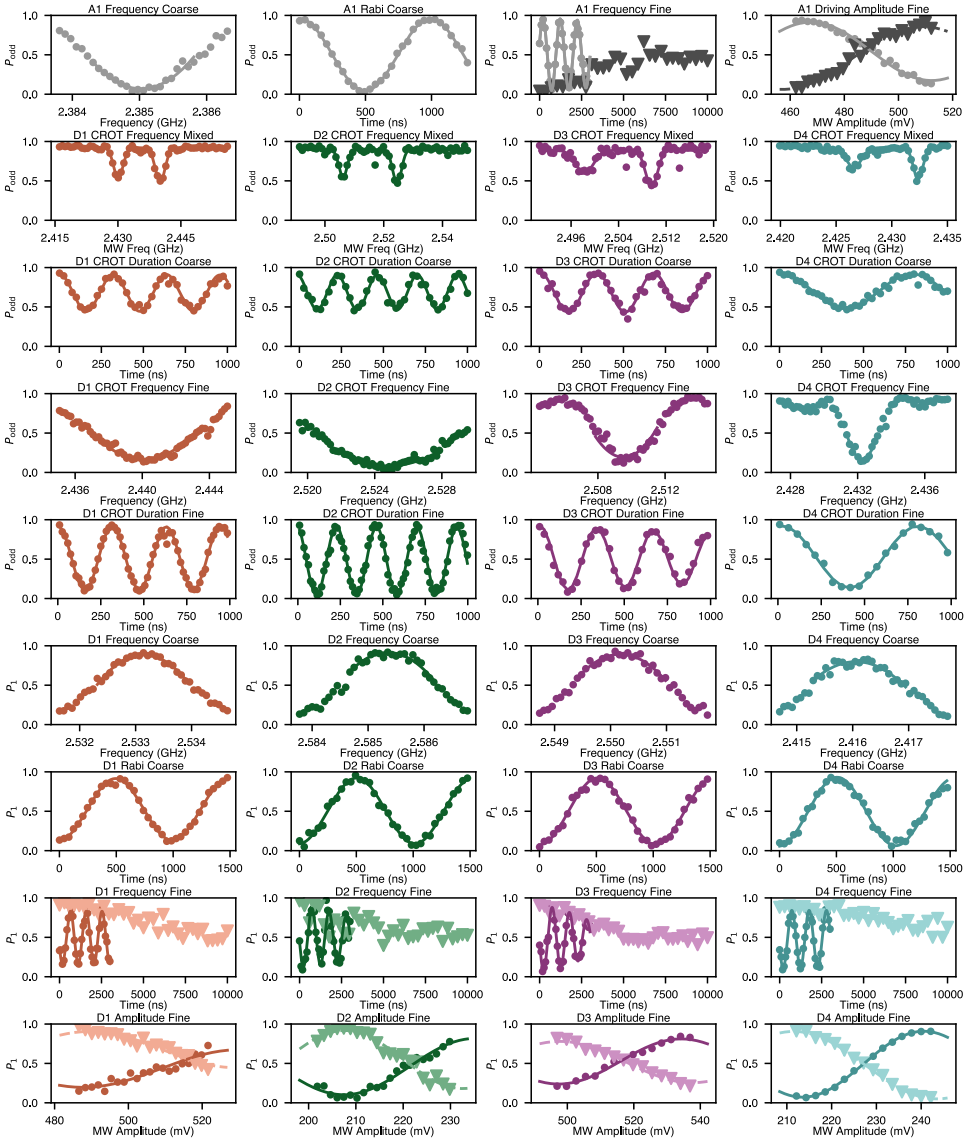


Figure 5.11: A calibration report for all resonant operations. The order of the experiments is from left-to-right and top-to-bottom. For fine frequency experiments, circles indicate a scan with a virtual detuning, and triangles indicate a verification scan. For fine driving amplitude experiments, circles and triangles indicate whether a final X_{-90} or X_{90} gate was applied. Ancilla measurements are reported as the probability P_{odd} of an odd-parity PSB outcome. Data qubit QND measurements are reported as the probability P_1 of inferring the $|1\rangle$ state.

shaped by Hamming window of varying duration and we fit the Rabi oscillations to extract the current Rabi frequency f_R^{fit}. Since we aim for $f_R^{targ} = 1$ MHz, or $t_{90} = 250$ ns, we rescale the driving amplitude by f_R^{targ}/f_R^{fit}.

A finer calibration is then performed using a Ramsey experiment, with the rotating frame virtually detuned by 1 MHz from the coarsely-calibrated Larmor frequency. Fitting the resulting Ramsey oscillations yields a frequency correction. Finally, we fine-tune the 250 ns microwave burst amplitudes. The procedure applies multiple 2π qubit rotations (typically 4), each decomposed into four repeated X_{90} gates, to amplify any systematic over-rotation. The sequence is terminated with either an X_{90} or a X_{-90} gate to prepare the qubit in a superposition state. By sweeping the pulse amplitude, we select the value that yields a 50% odd-parity measurement probability for both final states (corresponding to $\langle Z \rangle = 0$). The last two calibration steps are often iterated until they converge.

The CROT is calibrated using a four-step procedure, beginning with a coarse frequency estimation obtained by fitting a double-Gaussian function to an exchange spectroscopy trace acquired with the relevant data qubit in a mixed state and the exchange activated. This is possible before resonant control of the data qubits has been calibrated. For all CROTs, the higher-frequency branch is selected to drive the ancilla conditional on the data qubits occupying the $|\uparrow\rangle \equiv |1\rangle$ state. The Rabi frequency of the conditional rotations is used to calibrate the driving amplitude required to meet the synchronization condition.

The coarse CROT calibrations are sufficient to initialize the data qubits using QND measurement and postselection of the desired CROT outcome, and resonant control of D1-D4 may then be calibrated analogously to A1. A finer CROT calibration is then performed by initializing the data qubits to the $|1\rangle$ state. The same calibrations are repeated, yielding more accurate estimates of both the conditional resonance frequency and the required drive amplitude due to the improved trace visibility.

A finer calibration of the CROTs, along with resonant control of the data qubits, allows for higher visibility of the data qubits by using the full QND measurement framework presented in Fig. 5.3. Consequently, resonant control of the data qubits can be calibrated more precisely, and the process can be iterated until satisfactory convergence of the parameters has been achieved.

SINGLE-QUBIT PHASE CORRECTIONS

As all resonant control signals are applied to the same screening gate, operating the device as a five-qubit processor requires mitigating crosstalk effects when driving different qubits that may arise due to a combination of the AC Stark effect, device heating, and induced shifts

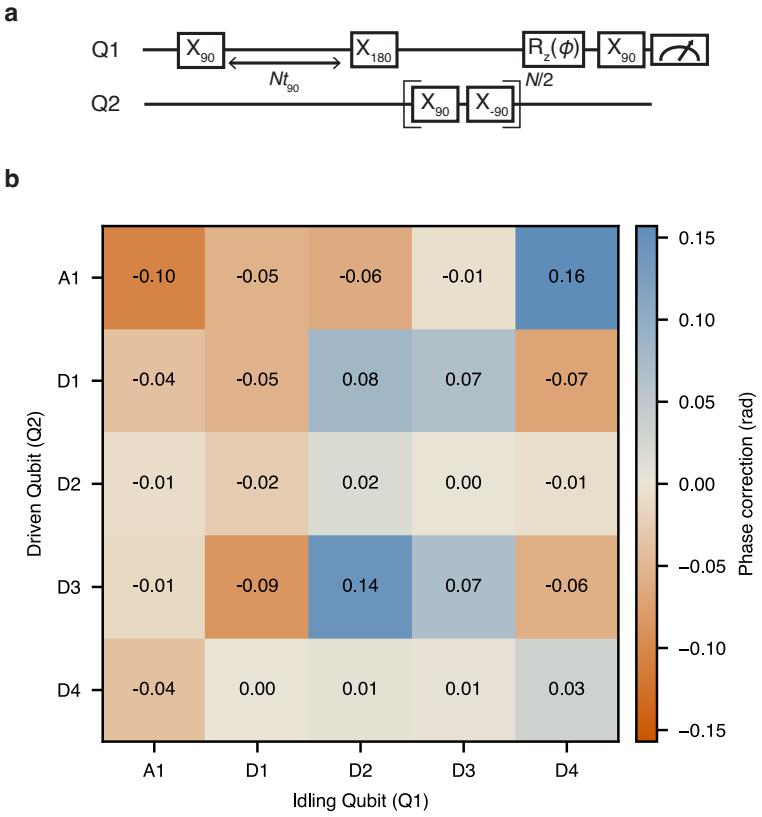


Figure 5.12: **a** Quantum circuit used to perform a Hahn-echo-type experiment and characterize the single-qubit phase crosstalk accrued by Q1 while performing single-qubit operations on Q2. **b** An example of the crosstalk phase corrections that are applied along with each corresponding X_{90} gate while operating the device as a five-qubit processor.

in the stray magnetic field gradient. As the addressability gradient and pulse-shaping limit off-resonant rotations given by Eq. 5.10, this crosstalk predominantly manifests as phase pickup, which can be compensated for by virtual $R_z(\phi)$ gates.

To characterize these phases and determine the corresponding per-gate phase corrections, we perform a series of Hahn-echo-like experiments as shown in Fig. 5.12a in which the target qubit remains idle while repeated sequences of X_{90} and X_{-90} gates are applied to each of the other qubits. We limit the number of applied gates to a maximum of $N = 4$ to remain in the linear regime, allowing us to extract the per-gate accumulated phase via a linear fit.

These induced phases can be compared with the predicted AC Stark shifts, showing partial qualitative agreement. However, the presence of self-induced phase accumulation (non-zero diagonal elements) as well as magnitude and sign discrepancies with the experimental data indicate that other effects, such as heating, play a significant role.

ADIABATIC CS CALIBRATION

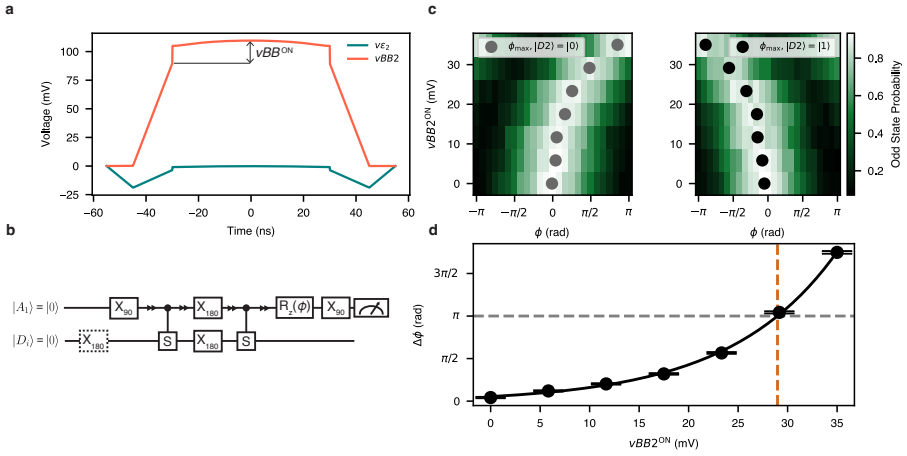


Figure 5.13: **a** An example of a Hamming-window exchange pulse for implementing a *CS* gate between A1 and D2. **b** Quantum circuit used to fine-tune the maximum amplitude of the Hamming pulse. **c** The phase pickup of the ancilla qubit for different maximum Hamming pulse amplitudes for both computational-basis preparations of the data qubit D2. The total gate time is fixed. The markers indicate the relative shift of the curves due to conditional phase pickup. **d** The difference in the conditional phase picked up by the ancilla is fit and we select the barrier amplitude that yields a total phase difference of π radians from the two successive *CS* gates.

We calibrate coherent two-qubit interactions between the ancilla qubit and data qubits using an approach similar to [20]. The dynamic range of the exchange interaction is probed to find a suitable empirical relation $J_i(vBBi)$ for all four bus stops. The charge-symmetry point is also identified via a fingerprint scan as an approximately linear function of the barrier voltage such that $v\epsilon_i \propto vBBi$. This allows for pulse-shaping of the exchange strength $J_i(t)$ to maximize the adiabaticity of the interaction while remaining robust to charge noise [66].

Each effective *CS* operation is actuated by a series of baseband pulse segments as exemplified in Fig. 5.13a. The first segment is a fast detuning ramp to the symmetry point. The second segment is a linear ramp to a sub-threshold exchange magnitude (e.g. $J < 1\,\mathrm{MHz}$). The central segment is a Hamming-shaped exchange modulation characterized by a pulse

duration and magnitude $vBBi^{\mathrm{ON}}$ which are selected to balance speed and adiabaticity. The remaining two segments are time-reversed copies of the first two to uncouple the qubits.

The pulse sequence in Fig. 5.13b is used to fine-tune the amplitude $vBBi^{\mathrm{ON}}$ in a decoupled CZ sequence such that the total conditional phase picked up by A1 can be identified for both computational-basis state preparations of the relevant data qubit Di. This is exemplified for the two-qubit interaction at bus stop 2 in Fig. 5.13c-d. A total conditional phase difference of π is selected to ensure each individual CS operation accrues $\pi/2$ radians of conditional phase.

5.7.11. SINGLE-QUBIT CHARACTERIZATION

The dephasing times measured using CPMG decoupling can be used to gain insight into the noise spectrum influencing each qubit (see Fig. 5.3e). We assume a monotonic noise spectrum $S(\omega) = A/\omega^{\alpha}$ acting on each qubit such that $T_2 = T_2^0 N_\pi^{\alpha/(1+\alpha)}$ and $T_2^0 = (2/A)^{1/(\alpha+1)}\pi^{\alpha/(1+\alpha)}$ and observe a good fit in all cases [67]. T_2^* measurements use a total integration time of about 25 minutes.

Single-qubit gate fidelities are evaluated using randomized benchmarking. We use the primitive gate set $\{I, X_{90}, Y_{90}\}$ of only positive rotations such that a Clifford gate is composed of 3.125 primitive gates on average [68]. A X_{90} gate duration of 250 ns is used for each primitive gate. The single-qubit Clifford gate fidelities are 98.98(3)%, 99.930(5)%, 99.90(1)%, 99.87(1)%, and 99.924(6)% for A1, D1, D2, D3, and D4 respectively. Individual single-qubit gate fidelities in the single-qubit subspace are all well above 99.9% for the data qubits, and slightly lower for the ancilla qubit (see Fig. 5.3g). In the experiment, pairs of single-qubit operations were performed simultaneously when applicable. When all four bus stops were used, D1/D2 and D3/D4 were parallelized. When three bus stops were used, the ancilla would be driven in parallel with one of the bus stops.

To benchmark the shuttling performance, we use interleaved randomized benchmarking. The resonant control of qubit A1 when localized below P2 is used as the reference set. The interleaved operation consists of shuttling from below P2 to a location in the shuttling bus adjacent to a bus stop, idling for 50 ns, and shuttling back. A calibrated phase correction is added to make the targeted interleaved operation an identity gate. The measured fidelities do not change substantially with a small increase in the idling time, therefore we believe most of the infidelity originates during shuttling itself. A significant fraction of the shuttling error originates during loading and unloading the conveyor, when A1 moves from below gate P2 to below gate C0, as seen from the 97.9% round-trip shuttling fidelity to bus stop 1. This transition is induced with

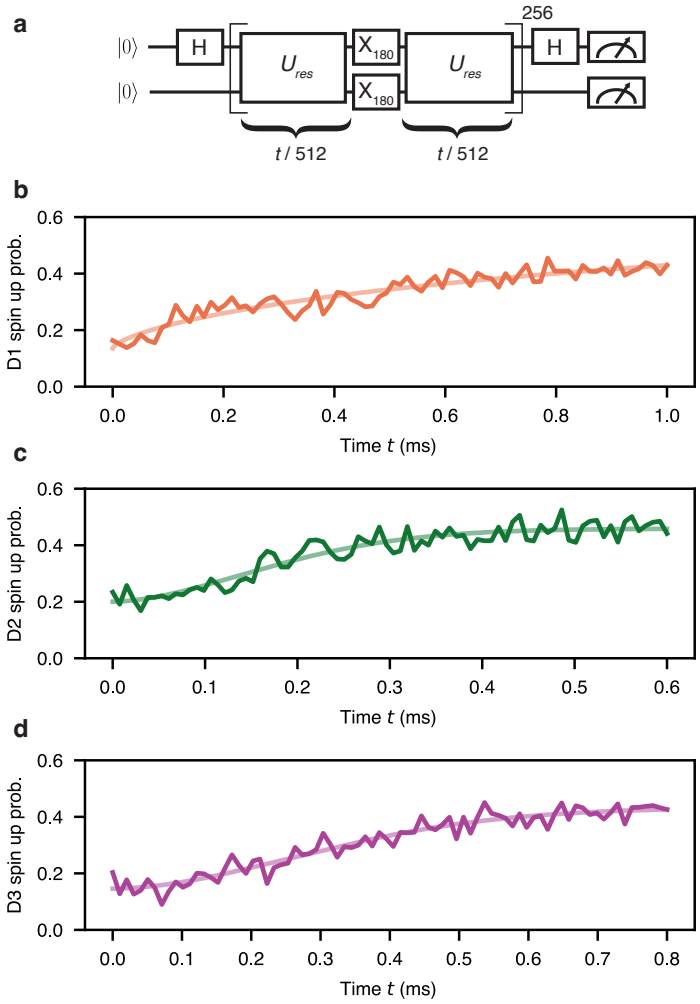


Figure 5.14: **a** Circuit to measure the residual exchange between two data qubits localized in bus stops. The unitary evolution under idling is Ising-like as $J_{\text{res}} < \Delta E_Z$, and $U_{\text{res}} \approx \text{diag}\left(1, e^{iJ_{\text{res}}t/2}, e^{iJ_{\text{res}}t/2}, 1\right)$, therefore the oscillations of the qubit placed in superposition will have a frequency $J_{\text{res}}/2$ as a function of the total idling duration. **b-d** Measurements of residual exchange between D1 and D2, D2 and D3, and D3 and D4 respectively. In all cases, no residual exchange on the order of kilohertz is discernible from decoherence and is therefore negligible for any experiment conducted in this work. Due to the relatively large separation and large potential barrier between data qubits, the actual residual exchange is likely much lower.

a linear voltage ramp of 40 ns duration and may be possible to optimize further. Only a 0.2% decrease in fidelity is observed when shuttling

the remaining round-trip distance to bus stop 4. One round-trip of the ancilla from below P2 to bus stop 4, in the absence of any two-qubit interactions, takes place in 730 ns. Considering the T_2^H of A1 is 47.6 µs with a decay exponent of 1.7 when localized below P2, we estimate that dephasing alone could contribute about 0.1% to the infidelity. Increasing the speed of the traveling-wave potential would be the most effective way to increase this limit (in [15], conveyor speeds were up to 25 times faster).

We did not observe any clear evidence of valley excitations limiting the quality of the multi-qubit demonstration. For example, such excitations could result in observing two closely-spaced resonance frequencies as spins occupying different valley-orbit states will have slightly different g-factors [69, 70]. This effect was observed during the initial tuning of the exchange coupling of bus stop 1, but subsequent changes to the loading pulse sequence removed the effect.

It is understood that fluctuations in the valley splitting across a silicon shuttling channel can limit the quality of spin shuttling [47, 71, 72]. It is possible that we would be able to resolve such effects by further optimizing the shuttling channel and rigorously characterizing the valley splitting across the array.

5.7.12. TWO-QUBIT CHARACTERIZATION

Bus stop	Qubits	F_{ref} (%)	F_{DCZ} (%)	F_{Dsh} (%)
1	A1 and D1	96.2(2)	84.2(8)	91.9(5)
2	A1 and D2	97.4(3)	87.9(6)	93.0(4)
3	A1 and D3	96.7(2)	82.8(1.3)	92.6(3)
4	A1 and D4	97.7(1)	89.3(5)	93.9(8)

Table 5.1: Table of extracted fidelities using interleaved CRB. The reference fidelity F_{ref} corresponds to the fidelity of simultaneous single-qubit Clifford gates in the relevant two-qubit Hilbert space. The DCZ operation with fidelity F_{DCZ} is equivalent to the two-qubit version of the circuit displayed in Fig. 5.4a. The decoupled shuttling operation with fidelity F_{Dsh} is the same two-qubit operation but with the entangling CS interactions replaced by idling instead.

We use character randomized benchmarking (CRB) to evaluate the performance of the two-qubit interaction between the shuttled ancilla and the four data qubits [73]. CRB allows us to use simultaneous single-qubit Clifford gates as the reference gate set as opposed to general two-qubit Clifford operations, which require many native CZ gates to compile.

As seen in Fig. 5.4a, the entangling interaction used to implement parity checks is a composite operation consisting of coherent shuttling, two-qubit interactions, and single-qubit gates for refocusing phase pick-up. Furthermore, we take advantage of the fact that the native

controlled-phase interactions commute. We therefore benchmark each individual DCZ interaction to estimate the isolated error contribution from each component of this composite interaction.

We perform two different rounds of interleaved CRB for each two-qubit interaction. First, only the decoupled shuttling sequence is interleaved with no exchange activated. As this operation should be logically equivalent to $X_{180} \otimes X_{180}$, this provides an estimate of the error rate associated with qubit shuttling and the refocusing gates in the two-qubit Hilbert space of the ancilla and the relevant data qubit. Then, we interleave a maximally-entangling DCZ interaction such that the interleaved gate is $X_{180} \otimes X_{180}\mathrm{diag}(1, 1, 1, -1)$. The inverting Clifford gate is implemented using a directly calibrated CZ gate consisting of a single two-qubit interaction and explicitly calibrated phase corrections on both participating qubits. This allows us to use a verified lookup table to implement the inverting Clifford. We also verify with interleaved CRB that this direct CZ has comparable fidelity to the DCZ, in the range of 90%-95%. The decoupled version of the gate is conceptually closer to the compound interaction presented in Fig. 5.4a used to implement parity checks in this work. Table 5.1 summarizes all of the fidelities extracted from CRB.

Based on the interleaved CRB results, we coarsely estimate an error rate $r_{\mathrm{Dsh}} = 1 - F_{\mathrm{Dsh}}$ associated with the decoupled shuttling sequence, and an error rate $r_{\mathrm{DCZ}} = 1 - F_{\mathrm{DCZ}}$ associated with the full entangling two-qubit gate, including the evolution under exchange, shuttling and the refocusing pulses. By assuming these errors are stochastic, independent, and small, we approximate the error rate associated with the pure exchange component of the interaction as $r_J = r_{\mathrm{DCZ}} - r_{\mathrm{Dsh}}$. The fidelity of the two-qubit exchange interaction as reported in Fig. 5.3g is then given as $F_{2\mathrm{Q}} = 1 - r_J$.

To verify these fidelity estimates, we can compare them to the quality factors obtained from observing exchange oscillations in a decoupled sequence. Fig. 5.15 summarizes the effect of increasing exchange on qubit coherence, and the extracted quality factors Q for 1 MHz $< J <$ 10 MHz fall in the range of 10 to 30. The quality factor puts a bound on the achievable fidelity limited by incoherent noise as $F_J < 1 - 1/Q$, since quasi-static noise is removed by the refocusing pulses when exchange oscillations are measured. This limit is consistent with the benchmarked fidelities of 90%-95% that are obtained from interleaved CRB.

5.7.13. ERROR-BUDGET FOR LOGICAL STATE PREPARATION

The combination of qubit characteristics (Fig. 5.3e), operation benchmarks (Fig. 5.3g), and circuit compilation can be used to construct an error budget for the 5-qubit processor. We choose the relevant example of

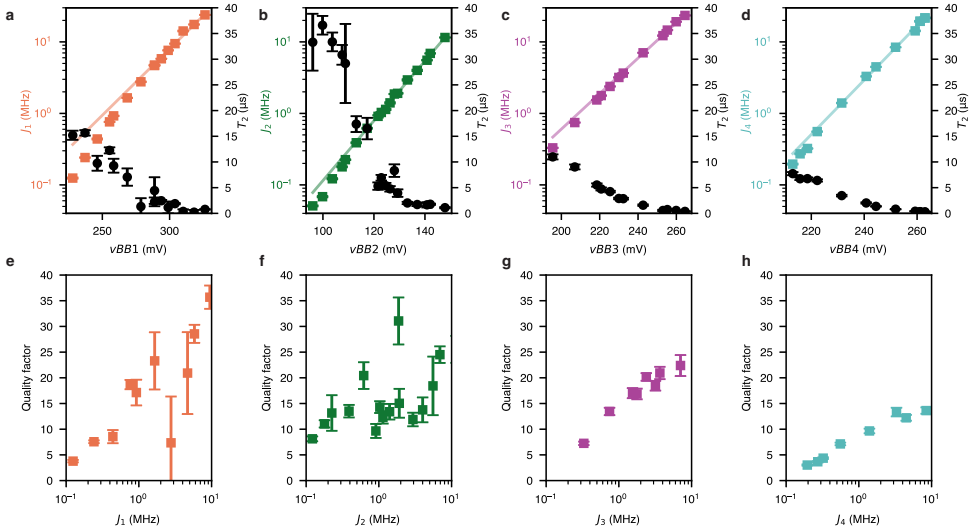


Figure 5.15: **a-d** Exchange strength and dephasing time of A1 as a function of barrier voltage for two-qubit interactions at the four bus stops respectively. **e-h** Quality factors for the two-qubit interactions at the four bus stops, calculated as $Q = 2JT_2$, estimating the number of maximally entangling two-qubit interactions that can take place within the characteristic decay time.

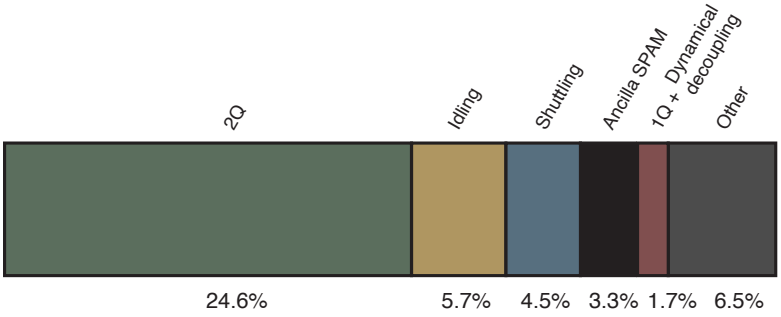


Figure 5.16: Graphical representation of the error budget for initializing a $[[4, 1, 2]]$ surface code logical state. The relative proportions are derived from the error estimates in Table 5.2.

preparing the logical $|0_L\rangle = \frac{1}{\sqrt{2}}(|0000\rangle + |1111\rangle)$ state for a $[[4, 1, 2]]$ surface code as it utilizes all operations. As shown in Fig. 5.4f and Fig. 5.19, the sparse processor produces such a state with a fidelity of about 63%. The quantum circuit producing this state, shown in Fig. 5.4c, utilizes all four two-qubit interactions between the ancilla and each data qubit, two round-trips of shuttling the ancilla qubit, 16 decomposed single-qubit gates, and initialization and measurement of the ancilla qubit.

Operation	Duration	Error estimate
A1 X_{90}	250 ns	0.0033
D1 X_{90}	250 ns	0.0002
D2 X_{90}	250 ns	0.0003
D3 X_{90}	250 ns	0.0004
D4 X_{90}	250 ns	0.0002
A1 and D1 exchange	440 ns	0.076
A1 and D2 exchange	220 ns	0.051
A1 and D3 exchange	360 ns	0.099
A1 and D4 exchange	360 ns	0.046
A1 round-trip shuttle	730 ns	0.023
A1 idling (excl. shuttling)	1.5 µs	0.003
D1 idling	3.65 µs	0.010
D2 idling	3.87 µs	0.020
D3 idling	3.48 µs	0.016
D4 idling	3.48 µs	0.010
A1 measurement	10 µs	0.017

Table 5.2: Table summarizing the operations required to initialize a surface code logical state and their associated timescales and estimated error rates. For operations with a fidelity F benchmarked with randomized benchmarking, the error rate is taken as $1-F$. The idling times t_{idle} are determined based on the nominal pulse sequence used to run the circuit shown in Fig. 5.4c where single-qubit gates on D1/D2 and D3/D4 are parallelized. The idling errors are estimated using $1-\exp(-(t_{\text{idle}}/T_2^{\text{H}})^{\alpha'})$ where T_2^{H} are the measured Hahn echo times for each qubit (47.6(10) µs, 43.2(10) µs, 32.6(8) µs, 37.8(7) µs, 65.1(16) µs for A1, D1, D2, D3, D4 respectively) and α' is the measured echo decay exponent (1.71(9), 1.86(11), 1.83(13), 1.74(8), 1.58(10) for A1, D1, D2, D3, D4 respectively). The A1 measurement error is commensurate with a qubit visibility of 97%.

The final single-qubit gates on each data qubit are compiled into the QST projections, and measurement errors associated with the data qubits are not considered as they are corrected during state reconstruction (see Sec. 5.7.14). Table 5.2 summarizes the error sources from all operations and idling taking place in the circuit.

Fig. 5.16 represents the relative proportions of errors originating from single-qubit gates and dynamical decoupling, two-qubit interactions, shuttling, idling, and measurement. For a first-order estimate, we assume all errors p_i are depolarizing such that the circuit produces a state $\rho = (1-P)\,|\psi_{\text{GHZ}}\rangle\langle\psi_{\text{GHZ}}| + P\frac{I}{16}$ where $(1-P) = \Pi_i(1-p_i)$, yielding a logical state fidelity of about 67%. A remaining error of about 6% between the estimated and measured state fidelities is unaccounted for, but this can reasonably be expected to originate from sources that are not captured by the individual benchmarking protocols. These sources include crosstalk beyond the benchmarked Hilbert spaces and slow device drift. We believe the latter is particularly relevant for longer experiments. For example,

collection of all tomographic projections of the five-qubit GHZ state shown in Fig. 5.20 took 2 hours, during which all control parameters are held constant, and the measured state fidelity of 53% is substantially lower than the four-qubit logical state initialization despite the circuits being very similar. Here, the solution is to interleave fine calibrations more densely through such experiments.

Although the presented analysis is coarse, the overall performance of the device is well-captured by the individual benchmarks. Crucially, we believe the most performance-limiting error sources are apparent. The two-qubit interaction fidelities represent the majority of the error present in the device, and the incoherent noise limiting them must be addressed. Fortunately, previous demonstrations of two-qubit gate fidelities well above 99% in similar device architectures provide evidence that this is possible. The next largest error sources are idling and shuttling. These processes are dominated by dephasing (see Sec. 5.7.11), meaning that increasing the speed of shuttling should suppress both sources of error.

5.7.14. QUANTUM STATE TOMOGRAPHY

QST for an n-qubit state is performed by measuring the expectation value of all 4^n Pauli observables A_k using the individual computational-basis readout available for all qubits in the system. We bin the results into a probability vector P_{meas} of length 2^n.

As the data qubits are read out indirectly and have finite visibility, readout errors are corrected by transforming P_{meas} according to the visibility of Rabi oscillations extracted using the same initialization and readout sequence [42]. We use a single round of QND measurement such that the data qubits have readout visibilities of about 80% to 85% (see Sec. 5.7.8). If qubit i has visibility limits $[V_{i,\min}, V_{i,\max}]$, the corrected probability vector P_{corr} is given by:

$$P_{\text{corr}} = S_i^{-1} P_{\text{meas}} = \begin{pmatrix} 1 - V_{i,\min} & 1 - V_{i,\max} \\ V_{i,\min} & V_{i,\max} \end{pmatrix}^{-1} P_{\text{meas}} \tag{5.11}$$

For multi-qubit corrections, the tensor product of the correction matrices S_i for all participating qubits is used. The pseudo-inverse is used to calculate the inverse numerically to improve stability, the elements of P_{corr} are clipped to 1 and 0, and the vector is renormalized to maintain physicality (if applicable, these corrections are small and tend to lower the fidelity of the reconstructed state). The expectation value of the relevant operator is then calculated by weighting the entries of P_{corr} and averaging appropriately. For example, the expectation value $\langle XIY \rangle$ is extracted as $\text{Tr}((Z \otimes I \otimes Z)\text{diag}(P_{\text{corr}}))$. When reconstructing states that include the ancilla qubit, we include its (relatively small) readout correction for consistency. For reconstructing states initialized via a parity

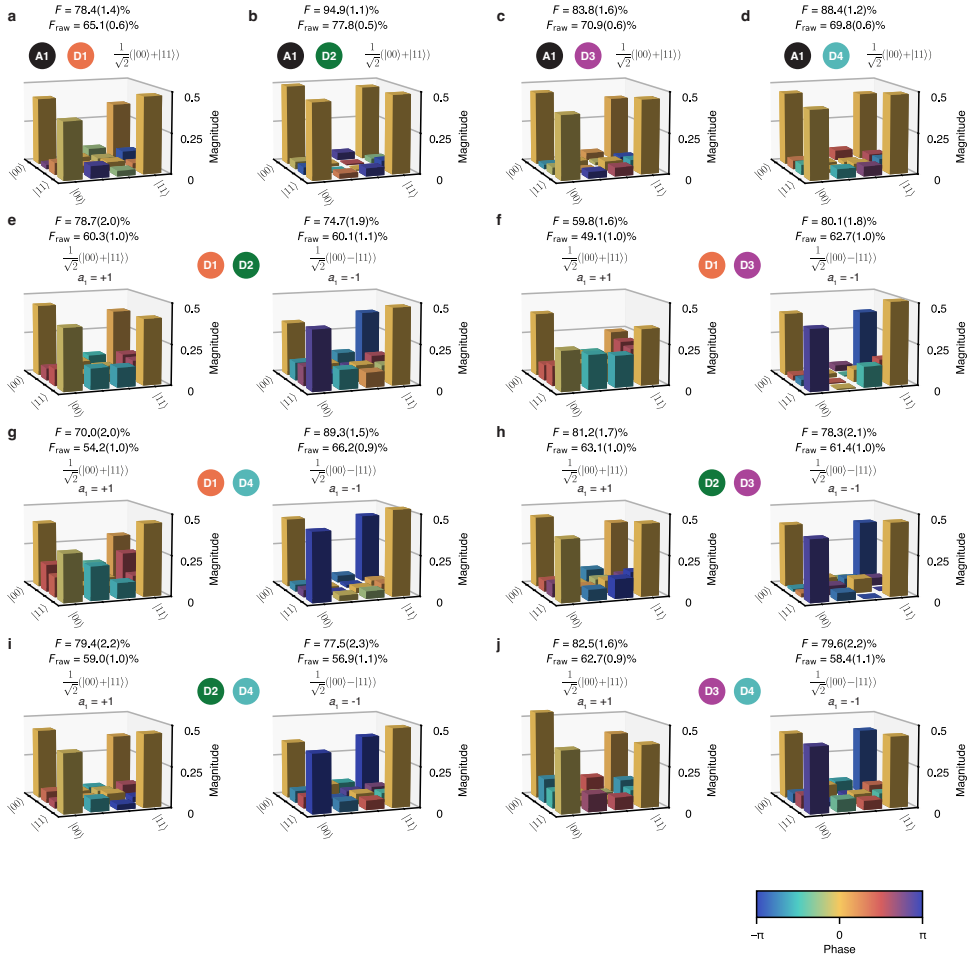


Figure 5.17: **a-d** Two-qubit GHZ state density matrices for all qubit combinations including the ancilla qubit A1. The states are prepared by running a circuit analogous to Fig. 5.4c and performing QST on all qubits at the dashed line. **e-j** Two-qubit GHZ state density matrices for the displayed data qubit combinations. For each combination, two GHZ states differing in phase are probabilistically generated depending on the outcome of the weight-two X-type parity check used to create them as displayed above the plots. The fidelity $F = \langle\psi_{\mathrm{GHZ}}|\,\rho_{\mathrm{meas}}\,|\psi_{\mathrm{GHZ}}\rangle$ is calculated with respect to the target state displayed next to each plot where ρ_{meas} is the reconstructed density matrix including corrections for readout errors. $F_{\mathrm{raw}} = \langle\psi_{\mathrm{GHZ}}|\,\rho_{\mathrm{raw}}\,|\psi_{\mathrm{GHZ}}\rangle$ provides the analogous fidelity where ρ_{raw} is the reconstructed density matrix in the absence of readout corrections. Error intervals represent $\pm 1\sigma$ and are calculated by bootstrapping in all cases. Uncertainties in the readout corrections are included in the boostrapping procedure and therefore yield larger uncertainties for F than F_{raw}.

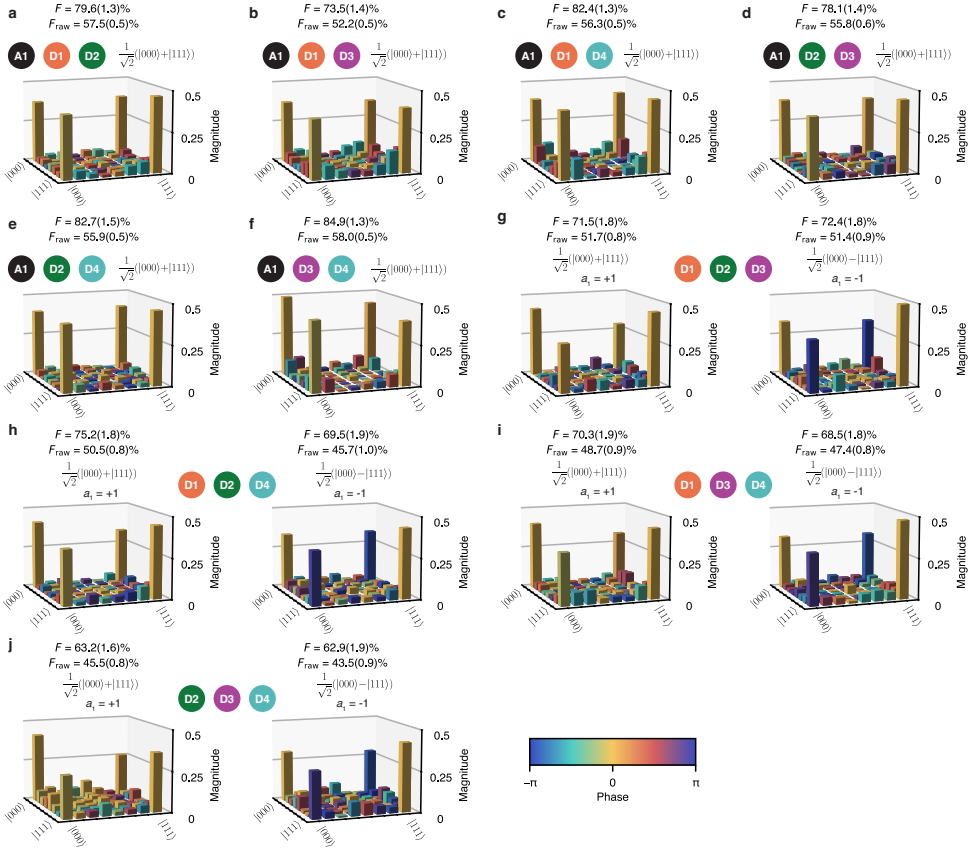


Figure 5.18: **a-f** Three-qubit GHZ state density matrices for all qubit combinations including the ancilla qubit A1. **g-j** Three-qubit GHZ state density matrices for the displayed data qubit combinations. For each combination, two GHZ states differing in phase are probabilistically generated depending on the outcome of the weight-three X-type parity check used to create them as displayed above the plots. The displayed fidelities are calculated as described by the caption of Fig. 5.17.

check, no ancilla measurement correction is possible as data must be binned shot-by-shot. These reconstructed states therefore necessarily include errors in the ancilla measurement.

The density matrix ρ_{meas} is reconstructed from all measured expectation values M_k using maximum likelihood estimation (MLE) to minimize $\sum_{k=1}^{4^n} |M_k - \text{Tr}(A_k \rho_{\text{meas}})|^2$ while enforcing the Hermiticity and unit-trace properties of ρ_{meas}. The optimization is implemented using the CVXPY convex optimization package.

We use bootstrapping to estimate a statistical error on the extracted fidelity by performing the reconstruction multiple times by sampling P_{meas}

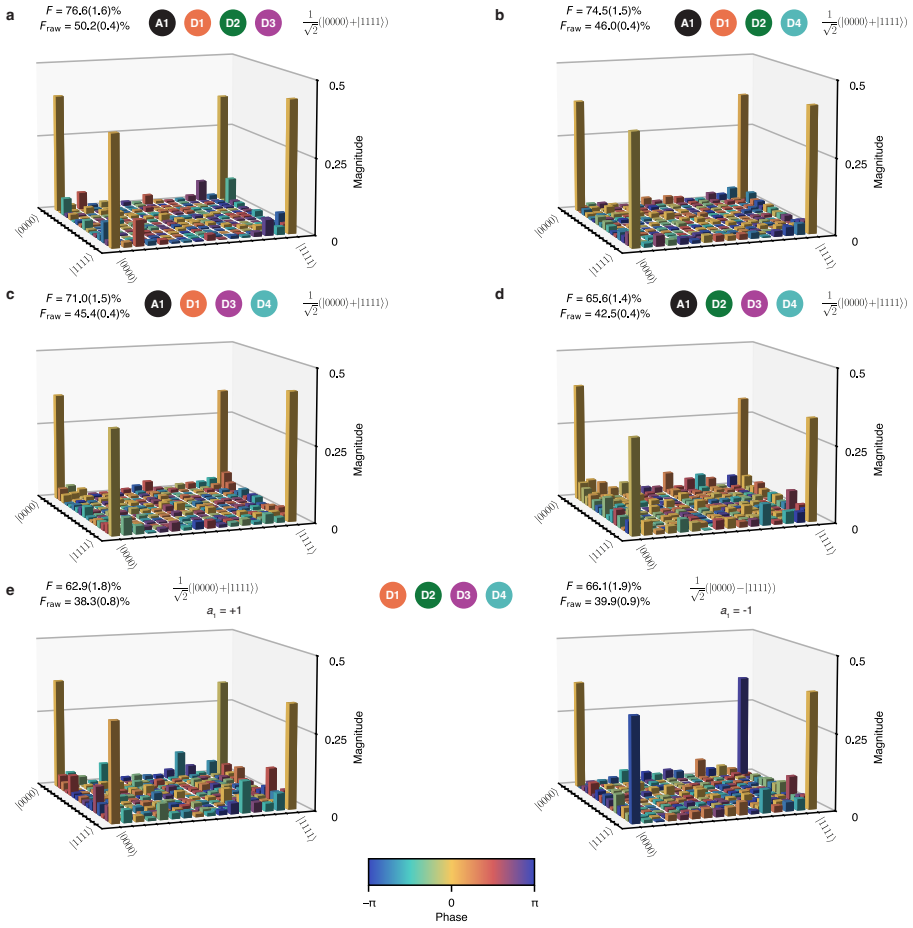


Figure 5.19: **a-f** Four-qubit GHZ state density matrices for all qubit combinations including the ancilla qubit A1. **g-j** Four-qubit GHZ state density matrices for all four data qubits. The two GHZ states differ in phase and are probabilistically generated depending on the outcome of the weight-four X-type parity check used to create them as displayed above the plots. The displayed fidelities are calculated as described by the caption of Fig. 5.17.

from a multinomial distribution according to the measured probability and number of shots. We also uniformly sample the visibility limits used for readout correction, using the Rabi oscillation fit errors as bounds. Each state reconstruction is performed 500 times to ensure good convergence, and the mean fidelity is reported along with the $\pm 1\sigma$ standard deviation of the distribution of reconstructed state fidelities.

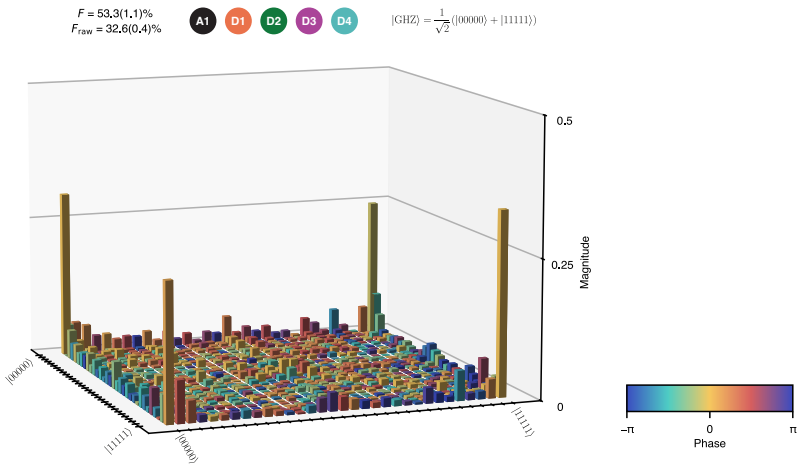


Figure 5.20: The five-qubit GHZ state density matrix supported by the ancilla qubit and all four data qubits. The displayed fidelities are calculated as described by the caption of Fig. 5.17.

5.7.15. PARITY CHECK ANALYSIS

To estimate the accuracy of the parity checks as applied to eigenstates of the stabilizer, we use a similar process as for full state reconstruction with QST. After performing the weight-w check and measuring the ancilla qubit, all data qubits are measured in the eigenbasis of the stabilizer. This yields a probability vector P_{meas} of length 2^{w+1}. Readout errors on the data qubits are corrected as in Sec. 5.7.14 to acquire a corrected vector P_{corr}. The ancilla qubit visibility is not corrected. We report the element of P_{corr} that corresponds to the intended data qubit state preparation and the correct ancilla measurement outcome. This yields a lower estimate for the parity check accuracy (Fig. 5.4e) than an average of the correct ancilla outcome probabilities for all state preparations (Fig. 5.4d), as it also accounts for instances where the parity check operation corrupted the data qubit state, even if the ancilla measurement gives the correct outcome.

We further assess the performance of a repetitive parity check circuit using bus stops 1 and 2. We initialize these bus stops in one of the states $|00\rangle, |01\rangle, |10\rangle$, or $|11\rangle$ and perform 35 rounds of ZZ parity checks (Fig. 5.22a). The measured parity is $+1(-1)$ if the first single-shot result returns a value of $+1(-1)$. Subsequent shots are compared with the previous shot to detect a flip or no flip in the parity; a trace of the single-shot values and the corresponding parity is shown in Fig. 5.22b. We took 2,000 single-shots to obtain the average parity value for each

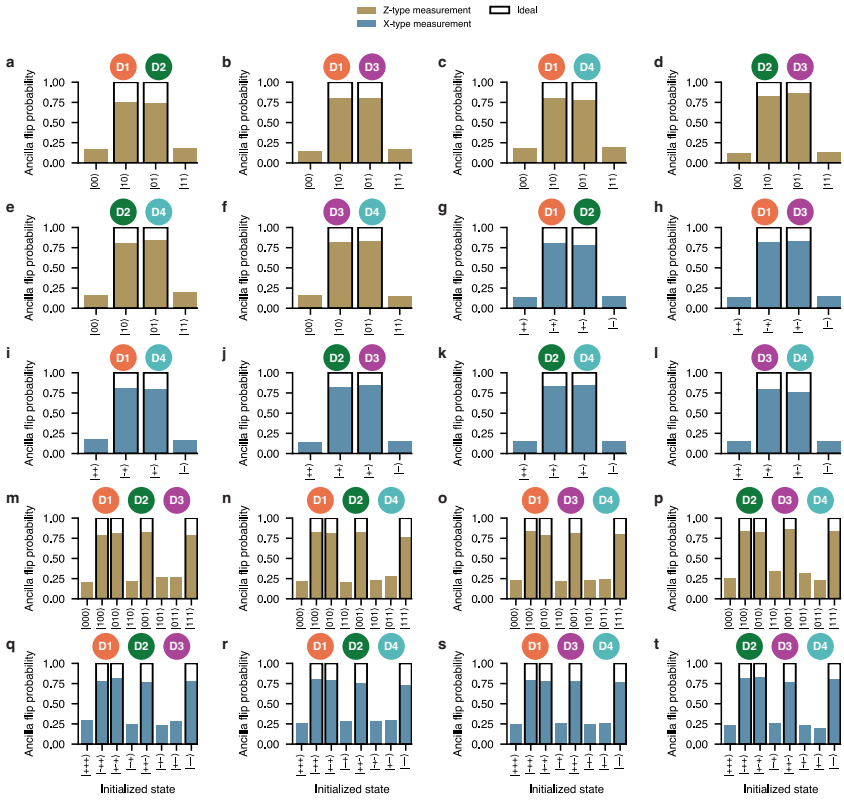


Figure 5.21: **a-f** Weight-two Z-type parity checks for all combinations of data qubits. **g-l** Weight-two X-type parity checks for all combinations of data qubits. **m-n** Weight-three Z-type parity checks for all combinations of data qubits. **q-t** Weight-four X-type parity checks for all combinations of data qubits.

parity check cycle. The decay of the average parity is fitted with the model $Ar^N + C$, where N is the number of rounds, to determine the parity retention rate r. The resulting retention rates are $r_{00} = 92.64(5)\%$, $r_{01} = 93.52(5)\%$, $r_{10} = 92.70(5)\%$, and $r_{11} = 94.89(4)\%$.

5.7.16. ELECTROSTATIC DESIGN

We use QTCAD to perform Poisson and Schrödinger simulations on a simplified device model [74]. We treat these simulations as a qualitative confirmation of intuition rather than an attempt at rigorous device modeling. We use a subset of the nominal gate design for a bus stop as shown in Fig. 5.23a and perform a 3D Poisson simulation of the electrostatics using the indicated gate voltages as Dirichlet boundary

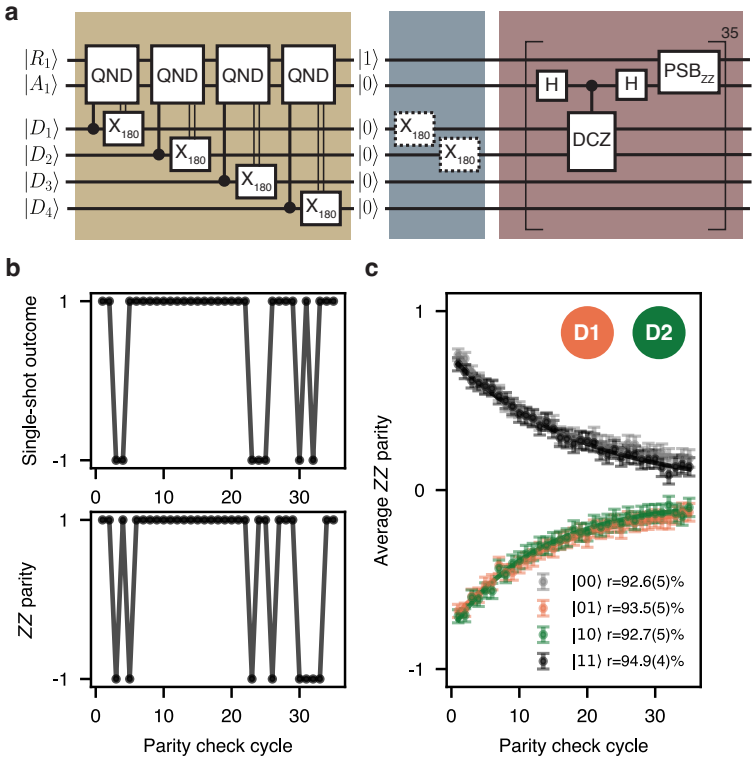


Figure 5.22: **a** Circuit for repetitive parity checks on bus stops 1 and 2. **b** Trace of the single-shot outcomes and the corresponding parity values for a single run of the circuit with the $|00\rangle$ input state for bus stops 1 and 2. **c** Average parity values for all input states $|D2D1\rangle$ as a function of the number of parity check cycles. The decay is fitted with $Ar^N + C$, where N is the number of rounds and r is the parity retention rate. Error bar represents the 95% confidence interval.

conditions. These voltages are physically reasonable but generally smaller than those used in experiment due to screening effects which are not considered here. The bounding area for the simulation is kept large enough such that the natural boundary conditions do not affect the converged solution. The electrostatic solution is used as the static potential for a 3D time-independent Schrödinger equation solver to find the eigenspectrum of a single-electron in the effective double-dot potential.

Fig. 5.23b-e illustrates x- and y-axis linecuts of the ground state when a single-electron is confined in the effective double-dot potential formed when the traveling-wave potential minimum is positioned adjacent to the bus stop. The simulated potential minima shift orthogonally to the

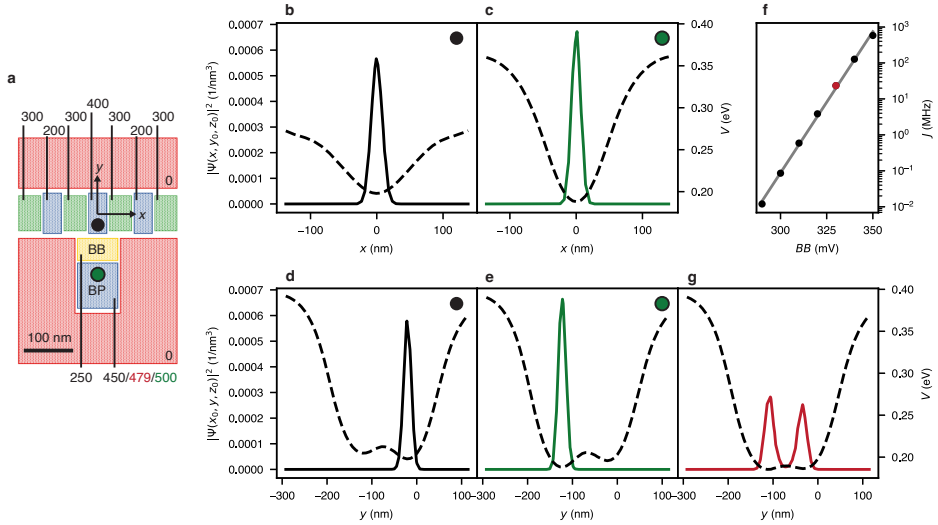


Figure 5.23: **a** Illustration of the boundary conditions used for electrostatic simulations of a double-dot potential at one of the bus stops. All numeric labels indicate a Dirichlet boundary condition in millivolts for the Poisson solver, which are set to approximate the potential landscape when a travelling-wave potential minimum is adjacent to the bus stop. Depending on the voltage applied to the plunger BP, the potential minimum is localized in the shuttling bus (black) or bus stop (green). **b** x-axis linecut of the potential and spatial wavefunction (probability density) of the ground state when the potential minimum is in the shuttling bus. **c** x-axis linecut of the potential and spatial wavefunction of the ground state when the potential minimum is in the bus stop. **d** y-axis linecut of the potential and spatial wavefunction of the ground state when the potential minimum is in the shuttling bus. **e** y-axis linecut of the potential and spatial wavefunction of the ground state when the potential minimum is in the bus stop. **f** Estimated relationship between barrier voltage BB and exchange coupling as calculated from the perturbative relationship $J = 4t_c^2/U$ where the onsite Coulomb potential $U \approx 12\,\text{meV}$ for all voltage settings. The linear fit corresponds to $J = J_{\text{off}} \exp(0.18BB/\text{mV})$. **g** y-axis linecut of the potential and spatial wavefunction of the ground state when the double-dot potential is balanced at the voltage setting highlighted in **f**. The orbital energy spacing to the first excited state is equal to $2t_c$.

axis of the shuttling bus as a result of the presence of the bus stops, as illustrated in Fig. 5.24a. Depending on the bus stop plunger voltage BP, the electron's orbital ground state is either localized in the shuttling bus or the bus stop. We can therefore extract estimated positions of the spin qubits as input to magnetostatic simulations as detailed in Sec. 5.7.17. Furthermore, we extract orbital energy splittings of 3.8 meV for the shuttled dot and 4.1 meV for the bus stop dot which are relevant for EDSR. Using a simplified many-body simulation, the onsite Coulomb potential is estimated to be 12 meV for both dots.

The microscopic valley degree of freedom is not accounted for in the simulations. Nevertheless, the tunability of the bare tunnel coupling t_c may be extracted from the energy difference $2t_c$ between bonding and antibonding states when the double-dot potential is balanced. An example is shown in Fig. 5.23g. The bare exchange coupling follows from perturbation theory as $J = 4t_c^2/U$ [2]. The true exchange coupling in silicon will be influenced by the valley phase difference between the occupied eigenstate of each dot. However, $J \propto t_c^2$ remains true. Therefore, the barrier lever arm can be estimated by fitting to a model $J = J_{\text{off}} \exp(\alpha BB/\text{mV})$ where BB is the barrier gate voltage modulating exchange at a balanced double-dot potential. As shown in Fig. 5.23f, we extract $\alpha = 0.18$ for exchange tunability in the model. This can be compared to the measured relations $\alpha_1 = 0.04$, $\alpha_2 = 0.10$, $\alpha_3 = 0.06$, and $\alpha_4 = 0.09$ for bus stops 1 to 4 respectively. The reasonable qualitative agreement provides a basis for improving design rules that will become increasingly relevant for larger device designs.

5

5.7.17. MAGNETOSTATIC DESIGN

The micromagnet is deposited with a window shape (see Fig. 5.1a) such that its stray field in the quantum well gives rise to a spin Hamiltonian that is practical for measuring and interacting qubits in the sparse array while being reasonably robust to small fabrication defects and microscopic variation. The design criteria are to permit single-spin control with EDSR at all sites in the array with addressability while maintaining resilience against electric charge noise. EDSR controllability enters the Hamiltonian through $b_\perp$, the magnetic field gradient transverse to the total field vector at each potential quantum dot location, and charge noise susceptibility is quantified by $b_\parallel$, the longitudinal magnetic field gradient parallel to the total field vector. $b_\parallel$ also gives rise to addressability between spins and the Zeemen energy differences required for high-fidelity parity-mode PSB readout [43] and fast adiabatic exchange interactions for two-qubit gates [75].

In order to calculate the relevant quantities, the point-like locations of the relevant quantum dots are extracted from electrostatic simulations as described in Sec. 5.7.16, qualitatively approximating the dot positions in the experiment. We use the magpylib Python package to estimate the stray field of the micromagnet assuming homogeneous polarization, which is an approximation [76]. We use a magnet polarization of 730 mT to match the simulated qubit Larmor frequencies to the values measured in experiment. As the saturation polarization for cobalt micromagnets has been observed in the range of 1.5 T to 1.8 T, the magnet is partially demagnetized. However, we do not observe signs of micromagnet instability over several months of experiments. A detailed description of

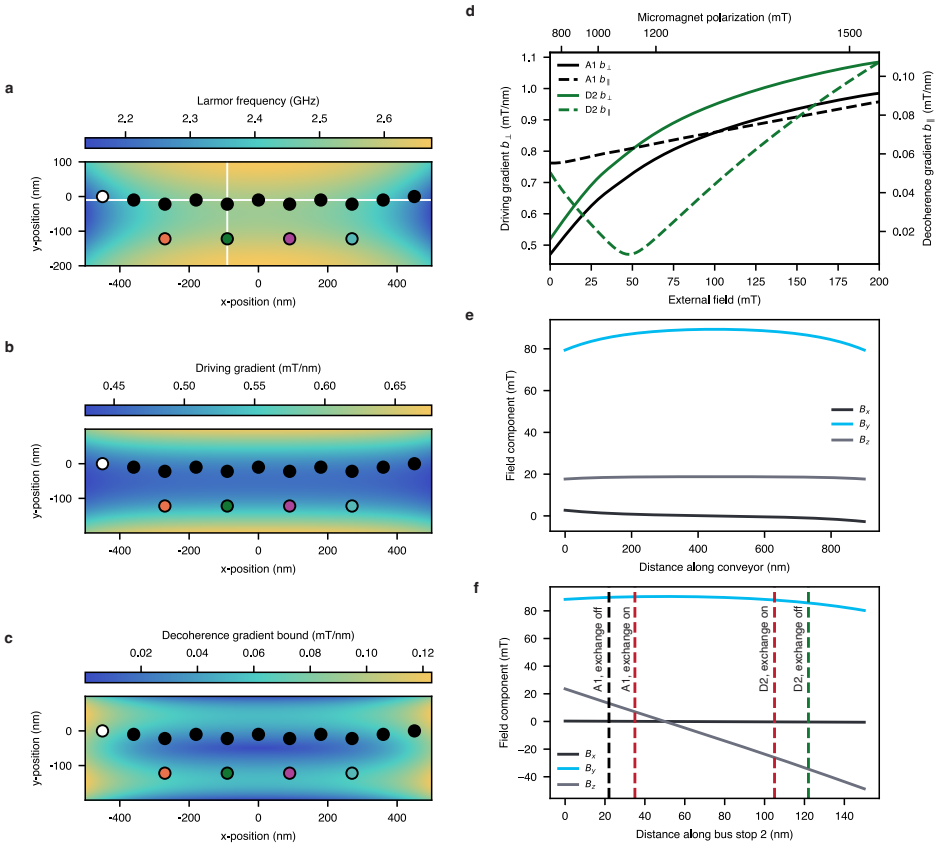


Figure 5.24: **a** Simulated Larmor frequencies of an electron spin (with $g = 2$) in the quantum well when $B_{\text{ext}} = 0$ after partial polarization of the micromagnet. Points represent estimated locations of the spin localized along the shuttling bus and the bus stops as a guide to the eye. **b** Simulated driving gradient in the quantum well when $B_{\text{ext}} = 0$ after partial polarization of the micromagnet, assuming a control field oriented along the y-axis. **c** Simulated decoherence gradient in the quantum well when $B_{\text{ext}} = 0$ after partial polarization of the micromagnet. (Continued on next page)

Figure 5.24: (Continued) **d** The estimated impact of the external field setting, and therefore micromagnet polarization, on the driving and decoherence gradients at two representative quantum dot locations in the array. A1 is assumed to be localized below gate P2, as this is where it is resonantly controlled and idles in our experiments. Generally, the driving gradient decreases monotonically with external field, while the decoherence gradient may exhibit non-monotonic behavior. The homogeneous polarization of the micromagnet, in units mT, is phenomenologically fit to $1.155 \times 10^{-4}x^3 - 5.515 \times 10^{-2}x^2 + 10.38x + 734.1$ [mT] where $x = B_{\text{ext}}/\text{mT}$ based on the measured Larmor frequencies of R1 and A1 as the external field is lowered from 200 mT to zero. **e** Simulated magnetic field components along the shuttling bus axis as indicated by the horizontal white line in **a** when $B_{\text{ext}} = 0$ after partial polarization of the micromagnet. The maximum estimated tip in magnetic field vector along this axis is 2°. **f** Simulated magnetic field components along the double-dot potential of bus stop 2 as indicated by the vertical white line in **a**. The vertical dashed lines indicate estimated spin qubit locations depending on whether the exchange interaction is pulsed on or off. The estimated tip in magnetic field vector between conveyor and bus stop dots ranges between 30° when exchange is off and 20° when exchange is on.

extracting the relevant quantities can be found in Sec. 2.4.1.

Fig. 5.24a shows the total magnetic field in the quantum well, expressed as the spin Larmor frequency $f_{\text{L}}(x, y)$ assuming a g-factor of 2. The theoretical distribution shown in Fig. 5.1c is taken along the dashed line, while the estimates for quantum dots localized in the bus stops are taken using the maximum of the simulated single-particle spatial wave functions. For three of the four bus stops, we measure the qualitatively-expected Zeeman energy difference between bus and bus stop spins. Bus stop 4 is an exception, where the bus stop spin is lower in frequency than the bus, and the Larmor frequencies only differ by about 20 MHz. This requires a slower two-qubit interaction to maintain adiabaticity. The exact reason for this discrepancy presumably depends on the microscopics of the device which we cannot deduce with certainty. The micromagnet design is quite robust to misalignments with the external field (i.e. the behavior is nearly unchanged if the magnetization vector does not point exactly along the y-axis). Therefore, it may be a result of either magnetic domain alignment in the micromagnet, which our simulations do not account for; a misalignment in the deposition of the micromagnet; or a shift in the actual position of the spins with respect to their estimated locations on the order of tens of nanometers along the y-axis. In fact, we rely on some degree of disorder, as the nominal micromagnet design with homogeneous polarization gives rise to a perfectly symmetric profile such that data qubits 1 and 4 as well as 2 and 3 should have identical frequencies. It is anticipated from previous experiments that microscopic variation will lift this degeneracy on the order of tens of megahertz, which is what we observe in experiment.

The estimated transverse gradient $b_\perp(x,y)$ for driving along the y-axis is shown in Fig. 5.24b and is dominated by the $\partial B_z(x,y)/\partial y$ gradient component. It is relatively constant over the sparse array, and we expect similar Rabi frequencies f_R to be achieved for equivalent driving amplitudes for all qubits. As f_R also depends on the microscopic dipole moment of the driven quantum dots (see Sec. 5.7.9), the driving amplitudes required to achieve a constant f_R across the array typically vary by an order-unity factor.

The longitudinal gradient $b_\parallel(x,y)$ through which electric noise couples to the spin depends on the spatial orientation of the fluctuation. We therefore take $|\nabla f_L(x,y)|$ as an estimate of the noise susceptibility, which will consist of primarily $\partial B_y(x,y)/\partial x$ and $\partial B_y(x,y)/\partial y$ components. Fig. 5.24c shows the sweet spot that emerges along the x-axis of symmetry. While this sweet spot cannot be shared by both the bus axis and the bus stops, in all cases the gradient remains below 0.1 mT/nm which is considered reasonable [42, 77].

Since the superconducting solenoid we used cannot be operated in persistent mode, the device is operated with only the remanence field of the micromagnet to avoid magnetic noise arising from current noise in the supply that drives the solenoid. The inclusion of a noiseless external field would have meaningful consequences. Two illustrative cases are plotted in Fig. 5.24d for the ancilla qubit A1 localized below P2 and data qubit D2 localized below BP2. In general, a monotonic decrease in driving gradient is observed as the external field is lowered to zero. The decoherence gradient generally decreases as the external field is lowered from 200 mT, but the trend is not necessarily monotonic and the minimum may not be located at zero external field. In fact, a performance boost would likely follow from operating with a noiseless external field of 50 mT oriented along the y-axis (instead of zero external field) as both the Rabi frequency should increase and most qubits would be more robust to charge noise.

Fig. 5.24e shows the magnetic field components along the shuttling bus and highlights the homogeneity of the estimated Larmor vector across the array. The orientation of the magnetic field vector at one end of the conveyor differs from that at the center by only about 2° which facilitates fast adiabatic spin shuttling. Fig. 5.24f shows the magnetic field components along the axis of bus stop 2 that are relevant for the two-qubit interaction taking place there. A sizable tip of about 25° exists between the magnetic field vectors at each quantum dot location. Such a tip gives rise to both spin-conserving and spin-flipping tunnel coupling between quantum dots. Along with the moderate expected Zeeman energy difference of about 50 MHz between the interacting qubits, this makes the adiabatic controlled-phase gate more appealing to implement than other possible two-qubit interactions. If the external field were made to oppose the micromagnet polarization, the spin Larmor frequencies

would decrease and the tip angle between bus stop and shuttling bus dots would increase, and baseband hopping control at the bus stop locations would also be possible [20, 78].

REFERENCES

[1] B. Undseth *et al.* *Weight-four parity checks with silicon spin qubits*. 2026. arXiv: 2601.23267 [cond-mat.mes-hall]. url: https://arxiv.org/abs/2601.23267.

[2] G. Burkard *et al.* "Semiconductor spin qubits". In: *Rev. Mod. Phys.* 95 (2 June 2023), p. 025003. doi: 10.1103/RevModPhys.95.025003. url: https://link.aps.org/doi/10.1103/RevModPhys.95.025003.

[3] K. Takeda *et al.* "Quantum error correction with silicon spin qubits". In: *Nature* 608.7924 (Aug. 2022), pp. 682–686. issn: 1476-4687. url: http://dx.doi.org/10.1038/s41586-022-04986-6.

[4] F. van Riggelen *et al.* "Phase flip code with semiconductor spin qubits". In: *npj Quantum Information* 8.1 (Oct. 2022), p. 124. issn: 2056-6387. url: https://doi.org/10.1038/s41534-022-00639-8.

[5] R. Raussendorf and J. Harrington. "Fault-Tolerant Quantum Computation with High Threshold in Two Dimensions". In: *Phys. Rev. Lett.* 98 (19 May 2007), p. 190504. doi: 10.1103/PhysRevLett.98.190504. url: https://link.aps.org/doi/10.1103/PhysRevLett.98.190504.

[6] A. G. Fowler *et al.* "Surface codes: Towards practical large-scale quantum computation". In: *Phys. Rev. A* 86 (3 Sept. 2012), p. 032324. doi: 10.1103/PhysRevA.86.032324. url: https://link.aps.org/doi/10.1103/PhysRevA.86.032324.

[7] J. M. Taylor *et al.* "Fault-tolerant architecture for quantum computation using electrically controlled semiconductor spins". In: *Nature Physics* 1.3 (Dec. 2005), pp. 177–183. issn: 17452481. doi: 10.1038/nphys174.

[8] T. Fujita *et al.* "Coherent shuttle of electron-spin states". In: *npj Quantum Information* 3.1 (June 2017). issn: 2056-6387. url: http://dx.doi.org/10.1038/s41534-017-0024-4.

[9] B. Jadot *et al.* “Distant spin entanglement via fast and coherent electron shuttling”. In: *Nature Nanotechnology* 16.5 (Feb. 2021), pp. 570–575. issn: 1748-3395. url: http://dx.doi.org/10.1038/s41565-021-00846-y.

[10] A. R. Mills *et al.* “Shuttling a single charge across a one-dimensional array of silicon quantum dots”. In: *Nature Communications* 10.1 (Mar. 2019). issn: 2041-1723. url: http://dx.doi.org/10.1038/s41467-019-08970-z.

[11] J. Yoneda *et al.* “Coherent spin qubit transport in silicon”. In: *Nature Communications* 12.1 (July 2021). issn: 2041-1723. doi: 10.1038/s41467-021-24371-7. url: http://dx.doi.org/10.1038/s41467-021-24371-7.

[12] T. Struck *et al.* “Spin-EPR-pair separation by conveyor-mode single electron shuttling in Si/SiGe”. In: *Nature Communications* 15.1 (Feb. 2024). issn: 2041-1723. url: http://dx.doi.org/10.1038/s41467-024-45583-7.

[13] R. Xue *et al.* “Si/SiGe QuBus for single electron information-processing devices with memory and micron-scale connectivity function”. In: *Nature Communications* 15.1 (Mar. 2024). issn: 2041-1723. url: http://dx.doi.org/10.1038/s41467-024-46519-x.

[14] F. van Riggelen-Doelman *et al.* “Coherent spin qubit shuttling through germanium quantum dots”. In: *Nature Communications* 15.1 (July 2024). issn: 2041-1723. doi: 10.1038/s41467-024-49358-y. url: http://dx.doi.org/10.1038/s41467-024-49358-y.

[15] M. De Smet *et al.* “High-fidelity single-spin shuttling in silicon”. In: *Nature Nanotechnology* 20.7 (June 2025), pp. 866–872. issn: 1748-3395. url: http://dx.doi.org/10.1038/s41565-025-01920-5.

[16] Z. Ademi *et al. Distributing entanglement between distant semiconductor qubit registers using a shared-control shuttling link*. 2025. arXiv: 2510.26860 [cond-mat.mes-hall].

[17] N. D. Foster *et al.* “Dephasing and error dynamics affecting a singlet-triplet qubit during coherent spin shuttling”. In: *npj Quantum Information* 11 (1 Apr. 2025). url: https://doi.org/10.1038/s41534-025-00996-0.

[18] D. Degli Esposti *et al.* “Low disorder and high valley splitting in silicon”. In: *npj Quantum Information* 10.1 (Mar. 2024). issn: 2056-6387. url: http://dx.doi.org/10.1038/s41534-024-00826-9.

[19] M. Volmer *et al.* “Mapping of valley splitting by conveyor-mode spin-coherent electron shuttling”. In: *npj Quantum Information* 10.1 (June 2024). issn: 2056-6387. doi: 10.1038/s41534-024-00852-7. url: http://dx.doi.org/10.1038/s41534-024-00852-7.

[20] C.-A. Wang *et al.* “Operating semiconductor quantum processors with hopping spins”. In: *Science* 385.6707 (July 2024), pp. 447–452. issn: 1095-9203. doi: 10.1126/science.ado5915. url: http://dx.doi.org/10.1126/science.ado5915.

[21] A. Noiri *et al.* “A shuttling-based two-qubit logic gate for linking distant silicon quantum processors”. In: *Nature Communications* 13.1 (Sept. 2022). issn: 2041-1723. url: http://dx.doi.org/10.1038/s41467-022-33453-z.

[22] Y. Matsumoto *et al. Two-qubit logic and teleportation with mobile spin qubits in silicon*. 2025. arXiv: 2503.15434 [quant-ph].

[23] X. Xue. “Performance benchmarking of silicon quantum processors”. Dissertation (TU Delft). Delft University of Technology, 2022. isbn: 978-90-8593-527-8. doi: 10.4233/uuid:20fce6ef-6bb3-42a1-bdd3-53b2a282f0ae.

[24] B. Buonacorsi *et al.* “Network architecture for a topological quantum computer in silicon”. In: *Quantum Science and Technology* 4.2 (Jan. 2019), p. 025003. issn: 2058-9565. doi: 10.1088/2058-9565/aaf3c4. url: http://dx.doi.org/10.1088/2058-9565/aaf3c4.

[25] J. M. Boter *et al.* “Spiderweb Array: A Sparse Spin-Qubit Array”. In: *Physical Review Applied* 18.2 (Aug. 2022). issn: 2331-7019. doi: 10.1103/physrevapplied.18.024053. url: http://dx.doi.org/10.1103/PhysRevApplied.18.024053.

[26] Z. Cai, A. Siegel, and S. Benjamin. “Looped Pipelines Enabling Effective 3D Qubit Lattices in a Strictly 2D Device”. In: *PRX Quantum* 4.2 (June 2023). issn: 2691-3399. url: http://dx.doi.org/10.1103/PRXQuantum.4.020345.

[27] M. Künne *et al.* “The SpinBus architecture for scaling spin qubits with electron shuttling”. In: *Nature Communications* 15.1 (June 2024). issn: 2041-1723. url: http://dx.doi.org/10.1038/s41467-024-49182-4.

[28] A. Siegel *et al.* “Quantum Snakes on a Plane: Mobile, Low-Dimensional Logical Qubits on a 2D Surface”. In: *PRX Quantum* 7 (1 Feb. 2026), p. 010339. doi: 10.1103/494s-jd8h. url: https://link.aps.org/doi/10.1103/494s-jd8h.

[29] S. Moses *et al.* “A Race-Track Trapped-Ion Quantum Processor”. In: *Physical Review X* 13.4 (Dec. 2023). issn: 2160-3308. url: http://dx.doi.org/10.1103/PhysRevX.13.041052.

[30] D. Bluvstein *et al.* “Logical quantum processor based on reconfigurable atom arrays”. In: *Nature* 626.7997 (Dec. 2023), pp. 58–65. issn: 1476-4687. url: http://dx.doi.org/10.1038/s41586-023-06927-3.

[31] N. P. Breuckmann and J. N. Eberhardt. “Quantum Low-Density Parity-Check Codes”. In: *PRX Quantum* 2.4 (Oct. 2021). issn: 2691-3399. url: http://dx.doi.org/10.1103/PRXQuantum.2.040101.

[32] I. Heinz *et al.* “Analysis and mitigation of residual exchange coupling in linear spin-qubit arrays”. In: *Phys. Rev. Res.* 6 (1 Feb. 2024), p. 013153. url: https://link.aps.org/doi/10.1103/PhysRevResearch.6.013153.

[33] A. S. Rao *et al.* “Modular Autonomous Virtualization System for Two-Dimensional Semiconductor Quantum Dot Arrays”. In: *Phys. Rev. X* 15 (2 Apr. 2025), p. 021034. url: https://link.aps.org/doi/10.1103/PhysRevX.15.021034.

[34] D. Jirovec *et al.* “Mitigation of exchange crosstalk in dense quantum dot arrays”. In: *Phys. Rev. Appl.* 24 (3 Sept. 2025), p. 034051. url: https://link.aps.org/doi/10.1103/qgnt-n527.

[35] G. Kiene *et al.* “DC-Readout of Semiconductor Spin Qubits: Opportunities and Limits”. In: *IEEE Transactions on Circuits and Systems I: Regular Papers* 72.10 (2025), pp. 5457–5470. url: http://dx.doi.org/10.1109/TCSI.2025.3542335.

[36] F. Vigneau *et al.* “Probing quantum devices with radio-frequency reflectometry”. In: *Applied Physics Reviews* 10.2 (Feb. 2023). issn: 1931-9401. url: http://dx.doi.org/10.1063/5.0088229.

[37] Y.-H. Wu *et al. Simultaneous High-Fidelity Single-Qubit Gates in a Spin Qubit Array*. 2025. arXiv: 2507.11918 [quant-ph].

[38] X. Xue *et al.* “Quantum logic with spin qubits crossing the surface code threshold”. In: *Nature* 601.7893 (Jan. 2022), pp. 343–347. issn: 1476-4687. doi: 10.1038/s41586-021-04273-w. url: http://dx.doi.org/10.1038/s41586-021-04273-w.

[39] A. Noiri *et al.* “Fast universal quantum gate above the fault-tolerance threshold in silicon”. In: *Nature* 601.7893 (Jan. 2022), pp. 338–342. issn: 1476-4687. doi: 10.1038/s41586-021-04182-y. url: http://dx.doi.org/10.1038/s41586-021-04182-y.

[40] A. R. Mills *et al.* “Two-qubit silicon quantum processor with operation fidelity exceeding 99%”. In: *Science Advances* 8.14 (Apr. 2022). issn: 2375-2548. doi: 10.1126/sciadv.abn5130. url: http://dx.doi.org/10.1126/sciadv.abn5130.

[41] K. Takeda *et al.* “Rapid single-shot parity spin readout in a silicon double quantum dot with fidelity exceeding 99%”. In: *npj Quantum Information* 10.1 (Feb. 2024). issn: 2056-6387. doi: 10.1038/s41534-024-00813-0. url: http://dx.doi.org/10.1038/s41534-024-00813-0.

[42] S. G. J. Philips *et al.* “Universal control of a six-qubit quantum processor in silicon”. In: *Nature* 609.7929 (Sept. 2022), pp. 919–924. issn: 1476-4687. doi: 10.1038/s41586-022-05117-x. url: http://dx.doi.org/10.1038/s41586-022-05117-x.

[43] A. E. Seedhouse *et al.* “Pauli Blockade in Silicon Quantum Dots with Spin-Orbit Control”. In: *PRX Quantum* 2.1 (Jan. 2021). issn: 2691-3399. url: http://dx.doi.org/10.1103/PRXQuantum.2.010303.

[44] A. Siegel, A. Strikis, and M. Fogarty. “Towards Early Fault Tolerance on a $2 \times N$ Array of Qubits Equipped with Shuttling”. In: *PRX Quantum* 5 (4 Nov. 2024), p. 040328. doi: 10.1103/PRXQuantum.5.040328. url: https://link.aps.org/doi/10.1103/PRXQuantum.5.040328.

[45] J. Park *et al. Highly Tunable Two-Qubit Interactions in Si/SiGe Quantum Dots by Interchanging the Roles of Qubit-Defining Gates*. 2025. arXiv: 2512.20142 [quant-ph].

[46] I. Seidler *et al.* “Conveyor-mode single-electron shuttling in Si/SiGe for a scalable quantum computing architecture”. In: *npj Quantum Information* 8.1 (Aug. 2022). issn: 2056-6387. url: http://dx.doi.org/10.1038/s41534-022-00615-2.

[47] V. Langrock *et al.* “Blueprint of a Scalable Spin Qubit Shuttle Device for Coherent Mid-Range Qubit Transfer in Disordered Si/SiGe/SiO_2”. In: *PRX Quantum* 4 (2 Apr. 2023), p. 020305. url: https://link.aps.org/doi/10.1103/PRXQuantum.4.020305.

[48] R. Hanson *et al.* “Spins in few-electron quantum dots”. In: *Reviews of Modern Physics* 79.4 (Oct. 2007), pp. 1217–1265. issn: 1539-0756. url: http://dx.doi.org/10.1103/RevModPhys.79.1217.

[49] J. Y. Huang *et al.* “High-fidelity spin qubit operation and algorithmic initialization above 1 K”. In: *Nature* 627.8005 (Mar. 2024), pp. 772–777. issn: 1476-4687. doi: 10.1038/s41586-024-07160-2. url: http://dx.doi.org/10.1038/s41586-024-07160-2.

[50] C. Jones *et al. Mid-circuit logic executed in the qubit layer of a quantum processor*. 2025. arXiv: 2512.12648 [quant-ph].

[51] T. Tanttu *et al.* “Assessment of the errors of high-fidelity two-qubit gates in silicon quantum dots”. In: *Nature Physics* 20.11 (Aug. 2024), pp. 1804–1809. issn: 1745-2481. doi: 10.1038/s41567-024-02614-w. url: http://dx.doi.org/10.1038/s41567-024-02614-w.

[52] P. Steinacker *et al.* “Industry-compatible silicon spin-qubit unit cells exceeding 99% fidelity”. In: *Nature* 646.8083 (Sept. 2025), pp. 81–87. issn: 1476-4687. url: http://dx.doi.org/10.1038/s41586-025-09531-9.

[53] I. Fernández de Fuentes *et al.* “Running a Six-Qubit Quantum Circuit on a Silicon Spin-Qubit Array”. In: *PRX Quantum* 7 (1 Jan. 2026), p. 010308. doi: 10.1103/f285-l2v5. url: https://link.aps.org/doi/10.1103/f285-l2v5.

[54] K. Takeda *et al.* “Quantum tomography of an entangled three-qubit state in silicon”. In: *Nature Nanotechnology* 16.9 (June 2021), pp. 965–969. issn: 1748-3395. url: http://dx.doi.org/10.1038/s41565-021-00925-0.

[55] C. K. Andersen *et al.* “Repeated quantum error detection in a surface code”. In: *Nature Physics* 16.8 (June 2020), pp. 875–880. issn: 1745-2481. url: http://dx.doi.org/10.1038/s41567-020-0920-y.

[56] R. Li *et al. A trilinear quantum dot architecture for semiconductor spin qubits*. 2025. arXiv: 2501.17814 [quant-ph].

[57] R. Versluis *et al.* “Scalable Quantum Circuit and Control for a Superconducting Surface Code”. In: *Phys. Rev. Appl.* 8 (3 Sept. 2017), p. 034021. url: https://link.aps.org/doi/10.1103/PhysRevApplied.8.034021.

[58] N. M. Linke *et al.* “Fault-tolerant quantum error detection”. In: *Science Advances* 3.10 (Oct. 2017). issn: 2375-2548. url: http://dx.doi.org/10.1126/sciadv.1701074.

[59] J. Kelly *et al.* “State preservation by repetitive error detection in a superconducting quantum circuit”. In: *Nature* 519.7541 (Mar. 2015), pp. 66–69. issn: 1476-4687. url: http://dx.doi.org/10.1038/nature14270.

[60] C. Zhang *et al.* “Quantum error detection in a silicon quantum processor”. en. In: *Nature Electronics* (Jan. 2026), pp. 1–9. issn: 2520-1131. doi: 10.1038/s41928-025-01557-1.

[61] B. Undseth *et al.* “Hotter is Easier: Unexpected Temperature Dependence of Spin Qubit Frequencies”. In: *Phys. Rev. X* 13 (4 Oct. 2023), p. 041015. doi: 10.1103/PhysRevX.13.041015. url: https://link.aps.org/doi/10.1103/PhysRevX.13.041015.

[62] Y.-Y. Liu *et al.* “Radio-Frequency Reflectometry in Silicon-Based Quantum Dots”. In: *Physical Review Applied* 16.1 (July 2021). issn: 2331-7019. doi: 10.1103/physrevapplied.16.014057. url: http://dx.doi.org/10.1103/PhysRevApplied.16.014057.

[63] S. R. Katiraee-Far *et al.* *Unified evolutionary optimization for high-fidelity spin qubit operations*. 2025. arXiv: 2503.12256 [quant-ph].

[64] T. Kobayashi *et al.* “Feedback-based active reset of a spin qubit in silicon”. In: *npj Quantum Information* 9.1 (June 2023). issn: 2056-6387. url: http://dx.doi.org/10.1038/s41534-023-00719-3.

[65] M. Russ *et al.* “High-fidelity quantum gates in Si/SiGe double quantum dots”. In: *Physical Review B* 97.8 (Feb. 2018). issn: 2469-9969. doi: 10.1103/physrevb.97.085421. url: http://dx.doi.org/10.1103/PhysRevB.97.085421.

[66] M. Reed *et al.* “Reduced Sensitivity to Charge Noise in Semiconductor Spin Qubits via Symmetric Operation”. In: *Physical Review Letters* 116.11 (Mar. 2016). issn: 1079-7114. doi: 10.1103/physrevlett.116.110402. url: http://dx.doi.org/10.1103/PhysRevLett.116.110402.

[67] J. Bylander *et al.* “Noise spectroscopy through dynamical decoupling with a superconducting flux qubit”. In: *Nature Physics* 7.7 (May 2011), pp. 565–570. issn: 1745-2481. url: http://dx.doi.org/10.1038/nphys1994.

[68] W. I. L. Lawrie *et al.* “Simultaneous single-qubit driving of semiconductor spin qubits at the fault-tolerant threshold”. In: *Nature Communications* 14.1 (June 2023). issn: 2041-1723. doi: 10.1038/s41467-023-39334-3. url: http://dx.doi.org/10.1038/s41467-023-39334-3.

[69] E. Kawakami *et al.* “Electrical control of a long-lived spin qubit in a Si/SiGe quantum dot”. In: *Nature Nanotechnology* 9.9 (Aug. 2014), pp. 666–670. issn: 1748-3395. doi: 10.1038/nnano.2014.153. url: http://dx.doi.org/10.1038/nnano.2014.153.

[70] R. Ferdous *et al.* “Valley dependent anisotropic spin splitting in silicon quantum dots”. In: *npj Quantum Information* 4.1 (June 2018). issn: 2056-6387. doi: 10.1038/s41534-018-0075-1. url: http://dx.doi.org/10.1038/s41534-018-0075-1.

[71] M. P. Losert *et al.* “Strategies for Enhancing Spin-Shuttling Fidelities in Si/SiGe Quantum Wells with Random-Alloy Disorder”. In: *PRX Quantum* 5 (4 Nov. 2024), p. 040322. doi: 10.1103/PRXQuantum.5.040322. url: https://link.aps.org/doi/10.1103/PRXQuantum.5.040322.

[72] M. Volmer *et al. Reduction of the impact of the local valley splitting on the coherence of conveyor-belt spin shuttling in ^{28}Si/SiGe*. 2025. arXiv: 2510.03773 [quant-ph].

[73] X. Xue *et al.* “Benchmarking Gate Fidelities in a Si/SiGe Two-Qubit Device”. In: *Phys. Rev. X* 9 (2 Apr. 2019), p. 021011. url: https://link.aps.org/doi/10.1103/PhysRevX.9.021011.

[74] F. Beaudoin *et al.* “Robust technology computer-aided design of gated quantum dots at cryogenic temperature”. In: *Applied Physics Letters* 120.26 (June 2022), p. 264001. issn: 0003-6951. doi: 10.1063/5.0097202.

[75] M. Rimbach-Russ *et al.* “Simple framework for systematic high-fidelity gate operations”. In: *Quantum Science and Technology* 8.4 (Sept. 2023), p. 045025. url: https://doi.org/10.1088/2058-9565/acf786.

[76] M. Aldeghi *et al.* “Simulation and Measurement of Stray Fields for the Manipulation of Spin Qubits in One- and Two-Dimensional Arrays”. In: *Nano Letters* 25.5 (Feb. 2025), pp. 1838–1844. issn: 1530-6984. doi: 10.1021/acs.nanolett.4c05037.

[77] J. Yoneda *et al.* “A quantum-dot spin qubit with coherence limited by charge noise and fidelity higher than 99.9%”. In: *Nature Nanotechnology* 13.2 (Dec. 2017), pp. 102–106. issn: 1748-3395. doi: 10.1038/s41565-017-0014-x. url: http://dx.doi.org/10.1038/s41565-017-0014-x.

[78] F. K. Unseld *et al.* “Baseband control of single-electron silicon spin qubits in two dimensions”. In: *Nature Communications* 16 (July 2025), p. 5605. url: https://doi.org/10.1038/s41467-025-60351-x.

6

CONCLUSIONS AND OUTLOOK

The original work in this thesis advances the degree to which silicon-spin-based quantum processors can be engineered for the purposes of quantum information processing. In the case of the heating effect which is the focus of Chapter 3 (and parts of Chapter 4), the impact can be contextualized based on the research that has been conducted in the meantime. I discuss these developments in Secs. 6.1. For the spin-shuttling architecture of Chapter 5, where the state-of-the-art results are relatively new at the time of writing this dissertation, I will discuss in Sec. 6.2 how the approach can be pushed further towards implementing logical qubits in silicon with quantum error detection, as well as some other fun proofs-of-principle that could be tested in such an architecture that would be valuable primitives in future devices leveraging spin shuttling. Finally, combining the ideas of baseband control from Chapter 4 and mobile spins from Chapter 5 offers what I believe to be the most promising way forward to build more powerful quantum processors with spin qubits. In Sec. 6.3, I will outline how the technical ideas in this thesis can be applied to a promising architecture to give a sense of what I believe is possible. Last, in Sec. 6.4 I will highlight what I believe are the most urgent problems the field must address in the near term.

6.1. THE HEATING EFFECT: REDUX

The work presented in Chapter 3 advanced our understanding of the heating effect, and particularly our ability to avoid it by operating at elevated device temperatures. However, we were unable to conclude a microscopic origin of the effect due to the limited statistics available from a single device and the presence of the micromagnet, which makes it challenging to decouple the potential contribution of the on-chip micromagnet.

Shortly after our manuscript became available, Choi and Joynt proposed thermally-activated charge defects, modelled as two-level systems (TLSs), as a plausible microscopic origin for the heating effect, both as it originates from dissipating control signals and from raising the device temperature [1]. In the theory, thermally-activated TLSs produce a net electric field which Stark-shifts the spins - either due to iSOI or a magnetic gradient. The theory is compelling, particularly because it provides an explanation for the non-monotonic temperature dependence: the (potentially-interacting) TLSs are thermally “activated” across a range of temperatures and those activated at lower temperatures may induce an electric field that is overcome by those activated at higher temperatures. This is not a guarantee of non-monotonicity, but it arises for certain configurations of randomly sampled TLSs.

There are two sticking points that arise when applying this theory to our measurements in Chapter 3. First, if TLSs give rise to a net electric field,

why were we unable to definitively observe an electrostatic shift in the SET Coulomb peak, charge stability diagram or exchange as a function of temperature? Second, as the net in-plane field produced by the TLSs should be oriented in any direction, the spins should be Stark-shifted both higher and lower in frequency depending on how they are pushed in the micromagnet gradient. Through this lens, the fact that we observed all six spins shift higher in frequency is not impossible, but it is unlikely. The additional statistics from Chapter 4 do not resolve the issue, and in fact compound the weirdness as we observed device temperature and pulse-induced heating impart frequency shifts of opposite sign.

Stronger experimental evidence consistent with thermally-sensitive electric dipoles was provided by [2], whereby the electrical susceptibility of a hole spin qubit (with no on-chip magnet) could be correlated with the temperature dependence of its Larmor frequency, and a thermal sweet-spot could be identified with respect to the orientation of the external magnetic field.

From the practitioner's point of view, pinpointing the origin is only as useful as the ability to then mitigate it. Raising the device temperature is easy, but also heavy-handed as a compromise must be struck between coherence times and thermal robustness. An ideal solution would be to eliminate the purported TLSs at their source. Here, evidence is more anecdotal than scientific, but that's better than nothing. In [3], it is reported that the heating effect in their devices became less pronounced by moving from depletion-mode devices with thicker oxide and titanium-gold electrodes to accumulation-mode devices with aluminum gates. However, the device measured in [4] also suffered from heating effects despite being an accumulation-mode device with aluminum gates. This leads to a more general discussion on the role of the gate stack that will be continued in Sec. 6.4. In short, the statistics are simply too limited to make definitive statements at this point in time.

A related conversation is the role of heating in rf-reflectometry, which is also a nuisance. Recent work on high-fidelity readout in germanium has also reported elevating the device temperature to eliminate transients in the readout circuit [5]. From my own experience in silicon, routing the rf-SET signal capacitively through the accumulation gate using the split-gate approach of [6], as opposed to through the resistive ohmic, appears to be more thermally robust. In both platforms, when transient behaviour is seen in the measured histogram over the course of a measurement, turning up the mixing chamber temperature even by a few tens of millikelvin is often a sufficient solution before resorting to prepulsing or long wait-times.

The heating effect still has its mysteries, but it is less mysterious than at the beginning of my PhD owing to all of the above work. Nonetheless, the heating effect remains a problem, albeit a smaller one when working

at elevated device temperatures. Our results in Chapters 3 and 4 showed that although raising the device temperature could avoid the most egregious errors due to PIRS, abnormal phase pickups are still present at higher temperatures. Although we did not study heating systematically in Chapter 5, we still had to calibrate single-qubit phase pickups as shown in Fig. 5.7.10, and these phase pickups are not always consistent in sign and magnitude with predictions based on the AC Stark shift of Eq. 2.13. In particular, the diagonal elements of the crosstalk matrix, which correct for the Bloch-Siegert shift, should theoretically be much smaller than what are observed. Furthermore, the phase pickups exhibit some nonlinearity as many resonant gates are applied in series. For shallow circuits, such as the parity check benchmarks, calibrating a linear approximation in the few-gate limit suffices. For deeper circuits, the heating bottleneck may resurface.

The recent demonstration of an 11-qubit dopant-based QPU provides a glimpse into the future for gate defined dots [7]. As donors exhibit very high fidelity ESR and NMR control, even very small frequency shifts cause meaningful degradations in performance, and they manifest differently for the nuclear and electron spins in the system. They present some unique observations which add useful points to the overall discussion. Unlike in our work, they do not observe a saturation with temperature. In the two-register device, each register exhibits different heating behaviour, even though they are 20 nm apart. According to Junliang Wang, heating effects are one of the primary performance bottlenecks in their processor. It appears that the better our semiconductor-based qubits become, the more we will continue to discuss heating.

For now, the advice “Hotter is easier” seems to be withstanding the test of time, both with regards to qubit control and rf-reflectometry, and the strategy of turning up the mixing chamber temperature has become a standard practice, when available, among the spin qubit groups at QuTech and beyond.

6.2. LOGICAL SPIN QUBITS AND MORE

In Chapter 5, we show how the connectivity of a weight-four stabilizer plaquette can be mapped to a sparse spin qubit array and that non-demolition parity measurements up to weight-four can be extracted. In my opinion, however, the most important contributions to the field will come through the methods. Importantly, we show how a sparse array can be tuned, including gate virtualization, without the need for local charge sensing by leveraging coherent spin shuttling. Anne-Marije Zwerver succinctly summarized that instead of tuning qubits from quantum dots, as is standard, we “use qubits to tune quantum dots”. In a future where charge sensing occupies precious device real estate, such methods will

be invaluable. In parallel to us, this approach has also been used by Sasha Ivlev and Harold Co in a large germanium array.

We also show how multi-qubit control can be achieved in spite of the complications arising from shuttling qubits around on a chip. Most notably, moving spins (and their static but nearby neighbours) pick up phases, and these phases depend on exactly where the spins went and the pulses that took them there. If we calibrated phase pickups for every qubit during all distinct weight-two through weight-four parity checks we implemented, this amounts to 55 additional calibrated parameters. If, say, the conveyor speed is adjusted, every single parameter would change. Automated tuning strategies will be wasted if they spend most of their time fighting combinatorial blow-up. In light of this, dynamical decoupling becomes an important friend, as does the adiabatic CZ and its handy commutation properties with single-qubit control in the rotating frame. Any large architecture taking advantage of spin shuttling will need to build upon these strategies to be feasible.

The parity checks we show are routine for other platforms, so their perceived importance depends on what we can actually build from them. To illustrate how these can be put to use, I will outline the remaining steps required to implement the creation and measurement of a logical Bell state with this device.

Of the many possible variations, the $[[4, 2, 2]]$ rotated toric code shown in Fig. 6.1a maps particularly well to the device with the connectivity that is already in place. The code has two weight-four stabilizers and encodes two logical qubits in the data qubit state $|D_1D_2D_3D_4\rangle$:

$$|\overline{00}\rangle = \frac{1}{\sqrt{2}}(|0000\rangle + |1111\rangle) \tag{6.1}$$

$$|\overline{01}\rangle = \frac{1}{\sqrt{2}}(|0011\rangle + |1100\rangle) \tag{6.2}$$

$$|\overline{10}\rangle = \frac{1}{\sqrt{2}}(|0101\rangle + |1010\rangle) \tag{6.3}$$

$$|\overline{11}\rangle = \frac{1}{\sqrt{2}}(|0110\rangle + |1001\rangle). \tag{6.4}$$

The logical operators required to measure the logical states are accessible by weight-2 or weight-3 parity checks (e.g. $\overline{Y}_1 = YZXI$ and $\overline{Y}_2 = YXZI$), and any Pauli-string observable up to weight-four can be measured using the decoupled CZ approach of Chapter 5.

The benefit of using an encoding that requires two stabilizer measurements is that the device naturally supports two shuttled ancilla qubits A1 and A2. While only the former was utilized in Chapter 5, the sensor and PSB pair on the right side of the device are functional and

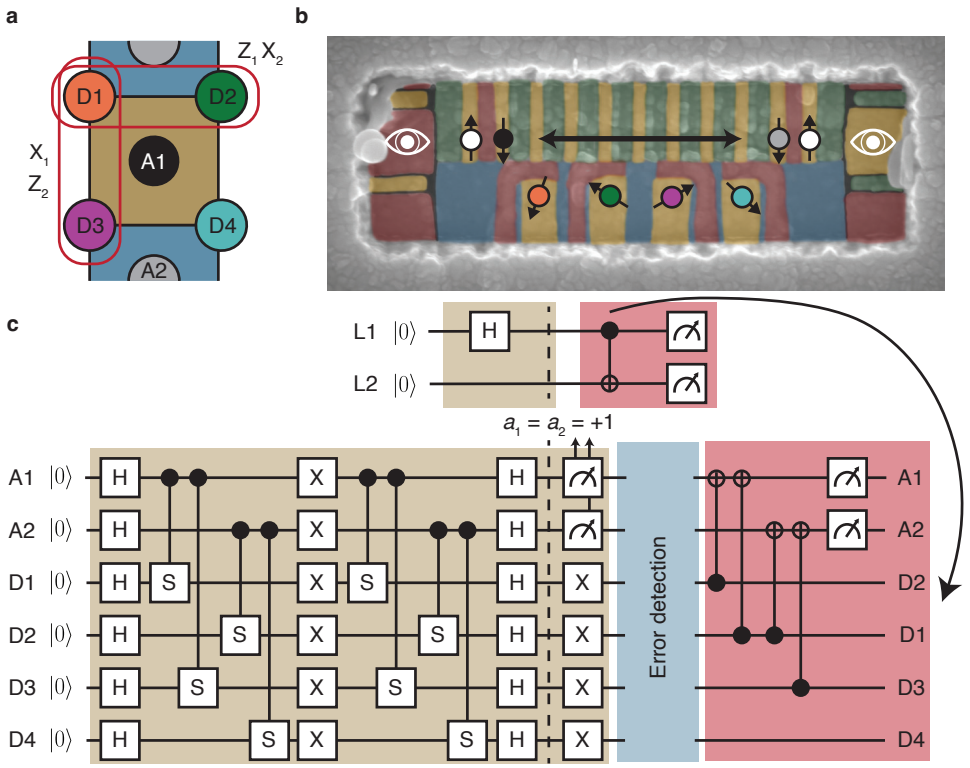


Figure 6.1: **a** Illustration of the $[[4, 2, 2]]$ rotated toric code. The data qubit and ancilla labels correspond to the colored spins in **b**. The two plaquettes correspond to the stabilizers $S_X = XXXX$ and $S_Z = ZZZZ$. The red rectangles highlight the logical qubit operators $\overline{X}_1 = XIXI$, $\overline{Z}_1 = ZZII$, $\overline{X}_2 = XXII$, and $\overline{Z}_2 = ZIZI$ [8]. **b** False-colored SEM of the device from Chapter 5 with the second ancilla qubit A2 and associated readout zone included. **c** Logical and physical quantum circuits for generating a logical Bell state. The logical Hadamard is implemented probabilistically by performing X-type parity measurements on qubit pairs D1/D3 and D2/D4 initialized in to the ground state. Error detection may be performed by serially extracting S_X and S_Z with the two mobile ancillas, and the two ancillas may be measured simultaneously while applying dynamical decoupling pulses to the data qubits. The logical-CNOT is performed by qubit relabeling and is physically realized when measuring the qubits. Measurement in the logical-Z basis is shown, but full logical or physical quantum state tomography may be performed to diagnose circuit performance.

could be measured simultaneously (see Fig. 6.1b). This would enable a full syndrome extraction every measurement cycle. As both Z-type and X-type stabilizer measurements have been demonstrated, the main challenge for each cycle is to ensure that the shuttled ancillas do not interfere with each other.

The logical Bell state preparation circuit is shown in Fig. 6.1c. To map the required logical-Hadamard and logical-CNOT to physical qubits, we

can take advantage of a couple tricks put forward by Minh Nguyen. For the Hadamard, we use:

$$\overline{H}_1 |\overline{00}\rangle = \frac{1}{\sqrt{2}}\left(|\overline{00}\rangle + |\overline{10}\rangle\right) \tag{6.5}$$

$$= \frac{1}{2}\left(|0000\rangle + |0101\rangle + |1010\rangle + |1111\rangle\right) \tag{6.6}$$

$$= \left(\frac{|00\rangle + |11\rangle}{\sqrt{2}}\right)_{13} \otimes \left(\frac{|00\rangle + |11\rangle}{\sqrt{2}}\right)_{24}, \tag{6.7}$$

meaning that the logical superposition state can be generated by creating two physical Bell states. From the physical $|0000\rangle$ state, these Bell states may be generated deterministically (though not fault-tolerantly) using two physical Hadamards and two physical CNOTs. Although direct interaction between the data qubits has not been implemented in the device, it is entirely possible to do so. As with the parity checks, finding a way to do so that does not require a mountain of phase-corrections would be desirable. The off-the-shelf alternative would be to use two weight-two parity checks to probabilistically generate the entanglement with a success rate of 25%. Fig. 6.1c illustrates the latter technique, where the two parity checks are weaved together around decoupling pulses that refocus phase pickups acquired by all qubits during shuttling sequences.

For the logical-CNOT, we take advantage of the structure of the $[[4, 2, 2]]$ code, which allows the gate to be performed simply by relabeling physical qubits as $1 \longleftrightarrow 2$ [9]. The validity of this method is readily verified by inspecting the form of the logical states. Although this logical two-qubit gate comes "for free" at first glance, it is only practical if we can also measure the logical state after relabeling. Fortunately, this is easy with the device's connectivity, because we have access to all possible parity checks. This means that, after generating a logical Bell state, we could perform quantum state tomography on the physical four-qubit state, as was done in Chapter 5, and on the logical two-qubit state with non-demolition parity-checks. Fig. 6.1c illustrates the uncompiled logical-Z-basis measurement to emphasize the role of qubit relabeling.

Upon being able to create and tomographically verify a logical Bell state, a natural next step would be to preserve it with rounds of error detection and compare this preservation to the case of a physical Bell state. Of course, the same approach could be repeated with cardinal states of the logical qubits in the same style as [8] and [10].

In addition to calibrating the second ancilla, the other required ingredient to perform error detection is mid-circuit measurement. As our readout time is approximately 10 µs, it is possible to dynamically

decouple the data qubits while the ancillas are measured since their CPMG coherence time extends to hundreds of μs. In fact, mid-circuit measurements of A1 already work, but we did not characterize them rigorously to include in Chapter 5. The biggest "obstacle" is that D1 experiences a frequency shift during the pulses required to perform PSB measurement, and the decoupling pulse must be calibrated accordingly. Presumably, the same mechanism would take place for A2 and D4. Whether any phase back-action arises as a result of conditional tunneling, as was the case in the demonstration of [11], remains to be characterized, but this would be manageable in either case.

Even if the realization of a $[[4, 2, 2]]$ code is not novel in the broader world of experimental quantum information, the unique features of spin qubits should lead to some qualitatively distinct conclusions from, say, superconducting qubits. For instance, residual ZZ coupling in the sparse spin array is effectively zero. Second, T_1 times are exceptionally long, meaning the noise is biased in ways that may alter the optimal implementation of error detection. Finally, the ability to extract repeated parity information from both neighbouring and distant qubits, even in the context of a simpler repetition code, should allow one to probe noise correlations over different distances. As a final remark, one benefit of following in the footsteps of more sophisticated platforms is that, once our devices satisfactorily fit into the "circuit model", many informative QEC experiments can be readily adapted.

"Friday afternoon" experiments

The combination of bus stops and shuttling permits other proof-of-principle demonstrations that may provide useful functionality in larger devices.

First, is it possible to perform PSB at bus stops? This question is motivated by needing to perform lots of measurements and parity checks in a scaled architecture. Although charge sensing is difficult to miniaturize, spin-to-charge conversion with PSB is compact. If PSB takes place along a shuttling bus, far from a charge sensor, the resulting presence/absence of a shuttled electron could be transported in a classical "time-bin" encoding as illustrated in Fig. 6.2. This would be the conveyor-mode analog of latched readout with a reservoir [12].

Conceptually, there should be no issue with performing PSB at the bus stops, though given our experience of how sensitive the PSB mechanism is to the precise electrostatic environment, calibration could be annoying, and good performance may require tweaking the gate structure. The more uncertain challenge would be to reliably shuttle the conditional charge state while maintaining the PSB condition. The robustness of the virtualization technique implemented in Chapter 5 would be tested.

A second, related question, is whether it is possible to use the

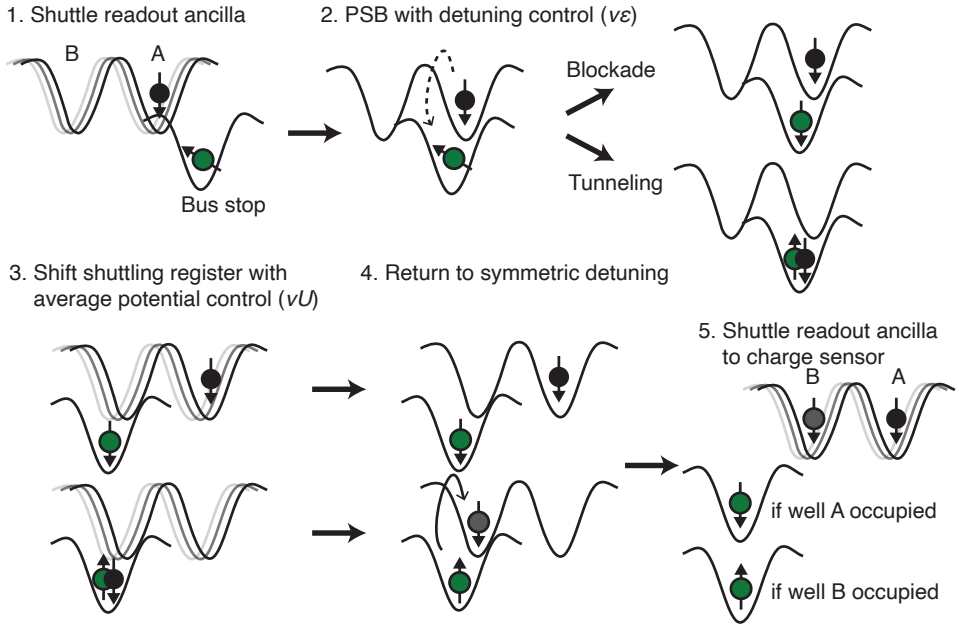


Figure 6.2: Procedure for performing spin-to-charge conversion at a bus stop. First, a readout ancilla (with a known spin state) is shuttled to the bus stop in a periodic potential with minima A and B as shown. Second, PSB is attempted using a virtual detuning pulse, calibrated as described in Chapter 5, and the readout ancilla may or may not tunnel to the bus stop. Next, the conveyor potential is shifted using the virtual average potential to latch the outcome of PSB to the charge occupation of the conveyor. By adiabatically returning to symmetric detuning, a tunneled ancilla will return to minimum B while initializing the bus stop spin to a known state (as drawn, I'm assuming a smaller Zeeman energy in the bus stop compared to the adjacent conveyor site). A projective measurement of the spin in the bus stop has been performed, and the classical outcome is encoded in the position of the shuttled electron, which may be shuttled to a distant charge sensor.

conditionally-present charge to impart a back-action that could serve as the basis for "in-layer" operations as discussed in [11]. To test this does not require tuning finicky PSB, but rather probing whether the phase of a data qubit in a bus stop is sufficiently sensitive to the presence/absence of a shuttled charge such that a Z-gate could be implemented with reasonable efficiency.

Although extending these operations to a full-fledged architecture would be very challenging - charges would need to be effectively routed according to the decoding of syndrome measurements - the more logic that could be performed in such a way would alleviate the amount of input/output between the QPU and control electronics. Similar ideas and extensions of this concept have been put forward in Stephan Philip's

thesis [13].

Third, can two-qubit gates be performed at the bus stops while spins are in-transit? This would be a useful extention of the previous realizations of two-qubit logic performed by shuttling [14, 15]. As the tunnel coupling between dots depends exponentially on the distance between the Gaussian wavefunctions, shuttling two spins past each other (or one moving past another confined in a bus stop) at constant velocity results in an effective Gaussian exchange "pulse-shape" as sketched in Fig. 6.3, with other conveyor speed modulations resulting in different effective pulse-shapes. The advantage of this would be to activate two-qubit control pseudo-digitally [16], where a step-like barrier pulse is sufficient to activate exchange between shuttled spins, and conveyor velocity control is sufficient to ensure the interaction is adiabatic.

A final question that would be informative for tuning sparse arrays with shuttling is how easily the bus stops may be statically populated using DC voltages. This was the initial idea when first tuning the device, but after realizing the convenience of populating the bus stops with AC pulses each experimental cycle, we did not return to DC tuning. For example, beginning with a depleted array avoids shuttling and loading errors due to an unintentionally confined charge. Although the 100 ms RC time of the bias-tees would be sufficient to sequentially populate hundreds of bus stops at a rate of 1 per 10 µs or so, for much larger devices this would form a big time bottleneck. It may also be desirable to load multiple electrons into dots far from reservoirs (e.g. to perform PSB at a (3,1) charge transition far from a reservoir), and it may require infeasible or undesirably large AC pulse amplitudes.

The challenge of tuning bus stops with DC voltages is that it is generally difficult to virtualize the conveyor with respect to the bus stop plunger. Therefore, sweeping the plunger's DC voltage while shuttling to determine when the charge transitions from the shuttling bus to the bus stop risks breaking the conveyor. In Chapter 5, we circumvented this problem by using two conveyor definitions: the first for loading the bus stops, and the second for shuttling while the bus stops were loaded. We also know from AC tuning what total voltage on the bus stop plunger is required to accumulate the first electron. It should be possible to blindly raise the bus stop plunger DC voltages to this level, then use the second conveyor definition to attempt to load the bus stops. This "first AC, then DC" approach could then be iterated to load multiple electrons and would be a valuable procedure for populating very large sparse arrays.

6.3. LOW-FIELD AND BASEBAND OPERATION

The most important consequence of the studies presented in Chapter 4 is the realization that on-chip magnets can be stably demagnetized

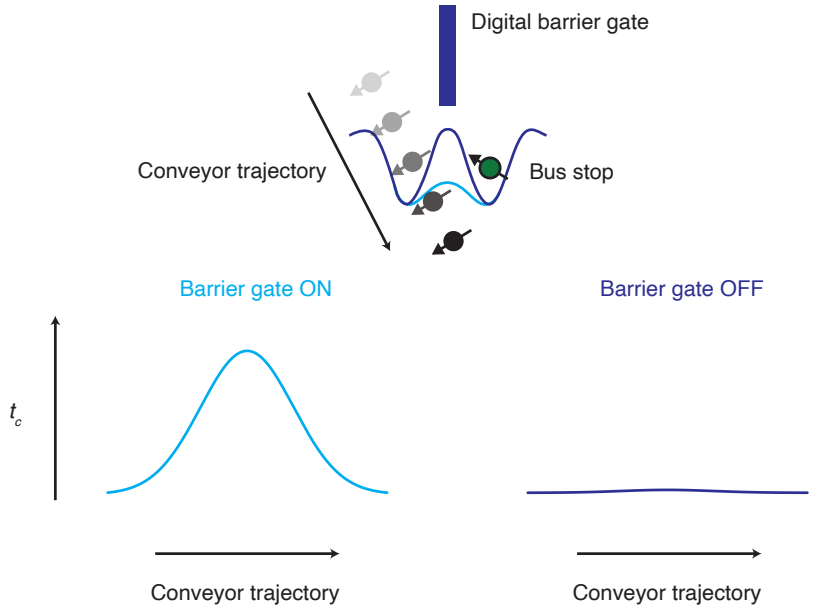


Figure 6.3: Schematic illustrating a pseudo-digitally-controlled two-qubit gate at a bus stop. If the digital barrier gate is activated, the minimum distance between the two spins during the conveyor trajectory is decreased, and the bare tunnel coupling t_c has a Gaussian profile as a function of time in the case of a constant conveyor velocity. Provided the bus stop plunger gate is virtualized with respect to the conveyor and barrier gates, symmetry can be maintained such that $J \propto t_c^2$ also evolves as a Gaussian. If the digital barrier gate is inactive, the minimum distance between the two spins suppresses the maximum value of t_c such that no spin-spin interaction takes place.

and subsequently used for engineering baseband control techniques. Furthermore, this behaviour is predictable, and, in light of the recent work on nanomagnets by Michele Aldeghi [17, 18], I predict that it is achievable to engineer much more intricate spin Hamiltonians with on-chip magnets that what has traditionally been expected.

While we demonstrated hopping gates using bucket-brigade style shuttling, the complexity of tunneling in silicon owing to the valley degree of freedom may impose limits on scaling this primitive operation. Furthermore, although hopping control can be performed with baseband pulses, the timing precision is very pushy and phase-tracking in the lab frame will be very challenging for multi-qubit control. Despite these apparent drawbacks, it quickly became apparent that this regime can be combined with conveyor-mode shuttling in larger arrays to realize a suite of low-frequency spin control methods. If these baseband control methods also circumvent the heating effects that persist with microwave

control, as we observed for the hopping gate, they could form the basis for a new way to think about operating mobile spin qubits.

A full manuscript is in preparation by Maxim De Smet and Yuta Matsumoto that details how conveyor-mode EDSR is enabled by shuttling on-resonance (or at sub-harmonics) with the average Larmor frequency, and hopping control by shuttling through a region of magnetic field inhomogeneity is finely-tunable via the one-way conveyor speed. Both of these techniques may fit well into shuttling-based architectures. Furthermore, the low total magnetic fields required and sparseness afforded by shuttling make the magnetic field engineering easier than the denser hopping array presented in Chapter 4.

With industrial fabrication efforts from the likes of Intel [19], IMEC [20], and HRL [21] bearing fruit, the prospect of scaling the number of gates in semiconductor quantum devices by orders of magnitude in the upcoming years appears more tangible than ever. Combining industrial yield with shuttling is, in my opinion, the most promising direction in which to also scale the number of spin qubits by orders of magnitude. To make this point more concrete, I will apply some of the ideas developed in this thesis to the looped pipeline architecture, first introduced in [22], to give a sense of what I believe is possible in the near-term.

In the looped pipeline architecture shown in Fig. 6.4a, spin qubits move in closed shutting tracks. These tracks may be arranged in a surface-code-like configuration such that alternating tracks represent data qubits and ancilla qubits, respectively. By populating the loops with more than one shuttled spin, multiple qubit arrays are loaded without any hardware overhead. The approach is well-studied architecturally, but the physical implementation is open-ended.

The constituent physical spins can be controlled by the baseband conveyor signals using conveyor-mode EDSR, pseudo-digital adiabatic exchange, and bus stops. This can be achieved as sketched in the primitive unit cell of Fig. 6.4b. On-chip magnetic sources provide (i) a small addressability and driving gradient isolated to each shuttling track and (ii) a small addressability gradient where tracks meet for two-qubit interaction.

Conveyor-mode EDSR is performed by oscillating the *c*-phase travelling-wave potential. The frequency of this oscillation should be set such that it matches, or is a sub-harmonic of, the average Larmor frequency of the spin at the location of the gate (left side of Fig. 6.4b). The addressability must be large enough that all other spins in the loop only pick up a phase from the off-resonant conveyor “drive”, as all of them will oscillate due to the shared control. By adjusting the duration of the oscillating travelling-wave potential, either Hadamard or Pauli-X gates may be performed. With each shuttling track controlled by its own set of clavier gates, all single-qubit gate durations can be made equal.

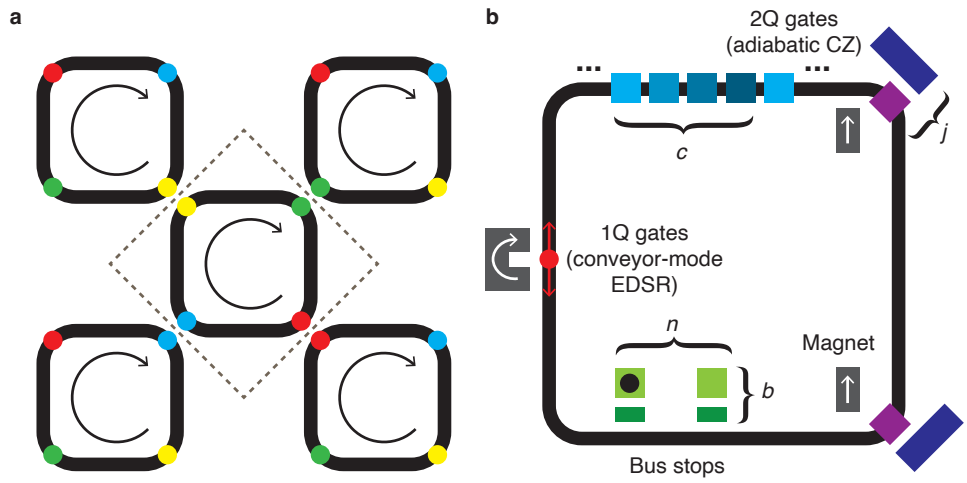


Figure 6.4: **a** Sketch of the looped pipeline architecture from [22]. In this instance, each shuttling track is populated with 4 physical spins that interact with each other periodically. The colours could indicate 4 logical qubits sharing the same hardware, for instance. The dashed line indicates the primitive cell for tiling this square layout to larger sizes. **b** Sketch of the hardware used to engineer each primitive cell (not to scale). Blue clavier gates create a c-phase travelling-wave potential for shuttling. Grey boxes indicate a possible configuration of on-chip magnets to generate qualitatively appropriate magnetic gradients. The horseshoe magnet on the left provides an inhomogeneous transverse gradient for (possibly sub-harmonic) conveyor-mode EDSR as well as addressability. The bar magnets at the right corners provide a longitudinal gradient for adiabatic CZ gates, and j magenta gates provide digital barrier control and virtualization. The n bus stops, each containing b gates, provide a means of initialization and measurement as well as logical qubit operation. The ohmic contacts and charge sensors also required for this are not shown.

Two-qubit gates are performed by activating a digital barrier gate between two tracks. If activated, the conveyors naturally pulse-shape the exchange interaction as described in Sec. 6.2 such that, with a modest addressability gradient present in the red region, an adiabatic CZ gate is performed. If the digital barrier is inactive, no conditional phase is acquired. To maintain the symmetry condition between the two shuttled spins, it is likely that at least one of the conveyor gates must also be independently controllable as to not interfere with the traveling-wave potential of all the other spins in the loop. Therefore $j \approx 2$ gates are needed per two-qubit interaction zone at the corners of the shuttling tracks. The magnitude of maximum exchange at each corner may be tuned such that all two-qubit interactions occur in the same duration and simultaneously at all inter-track zones.

SPAM and logical operations could be performed by adding n bus-stop-

like features to each shuttling track that each contain b additional control lines. These gates would be used to perform PSB for qubit initialization and readout, but they could also be used to delay or physically swap shuttled spins within each loop as may be necessary to operate logical qubits.

These operations are sufficient to perform the physical operations required for syndrome extraction, though a more detailed schedule including dynamical decoupling would need to be devised to practically perform logical computations. Here the point is mainly hardware efficiency: each primitive cell of the square lattice utilizes $c + nb + 2j$ unique control lines, where $c \approx 4$ for the conveyor, and $b \approx 2$ for each of $n \approx 2$ bus stops. Therefore, having 1200 external control lines available (an ambitious but plausible number of I/O connections) corresponds to about 100 primitive cells, or a distance-50 "surface code" tiling of shuttling tracks containing multiple logical qubits. In Fig. 6.4, four qubits per loop are arbitrarily chosen for illustration. Practically, this number will depend on the total length of the shuttling track, and more qubits would require a larger number of bus stops (or something similar) to efficiently implement SPAM and logical operations.

The looped pipeline and other shuttling-loop architectures, such as the snakes on a plane proposal [23], are not limited to the single-electron spin qubits which I have focused on. The same multiplexing arguments hold for qubits encoded in multiple spins. Singlet-triplet and exchange-only qubits encoded in a zero-momentum decoherence-free subspace are particularly friendly as they are robust to common-mode phase pickup that is an inevitability of shuttling. In the singlet-triplet case, on-chip magnets could also be engineered to give rise to the Zeeman energy differences required for single-qubit control.

Perhaps the most important feature of these shuttling-loop architectures, from the hardware point of view, is the homogenization of qubit properties [24]: electrons are fundamentally identical, but the solid state environment gives each static quantum dot "personality". Electrons shuttled in loops become identical (at least to the extent the noise environment is constant for all the electrons). This similarity is invaluable for multiplexing qubit control and, consequently, circumventing the wiring bottleneck. As shown here, the baseband control signals required for shuttling can perform much of the heavy-lifting for performing qubit operations in a low-field regime. Thanks to Chapter 4 and the ongoing work in this direction, we know such a regime is possible.

6.4. ADDITIONAL PERSPECTIVES

6.4.1. READOUT

One of the primary concerns from an architectural standpoint is readout. Spin-to-charge conversion via PSB is possibly future-proof as it has a small footprint, the singlet-triplet energy scale can exceed the thermal energy scale up to several Kelvin, and high visibilities suggesting a SPAM fidelity above 99% have been demonstrated [25]. Its biggest drawback is how "fiddly" it is to initially tune up and optimize with high-fidelity. Presumably, with some thankless effort, a suitable arrangement of gates can be identified which serves as a unit cell that may be copied as necessary and tuned modularly using automated strategies.

Charge sensing is generally difficult to miniaturize, whether done by DC or RF techniques [26, 27]. In the former case, an SET with current leads is needed, but integrating the necessary components of the signal chain is at least more space-efficient. The inductors and directional couplers required for reflectometry are outright bulky. If charge sensors are "precious", it is at least possible that they can function as demultiplexers. For example, a series of PSB-units can be coupled to a shuttling channel, as proposed in Sec. 6.2, such that the aggregate result of the spin-to-charge conversion results in a unique string of time-binned charges. With appropriate routing, such a charge string can constitute a syndrome which may be serially measured by a single charge sensor, and charge detection may optimistically take place on the order of 100 ns per charge [28].

6.4.2. TWO-QUBIT GATE FIDELITIES

The demonstration of two-qubit gate fidelities above 99% has been reproducible, but only within two-qubit devices to date. Our experience in Chapter 5, where the fidelity of the exchange coupling was limited by incoherent noise, suggests better design rules will be needed to reliably achieve high-fidelity two-qubit gates.

First, the gate geometry and material stack should be refined. The multi-layer Ti:Pd silicon devices currently made in the Vandersypen group look very different from the single-layer aluminum device from [4] where high fidelity CZ operations were first measured. The barrier lever arm α relating exchange strength J to the barrier voltage BB, where $\log(J) = \alpha BB + J_0$, was fit to be $0.024\,\mathrm{mV}^{-1}$. This is smaller than the lever arms of the bus stop barriers of Chapter 5 which ranged from $0.04\,\mathrm{mV}^{-1}$ to $0.10\,\mathrm{mV}^{-1}$ (simulations estimated a lever arm of $0.18\,\mathrm{mV}^{-1}$). A larger lever arm implies a smaller pulse is needed to both suppress residual exchange and activate desired exchange, but it also means that the same fluctuations in the control signal voltage impart more exchange noise

when spins are coupled.

We can also compare similar metrics with other devices from various groups around the world where high-fidelity two-qubit gates have been reported. In the Tarucha group, high-fidelity CROTs were achieved in a multilayer aluminum device in [29], but the device exhibited limited exchange tunability and this is tantamount to having a small lever arm[1]. In the Petta group, high-fidelity CZs were also achieved in a multilayer aluminum device [30], and I infer a relatively large lever arm of 0.09 mV^{-1}[2]. Diraq/UNSW has reported an exchange tunability of 18.4 dec/V, which translates to a lever arm of about 0.04 mV^{-1} as I defined above[3], in a foundry CMOS device supporting high-fidelity CZ gates with a polysilicon gate stack [20].

When designing the device of Chapter 5, it was decided that having too-strong barrier control would be superior to too-weak barrier control, because we were unsure how feasible it would be to uncouple the bus stops from the shuttling operations. As a result, the barrier gates were patterned in a lower layer than the plungers. With the bus stop functionality established, a subsequent bus stop design could be made with narrower barriers in a higher layer to bring the lever arms closer to 0.04 mV^{-1} which, based on the demonstrations listed, appears to be generally superior. Electrostatic simulations would be helpful to verify the extent to which these changes would reduce the lever arm. In Chapter 5, we also made use of only 20 dB of attenuation at the 4 K stage for all fast lines. While this allows for a wide dynamic range of pulsing (up to about 500 mV with QBlox AWGs), it also means that more noise can propagate down the lines from room temperature. This flexibility is useful while prototyping, but if one has better knowledge of the voltage range over which fast control is necessary, one is surely able to attenuate more noise.

Another factor is the gate material. While the heterostructures used to host ^{28}Si/SiGe spin qubits has nominally improved, the coherence times of present devices made with Ti:Pd gates (typically 2 µs to 8 µs, roughly speaking) are notably lower than those of [4] (about 10 µs and 20 µs) where Al gates (and a global screening gate) were used and a 99.5% two-qubit gate fidelity was measured. This is despite having a larger micromagnet-induced addressability gradient between the two spins ($d\omega_L/2\pi > 100$ MHz). With limited statistics (especially from older devices), it is not possible to distinguish between causality or a “hero” device.

[1] T_2^* is about 7 µs for both spins.

[2] I estimate this by eye from Fig. 2a from the two points at (530 mV,0.8 MHz) and (552 mV,6 MHz). Here, T_2^* of about 2 µs were observed for both qubits.

[3] $18.4 \log(10)/1000 = 0.042$. T_2^* of about 30 µs is observed, albeit using real-time Larmor frequency tracking, which makes comparisons to direct T_2^* measurements imperfect.

But there are a few signs that we should be wary of. First, we have repeatedly observed evidence in the lab that our T_2^* dephasing is not only dominated by charge noise. In Chapter 4, we observed T_2^{H} behave as though it was charge-noise limited as a function of the decoherence gradient as it was modulated by the external magnetic field. However, the measured T_2^* were insensitive to this change. Data in preparation by Irene Fernández de Fuentes and Kenji Capannelli, where a micromagnet was not used, points to similar conclusions. Theory suggests residual nuclear spins, both ^{29}Si in the quantum well and SiGe buffer, as well as ^{73}Ge in the buffer, could be coherence-limiting [31].

Second, it has been reported that the Ti:Pd gate stack leads to lower mobility and increased charge noise when compared to alternatives such as polysilicon [32]. However, the gate stacks and oxides that can be used with heterostructures, which have a finite thermal budget, are more limited than with Si-MOS devices. There is also the question of yield: the honed Ti:Pd fabrication in Delft has been remarkably successful at producing fully working devices on the first coupon as of late. Such reliability in an academic setting is invaluable for testing bold architectures where fidelity is not highest priority (but probably the second-highest priority). To what extent the advantages of good yield, low noise, and heterostructure-compatibility can be unified is an important open question.

6.4.3. ON-CHIP MAGNETIC SOURCES

Engineering local stray magnetic fields in larger devices will require more precise on-chip magnets than the bulky micromagnets used in this thesis. Fortunately, much work has already been done on this front, particularly by Michele Aldeghi at IBM Zurich [17, 18]. As showcased in Chapter 4, nanomagnets should permit more intricate variation in stray magnetic fields with more deterministic behaviour by leveraging shape anisotropy, for example. There, we used iron for its small uniaxial anisotropy. However, as Niccolo Martinolli of EPFL has pointed out to me, while iron is possible to deposit, it is also a contaminant that diffuses into silicon and silicon oxide and is avoided in industrial cleanrooms for this reason [33].

Industrial spintronics and CMOS-compatible technologies like magnetic random access memory (MRAM) use different alloys such as CoFeB, but their incorporation with spin qubit devices is almost entirely unexplored [34]. Combining more ideas from these fields into spin qubit devices would be beneficial.

Finally, there is the prospect of generating magnetic fields with on-chip current sources - either in the form of superconducting wires hosting DC currents or superconducting channels annealed into the material itself. Both options are relatively unexplored but may very well be

feasible. Originally, such strategies were dismissed due to the difficulty of producing a sizeable transverse gradient for EDSR without overshooting the critical current of the superconductors. However, control strategies like conveyor-mode EDSR and hopping gates require much smaller gradients and total magnetic fields. Therefore, it could prove useful to revisit some of these ideas.

6.5. WHY SINGLE-SPINS IN SILICON?

The field of semiconductor spin qubits has grown to encompass many platforms: donors vs. gate-defined quantum dots, the material host, the encoding of quantum information, and the methods of operation. Irene Fernández de Fuentes has aptly pointed out that to present novel work, one must resort to increasingly-wordy phrases and acronyms to distinguish one approach from the rest. I would therefore like to conclude this thesis by advocating for why gate-defined single-spin Si/SiGe-based spin qubits deserve continued attention.

David DiVincenzo has suggested in a QuTech division *werkbespreking* that a good quantum computer probably ought to be a physically simple and boring system. In this spirit, silicon hands us a reasonably-empty canvas upon which to make spin qubits as interesting as we desire. In addition to all of the instances of actively designing addressability, driving gradients and quantization axis tips showcased in the thesis, this privilege extends to the option of having very little spin-orbit coupling and nearly-isotropic g-tensors. Rather than hunting for sweet spots, one is gifted them from the outset.

By confining qubits in gate-defined quantum dots, we are able to locate and shuttle spin qubits for effective all-to-all connectivity, and on-chip magnetic field engineering allows us to choose both how spins behave as they are moved around as well as how they interact with each other in different locations on a chip. That we have pushed this flavor of semiconductor-based quantum computing the furthest towards error-correction (at the time of writing) is the strongest vindication of the approach.

This is not to say silicon is without its challenges. Things would be simpler without a potentially-problematic valley degree of freedom that is only probabilistically controllable. However, tolerating disorder that is "good enough" to avoid valley excitations is arguably preferable to relying on disorder for qubit control, for example. In this sense, the cleanliness of the Si/SiGe heterostructures over oxide interfaces also "should not be lightly given up" in the words of Davide Degli Esposti.

I predict that, for the purposes of building semiconductor-based quantum processors, the technology will be best served by using the qubits we currently have to run head-first into the really gritty scaling

challenges. Silicon spin qubits are not perfect, but they are good enough to go much, much further.

REFERENCES

[1] Y. Choi and R. Joynt. “Interacting random-field dipole defect model for heating in semiconductor-based qubit devices”. In: *Phys. Rev. Res.* 6 (1 Feb. 2024), p. 013168. doi: 10.1103/PhysRevResearch.6.013168. url: https://link.aps.org/doi/10.1103/PhysRevResearch.6.013168.

[2] V. Champain *et al. A heat-resilient hole spin qubit in silicon*. 2025. arXiv: 2509.15823 [cond-mat.mes-hall]. url: https://arxiv.org/abs/2509.15823.

[3] Y.-H. Wu *et al. Simultaneous High-Fidelity Single-Qubit Gates in a Spin Qubit Array*. 2025. arXiv: 2507.11918 [quant-ph].

[4] X. Xue *et al.* “Quantum logic with spin qubits crossing the surface code threshold”. In: *Nature* 601.7893 (Jan. 2022), pp. 343–347. issn: 1476-4687. doi: 10.1038/s41586-021-04273-w. url: http://dx.doi.org/10.1038/s41586-021-04273-w.

[5] E. G. Kelly *et al. Identifying and mitigating errors in hole spin qubit readout*. 2025. arXiv: 2504.06898 [cond-mat.mes-hall]. url: https://arxiv.org/abs/2504.06898.

[6] Y.-Y. Liu *et al.* “Radio-Frequency Reflectometry in Silicon-Based Quantum Dots”. In: *Physical Review Applied* 16.1 (July 2021). issn: 2331-7019. doi: 10.1103/physrevapplied.16.014057. url: http://dx.doi.org/10.1103/PhysRevApplied.16.014057.

[7] H. Edlbauer *et al.* “An 11-qubit atom processor in silicon”. en. In: *Nature* 648.8094 (Dec. 2025), pp. 569–575. issn: 1476-4687. doi: 10.1038/s41586-025-09827-w.

[8] N. M. Linke *et al.* “Fault-tolerant quantum error detection”. In: *Science Advances* 3.10 (Oct. 2017). issn: 2375-2548. url: http://dx.doi.org/10.1126/sciadv.1701074.

[9] H. Sayginel *et al.* “Fault-Tolerant Logical Clifford Gates from Code Automorphisms”. In: *PRX Quantum* 6 (3 Sept. 2025), p. 030343. doi: 10.1103/vf7v-cpq9. url: https://link.aps.org/doi/10.1103/vf7v-cpq9.

[10] C. K. Andersen *et al.* “Repeated quantum error detection in a surface code”. In: *Nature Physics* 16.8 (June 2020), pp. 875–880. issn: 1745-2481. url: http://dx.doi.org/10.1038/s41567-020-0920-y.

[11] C. Jones *et al. Mid-circuit logic executed in the qubit layer of a quantum processor*. 2025. arXiv: 2512.12648 [quant-ph].

[12] P. Harvey-Collard *et al.* “High-Fidelity Single-Shot Readout for a Spin Qubit via an Enhanced Latching Mechanism”. In: *Phys. Rev. X* 8 (2 May 2018), p. 021046. doi: 10.1103/PhysRevX.8.021046. url: https://link.aps.org/doi/10.1103/PhysRevX.8.021046.

[13] S. Philips. “Scaling a spin qubit quantum processor from two to six qubits”. English. Dissertation (TU Delft). Delft University of Technology, 2023. doi: 0.4233/uuid:62dcc7a6-df92-43e1-b40c-9879f97eabb6.

[14] A. Noiri *et al.* “A shuttling-based two-qubit logic gate for linking distant silicon quantum processors”. In: *Nature Communications* 13.1 (Sept. 2022). issn: 2041-1723. url: http://dx.doi.org/10.1038/s41467-022-33453-z.

[15] Y. Matsumoto *et al. Two-qubit logic and teleportation with mobile spin qubits in silicon*. 2025. arXiv: 2503.15434 [quant-ph].

[16] M. Friesen, R. Joynt, and M. A. Eriksson. “Pseudo-digital quantum bits”. In: *Applied Physics Letters* 81.24 (Dec. 2002), pp. 4619–4621. issn: 1077-3118. doi: 10.1063/1.1527692. url: http://dx.doi.org/10.1063/1.1527692.

[17] M. Aldeghi, R. Allenspach, and G. Salis. “Modular nanomagnet design for spin qubits confined in a linear chain”. In: *Applied Physics Letters* 122.13 (Mar. 2023). issn: 1077-3118. doi: 10.1063/5.0139670. url: http://dx.doi.org/10.1063/5.0139670.

[18] M. Aldeghi *et al.* “Simulation and Measurement of Stray Fields for the Manipulation of Spin Qubits in One- and Two-Dimensional Arrays”. In: *Nano Letters* 25.5 (Feb. 2025), pp. 1838–1844. issn: 1530-6984. doi: 10.1021/acs.nanolett.4c05037.

[19] H. C. George *et al.* “12-Spin-Qubit Arrays Fabricated on a 300 mm Semiconductor Manufacturing Line”. In: *Nano Letters* 25.2 (2025). PMID: 39721970, pp. 793–799. doi: 10.1021/acs.nanolett.4c05205. eprint: https://doi.org/10.1021/acs.nanolett.4c05205. url: https://doi.org/10.1021/acs.nanolett.4c05205.

[20] P. Steinacker *et al.* “Industry-compatible silicon spin-qubit unit cells exceeding 99% fidelity”. In: *Nature* 646.8083 (Sept. 2025), pp. 81–87. issn: 1476-4687. url: http://dx.doi.org/10.1038/s41586-025-09531-9.

[21] S. D. Ha *et al.* “Two-Dimensional Si Spin Qubit Arrays with Multilevel Interconnects”. In: *PRX Quantum* 6 (3 Aug. 2025), p. 030327. doi: 10.1103/sgn1-1t2d. url: https://link.aps.org/doi/10.1103/sgn1-1t2d.

[22] Z. Cai, A. Siegel, and S. Benjamin. “Looped Pipelines Enabling Effective 3D Qubit Lattices in a Strictly 2D Device”. In: *PRX Quantum* 4.2 (June 2023). issn: 2691-3399. url: http://dx.doi.org/10.1103/PRXQuantum.4.020345.

[23] A. Siegel *et al.* “Quantum Snakes on a Plane: Mobile, Low-Dimensional Logical Qubits on a 2D Surface”. In: *PRX Quantum* 7 (1 Feb. 2026), p. 010339. doi: 10.1103/494s-jd8h. url: https://link.aps.org/doi/10.1103/494s-jd8h.

[24] H. Jnane, A. Siegel, and M. F. Gonzalez-Zalba. *Harnessing electron motion for global spin qubit control*. 2025. arXiv: 2503.12767 [quant-ph]. url: https://arxiv.org/abs/2503.12767.

[25] K. Takeda *et al.* “Rapid single-shot parity spin readout in a silicon double quantum dot with fidelity exceeding 99%”. In: *npj Quantum Information* 10.1 (Feb. 2024). issn: 2056-6387. doi: 10.1038/s41534-024-00813-0. url: http://dx.doi.org/10.1038/s41534-024-00813-0.

[26] G. Kiene *et al.* “DC-Readout of Semiconductor Spin Qubits: Opportunities and Limits”. In: *IEEE Transactions on Circuits and Systems I: Regular Papers* 72.10 (2025), pp. 5457–5470. url: http://dx.doi.org/10.1109/TCSI.2025.3542335.

[27] F. Vigneau *et al.* “Probing quantum devices with radio-frequency reflectometry”. In: *Applied Physics Reviews* 10.2 (Feb. 2023). issn: 1931-9401. url: http://dx.doi.org/10.1063/5.0088229.

[28] D. J. Ibberson *et al.* “Large Dispersive Interaction between a CMOS Double Quantum Dot and Microwave Photons”. In: *PRX Quantum* 2 (2 May 2021), p. 020315. doi: 10.1103/PRXQuantum.2.020315. url: https://link.aps.org/doi/10.1103/PRXQuantum.2.020315.

[29] A. Noiri *et al.* “Fast universal quantum gate above the fault-tolerance threshold in silicon”. In: *Nature* 601.7893 (Jan. 2022), pp. 338–342. issn: 1476-4687. doi: 10.1038/s41586-021-04182-y. url: http://dx.doi.org/10.1038/s41586-021-04182-y.

[30] A. R. Mills *et al.* “Two-qubit silicon quantum processor with operation fidelity exceeding 99%”. In: *Science Advances* 8.14 (Apr. 2022). issn: 2375-2548. doi: 10.1126/sciadv.abn5130. url: http://dx.doi.org/10.1126/sciadv.abn5130.

[31] L. Cvitkovich *et al.* “Coherence limit due to hyperfine interaction with nuclei in the barrier material of Si spin qubits”. In: *Phys. Rev. Appl.* 22 (6 Dec. 2024), p. 064089. doi: 10.1103/PhysRevApplied.22.064089. url: https://link.aps.org/doi/10.1103/PhysRevApplied.22.064089.

[32] M. M. Rahman *et al. Gate Stack Engineering for High-Mobility and Low-Noise SiMOS Quantum Devices*. 2026. arXiv: 2603.02814 [cond-mat.mes-hall]. url: https://arxiv.org/abs/2603.02814.

[33] A. Istratov, H. Hieslmair, and E. Weber. “Iron contamination in silicon technology”. en. In: *Applied Physics A* 70.5 (May 2000), pp. 489–534. issn: 1432-0630. doi: 10.1007/s003390051074.

[34] M. Niknam *et al.* “Quantum control of spin qubits using nanomagnets”. en. In: *Communications Physics* 5.1 (Nov. 2022), pp. 1–10. issn: 2399-3650. doi: 10.1038/s42005-022-01041-8.

ACKNOWLEDGEMENTS

Hailing from oil-and-gas country in Alberta, my doctoral work in quantum computing at TU Delft would have been unlikely were it not for the outreach programs that expose young generations of students to cutting-edge science. In this regard, the **USEQIP** program at the **Institute for Quantum Computing** at the **University of Waterloo** was invaluable for planting the seed that led to my graduate studies in this field. My decision to cross the Atlantic to pursue my Master's at TU Delft would not have been possible without the QuTech scholarship offered through the **QuTech Academy**. I am grateful to the many people behind these and similar efforts. It reminds me that outreach, whether through lab tours, presentations, or beyond, can have impacts that are at the same time life-changing but also invisible in the moment.

Lieven: Thank you for having me in the group, first for my Master's end project and once again for the PhD. It's a privilege to work in a lab filled with always-amazing people and where there are ample resources and freedom to try bold ideas. Your leadership has a characteristic zen that admirably weathers the ups and downs of doing science. I'm very grateful for the very free hand you gave me in putting together Tintin and the bilinear project, as seeing all the details of the full project arc come together was a confidence-building experience that really made me feel independent by the end of the PhD, all the while knowing that you'd always be there if I needed a meeting or someone to ask really astute questions. I hope I can channel these qualities during my next scientific steps and beyond.

Eliška: Thank you for being my copromotor, and just as importantly for all of the great discussions we've had over the course of my PhD. I admire your leadership of the QMAI group, which always feels congenial even though you manage to work on everything from autotuning to particle physics.

To the remaining independent members joining my committee, **Prof. DiCarlo**, **Prof. Veldhorst**, **Prof. Benjamin**, and **Dr. Ladd**: thank you for taking the time to scrutinize my thesis. It has been a privilege to interact with you all over the years both at QuTech and at conferences abroad, and I'm very happy to have you on my defense committee.

To my paranymphs: **Kenji**, even though you've evolved into a fully-independent experimentalist, you'll always be my Master's student in my

heart. You have a unique calmness and poise that makes it a pleasure to work with you, and it's an invaluable energy to bring to the lab every day. **Algi**, the leader of the QuTech-adjacent crew, you've been my emotional rock over these past years, and your kitchen table became the "Monica's apartment" of my PhD with the countless dinners, board games, and general nonsense that added joy even on the days when nothing work-related was going well. It's an honor to have you both as my paranymphs.

Xiao: Were it not for my enjoyment of the Master's end project which you supervised, there's a good chance this PhD would not have happened. Thank you for teaching me everything you did - both about physics and otherwise. It has been fun to "re-learn" over the past four years many of the lessons I remember from during the Master's. Perhaps the most potent and recurring one is that optimization takes time, and when doing experimental work, it is invaluable to identify what the real priorities are. I have no doubt you're doing great work with all those fridges in China.

Mohammad: Even though you weren't officially supervising my Master's, you generously took the time to teach me a lot of theory about spin qubits and how to simulate them. Thank you for all your patience. I admire your tenacity in understanding those pesky TLFs, both for spin qubit noise and the heating effect, and you have a gift for explaining these very technical details.

Stephan and **Mateusz**: Thank you for mentoring me at the beginning of the PhD and trusting me to take over the six-dot hero device. The work in this thesis would not have happened were it not for being able to build on everything you guys accomplished. Stephan, you are a fountain of ideas and always a pleasure to talk to. Mateusz, your approach of calmly letting me struggle with PSB was both aggravating and invaluable.

Oriol: You taught me so much more than you probably realize. When we first started working together on the heating project, I knew the qubits but much less about all the other parts from the fridge to the electronics. You have an impressive ability to *make things happen* in the lab, with ethernet cables running every which way and measurement scripts aborted before they even knew they were started. You look in your element with Atlas in Barcelona, and I'm super happy we're in easy-visiting distance.

Eline: Working with you on the heating project and sharing an office made the first years of my PhD so much fun, not to mention a particularly great 30th birthday party. I was amazed at how quickly you learned about spin qubits coming from outside the field. That you were able to leverage your background for the magnet simulations that came later showed me why this type of knowledge exchange is so useful. It's great to see you, Jasper, Cas and Lena doing well in Malinas.

Florian: I'll always remember the adventures on the 2x2 as defining the core years of my PhD, along with Coffee Star, climbing, salsa, and long games of Terraforming Mars. Thank you for teaching me lots of wisdom

about fabrication and fridge building, but #$%& ! for the names you give your Python variables. In spite of that, it was a joy to make a lifelong friend from our time in the lab together, and I'm happy to see you thriving in your new home down under.

Nicola: What an adventure we had over the last year. From debugging a bunch of electronics and wondering why the heck our brand-new fridge wasn't cooling down the way it should, we managed to put together a super cool project. You were always eager to roll with the punches, and you learned spin qubit measurement faster than anyone can reasonably be expected to. I don't think I told you that enough. Above all, it was a pleasure to become friends along the way, and I can't wait to see what you put together in the second half of your PhD.

Yi-Hsien: How lucky we were that you joined the lab when you did! I remember feeling like I was doing a terrible job of showing you the setup, while the others were on vacation, and I was preoccupied between hacking together experiments, frantically preparing slides for silicon workshop, and being a paranymph. And yet somehow you made all of our fidelities go up and got mid-circuit measurements working to boot. From that point on, I knew I could trust everything you did. Moreover, you're such an easy-going guy to work with. I know Tintin is in good hands with you, Nicola, and Sam.

Sam: It was fortunate that we had some time to work on the 2x2 together so you could learn about automating spin qubit calibration. Little did I know you'd catch on in the blink of an eye and, just like that, everyone's readout, shuttling, and more worked so much better. The good karma paid off when we reunited with the bus stops, and the project wouldn't have turned into what it did without you. Your attention-to-detail and unshakable chill will no doubt serve you well in the rest of your PhD. You're doing hero's work.

Davide: I've said it before and I'll say it again, you're the best of us. You became the cog that made everything in the Vandersypen lab work - from cleaning up device designs to organizing material for fabrication runs to debugging fridges and readout chains - and that was *before* you even officially joined. The bilinear project would never have happened if you didn't take the time to teach me everything you did about fabrication and setup-building. It turns out science is actually quite easy when one simply follows your instructions. The calm, generous, and thoughtful way you approach both work and life is inspiring, and it was wonderful to have you in my radius during our PhD years.

Yuta: You are a one-of-a-kind fountain of ideas. It seemed like hardly a moment had passed after you joined the group before you knew everybody's projects and had seemingly limitless inspiration for what could be achieved with them. You combine an incredible depth of knowledge - from theory to simulation to measurement to deploying AI - with an unwaver-

ing physical intuition for what is possible. It's as if you will physics into obeying your rules. And despite this apparent superpower, you're an authentic, kind, and down-to-earth scientist. From first working together at the 2x2 when we realized that hopping gates could be done, to chatting about all the architectures and ideas that shuttling would make possible, it was great to get to know you. I'm eager to see everything you achieve in the future.

Sander: Your depth of knowledge of our work, from the physical setups to the technicalities of AWGs and IQ modulation to the software architecture for putting it all together, never ceases to amaze me. I breathed a sigh of relief anytime I informed you of a bug that a) was actually a bug and not my negligence, and b) took you more than a minute to figure out. Regardless, you selflessly give your time and energy to help everyone run the best possible experiments, and my PhD would not have been what it is without you.

Lara: Your enthusiasm for science and fabrication is contagious, and I always enjoyed every chat we shared over the previous years. I am indebted to you and your attention to detail for fabricating the legendary bus stop coupon which, as far as we know, has 100% yield.

Giordano: I have perhaps the widest and craziest range of things to thank you for: the heterostructures, the birthday parties, the last-minute burlesque tickets, the good lunch conversations filled with surf stories and great science ideas, and for being my reserve committee member. It's simply great to have you around.

Max: Even though you've joined the big leagues as a PI, you're always eager to share a cool new result, offer a well-founded suggestion, and simply explain a theoretical puzzle that would have otherwise remained a mystery to me for embarrassingly long. Your depth of knowledge from first-principles to QCVV and beyond astounds me, and I will miss having you just down the hall.

The work in this thesis would not exist were it not for the tireless background effort of many engineers and support staff. **Olaf**, **Tom**, **Erik**, and **Jason**, thank you for all of your patient explanations and creative cryogenic problem solving. To **Yannick** and the team at **DEMO**, thank you for all the work you put into designing our PCBs and tirelessly debugging all of the equipment. It would simply not be possbile to get an experiment running as quickly without you all. **Daan** and **Dennis**, thank you for the diligent software engineering even in the face of questionable coding practices from not-to-be-named suppliers. It's a relief to be able to trust what's going on under the hood when using your tools. **Marja**, **Frederieke**, **Julijana**, **Monica**, and the rest of the secretariat, project managers, and building staff, the amount of work you put in is directly related to the time I can spend playing with qubits. Thank you for being so diligent. It's difficult to emphasize how important the culture of "let's solve

this problem" is at TU Delft, and this extends well beyond the people that I can name here.

To the remainder of the Vandersypen group, past and present, thank you for being the best colleagues. **Nicky**, it was a pleasure to supervise your Bachelor's thesis, and it's great to see you've thrived in the bilayer graphene world in Zurich. **Rick**, thank you for your always-positive attitude and for teaching me squash. Stop getting injured. **Tzu-kan**, it's great to see you doing well in Taiwan! Thank you for answering my Proteox-related questions from the other side of the world. **Xin** and **Jurgen**, your smiles are contagious and I was glad I still got to see them after you both moved to Groove. You've done some super impressive stuff in very little time! **Minh**, it's great to have a theorist around in the group, and even better to have one who can communicate with experimentalists the way you do. I always felt wiser after talking to you. **Tobias** and **Parsa**, your indefatigable energy is beautiful, and it was great to see you breaking through with the hybrid project just as I wrapped up in Delft. **Stefano**, you were crushing it as soon as you arrived, and I know you'll put the well-earned Marie Curie to good use. **Noah**, you're such a diligent worker in the lab that the time we shared an office together passed in an instant. **Jaime**, **Elia**, and **Marcin**, it's great to see you guys already hitting the ground running in the lab, and just as great to see you carrying on the Saturday morning bouldering tradition. Albarracín, anyone?

The not-so-secret joy of working at QuTech is the sheer number of wonderful people you get to meet beyond one's daily colleagues. The amount of fun I've had because of you all is impossible to put into words. **Pablo**, you are brilliant in innumerable ways, and our long talks and games of Twilight Struggle kept me sane. **Hanifa**, if not for your unwavering desire to get people together and have a good time, my list of PhD memories would be so much smaller. **Daniel**, you have a one-of-a-kind wit and sense of humour that is matched only by your sharp knowledge of science. **Asser**, I can always trust you to have a smile on your face. Despite of all the crazy stories you have brought up over the years, you are an unreasonably-kind person. **Maxim** and **Liza**, thank you for the poker nights, escape rooms, board games, and cat therapy that has broken up our PhD generation into more digestible pieces. **Karina**, thank you for understanding my commonwealth humour and for adding a unique glamour to everything you do. **Santi**, we've done the long haul from the Master's, and I hope we can still get together for beers and talking about fridge drama for years to come.

Lucas, **Valentin**, **Sasha**, **Damien**, **Dario**, **Barnaby**, **Job**, **Corentin**, **Francesco**, **Chris**, **Edmundo**, **Daniel**, **Alberto**, **Federico**, **Nick**, **Corny**, **Sean**, **Matteo**, **Christina**, **Gustavo**, **Julia**, **Sebastian**, **Anton**, **Tobi**, **Isidora**, **Vicky**, **Matt**, **Nikiforos**, **Torbjørn**, and the remainder of the QuTech world that has become too large to feasibly list by name: thank

you for sharing the ups-and-downs of academia, the science, the life chats, the ski trips, the sailing, the music, the dancing, the climbing, the concerts, the dinners, the games, and the conferences.

Outside of the institute, I'm grateful to all of the other friends whose paths I crossed during my time in Delft. I know I'm not alone in cherishing the uniqueness of the city, the community of open-minded immigrants and the astonishingly welcoming nature of my Dutch hosts. It has all served as the backdrop for the greatest years of my life so far.

I'd like to thank my parents for their limitless love and support, and for tolerating my moving halfway around the world. It is not lost on me that none of this would be possible were it not for the education you gave me, the stable foundation from which to take this kind of career risk, and the consistent affirmations from childhood that "my job probably hasn't been invented yet". I love you both more than I can tell you. Importantly, I'd also like to extend my appreciation to Christopher Eggertson for handling a surprisingly long list of CRA-related surprises over the past years. Thank you for allowing me to focus on the science instead.

Finally, **Irene**, thank you for being an amazing partner, an amazing human being, and an amazing scientist. I will never be able to explain by what miracle our paths happened to cross at the exact time and place that they did, but my life will forever be better for it. Not a day goes by where you don't inspire me to think more deeply, live more freely, or be a more authentic version of myself. I'd say I can't wait to see where life takes us, but I'd rather savour each moment on the way. *Te quiero, Cari.*

CURRICULUM VITæ

Brennan Wade Undseth

24-02-1996	Born in Calgary, Alberta, Canada.

EDUCATION

2011–2014	High School Webber Academy, Calgary
2014–2019	BSc in Engineering Physics with Distinction Cooperative Program
2019–2021	MSc Applied Physics *cum laude* Annotation in Quantum Technology Delft University of Technology, The Netherlands *Thesis:* The Microscopic Origin of Crosstalk in an Electric Dipole Spin Resonance Device *Promotor:* Prof. dr. ir. L.M.K. Vandersypen
2021–2026	PhD. Applied Physics Delft University of Technology, The Netherlands *Thesis:* Engineering Silicon Spin Qubits *Promotors:* Prof. dr. ir. L.M.K. Vandersypen and Dr. E. Greplová

AWARDS

2014	President's Citation, University of Alberta
2019	QuTech Scholarship, Delft University of Technology

LIST OF PUBLICATIONS

12. V. Hernandes, J. Rogers, R. Koch, T. Spriggs, B. Undseth, A. Chatterjee, L. M. K. Vandersypen, and E. Greplova. *Reconstructing Quantum Dot Charge Stability Diagrams with Diffusion Models*. 2026. arXiv: 2603.26432 [quant-ph]. url: https://arxiv.org/abs/2603.26432

11. B. Undseth, N. Meggiato, Y.-H. Wu, S. R. Katiraee-Far, L. Tryputen, S. L. de Snoo, D. D. Esposti, G. Scappucci, E. Greplová, and L. M. K. Vandersypen. *Weight-four parity checks with silicon spin qubits*. 2026. arXiv: 2601.23267 [cond-mat.mes-hall]. url: https://arxiv.org/abs/2601.23267. Accepted for publication in *Nature*.

10. I. Fernández de Fuentes, E. Raymenants, B. Undseth, O. Pietx-Casas, S. Philips, M. Mądzik, S. de Snoo, S. Amitonov, L. Tryputen, A. Schmitz, A. Matsuura, G. Scappucci, and L. Vandersypen. "Running a Six-Qubit Quantum Circuit on a Silicon Spin-Qubit Array". In: *PRX Quantum* 7 (1 Jan. 2026), p. 010308. doi: 10.1103/f285-l2v5. url: https://link.aps.org/doi/10.1103/f285-l2v5

9. K. Capannelli, B. Undseth, I. Fernández de Fuentes, E. Raymenants, F. K. Unseld, O. Pietx-Casas, S. G. J. Philips, M. T. Mądzik, S. V. Amitonov, L. Tryputen, G. Scappucci, and L. M. K. Vandersypen. "Tracking spin qubit frequency variations over 912 days". en. In: *npj Quantum Information* 11.1 (Dec. 2025), p. 192. issn: 2056-6387. doi: 10.1038/s41534-025-01134-6

8. F. K. Unseld, B. Undseth, E. Raymenants, Y. Matsumoto, S. L. de Snoo, S. Karwal, O. Pietx-Casas, A. S. Ivlev, M. Meyer, A. Sammak, M. Veldhorst, G. Scappucci, and L. M. K. Vandersypen. "Baseband control of single-electron silicon spin qubits in two dimensions". In: *Nature Communications* 16 (July 2025), p. 5605. url: https://doi.org/10.1038/s41467-025-60351-x

7. B. Undseth, O. Pietx-Casas, E. Raymenants, M. Mehmandoost, M. T. Mądzik, S. G. J. Philips, S. L. de Snoo, D. J. Michalak, S. V. Amitonov, L. Tryputen, B. P. Wuetz, V. Fezzi, D. D. Esposti, A. Sammak, G. Scappucci, and L. M. K. Vandersypen. "Hotter is Easier: Unexpected Temperature Dependence of Spin Qubit Frequencies". In: *Phys. Rev. X* 13 (4 Oct. 2023), p. 041015. doi: 10.1103/PhysRevX.13.041015. url: https://link.aps.org/doi/10.1103/PhysRevX.13.041015

6. N. Paraskevopoulos, M. Steinberg, B. Undseth, A. Sarkar, L. Vandersypen, X. Xue, and S. Feld. "Near-Term Spin-Qubit Architecture Design via Multipartite

Maximally Entangled States". In: *PRX Quantum* 6.2 (Apr. 2025). issn: 2691-3399. doi: 10.1103/prxquantum.6.020307. url: http://dx.doi.org/10.1103/PRXQuantum.6.020307

5. S. R. Katiraee-Far, Y. Matsumoto, B. Undseth, M. D. Smet, V. Gualtieri, C. V. Meinersen, I. F. de Fuentes, K. Capannelli, M. Rimbach-Russ, G. Scappucci, L. M. K. Vandersypen, and E. Greplova. *Unified evolutionary optimization for high-fidelity spin qubit operations*. 2025. arXiv: 2503.12256 [quant-ph]

4. J. P. Zwolak, J. M. Taylor, R. W. Andrews, J. Benson, G. W. Bryant, D. Buterakos, A. Chatterjee, S. Das Sarma, M. A. Eriksson, E. Greplová, M. J. Gullans, F. Hader, T. J. Kovach, P. S. Mundada, M. Ramsey, T. Rasmussen, B. Severin, A. Sigillito, B. Undseth, and B. Weber. "Data needs and challenges for quantum dot devices automation". en. In: *npj Quantum Information* 10.1 (Oct. 2024), p. 105. issn: 2056-6387. doi: 10.1038/s41534-024-00878-x

3. B. Undseth, X. Xue, M. Mehmandoost, M. Rimbach-Russ, P. T. Eendebak, N. Samkharadze, A. Sammak, V. V. Dobrovitski, G. Scappucci, and L. M. Vandersypen. "Nonlinear Response and Crosstalk of Electrically Driven Silicon Spin Qubits". In: *Physical Review Applied* 19.4 (Apr. 2023). issn: 2331-7019. doi: 10.1103/physrevapplied.19.044078. url: http://dx.doi.org/10.1103/PhysRevApplied.19.044078

2. H. Jnane, B. Undseth, Z. Cai, S. C. Benjamin, and B. Koczor. "Multicore Quantum Computing". In: *Physical Review Applied* 18.4 (Oct. 2022). issn: 2331-7019. doi: 10.1103/physrevapplied.18.044064. url: http://dx.doi.org/10.1103/PhysRevApplied.18.044064

1. X. Xue, M. Russ, N. Samkharadze, B. Undseth, A. Sammak, G. Scappucci, and L. M. K. Vandersypen. "Quantum logic with spin qubits crossing the surface code threshold". In: *Nature* 601.7893 (Jan. 2022), pp. 343–347. issn: 1476-4687. doi: 10.1038/s41586-021-04273-w. url: http://dx.doi.org/10.1038/s41586-021-04273-w

